

STUDIES ON FREE AND IMPINGING JETS

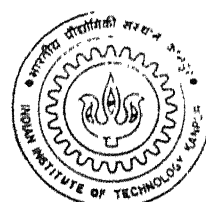
by

THERATIL IGNATIUS JOHN

AE
1994

D

JOH
STI



DEPARTMENT OF AEROSPACE ENGINEERING
INDIAN INSTITUTE OF TECHNOLOGY KANPUR
DECEMBER, 1994

23 JUN 1963

CHATHAM LIBRARY
121745
A121745

AF-1994-ORD-JOH-STU



A121745



Certificate

It is certified that the work contained in the thesis entitled "Studies on free and impinging jets" by "Theratil Ignatius John" has been carried out under my supervision and that this work has not been submitted elsewhere for a degree.

E Rav
Dec 7, 1994

(Dr. E RATHAKRISHNAN)

Department of Aerospace Engineering
Indian Institute of Technology, Kanpur 208 016, INDIA
December 1994

Abstract

This thesis gives the results of an experimental investigation carried out to examine the possibility of a unique length scale to obtain similarity of velocity profiles in the subsonic and underexpanded sonic freejet field right from the nozzle exit. The flow field has been investigated based on Mach number as well as measured pressure distribution. Contours of equal fraction of exit Mach numbers were constructed and termed as *iso-Mach lines*. The iso-Mach lines exhibited positive as well as negative gradients. The positive gradients are due to the dominance of the viscous effects, and the negative gradients are due to dominance of the inertia effects. The half velocity width when plotted in the spatial field of iso-Mach lines demarcated the jet field into two zones, namely, the zone of dominance of viscous effects above the half width and the zone of dominance of the inertia effects below the half width. The physical significance of the half velocity width is thereby established as follows : the half velocity width demarcates the flow field into zones of dominance of viscous and inertia effects.

On comparing the iso-Mach lines for a wide range of jet exit Mach numbers from 0.2 to correctly expanded sonic jet, in steps of 0.2, the positive gradient iso-Mach lines were found to collapse irrespective of the exit Mach numbers. The negative gradient iso-Mach lines show the effect of the initial inertia; iso-Mach lines of lower exit Mach number show lesser lateral and axial extent compared to those of higher exit Mach

numbers. Several length scales have been proposed by various investigators in the underdeveloped region of the jet flow field to obtain similarity of the velocity profiles, but only one scale exists for the developed region. Since the positive gradient iso-Mach lines collapse over a wide range of exit Mach numbers, it was assumed that similarity exists in the mixing region of the jet field excluding the inviscid core region. The half velocity width in the entire jet field right from the nozzle exit was taken with respect to the edge of the lateral extent of the potential core in the underdeveloped region, and with respect to the centre line in the region beyond the potential core. With this as the length scale complete velocity similarity of the flow field was established irrespective of the nozzle exit Mach numbers. The similarity profiles in the mixing region exhibited normal-distribution.

The flow field was also analyzed based with the measured (gauge) pressures. The isobars exhibited positive as well as negative gradients. The positive gradients are due to the expansion of the jet into the ambient, whereas the negative gradients are due to contraction or the retention of the initial pressure potential. The half pressure width was found to demarcate the flow field into zones of dominance of expansion above the half pressure width and zones of dominance of retention of the pressure potential below the half pressure width. Defining a pressure scale in terms of the gauge pressure and the length scale in terms of the half pressure width, complete similarity of the pressure field was obtained. This pressure similarity also exhibited normal-distribution.

The length scale for velocity similarity, the pressure scale and the corresponding length scale for pressure similarity was applied to the impinging jet field for exit Mach numbers from 0.2 to correctly expanded sonic in steps of 0.2. The pressure and the

velocity similarity in the impinging jet field was also found to exhibit normal distribution.

These scales were further extended to underexpanded free and impinging jets having the underexpansion levels $Pr = P_e/P_a$ as 1.2, 1.5, 2.0 and 2.25. The similarity of the velocity and pressure profiles exhibited normal-distribution for the underexpanded jets also.

The above scales were extended to bounded shear flows, namely, flow over flat plate. The origin of the local axis for similarity was taken at the maximum velocity contour. The half pressure width and the half velocity width as the length scale were defined with respect to the maximum velocity instead of the zero velocity at the boundary. The similarity obtained exhibited a fifth order polynomial variation. Similarity in the bounded shear flows and the free shear flows are compared. The bounded shear flow similarity switch to normal-distribution the moment the boundary is removed. This indicates thorough mixing in the free shear flows as compared to bounded shear flows. Further, the length scales obtained in the above analysis are independent of Reynolds number Schlichting [91].

The scales were also applied to radial walljet flow which is a combination of freeshear and bounded shear flows. The inner region of the walljet form the bounded shear flow, whereas the outer region of the walljet form the freeshear flow. Taking the location of the maximum velocity as the origin as before for defining the length scales, complete similarity of velocity profiles are obtained for the wallet field. Similarity in the inner region which is similar to the bounded shear flow and the outer region is similar to the freeshear flow. By the choice of these scales, the velocity similarity in the radial walljet region is independent of the α proposed by Glauert [38]. These scales are therefore

universal and are applicable to a wide variety of flow fields, which are either bounded or free or a combination or a combination of both or if they occur in succession.

The wall surface pressure distribution exhibits positive pressure zone as well as alternate pressure zones. Similarity of the wall positive pressure zone exhibits normal distribution, irrespective of the exit Mach number or levels of underexpansion. A force scale is also presented which exhibits similarity of forces on the wall for a wide range of Mach numbers upto correctly expanded sonic and for different nozzle-wall distances. The normalized force for underexpanded jets exhibits lower distribution as compared to subsonic to correctly expanded sonic jets. This is due to higher dissipation of energy across the potential core cellular structure.

In addition to the above mentioned analysis by actual measurements the free and impinging jet flow fields have been studied by visualizing them. For visualizing the underexpanded free and impinging sonic jets Schlieren technique has been employed and for the wall surface pressure field a surface coating technique has been used. From these pictures the effect of the jet Mach number, level of underexpansion, and the location of impingement wall on the freejet cellular structure, the impingement cellular structure, and on the stand-off shock wave were clearly broughtout. The wall surface coating revealed the information of the shear distribution on the impingement wall as a function of flow and geometrical parameters.

Acknowledgement

I take this opportunity to express my deep sense of gratitude for *Dr E. Rathakrishnan*, my thesis supervisor. During my association with him for nearly a decade as a teacher and as a person, I have had several experiences with him. He was easily accessible, patient, sincere and hospitable. His strong support and setting of a suitable environment to set up the experimental facility, his suggestions and open debates with appropriate course correction in the course of research has nourished my intellectual aspirations. A mere word of gratitude is insufficient to express my regard and respect to him.

My co-scholars with whom I had very special interaction to be remembered with thanks are *Prof Elangovan* gifted with sharp mind and openness to discuss, *Mr Himan-shu* gifted with excellent knowledge of computers and software, and *Mr. Srinivasan's* zeal to help and support.

During the setting up of the experimental apparatus and initial stages of the work *Mr. R Kannan* and *Mr Sanjeev* have been of immense help and special word of thanks for them. I also thank *Mr. Solaiappan* and *Mr Verma* for their help.

The supporting staff of our laboratory *Mr. Chauhan*, *Mr Bantu*, *Mr Tewari*, *Mr. Rajpal* and *Mr Shishupal* have given their whole hearted co-operation and assistance during the experimentation, and deserves special thanks. The technical support provided by *Mr Bhattacharya and his workshop staff* are thanked duly.

Mr. Mudappa's skilled technical support and timely location of treasures from his chesters at the time of need, and his personal concern has been very valuable.

A special word of thanks to *Mr. Ahmed*, *Mr Sushil* and the supporting staff of the office who have always supported me to the best of their ability.

I thank *Fr. Pereria* for his regular visits to take care of our spiritual needs in the

company of *Ms Hazel, Ms Ligi, Mr. Ravindra and fly., Ms. Viji, Mr. Johnson and Mr. Alphonse.*

My stay in the campus is incomplete without the mention of the homely environment provided by *Dr. Rathakrishan and fly., Prof. Elangovan and fly. and Mr. Mudappa and fly.*

The company of *Ms. Sobha, Mr. Neel and Mr Vydy* have been encouraging as well as dear. I appreciate their patience to listen to my endless discourses on this thesis.

I also thank *Ms Beena, Ms Pratima, and Mr Madhav* for their lively company. My stay in the hostel was filled by the company of Jebi, Murali, Stanley, Shaji, Appu, Sajid, George, Kishore and Jayakumar.

Fr. Felix's encouragement and support given to me during the vaccinations at Pune and *Fr. Vaz's* contribution towards taking the thesis photographs are remembered with gratitude.

This thesis has taken the present shape with the ideals, confidence and the strong support provided by my *parents, brother and sister.* Their contribution and total involvement in the preparation of the thesis has been of immense help.

*In the silence of our hearts, God speaks
and from the fulness of our hearts we speak. Mother Theresa*

to

Dad, Mom, Rency and Bobby

and

my

teachers

Contents

Certificate	ii
Abstract	iii
Acknowledgement	vii
List of Figures	xv
Nomenclature	xxvii
Synopsis	xxx
1 Introduction	1
2 Literature Survey	5
2.1 Freejets	5
2.2 Impinging jets	11
3 Experimental Apparatus and Procedure	20
3.1 Compressor unit	20
3.2 Flow system	21

3.3	Experimental models	22
3.3.1	Freejet studies	22
3.3.2	Impinging jet studies	22
3.4	Measurement systems	24
3.5	Flow visualization techniques	32
3.5.1	Schlieren technique	32
3.5.2	Surface coating technique	32
3.6	Calibration	33
3.7	Experimental runs	33
3.7.1	Freejet studies	34
3.7.2	Impinging jet studies	34
3.8	Data analysis procedure	35
3.9	Data accuracy	35
4	Freejet	36
4.1	Mach number based approach	38
4.1.1	Iso-Mach lines	39
4.1.2	Iso-Mach Spreads	41
4.1.3	Iso-Shear	48
4.1.4	Volume flow rate distribution	50
4.1.5	Coherent structures	52
4.1.6	Conclusions	54
4.2	Pressure based approach	57
4.2.1	Isobars	57

4.2.2	Iso-pressure-spreads	59
4.2.3	Conclusions	61
4.3	Comparative studies	63
4.3.1	Concluding remarks	66
5	Normal Impinging Jets	67
5.1	Mach number based approach	68
5.1.1	Iso-Mach lines	68
5.1.2	Iso-Mach spreads	71
5.1.3	Iso-shear	77
5.1.4	Volume flow rate distribution	82
5.1.5	Coherent structures	83
5.1.6	Conclusions	87
5.2	Pressure based approach	88
5.2.1	Impinging jet field	88
5.2.2	Wall surface distribution	93
5.2.3	Conclusions	98
6	Flat Plate and Radial walljet Flow	102
6.1	Velocity based approach	102
6.1.1	Flow over flat plate	103
6.1.2	Radial wall jet	105
6.1.3	Concluding remarks	112
6.2	Pressure based approach	113
6.2.1	Flow over a flat plate	113

6.3 Comparative studies	114
6.3.1 Concluding remarks	114
7 Underexpanded Freejets	118
7.1 Flow visualization	118
7.2 Pressure based analysis	123
7.2.1 Potential core	123
7.2.2 Decay	126
7.2.3 Isobars	128
7.2.4 Shear	128
7.2.5 Similarity	131
7.3 Conclusions	131
8 Underexpanded Normal Impinging Jets	134
8.1 Flow visualization	137
8.2 Impinging jet field	142
8.2.1 Decay	142
8.2.2 Isobars	142
8.2.3 Similarity	149
8.2.4 Shear	149
8.2.5 Wall pressure distribution	149
8.3 Conclusions	156
9 Oblique Impingement and Surface Visualization	157
9.1 Flow visualization	157

9.2	Impinging jet field	164
9.2.1	Spread characteristics	164
9.2.2	Wall surface pressure distribution	173
9.3	Surface patterns	188
9.4	Conclusions	189
10	Summary	196
	Scope for Further Research	198
	List of Publications	200
	Bibliography	201

List of Figures

1. Fig. 3.1 Schematic of the convergent nozzle
2. Fig. 3.2 Details of the plate
3. Fig. 3.3 Schematic of pitot tube
4. Fig. 3.4 Schematic of 3-hole probe
5. Fig. 3.5 Schematic of static probe
6. Fig. 3.6 U-tube mercury manometers
7. Fig. 3.7 Pitot probe in the impinging jet field
8. Fig. 3.8 Traversing mechanism for mounting the probe
9. Fig. 3.9 Multi-tube mercury manometer
10. Fig. 3.10 Multi-tube water manometer
11. Fig. 3.11 Lamp source and parabolic mirrors for Schlieren set-up
12. Fig. 3.12 Schematic of freejet and impinging jet test facility
13. Fig. 3.13 Test facility for impinging jet studies
14. Fig. 4.1 Schematic of the axisymmetric freejet flow field.
15. Fig. 4.2 Characteristics of freejet with $M_e = 0.4$...

16. Fig 4.3 Mach number distribution of freejet with $M_e = 0.8$...
17. Fig 4.4 Iso-Mach lines for freejet with $M_e = 0.4$ ($Re = 0.89 \times 10^5$) ...
18. Fig. 4.5 Effect of initial inertia on the iso-Mach lines ...
19. Fig 4.6 Spatial extent of compressible zones ...
20. Fig. 4.7 Comparison of centreline Mach number decay for different M_e ...
21. Fig. 4.8 Iso-spreads for various fractions b of centreline Mach number M_c with $M_e = 0.4$...
22. Fig. 4.9 Comparison of half velocity width $b = 0.5$ for different M_e ...
23. Fig 4.10 Complete similarity of velocity in *the underdeveloped and the developed region* for $M_e = 0.4$...
24. Fig 4.11 Complete similarity of velocity in *the underdeveloped and the developed region* for subsonic to correctly expanded sonic jet Mach numbers ...
25. Fig 4.12 Representation of shear ...
26. Fig. 4.13 Comparison of iso-volume flow rate ...
27. Fig 4.14 Comparison of entrained volume flow rate for different M_e .
28. Fig 4.15 Spatial rate of change of entrained volume flow rate ...
29. Fig. 4.16 Variation of g for free and impinging jets ...
30. Fig. 4.17 Change of volume flow rate at a radial location ...
31. Fig. 4.18 Radial location of volume flow rate change (max) ...
32. Fig. 4.19 Iso-Mach lines for various fractions f of exit Mach number ...
33. Fig. 4.20 Isobars and half pressure width for $M_e = 1.0$...

- 34 Fig. 4.21 Comparison of isobars for jet Mach numbers ranging from subsonic to correctly expanded sonic freejets ...
35. Fig. 4.22 Centreline pressure decay ...
36. Fig. 4.23 Iso-pressure spread lines for $M_e = 1.0$...
37. Fig. 4.24 Complete similarity of freejet field pressure distribution for $M_e = 0.4$
...
38. Fig. 4.25 Complete similarity of freejet field pressure distribution for subsonic to correctly expanded sonic jets ...
39. Fig. 4.26 Comparison of centreline pressure decay and Mach number decay ...
40. Fig. 4.27 Comparison of half pressure widths and velocity widths for freejets ...
41. Fig. 4.28 Comparison of pressure and velocity similarity for freejets ...
42. Fig. 5.1 Characteristic features of impinging jet
43. Fig. 5.2 Impinging jet with wall at $D_w = 7.5$ for $M_e = 0.2$...
44. Fig. 5.3 Impinging jet with wall at $D_w = 30.0$ for $M_e = 1.0$...
45. Fig. 5.4 Comparison of Iso-Mach lines of freejet with impinging jets at various wall locations for $M_e = 0.8$...
46. Fig. 5.5 Centre line decay of freejet compared with impinging jet centre line decay at various wall locations ...
47. Fig. 5.6 Impinging jet iso-spread lines with wall at $D_w = 30$ for $M_e = 0.6$...
48. Fig. 5.7 Comparison of half velocity widths between freejet and impinging jets at various wall locations ...
49. Fig. 5.8 Comparison of half velocity widths between freejet and impinging jets at various wall locations ...

50. Fig. 5.9 Comparison of half velocity widths at various wall locations ...
51. Fig. 5.10 Complete similarity of freejet and impinging jet field for $M_e = 0.4$...
52. Fig. 5.11 Complete similarity of freejet and impinging jet field for $M_e = 1.0$...
53. Fig. 5.12 Shear representation at various wall distances for $M_e = 0.2$...
54. Fig. 5.13 Shear representation at various wall distances for $M_e = 1.0$...
55. Fig. 5.14 Shear representation at various wall distances for $M_e = 0.8$...
56. Fig. 5.15 Comparison of iso-volume flow rate for different wall locations ...
57. Fig. 5.16 Comparison of impinging jet flow reversal location R with freejet $M_e = 0.4$...
58. Fig. 5.17 Comparison of impinging jet flow reversal location R with freejet $M_e = 0.6$...
59. Fig. 5.18 Mean coherent structures $M_e = 0.2$...
60. Fig. 5.19 Mean coherent structures $M_e = 0.4$...
61. Fig. 5.20 Mean coherent structures $M_e = 1.0$...
62. Fig. 5.21 Pressure of freejet compared with impinging jet at various wall locations for $M_e = 0.4$...
63. Fig. 5.22 Isobars of various fractions and half pressure width for $M_e = 0.2$ with wall at $D_w = 7.5$...
64. Fig. 5.23 Isobars of various fractions and half pressure width for $M_e = 0.4$ with wall at $D_w = 20.0$...
65. Fig. 5.24 Isobars of various fractions and half pressure width for $M_e = 0.8$ with wall at $D_w = 30.0$...

66. Fig. 5.25 Comparison of iso-bars of various fractions of freejet and impinging jet
...
67. Fig. 5.26 Comparison of half pressure widths between freejet and impinging jets
 $M_e = 0.6$: ...
68. Fig. 5.27 Complete similarity of freejet and impinging jet field for $M_e = 0.6$:
...
69. Fig. 5.28 Gauge wall pressure normalised with settling chamber pressure for
 $M_e = 0.4$...
70. Fig. 5.29 Wall isobars of various fractions $M_e = 0.6$...
71. Fig. 5.30 Comparison of wall isobars of various fractions ...
72. Fig. 5.31 Comparison of half pressure width for jet Mach numbers ...
73. Fig. 5.32 Similarity of wall pressures for jet Mach number $M_e = 0.8$...
74. Fig. 5.33 Comparison of similarity of wall pressures for jet Mach numbers ...
75. Fig. 5.34 Normalised force coefficient variation (computed upto 10 % of settling
chamber pressure) ...
76. Fig. 5.35 Zone of influence of positive pressure (radial extent upto 10 % of
settling chamber pressure) ...
77. Fig. 6.1 Characteristics of boundary layer on flat plate ...
78. Fig. 6.2 Normalised velocity distribution in the boundary layer over a flat plate
...
79. Fig. 6.3 Iso-velocity (iso-spread) lines in the boundary layer over flat plate ...
80. Fig. 6.4 Complete similarity of velocity distribution within the boundary layer
over flat plate ...
81. Fig. 6.5 Characteristics of radial wall jet ...

82. Fig. 6.6 Velocity distribution in the impinging radial wall jet reported by Tsuei(1962)
...
83. Fig. 6.7 Iso-velocity lines in the radial walljet field : ...
84. Fig. 6.8 Iso spread lines in the radial walljet field : ...
85. Fig. 6.9 Complete similarity of velocity distribution in the inner region of the
radial wall jet ...
86. Fig. 6.10 Complete similarity of velocity distribution in the outer region of the
radial wall jet ...
87. Fig. 6.11 Comparison of similarity between freejet and the outer region of radial
walljet ...
88. Fig. 6.12 Similarity comparison between freeshear flow and bounded shear flow
...
89. Fig. 6.13 Complete similarity of the pressure distribution for the boundary layer
over a flat plate ...
90. Fig. 6.14 Comparison between pressure and velocity similarity for flat plate :
...
91. Fig. 6.15 Comparison of pressure similarity for freejet and flat plate ...
92. Fig. 7.1 Characteristics of underexpanded sonic jets a) moderately underex-
panded b) highly underexpanded.
93. Fig. 7.2a Schlieren photograph of freejet $Pr = 1.2$
94. Fig. 7.2b Schlieren photograph of freejet $Pr = 1.5$
95. Fig. 7.2c Schlieren photograph of freejet $Pr = 2.0$
96. Fig. 7.2d Schlieren photograph of freejet $Pr = 2.25$
97. Fig. 7.3 Potential core : freejet $Pr = 1.2 \circ$ mean pressure * static pressure

98. Fig. 7.4 Potential core : freejet $Pr = 1.5$ o mean pressure * static pressure
99. Fig. 7.5 Potential core : freejet $Pr = 2.0$ o mean pressure * static pressure
100. Fig. 7.6 Potential core : freejet $Pr = 2.25$ o mean pressure * static pressure
101. Fig. 7.7 Decay of centre line pressure for sonic jet P_s ...
102. Fig. 7.8 Decay of centre line pressure for sonic jet P_C ...
103. Fig. 7.9 Isobars and half pressure width $Pr = 1.5$...
104. Fig. 7.10 Isobars and half pressure width $Pr = 2.0$...
105. Fig. 7.11 Comparison of isobars for sonic jets ...
106. Fig. 7.12 Comparison of half pressure widths ...
107. Fig. 7.13 Representation of shear : $Pr = 2.0$...
108. Fig. 7.14 Comparison of pressure similarity of sonic jet : ...
109. Fig. 8.1 Characteristics of cellular wave structure on normal impingement of underexpanded jet
110. Fig. 8.2 Schlieren photograph of normal impinging jet $D_w = 1.0$ and $Pr = 2.0$
111. Fig. 8.3 Schlieren photograph of normal impinging jet $D_w = 1.0$ and $Pr = 2.25$
112. Fig. 8.4 Schlieren photograph of normal impinging jet $D_w = 2.5$ and $Pr = 1.5$
113. Fig. 8.5 Schlieren photograph of normal impinging jet $D_w = 2.5$ and $Pr = 2.0$
114. Fig. 8.6 Schlieren photograph of normal impinging jet $D_w = 2.5$ and $Pr = 2.25$
- ~~115.~~ Fig. 8.7 Schlieren photograph of normal impinging jet $D_w = 4.0$ and $Pr = 1.2$
116. Fig. 8.8 Schlieren photograph of normal impinging jet $D_w = 4.0$ and $Pr = 2.0$
117. Fig. 8.9 Schlieren photograph of normal impinging jet $D_w = 4.0$ and $Pr = 2.25$

118. Fig. 8.10 Schlieren photograph of normal impinging jet $D_w = 5.0$ and $Pr = 2.25$...
119. Fig. 8.11 Decay of centre line gauge pressure for sonic jet at $Pr = 2.0$...
120. Fig. 8.12 Isobars and half pressure width $Pr = 1.2$ with $D_w = 8$...
121. Fig. 8.13 Isobars and half pressure width $Pr = 2.0$ with $D_w = 8$...
122. Fig. 8.14 Isobars and half pressure width $Pr = 1.5$ with $D_w = 20$...
123. Fig. 8.15 Comparison of half pressure widths $Pr = 2.0$...
124. Fig. 8.16 Comparison of isobars for sonic jet $Pr = 1.2$ at various wall locations
...
125. Fig. 8.17 Comparison of isobars for sonic jet $Pr = 1.5$ at various wall locations
...
126. Fig. 8.18 Comparison of isobars for sonic jet $Pr = 2.0$ at various wall locations
...
127. Fig. 8.19 Comparison of isobars for sonic jet $Pr = 2.25$ at various wall locations
...
128. Fig. 8.20 Comparison of pressure similarity of sonic freejet and impinging jets
...
129. Fig. 8.21 Comparison of pressure similarity of sonic freejet and impinging jets
...
130. Fig. 8.22 Representation of shear with wall at $D_w = 10$...
131. Fig. 8.23 Comparison of wall isobars ...
132. Fig. 8.24 Zone of influence upto 10 % of settling chamber pressure ...
133. Fig. 8.25 Normalised force coefficient distribution computed upto 10 % of settling chamber pressure ...

134. Fig 8.26 Comparison of wall pressure similarity ...
135. Fig 9.1 Characteristics features of oblique impinging jets :
136. Fig. 9.2 Schlieren photograph of oblique impinging jet $D_w = 1.0$, $\theta = 5$ and $Pr = 1.5$
137. Fig. 9.3 Schlieren photograph of oblique impinging jet $D_w = 1.0$, $\theta = 5$ and $Pr = 2.25$
138. Fig. 9.4 Schlieren photograph of oblique impinging jet $D_w = 2.0$, $\theta = 5$ and $Pr = 1.2$
139. Fig. 9.5 Schlieren photograph of oblique impinging jet $D_w = 2.0$, $\theta = 5$ and $Pr = 1.5$
140. Fig. 9.6 Schlieren photograph of oblique impinging jet $D_w = 2.0$, $\theta = 5$ and $Pr = 2.0$
141. Fig. 9.7 Schlieren photograph of oblique impinging jet $D_w = 2.5$, $\theta = 5$ and $Pr = 1.2$
142. Fig. 9.8 Schlieren photograph of oblique impinging jet $D_w = 2.5$, $\theta = 5$ and $Pr = 2.0$
143. Fig. 9.9 Schlieren photograph of oblique impinging jet $D_w = 2.5$, $\theta = 5$ and $Pr = 2.25$
144. Fig. 9.10 Schlieren photograph of oblique impinging jet $D_w = 4.0$, $\theta = 5$ and $Pr = 2.0$
145. Fig. 9.11 Schlieren photograph of oblique impinging jet $D_w = 4.0$, $\theta = 5$ and $Pr = 2.0$
146. Fig. 9.12 Schlieren photograph of oblique impinging jet $D_w = 1.5$, $\theta = 10$ and $Pr = 2.25$

147. Fig. 9.13 Schlieren photograph of oblique impinging jet $D_w = 2.0$, $\theta = 10$ and $Pr = 1.2$
148. Fig. 9.14 Schlieren photograph of oblique impinging jet $D_w = 2.0$, $\theta = 10$ and $Pr = 1.5$
149. Fig. 9.15 Schlieren photograph of oblique impinging jet $D_w = 2.0$, $\theta = 10$ and $Pr = 2.0$
150. Fig. 9.16 Schlieren photograph of oblique impinging jet $D_w = 2.0$, $\theta = 10$ and $Pr = 2.25$
151. Fig. 9.17 Schlieren photograph of oblique impinging jet $D_w = 2.5$, $\theta = 10$ and $Pr = 1.2$
152. Fig. 9.18 Schlieren photograph of oblique impinging jet $D_w = 2.5$, $\theta = 10$ and $Pr = 1.5$
153. Fig. 9.19 Schlieren photograph of oblique impinging jet $D_w = 2.5$, $\theta = 10$ and $Pr = 2.0$
154. Fig. 9.20 Schlieren photograph of oblique impinging jet $D_w = 2.5$, $\theta = 10$ and $Pr = 2.25$
155. Fig. 9.21 Schlieren photograph of oblique impinging jet $D_w = 3.0$, $\theta = 10$ and $Pr = 1.5$
156. Fig. 9.22 Schlieren photograph of oblique impinging jet $D_w = 3.0$, $\theta = 10$ and $Pr = 2.0$
157. Fig. 9.23 Schlieren photograph of oblique impinging jet $D_w = 4.0$, $\theta = 10$ and $Pr = 1.5$
158. Fig. 9.24 Schlieren photograph of oblique impinging jet $D_w = 4.0$, $\theta = 10$ and $Pr = 2.0$
159. Fig. 9.25 Schlieren photograph of oblique impinging jet $D_w = 4.0$, $\theta = 10$ and $Pr = 2.25$

160. Fig. 9.26 Fraction of spreads at $x = 4d$ with wall at $D_w = 5$ and $\theta = 5 \dots$
161. Fig. 9.27 Comparison of half pressure width in the impinging jet field with wall at $D_w = 5$ with $\theta = 5 \dots$
162. Fig. 9.28 Fraction of centre spread near the wall at $x = 4$, $D_w = 5$ $\theta = 5$ and $M_e = 1.0 \dots$
163. Fig. 9.29 Comparison of fractions of pressure widths in the impinging jet field with wall at $D_w = 5$, $x = 4d$ and $\theta = 5$ for $M_e = 0.6 \dots$
164. Fig. 9.30 Comparison of fractions of pressure widths in the impinging jet field with wall at $D_w = 5$, $x = 3.5d$ and $\theta = 10$ for $M_e = 0.6 \dots$
165. Fig. 9.31 Comparison of fractions of pressure widths in the impinging jet field with wall at $D_w = 5$, $x = 3.5d$ and $\theta = 10$ for $M_e = 0.6 \dots$
166. Fig. 9.32 Comparison of fractions of pressure widths in the impinging jet field with wall at $D_w = 10$, $x = 8.0d$ and $\theta = 10$ for $M_e = 0.6 \dots$
167. Fig. 9.33 Wall half pressure width for various settling chamber pressure conditions : $\theta = 5 \dots$
168. Fig. 9.34 Wall half pressure width for various settling chamber pressure conditions : $\theta = 10 \dots$
169. Fig. 9.35 Wall pressure distribution $\theta = 5$ $D_w = 2.5 \dots$
170. Fig. 9.36 Wall pressure distribution $\theta = 5$, $D_w = 5.0 \dots$
171. Fig. 9.37 Wall pressure distribution $\theta = 5$, $D_w = 7.5 \dots$
172. Fig. 9.38 Wall pressure distribution $\theta = 5$, $D_w = 10.0, \dots$
173. Fig. 9.39 Wall pressure distribution $\theta = 10$, $D_w = 2.5, \dots$
174. Fig. 9.40 Wall pressure distribution $\theta = 10$, $D_w = 5.0, \dots$
175. Fig. 9.41 Wall pressure distribution $\theta = 10$, $D_w = 7.5, \dots$

176. Fig. 9.42 Wall pressure distribution $\theta = 10, D_w = 10.0, \dots$
177. Fig. 9.43 Similarity of wall surface pressures $\theta = 5 +ve z \dots$
178. Fig. 9.44 Similarity of wall surface pressures $\theta = 5 -ve z \dots$
179. Fig. 9.45 Similarity of wall surface pressures $\theta = 10 +ve z \dots$
180. Fig. 9.46 Similarity of wall surface pressures $\theta = 10 -ve z \dots$
181. Fig. 9.47 Surface coating pattern $M_e = 0.4 D_w = 1.0$
182. Fig. 9.48 Surface coating pattern $M_e = 0.4 D_w = 2.0$
183. Fig. 9.49 Surface coating pattern $M_e = 0.4 D_w = 5.0$
184. Fig. 9.50 Surface coating pattern $M_e = 0.8 D_w = 2.0$
185. Fig. 9.51 Surface coating pattern $M_e = 0.8 D_w = 4.0$
186. Fig. 9.52 Surface coating pattern $M_e = 0.8 D_w = 10.0$
187. Fig. 9.53 Surface coating pattern $Pr = 1.2 D_w = 4.0$
188. Fig. 9.54 Surface coating pattern $Pr = 1.2 D_w = 10.0$
189. Fig. 9.55 Surface coating pattern $Pr = 1.5 D_w = 4.0$

Nomenclature

- a* experimentally deduced constant
- b* fraction of the centre line Mach number
- d* nozzle exit diameter
- f* fraction of nozzle exit Mach number
- g* $\frac{\Delta Q}{Q_e}$ at a given radial location
- l* flat plate length = 800 mm
- p_f* fraction of initial exit pressure
- q* fraction of initial volume flow rate
- r* lateral distance from the centre line
- r_e* nozzle exit radius
- x* axial distance from the nozzle exit
- y* transverse axis
- z* normal to x-y plane
- I.D.** inner diameter
- O.D.** outer diameter
- C* rate of increase of entrained volume flow rate

D plate diameter = 300 mm

D_w nozzle-wall distance in terms of nozzle diameter

D_m Mach disc diameter

F_N normalized force coefficient

K spatial decay rate of Mach number

L length of the nozzle

M jet field Mach number

M_c jet centre line Mach number

M_e nozzle exit Mach number

P absolute jet field pressure

P_a atmospheric pressure

P_g field gauge pressure normalized with settling chamber pressure

P_e jet exit gauge pressure

Pr degree of underexpansion

P_s settling chamber gauge pressure

P_{st} static pressure (absolute)

P_w gauge wall pressure normalized with settling chamber pressure

P_C normalized centre line gauge pressure

P_G gauge pressure in the jet field

P_S pressure scale for similarity

P_W wall pressure scale for similarity (underexpanded jets)

P_* field gauge pressure normalized with correctly expanded gauge pressure

Q volume flow rate

Q_e initial exit volume flow rate

R radial location of maximum change of volume flow rate

Re Reynolds number

S normalized representation of shear

V local velocity

V_c local maximum velocity along x

V_e jet exit velocity

V_∞ free stream velocity

V_m maximum velocity

X_m Mach disc distance from the nozzle exit

η universal length scale for similarity profiles

σ non-dimensional parameter in normal-distribution

θ angle of inclination with respect to the z-axis

Δ length of a single cell

Synopsis

Introduction

Freejets as well as impinging jets find application in a wide range of practical problems starting from household appliances to high-tech rocket missions. They are used in several application processes such as cooling, impact loading, launch vehicle operations, attitude control operations, etc.

Freejets and impinging jets, being problems of practical interest, have been studied by a large number of researchers over many decades. Continued attempt is being made by researchers to understand the structure of these jets for better utilization of them for practical applications. Both experimental and theoretical techniques are applied to throw more light on the qualitative as well as quantitative nature of these flow fields. The present work aims at a deeper understanding of this practical problem to investigate the possibility of establishing some scales like; velocity scale, pressure scale, length scale and force scale to develop some unique relations based on the mean pressure measurements of the jet flow field and impingement wall surface pressure distribution.

With the above goals in mind, a modest experimental attempt has been made to understand the jet structure for jet Mach numbers M_e ranging from 0.2 to 1.0, in steps of 0.2, and sonic jets with underexpansion level $Pr = 1.2, 1.5, 2.0$ and 2.25 based on

the mean pressure measurements. Normal impingement has been investigated for the above range of M_e and underexpansion levels of the freejet with wall locations varying from 2.5d to 40.0d. Oblique impingement for $\theta = 5^\circ$ and $\theta = 10^\circ$ has been investigated for wall locations at 5.0d, 7.5d and 10.0d, with the following exit conditions : $M_e = 0.6$, 0.8 and 1.0 and underexpansion levels $Pr = 1.0$, 1.2 and 1.5.

The experimentally measured mean pressure data have been analyzed to yield the jet decay, spread, contours of constant fraction of the initial velocity and pressure in the jet field, velocity and pressure similarities right from the nozzle exit to the far field for free and impinging jet fields. The measured wall pressure distribution has been analyzed to reveal results of the zone of influence and the non-dimensional force as a function of various flow and geometrical parameters.

In addition to the actual quantitative measurements, visualization of the flow field has been carried out with Schlieren and surface coating techniques.

Experimental Procedure

Freejet was generated by discharging high pressure air from a settling chamber through a convergent nozzle into quiescent surrounding atmosphere. The desired Mach numbers were achieved by controlling the settling chamber pressure.

For impinging jet studies, the above freejet was made to impinge on a rigid wall kept normal as well as oblique to the axis of the freejet. The jet field pressures were measured by a pitot probe mounted on a traverse mechanism with six degrees of freedom (three translational and three rotational). This enabled the measurements at desired locations in the jet field.

For the measurements of wall pressures on the impingement wall, number of wall pressure taps were arranged along a diameter of the disk used as the wall. For measurement of centreline static pressure distribution, a disk probe was used. All the pressures were measured using mercury-in-glass and water-in-glass manometers.

For visualizing the wave cell structure in the underexpanded sonic jets (free as well as impinging) Schlieren technique was employed. For visualizing the surface flow pattern on the impingement wall, a surface coating with lamp black and water pump grease was used.

RESULTS

The main results of the present experimental investigation on free and impinging jets are the following. The scales obtained for the velocity (Mach number) similarity, pressure similarity and force similarity:

Velocity similarity

Velocity scale

$$M/M_c \quad (1)$$

where, M - field Mach number and M_e - centre line Mach number

Length scale

$$\eta = \frac{(r - r_{b=1.0})}{(r_{b=0.5} - r_{b=1.0})} \quad (2)$$

where, η - non-dimensional length scale, r - local axis in the y -direction with the origin along $b = 1.0$, b - fraction of the centre line velocity ranging from 1.0 (lateral extent of the potential core in the underdeveloped region and centreline in the region beyond the potential core) to 0.0 (edge of the jet) and $r_{b=0.5}$ - half velocity width from $b = 1.0$ contour

Pressure similarity

Pressure scale

$$P_S = (P/P_a - 1.0)/(P_c/P_a - 1.0) \quad (3)$$

where, P_S - similarity pressure scale, P_a - atmospheric pressure, P_c - centre line pressure, and P - absolute field pressure

Length scale

This length scale for pressure similarity is the same as that for velocity similarity, where the corresponding terms are related to measure gauge pressures

Force similarity

$$F_N = \frac{2 \int_{y=0.0}^{y=p_f} y P(w) dy}{r_e^2 P_e} \quad (4)$$

where, F_N - normalized force coefficient, p_f - fraction of exit gauge pressure, P_e - exit gauge pressure, P_w - wall surface pressures and y - lateral co-ordinate

The above velocity and pressure similarity scales were applied to free and impinging jet fields. Complete similarity of the field was obtained right from the nozzle exit in

the mixing region, for jet Mach numbers from 0.2 to sonic level with correct as well as different levels of underexpansion. The typical similarity profiles are given in Figs. 1 and 2. They exhibit normal-distribution.

The normal impingement force field similarity is shown in Fig 3.0 for jet Mach numbers from subsonic to correctly expanded sonic jets.

The above pressure and velocity similarity scales have been applied to bounded shear flows, namely, to the boundary layer flow over a flat plate. The origin for the local axis was taken on the contour defined by the maximum freestream velocity. Complete similarity of the flow field has been established in the boundary layer and it is independent of Reynolds number. The similarity distribution exhibited a fifth order polynomial variation. Comparison of similarity between free and bounded shear flows indicate the effect of entrainment on similarity profiles caused by the presence of boundary as seen in Fig. 4.0. These scales were also extended to the inner region and the outer region of the radial walljet flow.

In addition to the above mentioned similarity, the flow fields have been analyzed by constructing contours of equal fractions of exit Mach number termed as iso-Mach lines, equal fraction of centre-line Mach number termed as iso-spreads, in terms of isobars, and volume flow rate distribution. The field characteristics are also investigated in terms of iso-shear. It was interesting to note that the analysis with contours of constant values of spatial rate of change of volume flow rate resulted in the mapping of coherent structures in the jet field.

The physical significance of half velocity width has been established. It demarcates the jet field into zones of dominance of viscous and inertia forces. The impingement wall location is found to strongly influence the viscous dominant zone of the jet field

compared to the inertial dominant zone.

The effect of the level of underexpansion on the cellular structure on the freejet field characteristics has been studied and compared with correctly expanded sonic jet.

The effect of the parameters such as

- location of the plate within a cell or beyond a cell
- the level of underexpansion on the stand-off shock
- retention of the freejet characteristics when a plate is placed beyond a complete cellular structure
- nozzle-wall distance

on the cellular wave structure are investigated.

Surface coating technique has been employed to study the surface flow pattern for subsonic as well as sonic underexpanded jets.

- the surface flow patterns are divided into two zones for subsonic impingement:
 - a) zone of positive pressure b) zone of dominance of shear displaying concentric discontinuous repetitive deposits
- for underexpanded impingement, there are four distinct zones a) zone of positive pressure b) zone of high shear due to acceleration of fluid into the walljet region c) zone of intersecting arcs resulting from the expansion and compression waves, and d) zone of shear similar to subsonic impingement.

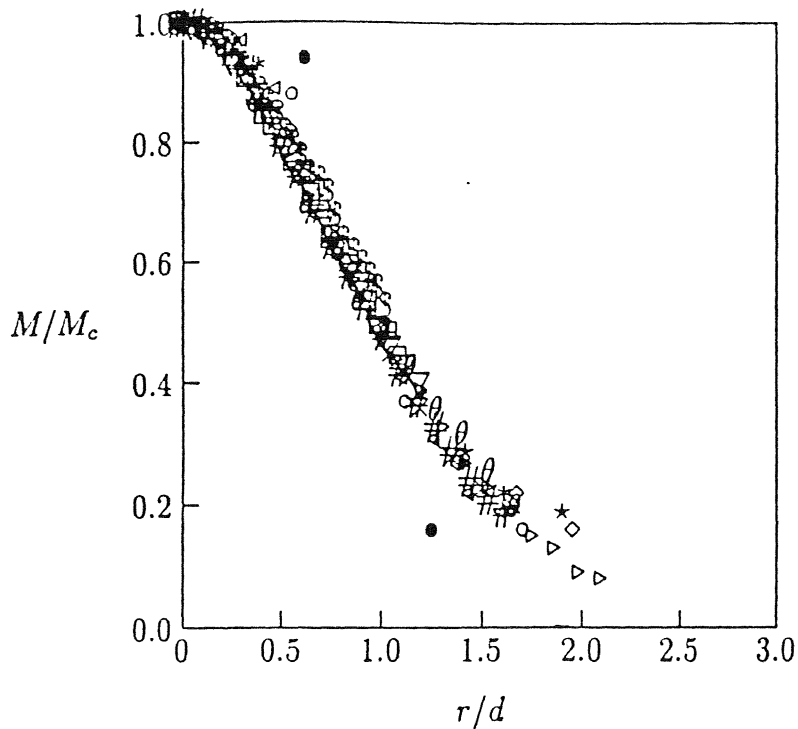


Fig. 1 Complete similarity of Mach number distribution in the underdeveloped zone and the developed zone for $M_e = 0.4$. • $0.5d$, ○ $1.0d$, ★ $2.0d$, ◇ $3.0d$, * $4.0d$, ▲ $5.0d$, × $6.0d$, θ $8.0d$, ▽ $11.0d$, # $14.0d$, ∇ $19.0d$, □ $25.0d$, and § $30.0d$.

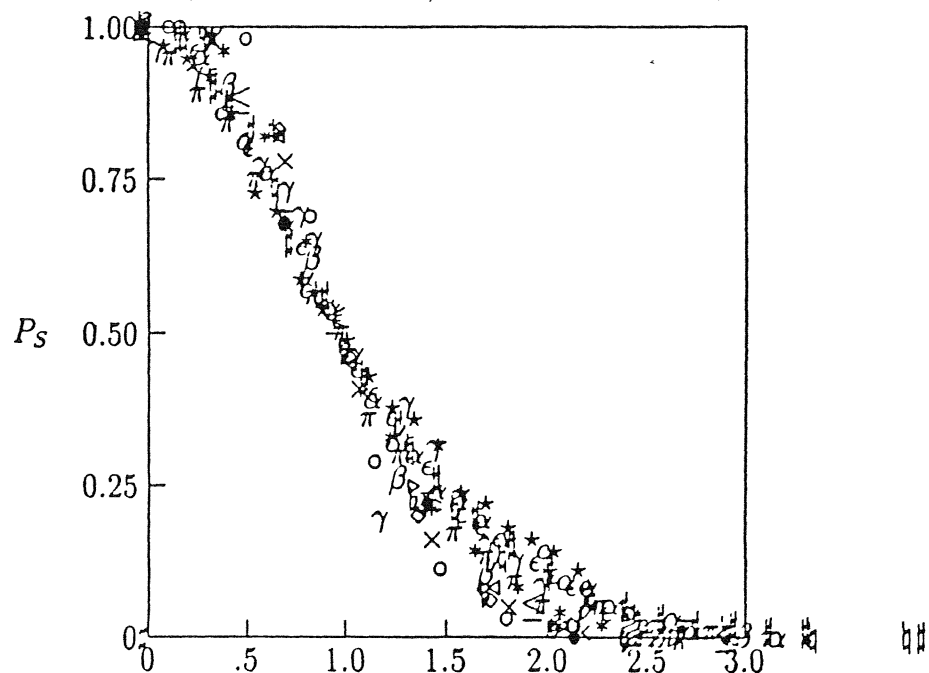


Fig. 2 Complete similarity of pressure for free and impinging jet at various wall locations for Mach number $M_e = 0.6$ freejet ○ $2.5d$, ★ $17.0d$, impinging jet • $D_w = 2.5$ $1.5d$, ◇ $D_w = 5.0$ $3d$, ▲ $D_w = 7.5$ $3.0d$, * $D_w = 10.0$ $3d$, # $D_w = 12.5$ $3.0d$, ∫ $D_w = 15.0$ $3d$, π $D_w = 13d$, ≤ $D_w = 20.0$ $3d$, α $D_w = 17d$, ν $D_w = 25.0$ $3d$, β $D_w = 30.0$ $3d$, γ $D_w = 27d$.

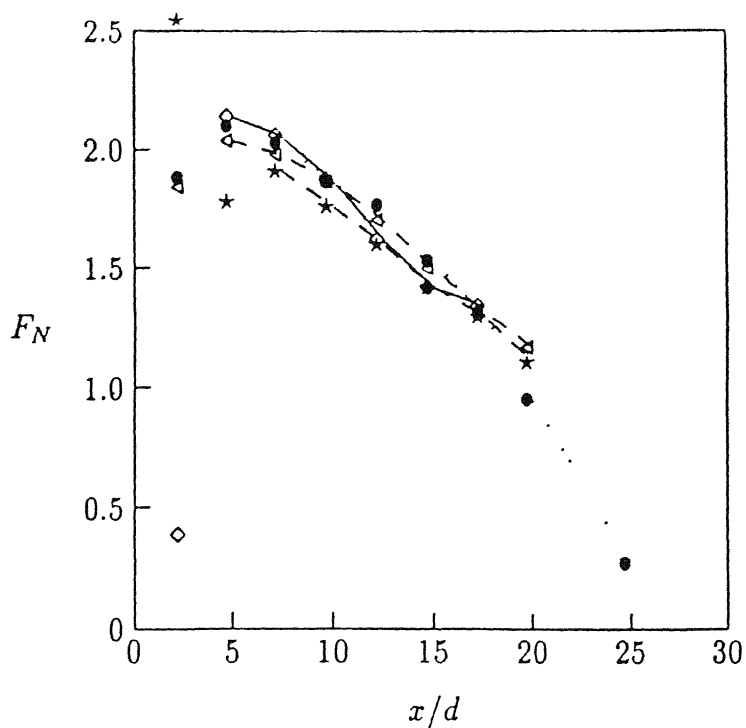


Fig. 3 Normalised force coefficient computed upto 10 % of settling chamber pressure $\star M_e = 0.4$, $\bullet M_e = 0.6$, $\diamond M_e = 0.8$, $\triangle M_e = 1.0$.

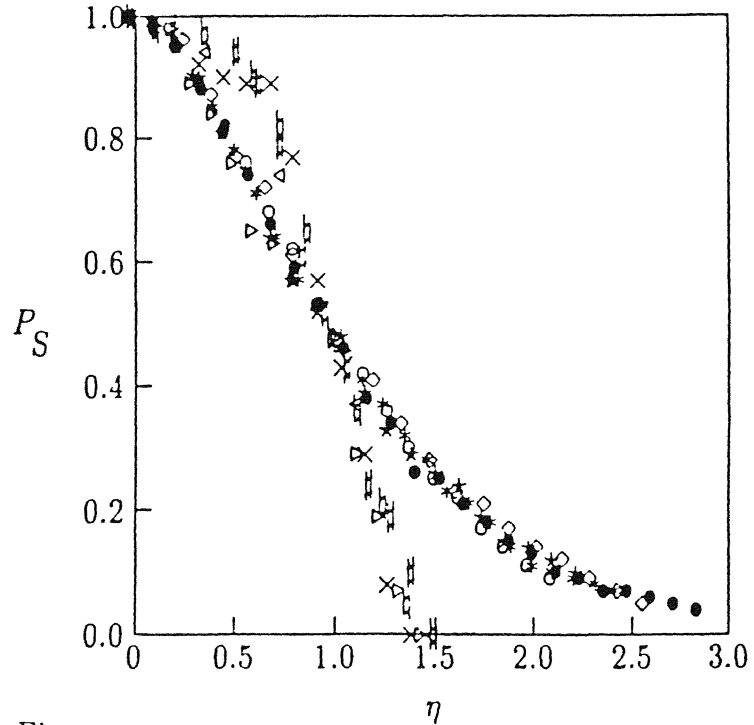


Fig. 4 Comparison of pressure similarity for free jet and flat plate. freejet : $M_e = 0.2 \bullet 15.0d$, $M_e = 0.4 \circ 17.0d$, $M_e = 0.6 \star 16.0d$, $M_e = 0.8 \diamond 15.0d$, $M_e = 1.0 \times 20.0d$, flat plate: $\triangle x/l = 0.06$, $\times x/l = 0.29$, $\square x/l = 0.51$, $\diamond x/l = 0.69$, and $\# x/l = 0.88$.

Chapter 1

Introduction

Freejets are freeshear flows driven by pressure potential issuing into ambient surrounding which is either at rest or in motion. The propagation of freejet is always associated with broadening of the jet width, and the decay of the mean and radial velocity. The jet flow field may be broadly divided into different zones, namely, the potential core which is inviscid and the mixing zone which is highly viscous and is characterized by the transfer processes of mass, momentum and energy. The mixing zone results due to penetration of the ambient mass into the jet field because of the shear due to the differential velocity at the jet boundary. This process is called *entrainment*.

Jets may be classified based on the nozzle exit Mach number M_e , as follows:

- when $M_e < 1$, the jet is called a **subsonic** jet
- when $M_e = 1$, the jet is termed as **sonic** jet
- when $M_e > 1$, the jet is referred to as **supersonic** jet

The subsonic jets are always correctly expanded implying that the static pressure at the nozzle exit P_e is exactly equal to the ambient atmospheric pressure P_a . This

is due to the fact that if the flow is underexpanded it has to expand outside the nozzle in order to come to equilibrium with the ambient pressure. This action would decrease the velocity in the jet according to isentropic flow theory, and consequently the pressure would increase, thus aggravating the situation further and creating an impossible process. In the same manner, if the subsonic jet were to be overexpanded then there would be contraction of the jet according to the isentropic theory and increase in velocity. This would result in further decrease of the pressure again leading to an impossible situation.

The sonic jets are said to be correctly expanded or underexpanded depending on whether $P_e = P_a$ or $P_e > P_a$, respectively. The ratio of P_e/P_a is called *the degree of underexpansion* denoted by Pr . For values of P_e/P_a upto 2.0, the jet is said to be moderately underexpanded, and is called highly underexpanded for $P_e/P_a > 2.0$.

The supersonic jets are designated as correctly expanded, underexpanded, and overexpanded depending on whether $P_e = P_a$, $P_e > P_a$ and $P_e < P_a$, respectively. The jet Mach number has strong influence over the potential core. For subsonic jets, the potential core extends upto about $5d$, where d is the equivalent diameter of the nozzle exit. The velocity within the potential core is the same as the nozzle exit velocity. The potential core for correctly expanded sonic jets also possesses similar nature as that of subsonic jet. However for underexpanded sonic and supersonic jets, the potential core is dominated by the cellular wave structure that extends upto the axial location where the axial velocity becomes subsonic. The length of the potential core for these jets extends even upto $12d$ for supersonic jets.

A freejet when allowed to impinge on a solid surface is called an *impinging jet*. If the solid surface is kept normal to the jet axis, then the impingement is called *normal*

impingment, and if it is kept at an angle to the jet axis the impingement is termed as *oblique* impingment. Impinging jet has the characteristics of freeshear flow in the freejet regime, bounded shear flow in the impingement regime, and free and bounded shear flow in the walljet regime. In the case of underexpanded near field impinging jets, the cellular structure of the potential core is altered by the presence of the wall with a normal standoff shock ahead of the solid surface. The flow downstream of the shock is subsonic and accelerates into the walljet regime with expansion and compression waves.

Freejets as well as impinging jets find applications in a wide range of practical problems starting from household appliances to high-tech rocket missions. Free and impinging jets are used in several application processes such as cooling, impact loadings, launch vehicle operations, attitude control operations, stage separation of multistage rockets, extraterrestrial landing, combustion chamber, docking of spacecrafts, ground cushion vehicles, etc.. Freejets and impinging jets being problems of practical interest have been studied by a large number of researchers over many decades. Continued attempt is being made by researchers to understand the structure of these jets for better utilization of them for practical applications.

Both experimental and theoretical techniques are applied to throw more and more light on the qualitative as well as quantitative nature of these flow fields. The present work aims at a deeper understanding of this interesting practical problem to investigate the possibility of some scales like; velocity scale, pressure scale, length scale and force scale to develop some unique solutions based on the mean pressure measurements of the jet flow field and impingement wall pressure distribution.

With the above goals in mind, a modest experimental attempt has been made to

understand the jet structure for Mach numbers M_e ranging from 0.2 to 1.0, in steps of 0.2, and sonic jets with underexpansion level $Pr = 1.2, 1.5, 2.0$ and 2.25 based on the mean pressure measurements. Normal impingement has been investigated for the above range of M_e and underexpansion levels of the freejet with wall locations varying from $2.5d$ to $40.0d$. Oblique impingement for $\theta = 5^\circ$ and $\theta = 10^\circ$ has been investigated for wall locations at $5.0d$, $7.5d$ and $10.0d$, with the following exit conditions $M_e = 0.6, 0.8$ and 1.0 and underexpansion levels $Pr = 1.2$ and 1.5 .

The experimentally measured mean pressure data have been analyzed to yield the jet decay, spread, contours of constant fraction of the initial velocity and pressure in the jet field, velocity and pressure similarities right from the nozzle exit to the far field for free and impinging jet field. The measured wall pressure distribution has been analyzed to reveal results of the zone of influence and the non-dimensional force as a function of various flow and geometrical parameters.

In addition to the actual quantitative measurements, visualization of the flow field has been carried out with Schlieren and surface coating techniques.

Chapter 2

Literature Survey

The study of freejets and impinging jets has been of their considerable importance because of their wide range of applications. Large amount of literature is available on free and impinging jets. Complete survey of literature on jets is almost a formidable task. Therefore in the following literature survey, the works which are of direct relevance to the present investigation alone have been presented.

2.1 Freejets

Tollmien seems to be the first to investigate the freejets theoretically, based on the Prandtl's mixing length hypothesis, in the year 1926. The mean flow characteristics predicted through the semi-empirical relations were found to agree well with the experimental results, but required an experimentally deduced constant. These experimental as well as the later theoretical works are well documented in the monographs by Abramovich, (1963) [1], Birkhoff and Zarantonello, (1957) [12], Hinze (1975) [47],

Pai (1954) [81], Rajaratnam (1976) [85], Schlichting (1954) [91], and Townsend (1956) [97].

The jet structure essentially comprises of two regions ; underdeveloped (*potential core and transition zone*) and fully developed zones. One of the prime objectives of jet research seem to be the identification of appropriate length and velocity scales to achieve similarity of the field. However, earlier investigations on jets revealed the possible existence of more than one length scale. Even though these scales resulted in similarity under certain specified conditions, the similarities cannot be called complete similarity, since the existence of more than one length scale and velocity scale implies incomplete or imperfect similarity, Hinze [47].

Velocity similarity in the fully developed flow region with centreline velocity and the half velocity width as the velocity and the length scale, respectively , were reported by Bradbury, (1981) [13], Bynton (1963) [16], Schlichting (1954) [91], Townsend (1956) [97], and Wygnanski and Fiedler (1969) [102]. These similarities are restricted to fully developed regions only. The underdeveloped region was forced towards similarity by Abramovich (1963) [1], Bradshaw et al. (1964) [14], Davies et al. (1963) [25], Lau et al. (1979) [66], Hussain and Clark (1981) [52], Islam (1980) [56], and Koplin (1964) [63] , each defining an appropriate lateral length scale.

Non-dimensionalized axial length scale as a function of Reynolds number was defined by Rankin et al. (1983) [86] to obtain collapse of the velocity distribution for the later part of the underdeveloped region. The jet spread parameter defined by Maydew and Reed (1963) [74] to obtain collapse of the velocity profiles, was found to be invariant in the Mach number regime 0.7 to 0.95, but is found to increase for supersonic Mach number regime. Albertson et al. (1950) [6], on the other hand assumed complete

similarity of the diffusion process in the underdeveloped and developed flow field of the freejet. With further assumptions of normal-probability variation of the velocity and the spread width of the jet as 0.605 of the centreline velocity, analytical expressions to predict the mean flow pattern were derived. These expressions which were verified experimentally also depended on experimentally deduced constant.

The developing and the developed region of the jet are characterized by the presence of large-scale organized motions and fine-scale random motions. The large-scale motions known as *coherent structures* are responsible for the transport of mass, momentum and heat without being highly energetic itself, whereas incoherent structures (*fine-scale motions*) are associated with high level of kinetic energy. The initial instability at the nozzle exit causes the rollup of the outer shear layers, resulting in the engulfment of the ambient mass into the jet stream through diffusion, and subsequent formation of organized large-scale turbulent fluid mass downstream. The underdeveloped region is also characterized by a faster moving inner shear layer and a slower moving outer shear layer. The slower moving shear layers carrying the entrained mass drift away from the faster moving shear layers. Further downstream, the faster moving shear layers fragment. These observations were reported by Wygnanski and Fiedler (1970) [103] for plane mixing layers and by Hussain and Clark (1981) [52] for free jets. The existence of large-scale structures in the jet was suggested by Townsend (1956) [97] as big eddies, and numerically investigated by Grant (1978) [40], and Acton (1980) [2]. Presence of large-scale, quasi-periodic or eddy structures in the initial noise producing region were reported by Bradshaw et al. (1964) [14], Crow and Champagne (1971) [22], Davis (1982) [26], Lau et al. (1979) [66], Hussain and Zaman (1980a,1980b) [53, 54], Hussain and Clark (1981) [52], Maestrello and Fung (1979)

[72], Moore (1977) [77], and Mollo-Christensen et al. (1964) [76]. The presence of large-scale structures in the similarity region was examined by Komori and Ueda (1983) [62], Oler and Goldschmidt (1982,1984) [78, 79], Shinich et al. (1989) [94], Tso et al. (1981), Tso and Hussain (1983) [99, 98], and Yule (1978) [104]. Contribution to noise by large-scale structures was reported by Ffowcs Williams and Kempton (1978) [31]. Comparison of the actual spatial distributions of the structure properties with those deduced through the use of Taylor's hypothesis from the temporal measurements was reported by Zaman and Hussain (1981) [105]. The review articles by Fiedler (1988) [32] and Hussain (1983,1986) [50, 51] provide analytical and experimental constraints in the deduction of coherent structures. Various aspects of the coherent structures such as the effects of initial conditions, the role of coherent structures in jet noise production and broadband noise amplification, the feedback effect of coherent structures, the use of Taylor hypothesis in coherent structure description, negative production, turbulence suppression via excitation, validity of Reynolds number similarity, etc.. are also covered in the review.

Flow visualization has been employed for qualitative description of the large-scale coherent structures. The picture on the existence of coherent structures was first reported by Brown and Roshko (1974) [15], and the mechanism of amalgamation of the structures and its relation to the growth of the shear layer was studied by Winant and Browand (1974) [101]. Quantitative information on the coherent structures was based on the coherent vorticity, defined as "spatially phase-correlated large scale instantaneous vorticity" obtained through measurements. Digital image processing technique applied by Chao et al. (1990) [18], based on jet fluid concentration contours provided reasonable quantitative as well as qualitative information on the mechanism of

the growth and degeneration of the coherent structures. Gouldin (1988) [39] assumed that the instantaneous jet structure to be a constant property surface, and established a semi-empirical model based on fractal concepts. Schlieren, pH indicator techniques, etc. are also employed by researchers to obtain qualitative information on coherent structures.

The growth of the jet downstream, defined on the basis of the half velocity width as the length scale was found to be dependent on the initial shear layer instability as reported by Crow and Champagne (1971) [22], Drubka et al. (1989) [30], HO and Huang (1982) [48], and Laufer and Zhang (1983) [67]. The growth is shown to depend on the acoustical feed back by HO and Nosseir (1981) [49] and Laufer and Zhang (1983) [67], Gutmark and HO (1983) [43] reported that the growth of the jet is influenced by the inherent characteristics of the individual testing facilities, in addition to the initial shear layer instabilities and the acoustical feedback. The spreading of the jet was reported to be on an average, a linear step wise phenomena associated with saturation locations by Laufer and Zhang (1983) [67]. Control of the jet spread by optimizing the initial conditions was also shown theoretically by Lee and Liu (1993) [68], through the integral formulation.

The phenomenon of entrainment of fluid mass occurs by a diffusion process. The exact mechanism of entrainment is also believed to be attributed mainly to the engulfment of the irrotational fluid mass by large-scale coherent structures Hussain (1983,1986) [50, 51], Fiedler (1988) [32] and Dahm and Dimotakis (1987) [23]. The flow visualization by Shlien (1987) [95] concluded that the entrainment activity to be the result of engulfment by the large scale structures in the self preserving region. Hill (1972) [46] measured the local entrainment rate in the initial region using the 'porous-wall

technique' developed by Ricou and Spalding (1961) [87]. The local entrainment rate is dependent on the jet Reynolds number. For Reynolds number more than 6×10^4 , it was found to depend strongly upon the axial distance. The review article by Thomas (1991) [96] on the structure of plane mixing layers presents the more recent and earlier investigations on the problem.

Underexpanded jets are characterized by cellular wave structures in the near field. The sensitivity of the degree of expansion on the parameters, namely the Mach disk diameter and its location, the jet boundary and the characteristics of the mixing zone has been the subject of investigation over several years. Highly underexpanded sonic and supersonic jets were investigated by Adamson and Nichols (1959) [3]. They proposed a technique to identify the Mach disc location. They predicted location of the Mach disk was verified experimentally. An approximate method to compute the boundary of the jet was also presented. The effect of the ratio of specific heats, condensation, nozzle lip geometry and the absolute pressure level on the Mach disk location and its diameter was reported by Crist et al. (1966) [21]. Donaldson and Snedeker (1971) [28] reported the spreading and decay characteristics of moderately underexpanded and highly underexpanded jets. Addy (1981) [4] studied the effects of axisymmetric sonic nozzle geometry on Mach disk characteristics and established semi-emperical relation and bounds for Mach disk diameter and locations.

From the above survey it is evident that large quantity of literature revealing different aspects of the freejet field is available. Even though all possible parameters of this problem have been covered in the investigation reported, they aim at specific features of the jet structure. The similarity scales reported are either partial or valid only for the fully developed zone. Likewise, the underexpanded jet studies reported are for a

specific range of underexpansion. Therefore, there is a need for further investigation on the problem of freejets covering a wide range of parameters to investigate the jets

- With the range of Mach numbers from low subsonic to Mach 1.0.
- Covering a range of underexpansion from low to highly underexpanded.
- To examine the existence of a universal length scale to result in complete similarity of velocity profiles, as well as pressure and the corresponding pressure scales to obtain similarity of pressure profiles.
- To study the possibility of capturing the large scale structures based on the mean measurements.
- To study the effect of cellular structures on the mixing characteristics.

2.2 Impinging jets

The freejet characteristics are bound to be influenced when a solid surface intercepts the jet axis either normally or obliquely. The impinging jet flow field consists of the freejet part and the flowfield on the impingement plane. The freejet part of the impinging jet exhibits all the features of the jet, of course with the effect of the impingement plane on them. The flow field on the wall basically consists of two distinct zones; the positive pressure zone around the axis of impingement followed by a walljet type of flow.

Jet impingement studies scanning the similarity of velocity profiles, the length scale, centre line velocity decay, and other characteristics have been carried out by Donaldson and Snedeker (1971) [28], Beltaos and Rajarathnam (1974) [11], Beltaos (1976)

[10], Davanipour and Sami (1977) [24], Gutmark et al. (1958) [44], and Looney and Walsh (1984) [71]. In these studies they concentrated on the above mentioned features. Similarity pressure profiles in the impingement zone above the wall and at the wall surface have been investigated by Beltaos and Rajarathnam (1974) [11]. They established similarity of the wall pressure with the wall half pressure width as the length scale. Similarity of wall surface pressures for single and multijet impingements were correlated with the length scale which is the half velocity width of the freejet at the corresponding location of the wall by Bradbury (1981) [13].

A model for characterization of the impingement region was proposed by Giralt et al. (1977) [37]. In which the velocity and the jet width at the location above the wall surface where the jet deflects have been chosen as the velocity and length scales, respectively. These results were found to agree closely to inviscid solutions. A laminar non-uniform impinging jet was studied theoretically and experimentally by Scholtz and Trass (1970) [93]. The theoretically predicted velocity and pressure distribution agree with the experimental results. Donaldson and Snedeker (1971) [28] conducted parametric study of the wall pressure distribution, choosing various surface shapes such as concave, convex hemispheres, cylindrical cup and flat plate. Wall pressure distribution due to three types of jets from a convergent nozzle, namely, subsonic, moderately and highly underexpanded were considered by them. The pressure distribution are used to compute the radial velocity gradient at the impingement stagnation point. It is found that for normal impingement, this gradient correlates with the freejet centreline velocity and half-radius at the same axial location.

Forrest and Shin (1987) [33] measured impact forces and axial depressurization

of initially subcooled water jets discharging into the atmosphere. The change in critical mass flux with the nozzle size was found to be invariant with increasing reservoir pressure and subcooling. Kastner and Rippel, (1988) [60] investigated impingement from circular and non-circular nozzles. On the basis of the information obtained under quasi-steady-state test conditions on discharge rate, pressure distribution, central dynamic pressure on the respective structure, etc., an empirical method of calculating jet impingement forces has been developed over a wide range of parameters. Chilukuri et al. (1984) [19] proposed a theoretical model to estimate the rate of thinning of surface from the wall surface pressures.

The generic form of impinging jets are associated with complexities such as fine-scale incoherent structures and coherent structures. In addition to these complexities the impinging jets are associated with vortex rebounding phenomena, reversal of axial velocity, and unsteady separation at the wall resulting in the formation of secondary vortex structures which have vorticity of opposite sense as compared to the primary vortices of the free jet. Interaction between primary vortices also results in the generation of tertiary vortices. A physical model on the formation of the secondary vortex as a result of impingement of the primary vortex was proposed and investigated by Harvey and Perry (1971) [45].

Vortex formation, interaction and the boundary layer separation near the wall was reported by Lim (1989) [69], Lim et al. (1991) [70], Barker and Crow (1977) [9], Walker et al. (1987) [100] and Didden and HO (1985) [27]. Though flow visualization techniques are employed to study the phenomena near the wall, they are only qualitative. But, Landreth and Adrian (1990) [65] extracted the information on the vortex structures and their interaction using PIV systems. The instantaneous velocity

field, rate of strain and vorticity fields revealed the process of interaction, growth and boundary layer separation.

The spectral measurements of Gutmark et al. (1958) [44] revealed a neutral frequency above which energy is attenuated due to viscous effects and below which the energy is augmented due to vortex stretching near the wall. The effect of wall has also resulted in the excitation of the thin shear layers near the nozzle exit by the upstream propagating waves as a result of impingement of the downstream coherent structures on the wall. These periodic excitation resulted in the generation of periodic coherent structures as reported by HO and Nossier (1981) [49]. The studies on the aerodynamics and thermal aspects of wall jet flow with emphasis to transport properties were reported by Ozdemir and Whitelaw (1992) [80].

The surface pressures on the wall are divided into two distinct zones, the positive pressures and the periodic pressure variations. The positive pressure zone corresponds to the impact zone, while the oscillating pressure zones are due to the vortex growth in the radial direction. Knowles (1991) [61] reported that minimum pressure point corresponds to ground vortex core position, while the maximum pressure point corresponds to the ground vortex penetration point, and the zero pressure corresponds to the ground vortex separation point.

Oblique impingement wall surface pressure distribution was investigated by Beltaos (1976) [10], Foss and Kleis (1976) [35], Foss (1979) [34] and Donaldson and Snedeker (1971) [28]. Donaldson and Snedeker (1971) [28] reported a fall-off in the radial velocity gradient at the impingement stagnation point for oblique impingement as compared to normal impingement. Analytical investigations of impingement of jets on curved deflectors to determine the reverser performance was reported by Schnurr et al.

(1972) [92]. The theoretical results were verified experimentally.

The underexpanded freejet impingement results in two different types of flow field near the wall, depending on whether the nozzle to wall distance is greater than or less than that of the cellular potential core length. For nozzle to wall locations less than the potential core a normal shock forms ahead of the plate. For wall locations greater than the potential core length, the flow field is similar to the subsonic impingement except that the influence of the cellular structure on the mixing zone is dominant.

Underexpanded impingement for various surface shapes was investigated by Donaldson and Snedeker (1971) [28]. Powell (1988) [84] investigated on the acoustic oscillations due to impingement for small and large plates. Periodic unstable oscillations was found to occur over a wide variation of control parameters, namely, pressure ratio, plate size, and spacing of the plate from the nozzle with the resultant radiation of sound of discrete frequencies. For small plates, the principal oscillations for acoustic wavelength / nozzle diameter of about 4 occur when the stand-off shock wave lies in a pressure recovery region of the periodic cellular structure of the choked jet and is, therefore highly unstable. For large plates, acoustic feedback to nozzle occurs with the principal tones having acoustic wavelength / nozzle diameter of 2 with frequencies nearly independent of pressure ratio and plate size. They suggested a acoustic feed-back mechanism, and a formula for the frequency of oscillations were derived. For highly underexpanded jets, the mechanism for small and large plates merge. Iwamoto and Deckker (1981) [58] applied fluid-in-cell method to study the formation of the shock waves near the wall. Iwamoto (1990) [57] presented experimental and numerical simulations on the flow pattern in the jet field on impingement.

The shock structure near the wall due to supersonic impinging jets were experimentally and theoretically investigated to understand the variation of the shock-plate height and shock shapes by many researchers. Carling and Hunt (1971) [17] applied method of characteristics and experimentally studied the walljet region consisting of series of expansion and compression waves. Gummer and Hunt (1971) [41] applied single-strip version of the method of polynomial approximations and integral relations to the flow to determine the shock height and verified the results experimentally. Gummer and Hunt (1974) [42] applied the single strip method of integral relations to study shock shapes at small nozzle-wall distances and experimentally verified the results Lamont and Hunt (1980) [64] also investigated the normal impinging shock structure. From the survey on the shock structure of supersonic impinging jets the shock shapes near the wall, the shock-plate height, various theoretical techniques to predict the characteristics of the shock structure and the effect of oblique impingement are found to be the important parameters of the studies.

Studies on supersonic oblique impingement shock structure were reported by Lamont and Hunt (1980) [64]. They reconstructed the wave interactions using inviscid analyses. The flow field was reported to be extremely complex due to the local structure of the freejet and, particularly, due to interactions between shock waves in the freejet and those created by the plate. In the far field, the mixing effects become increasingly important. They also reported that the maximum pressure on the plate when it is inclined can be very much larger than when the plate is perpendicular, owing due to the possibility of high pressure recovery through multiple shock systems. The load on the plate both for normal and oblique impingement was predicted by a simple momentum balance.

The surface flow visualizations with supersonic impingement showed periodic repetitive deposits of the coating due to the local variation of the pressure from maximum to minimum on the surface, these patterns were examined by Kalghatgi and Hunt (1976) [59], Donaldson and Snedeker (1971) [28], Carling and Hunt (1974) [17] and Masuda et al. (1990) [73]. Kalghatgi and Hunt (1976) [59] reported the effect of the bubble on the surface characteristics resulting from the interactions of the plate shock with very weak shock waves which are produced in the jet either by small imperfections in the nozzle wall or by slight inaccuracies in the design of the supersonic nozzle. The surface pattern reported by Donaldson and Snedeker (1971) [28] showed a central deposits surrounded by a region of inward and outward flow. A dividing ring divides the inward and outward flow with topological features of nodes and saddle points. The pattern was found to be segmented, which decreased with distance. A comparison of the surface pattern, schlieren photographs and surface pressure distribution showed that the local peaks are definitely related to the observed pattern, with less grease remaining where the pressure is higher. These local pressure maxima correspond to the dark regions of increasing density near the surface. The pressure peaks were found not to correspond to the location of the dividing ring. From the Dayglo pattern and the wall surface pressure distribution, Carling and Hunt (1974) [17] concluded that there is a Dayglo deposit corresponding to pressure minimum of every cycle, except for the weakest last cycle. The deposits are disposed roughly symmetrically around the second and later minima but commence over much of the region of pressure rise in the case of the first minimum. The Dayglo deposits and the pressure distributions in the region of the first minima of higher Mach number jets showed some complexity of structure. Masuda et al. (1990) [73] reported annular deposits which corresponds to the pressure minimum

with deposits near the central stagnation point where the wall shear stress is not very high. The shear stress near the central region is also reduced in the presence of an adverse pressure gradient.

The heat transfer characteristics due to impingement were investigated by several researchers. Some of them are those studies reported by Donaldson et al. (1971) [29], Saad et al. (1977) [90], and Gardon and Akfirat (1965) [36]. Theoretical and simulation studies examining the several features of the impinging jet are reported by Chuang and Wei (1991) [20], Agarwal and Bower (1982) [5], Rubel (1981) [89], Amano and Brandt (1984) [7], Mejak (1991) [75], Rubel (1980) [88] and Parameswaran and Alpay (1974) [82].

From the survey of literature, it is clear that a detailed study scanning the following aspects is essential to have a better understanding about the jet impingement problems.

- The effect of jet Mach number, covering a wide range, on the impingement field.
- The effect of degree of underexpansion on the impingement field
- The influence of wall distance on the positive pressure zone and the walljet zone.
- To investigate about the possibility of obtaining similarity for the force field on the impingement plane.

Since, freeshear flows and bounded shear flows are closely coupled, some of the results are extended to flow over flat plate and the walljet flow. Flow over flat plate has been extensively studied and a length scale to obtain similarity in the boundary layer region has been well established. This length scale is a function of half velocity width from the plate, the free stream velocity, kinematic viscosity and the distance

along the length of the plate. The wall jet region was first theoretically investigated by Glauert (1956) [38]. The experimental verification of Glauert's work was carried out by Bakke (1956) [8] and others. Poreh et al. (1967) [83] also theoretically investigated walljet flows and verified the results with the existing experimental investigations. Glauert distinguished the outer and the inner region of the wall jet. In the inner region the mean shear stress variation was assumed to be same as that in the turbulent pipe flow, whereas in the outer region the eddy viscosity is described by Prandtl's model. The solutions in the inner and the outer region were matched at the point of the maximum mean velocity, where the shear stress was assumed to be zero, giving a combined dimensionless velocity profile which depends on single parameter α . Two different velocity and length scales resulted in the inner and the outer region for $\alpha = 1.3$, respectively.

The proposed free shear similarity scale are applied to the bounded shear flow, namely, flow over a flat plate and the walljet to check their validity for bounded shear flows.

Chapter 3

Experimental Apparatus and Procedure

The experimental apparatus of the present study consists of four main components. They are

1. the compressor unit
2. the flow system
3. the experimental models and
4. the pressure measuring instruments.

3.1 Compressor unit

The high pressure dry air required for the experimental investigation on freejets and impinging jets studies are supplied by piston-cylinder type INGERSOLRAND make

compressor driven by 150 HP a.c. motor. The compressed air is passed through a drier charged with silica gel which is heated electrically. The hot air coming out of the drier system is passed through an after cooler with water circulation to reduce its temperature. The high pressure air at normal temperature (approximately atmospheric temperature) coming out of the after cooler is stored in high pressure storage tanks. This arrangement facilitated supply of moisture free dry air at high pressure for the experimental runs.

3.2 Flow system

The flow system consists of pipe lines, pressure regulating valves and the settling chamber. The compressed air is allowed through a gate valve and a pressure regulating valve before reaching the settling chamber. This air is brought to stagnation in the settling chamber. Uniform pressure at the inlet of the nozzle mounted at the free end of the settling chamber by two sets of wire meshes. The settling chamber is fabricated out of mild steel pipe having inner diameter of 406 mm, length 546 mm and wall thickness 6 mm. A pressure lead from the settling chamber is connected to the U-tube mercury-in-glass manometer to measure the settling chamber pressure P_s . It was also read by a dial gauge. The level of stagnation pressure in the settling chamber is controlled from few mm of mercury to few atmospheres, using a pressure regulating valve. The dry air at a settled equilibrium and at a desired pressure in the settling chamber was allowed to expand into the ambient surrounding as freejet through a convergent nozzle. The entire flow system was pressure tested upto a pressure of 500 psi.

3.3 Experimental models

The experimental model for freejet and impinging jet studies are presented in this section.

3.3.1 Freejet studies

To ensure a tophat velocity profile at the exit of the convergent nozzle, a nozzle shown schematically in Fig. 3.1 has been fabricated on an aluminium block. The inner surface has been given a very smooth finish to result in uniform flow at the nozzle exit. The nozzle has inlet diameter of 28 mm with faired entry, exit diameter $d = 10$ mm, and length $L = 25$ mm. By controlling the stagnation chamber pressure levels, freejets of exit Mach numbers ranging from low subsonic to sonic, and various degrees of underexpansion are achieved. An 'O' ring between the free end of the settling chamber and the convergent nozzle ensures a leak proof system.

3.3.2 Impinging jet studies

A solid circular perspex plate of diameter $D=300$ mm and thickness 12 mm with a smooth surface serves as the impinging surface for normal as well as oblique impingement. The plate is mounted on a rigid traversing mechanism having two degrees of freedom. One for linear motion to control the nozzle to wall distance and the other to control the inclination of the plate with respect to the jet axis. The details of the plate are shown in Fig. 3.2. The wall pressure ports are connected to the multi-tube manometers to measure the surface pressures. The ratio of plate diameter to nozzle exit diameter being 30, the edge effects may be neglected.

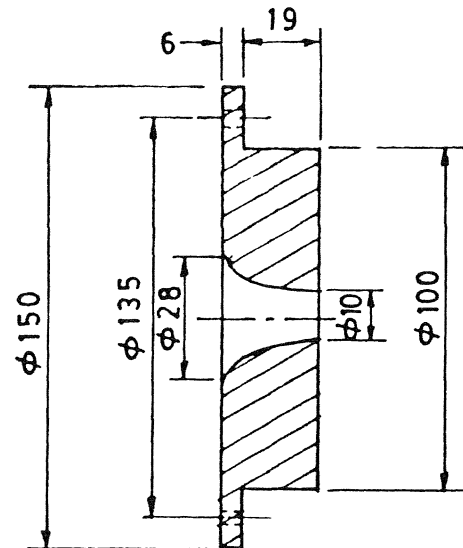


Fig. 3.1 Schematic of the convergent nozzle

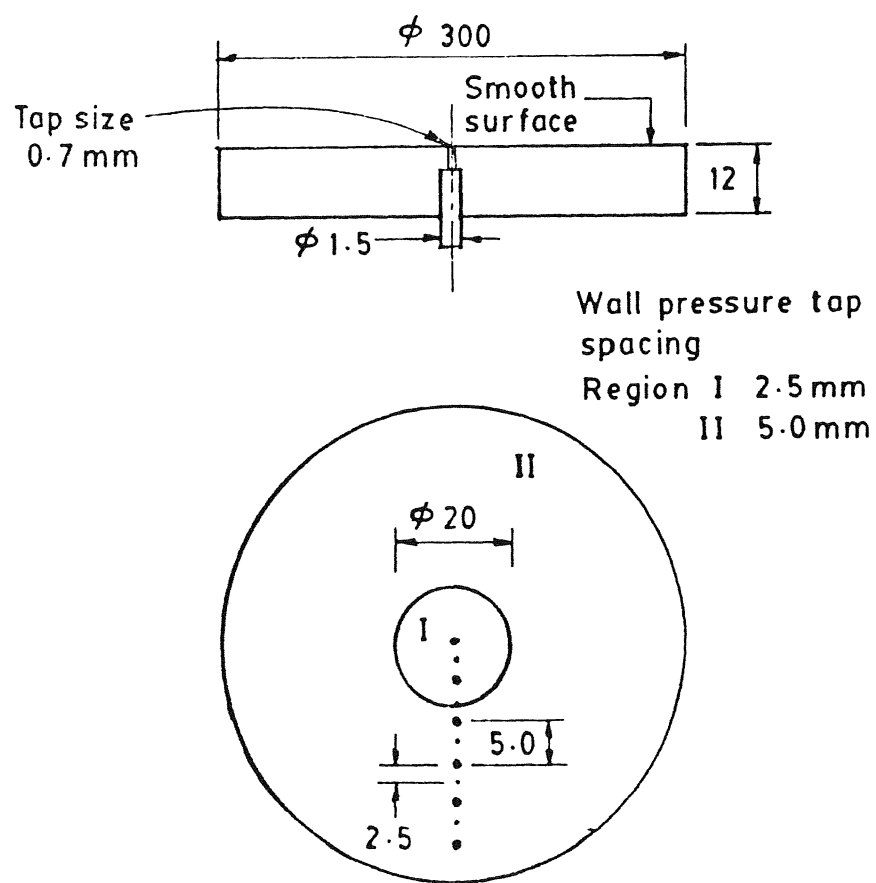


Fig. 3.2 Details of the plate

3.4 Measurement systems

The following measuring instruments are used in the experimental investigation on free and impinging jets.

1. A total probe having inner diameter 0.6 mm and outer diameter of 1.0 mm shown in Fig. 3.3 was used to measure the freejet pressure field. It was also used to measure the impinging jet pressure field, shown in Fig. 3.7. A three hole pitot probe shown in Fig. 3.4 has been fabricated to check the pitot probe measurements with a single hole probe. For the present scheme it was found that the measurements using three hole and single hole agree closely due to the insensitive nature of the pitot probe for yaw involved in the jet field.
2. Two long column 'U'- tube mercury manometers were fabricated, as shown in Fig. 3.6. One was used to determine the settling chamber pressure P_s in conjunction with a dial gauge, and the other was used to measure the free jet field and the impinging jet field.
3. A mercury in glass thermometer was used to measure the settling chamber temperature.
4. A mercury barometer was used to measure the ambient pressure P_a .
5. A disk pressure probe shown in Fig. 3.5 was used to measure the static pressure variation in the potential core of the underexpanded jets.
6. The probes are mounted on a traversing mechanism, shown in Fig. 3.8. The probes are connected to the manometer through a polythene tube having a inner

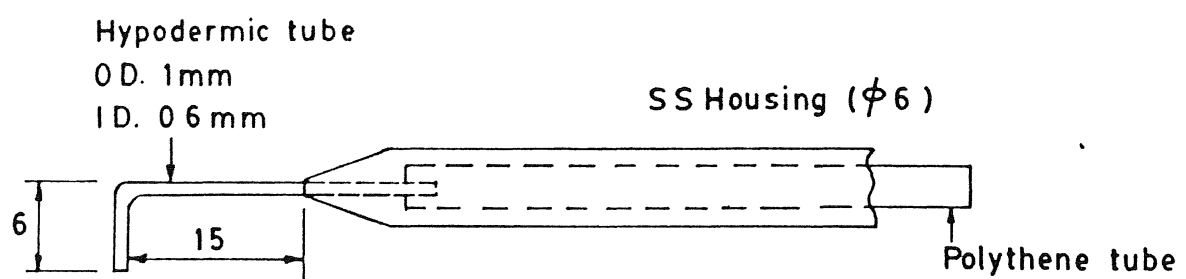


Fig. 3.3 Schematic of pitot tube

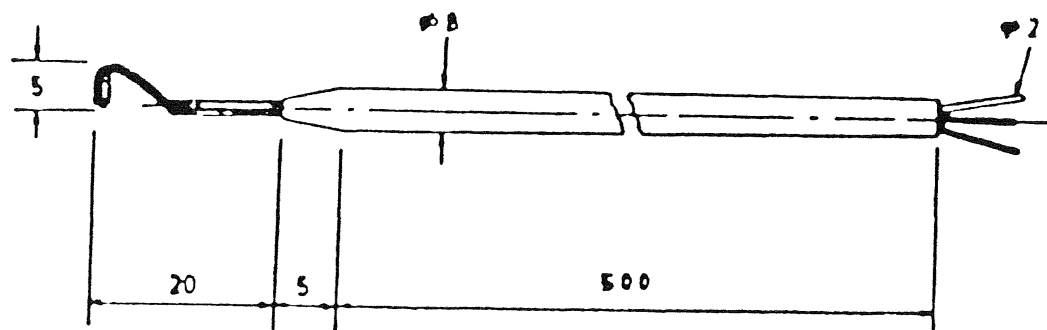


Fig. 3.4 Schematic of 3-hole probe

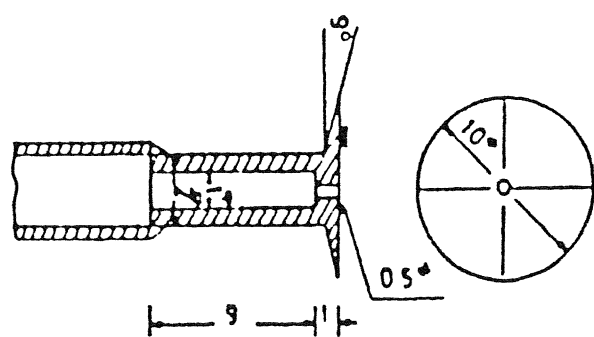


Fig. 3.5 Schematic of static probe

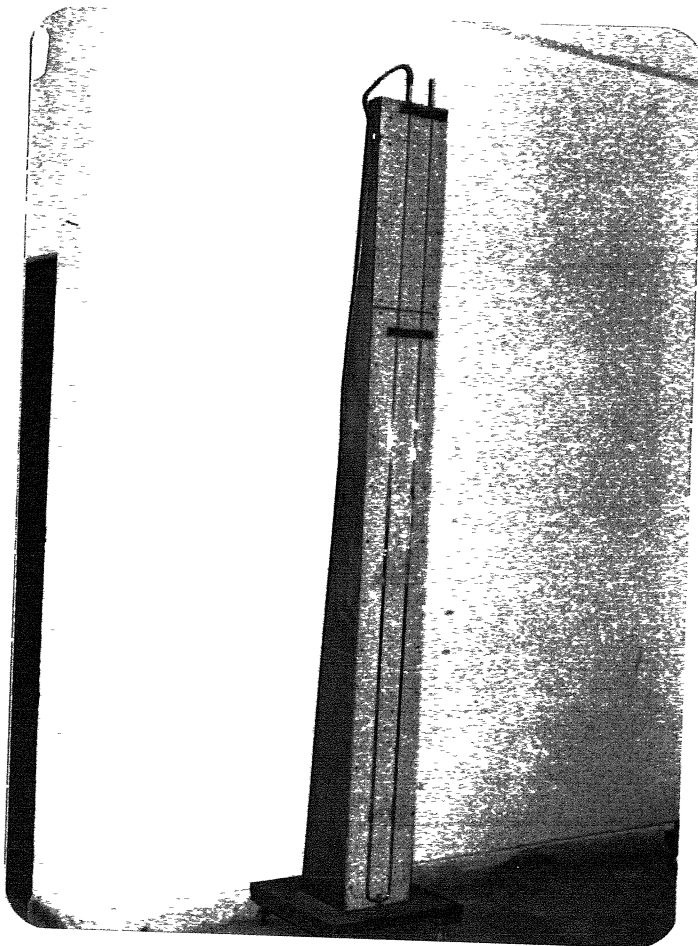


Fig. 3.6 U-tube mercury manometer

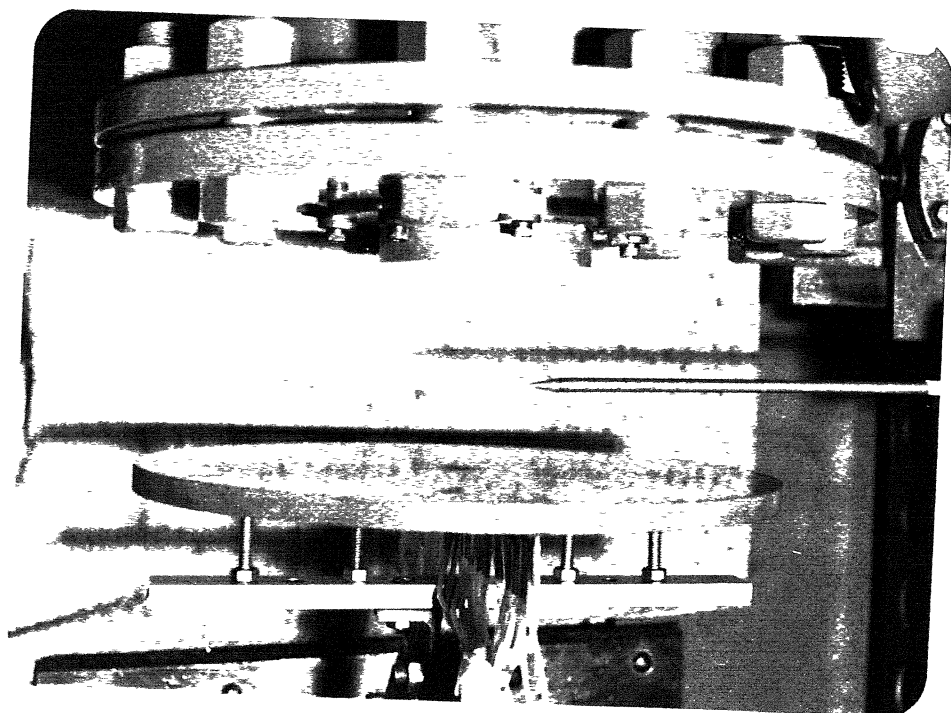


Fig. 3.7 Pitot probe in the impinging jet field

diameter of 0.7 mm. The traversing mechanism has 6 degrees of freedom with a least count of 0.1 mm in the linear, and 0.5 deg in the angular measurements.

7. Two multitube manometers are fabricated to measure the wall surface pressures. A 10 port multitube mercury manometer shown in Fig. 3.9 was used to measure the wall pressures in region I, and a 39 port multitube water manometer shown in Fig. 3.10 was used to measure wall pressures in region II (Fig. 3.2).
8. A Schlieren system consisting of two parabolic mirrors and a monochromatic arc lamp source, as shown in Fig. 3.11 and a video camera with color monitor and VCR unit was used to record the Schlieren images.
9. To investigate the surface flow pattern, grease mixed with lamp black and few drops of oil, along with a source lamp and a still camera were used to capture the surface pattern, photographically.
10. A schematic of the complete experimental facility used for the present experimental investigation is shown in Fig. 3.12. A rigid traversing mechanism capable of taking the force of impingement is used to mount the circular plate. The traversing mechanism has two degrees of freedom; one controls the nozzle-wall distance and the other controls the inclination. The traversing mechanism and the impinging jet set up is shown in Fig. 3.13.

The photograph shown in Fig. 3.13 consists of the assembly of the measurement systems, the experimental models, and the flow system to investigate impinging jets.

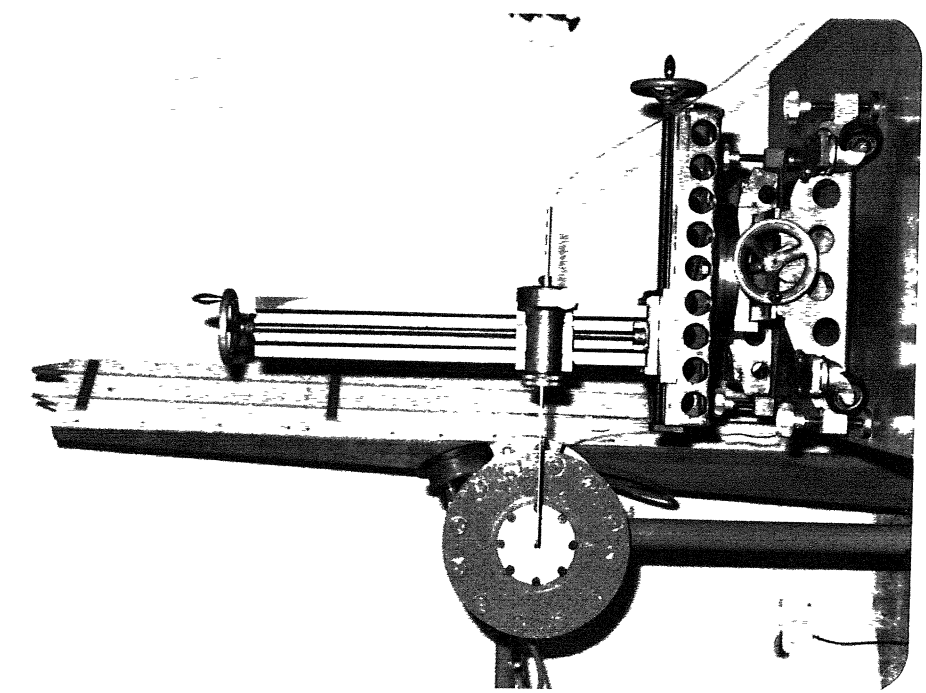


Fig. 3.8 Traversing mechanism for mounting the probe

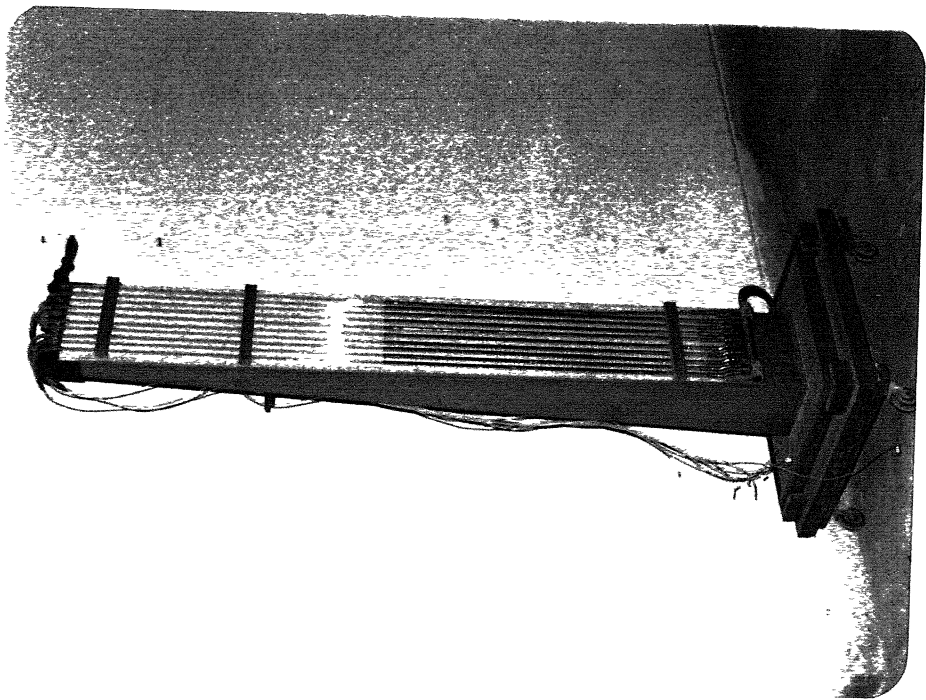


Fig. 3.9 Multi-tube mercury manometer

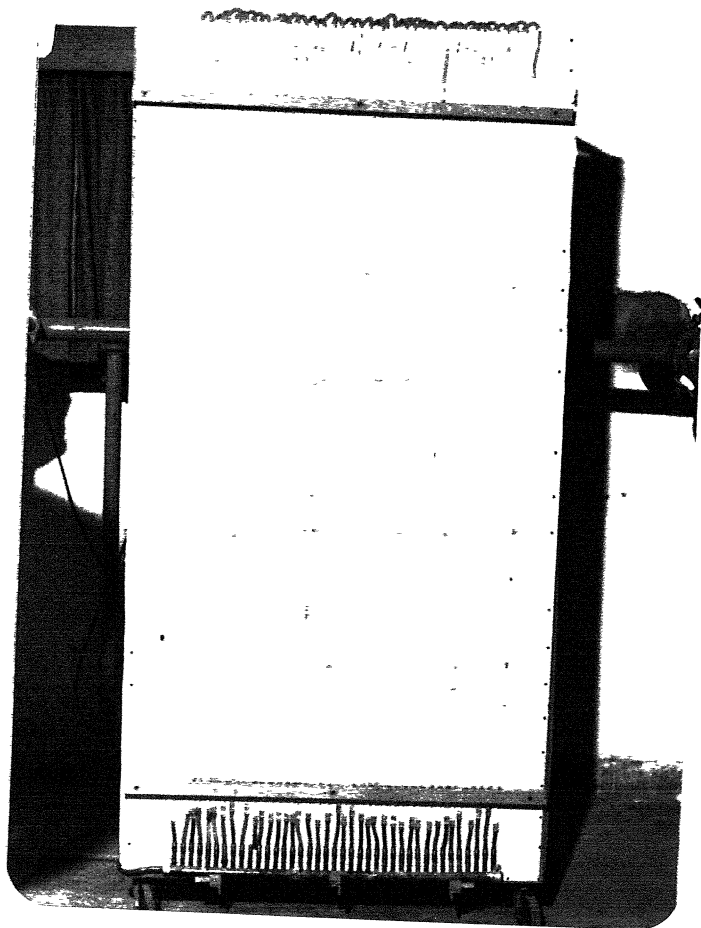


Fig. 3.10 Multi-tube water manometer

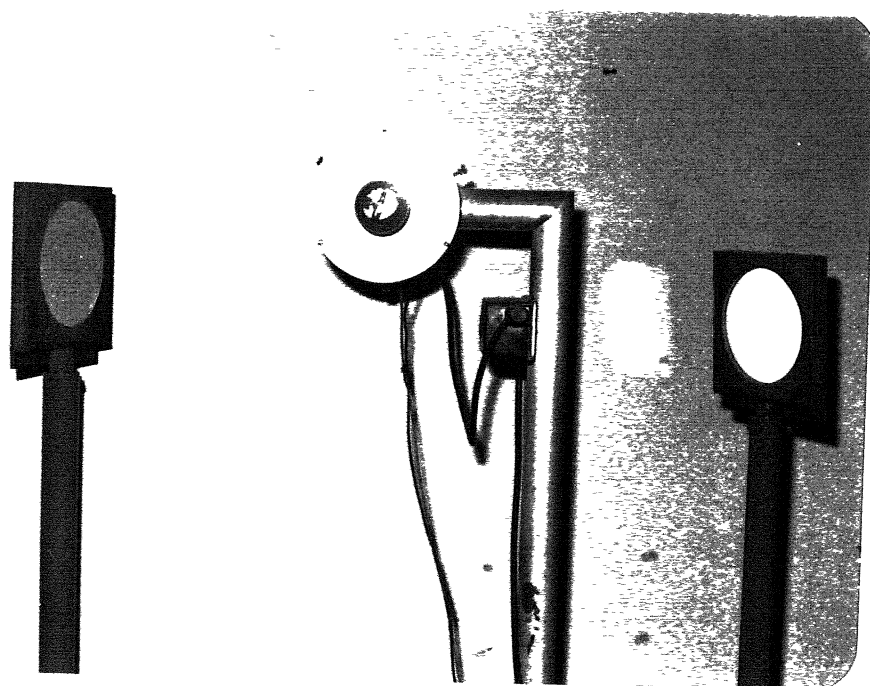


Fig. 3.11 Lamp source and parabolic mirrors for Schlieren set-up

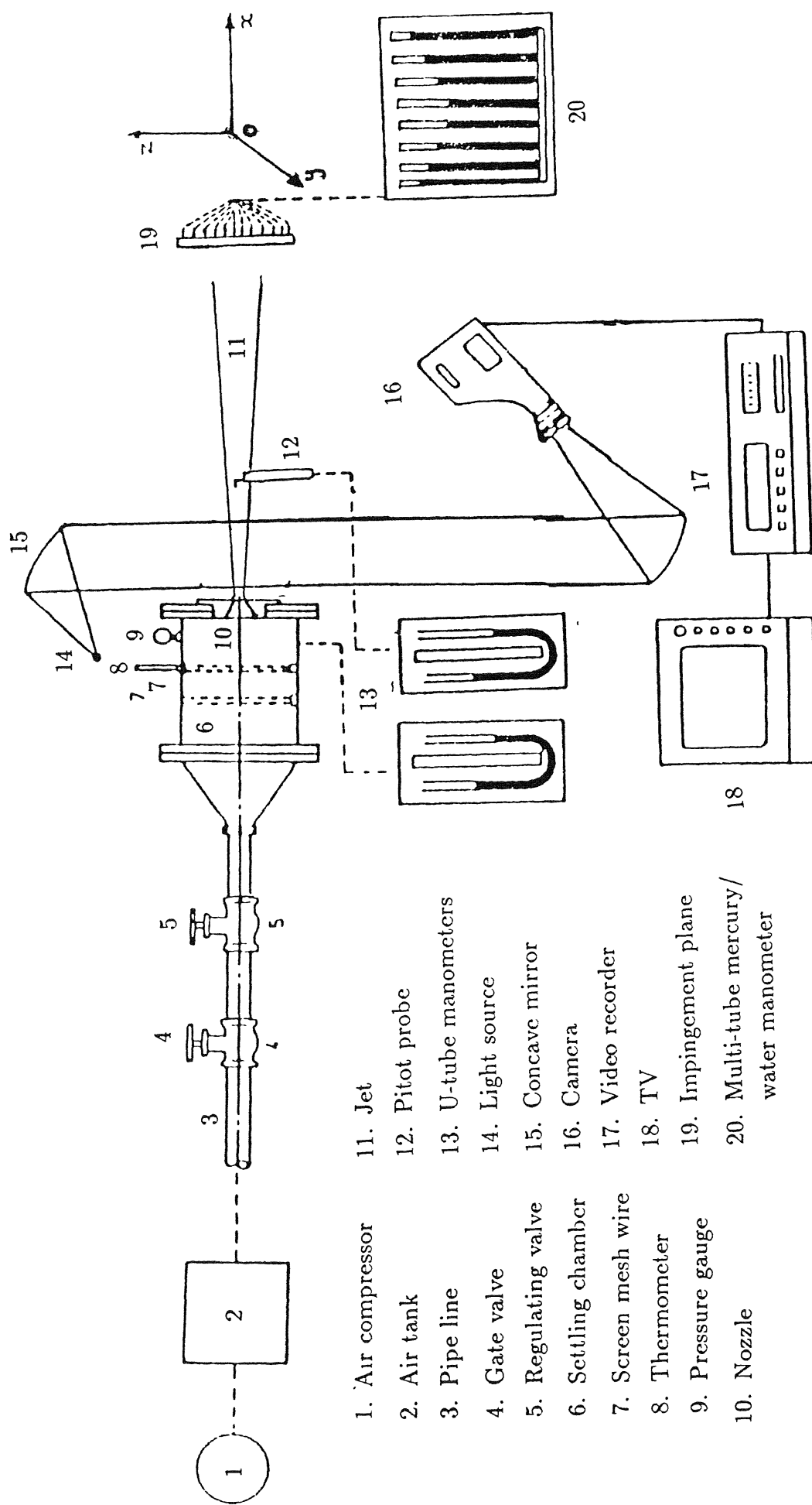


Fig. 3.12 Schematic of freejet and impinging jet test facility

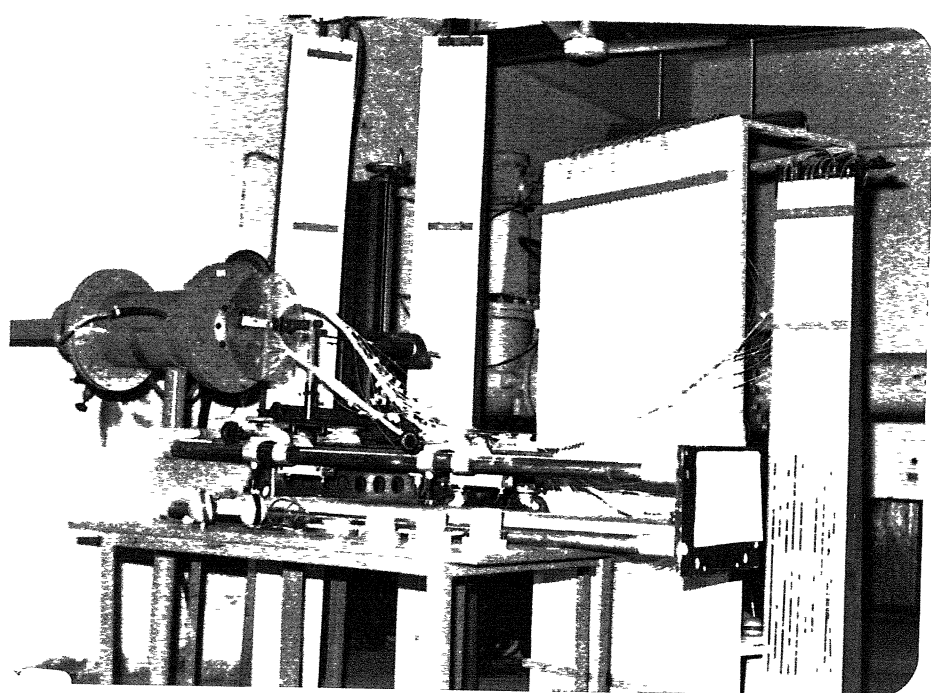


Fig. 3.13 Test facility for impinging jet studies

3.5 Flow visualization techniques

Two flow visualization techniques Schlieren and surface coating techniques are used to study freejet as well as impinging jet characteristics.

3.5.1 Schlieren technique

Schlieren technique is employed to study flow field which exhibits density gradients. The system requires a monochromatic point source which is placed at the focal length of the parabolic mirror so as to have parallel reflected beam. This beam is then allowed to pass through the flow field having density gradients. The density gradients cause refraction of the parallel beam of light. The refracted beam of light is allowed to fall on a second parabolic mirror. On placing a screen or a camera system immediately after the focal length of the second mirror, the change in the density gradients can be visualized. The intensity of illumination of the image, can be controlled by placing a knife edge at the focal point of the second mirror. Using a Schlieren system, gradients of density in the flow field of interest may be captured. In the present study, the cellular wave structure formed due to underexpanded free and impinging jets are captured for different degrees of underexpansion and nozzle to wall distances.

3.5.2 Surface coating technique

The surface pattern at the wall are studied for various axial to wall distances and jet exit Mach numbers and different degrees of underexpansion by applying a surface coating on the wall. In this method, grease mixed with lamp black and few drops of oil are evenly smeared on the wall surface. The plate is then placed in the jet field,

and the jet flow is turned on. It was observed, that the small change in the duration of the flow did not affect the surface patterns. On switching off the flow, a lamp source was placed behind the wall made of perspex sheet to illuminate the regions on the surface where the coating is removed by the shearing action. A still camera was used to capture the flow pattern on the wall surface. This process was repeated for various nozzle exit conditions and wall locations.

3.6 Calibration

The fabricated jet nozzle and the pitot probe have been calibrated before using them. The jet flow field issuing out of the nozzle was studied by measuring the pitot pressure in the field. It was ensured from these measurements that the stream coming out of the nozzle exhibits the characteristics of a jet field at low incompressible Mach numbers; i.e., the jet issuing out of the nozzle bears a constant ratio of the jet width to axial distance of about 8.0. The fabricated pitot probe was calibrated for its insensitivity to yaw. It was found that it is insensitive to yaw upto yaw angles of ± 20 degrees. In fact even at 20 degrees, the error introduced into the pitot pressure is insignificant.

3.7 Experimental runs

A total probe was used to measure the mean pressures of the freejet field as well as the impinging jet field. Disk pressure probe are used to measure the centreline static pressures of the freejet at various degrees of underexpansion.

3.7.1 Freejet studies

Freejets issuing into quiescent surroundings with exit Mach numbers M_e of 0.2, 0.4, 0.6, 0.8 and 1.0 were achieved by controlling the stagnation chamber / ambient pressure ratio ' P_s/P_a '. The mean pitot pressures in the jet field along the x-direction are measured at interval of 0.5d upto 6.0d, followed by intervals of 1.0d upto 30.0d using a pitot probe mounted on the traversing mechanism. Across the jet width along y-directions the mean pressures are measured at intervals of 1.0 mm. The mean pressures are noted on the mercury/water in-glass U-tube manometers depending on whether the local pressure level is high or low. Similar measurements are carried out for sonic underexpanded jets with degrees of underexpansion defined as the ratio of nozzle exit static pressure/ambient atmospheric pressure as $Pr = P_e/P_a = 1.2, 1.5, 2.0$ and 2.25.

3.7.2 Impinging jet studies

Normal impingement studies were carried out by placing the wall at nozzle-wall distances $D_w = 2.5, 5.0, 7.5, 10.0, 12.5, 15.0, 20.0, 25.0$ and 30.0 for subsonic and correctly expanded jets. In the case of sonic underexpanded jets the D_w is varied as 5.0, 7.5, 10.0, 15.0, 20.0, 30.0 and 40.0. The impinging jet field measurements were carried out at selected locations along the x-direction. The measurements along the lateral y-direction are carried out in steps of 1.0 mm.

Oblique impingement studies are carried out with the plate kept at two inclined positions with respect to the z-axis, namely, $\theta = 5^\circ$ and $\theta = 10^\circ$. Since the flow field is asymmetric due to the inclination of the plate, measurements are carried out from the centre to the jet edge at lattice points of 2 mm \times 2 mm at three wall locations

$D_w = 5.0$, 7.5, and 10.0. The jet Mach numbers covered for oblique impingement are 0.6, 0.8 and 1.0, and the underexpansion levels studied are $Pr = 1.2$, and 1.5.

3.8 Data analysis procedure

The measured pitot (gauge) pressures P_G are converted to absolute form, and the Mach number distribution in the jet field and the impinging jet field are calculated by the following isentropic relations.

$$\frac{P}{P_a} = \frac{P_G + P_a}{P_a} = \left(1.0 + \frac{\gamma - 1}{2} M^2\right)^{\frac{\gamma}{\gamma - 1}} \quad (1)$$

Since the measurements are carried out at intervals of 1.0 mm, a linear polynomial is used to interpolate the data at intermediate locations to study the field characteristics in detail.

3.9 Data accuracy

The pressure measurements were made with mercury and water manometers. They are accurate upto $\pm 3\%$. The length measurements along the axial and radial directions are accurate upto $\pm 0.1mm$. The flat plate boundary layer measurements were made with digital manometer. The fluctuations of the manometer is found to introduce an error, even after 10 samples, of $\pm 2\%$.

Chapter 4

Freejet

In this chapter, the mean characteristics of freejets for a wide range of nozzle exit conditions from low subsonic to correctly expanded sonic are investigated based on pitot pressure measurements. The main features of the freejet is shown schematically in Fig. 4.1 for an axisymmetric jet issuing from a convergent nozzle into an ambient surrounding. This figure shows the potential core zone, the mixing zone and the corresponding velocity profiles in these regions.

In Fig. 4.2, the measured distribution of the Mach number as well as the potential core and the half velocity width are plotted for jet Mach number $M_e = 0.4$. The Mach number distribution in the underdeveloped region (*potential core and transition region*) and the fully developed region are also plotted at various axial locations. This figure illustrates, the development of the flow from the potential core to the transition region and to the developed zone.

In the following analysis of freejets, the jet Mach numbers covered range from

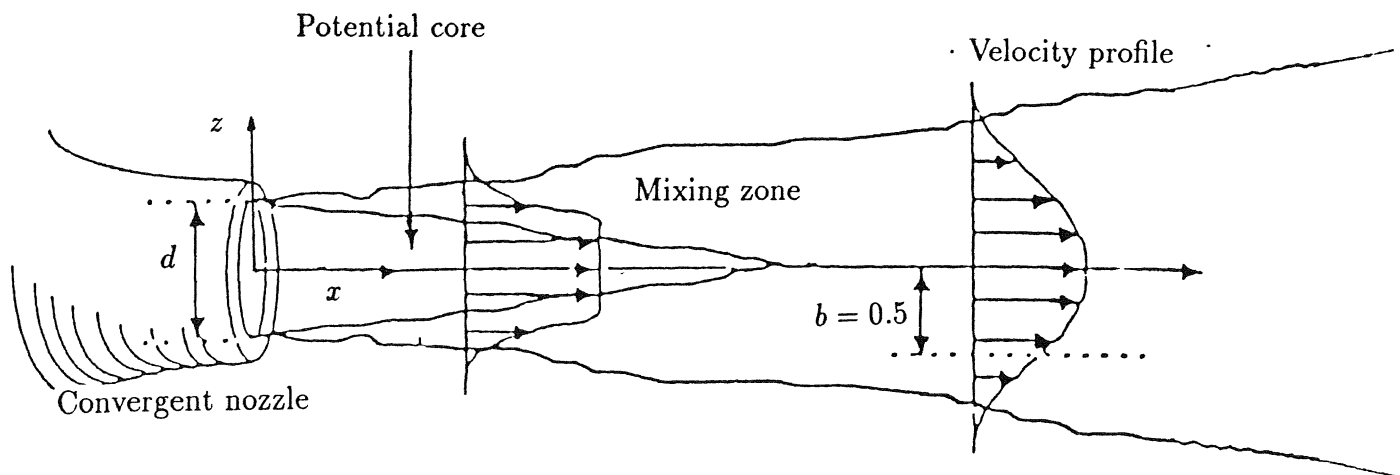


Fig. 4.1 Schematic of the axisymmetric freejet flow field.

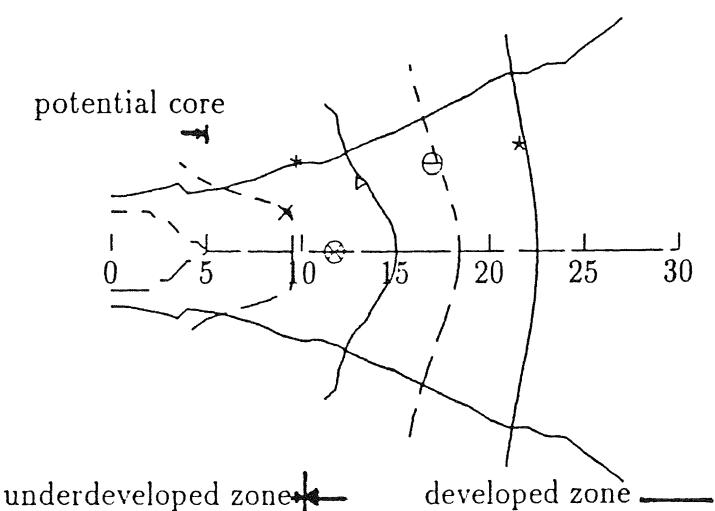


Fig. 4.2 Characteristics of freejet with $M_e = 0.4$: at $x = \times 2.5d$, $\diamond 10.0d$, $\ominus 15.0d$, $*$ $20.0d$, $\otimes b = 1.0$, and $\star b = 0.5$

$M_e = 0.2$ to correctly expanded sonic $M_e = 1.0$, in steps of 0.2. In the first part of this chapter, the analysis is carried out in terms of the Mach number. The Mach number distribution is normalized by the jet Mach number to generalize the results for this range. In the second part of the analysis, the jets are investigated in terms of the corresponding measured gauge pressures. The third part of the study is a comparative study between the Mach number based approach and the pressure based approach.

In most of the figures, just one marker is shown to indicate the parameters along the curve, in order to avoid crowding of points. This is done to have better clarity of the plots. However, each curve in a figure is made up of a number of experimental points.

4.1 Mach number based approach

The Mach number distribution for a freejet at various axial locations are shown in Fig. 4.3. The Mach number is normalized by the jet Mach number and the lateral co-ordinate by the exit diameter of the convergent nozzle. In this figure, point **A** is the intersection point of the Mach number distribution upto an axial location of 3.5d. This point is defined as *iso-Mach point*, as at a radial location and over an axial distance the Mach number is constant in the (x,y) space. Points **B**, **C** ... are also the iso-Mach points in the jet field. The present analysis stemmed from the analysis of iso-Mach points by Ignatius, et al. (1992) [55] on normal impinging jets. They observed the variation of iso-Mach points as a function of the jet exit Mach number and the nozzle-plate distance. In the present analysis, an attempt has been made to understand the physical significance of the iso-Mach points by constructing constant property contours

such as iso-Mach lines, iso-spreads, iso-shear and volume flow rate distribution.

4.1.1 Iso-Mach lines

Fractions of the nozzle exit Mach number distribution denoted by f and defined as iso-Mach lines are shown in Fig. 4.4 for jet Mach number $M_e = 0.4$. The iso-Mach lines originating from the nozzle exit varied from $f = 0.99$ to 0.2 and meet at the jet centre line. From the geometry of the iso-Mach lines, it may be inferred that the jet edge ($f = 0.0$) would meet at the centreline far downstream of the nozzle exit. These iso-Mach lines have positive as well as negative gradients in space. At the nozzle exit, the gradients vary from negative to positive with respect to the jet axis. The maximum negative gradient and the maximum positive gradient correspond to the outer edge of the potential core ($f = 1.0$) and the outer edge of the jet ($f = 0.0$), respectively. The maximum positive gradient is due to the counterclockwise moment with respect to the jet axis, resulting from maximum differential Mach number gradients between the stagnant surrounding and the jet exit Mach number at the nozzle exit. The gradients change from maximum positive to maximum negative through zero gradient due to relative decrease in the Mach number gradients or penetration of the viscous effects into the jet field from the jet edge towards the jet axis.

Since the maximum negative gradient correspond to the maximum inertia which decreases due to penetration of the viscous action, *the negative gradient iso-Mach lines correspond to dominance of inertia effect over viscous effect*. On the other hand, the maximum positive gradient is due the maximum shearing effect at the jet edge which decreases towards the jet axis due to the presence of the inertia of the jet, hence *the positive gradient iso-Mach lines correspond to the dominance of viscous effects*.

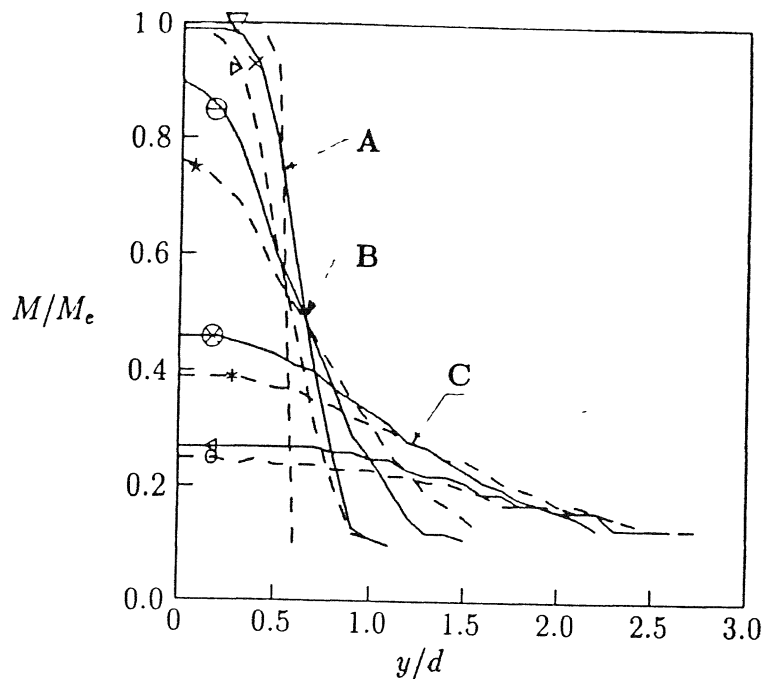


Fig. 4.3 Mach number distribution of freejet with $M_e = 0.8$: at $x = \nabla 0.5d$, $\times 3.5d$, $\blacktriangleright 4.0d$, $\ominus 7.5d$, $\star 10.0d$, $\otimes 17.0d$, $*$ $20.0d$, $\triangleleft 27.0d$, and $\circ 30.0d$.

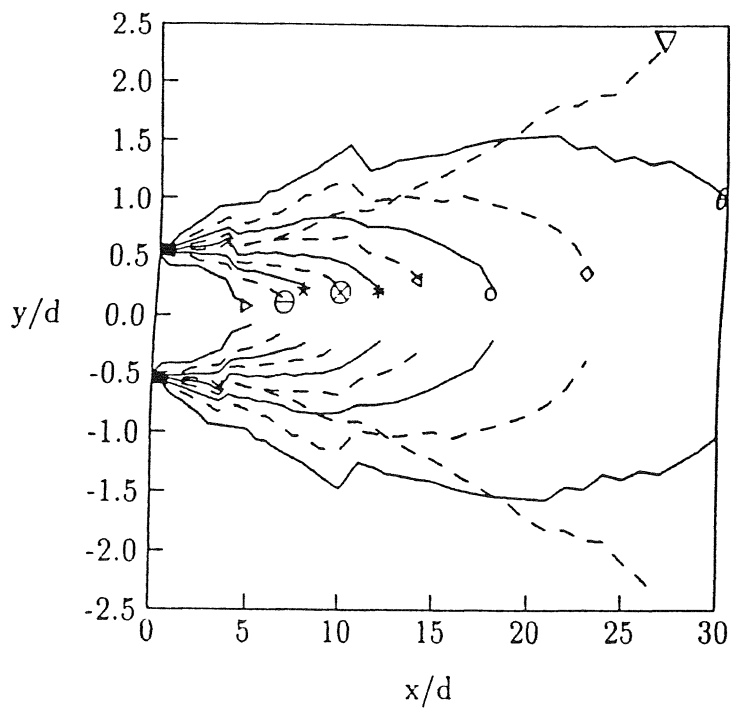


Fig. 4.4 Iso-Mach lines for freejet with $M_e = 0.4$ ($Re = 0.89 \times 10^5$): $\blacktriangleright f = 0.99$, $\ominus f = 0.90$, $\star f = 0.80$, $\otimes f = 0.70$, $*$ $f = 0.60$, $\triangleleft f = 0.50$, $\circ f = 0.40$, $\diamond f = 0.30$, $\theta f = 0.20$, and $\nabla b = 0.50$.

over the inertia effects. The zero gradient iso-Mach lines demarcate the jet field into zone of dominance of inertia effects and zone of dominance of viscous effects. Further downstream, a given iso-Mach line has positive gradients as well as negative gradient with increasing axial distance. This implies that for an iso-Mach line, the viscous penetration dominates upto an axial location where the gradients change from positive to zero, and beyond zero gradient the inertia effect tends to dominate. Comparison of the iso-Mach lines for various fractions of the exit Mach numbers are shown in Fig. 4.5. The positive gradient collapse for the entire range of jet Mach numbers, while the negative gradient exhibit the effect of inertia. The lower jet Mach number has lower spatial extent compared to higher jet Mach number. This is an interesting observation, which implies that *the viscous dominant region are the same irrespective of the jet exit conditions from low subsonic to correctly expanded sonic Mach number.* The spatial extent of compressible zones defined as the limit of field Mach number upto $M = 0.3$ are shown in Fig. 4.6 for M_e upto correctly expanded sonic level. It is seen from these results that with increasing exit Mach number the compressible zones extend spatially as expected

4.1.2 Iso-Mach Spreads

The centre line Mach number decay of the jet is compared for the present range of jet Mach numbers in Fig 4.7. The decay is governed by the semi-empirical relation

$$\frac{M_c}{M_e} = K \frac{1.0}{x/d} \quad (2)$$

where, $K = 0.4825/a$ and a is an experimentally deduced constant. Abramovich [1] had reported that a remains constant for a wide range of Reynolds number, but

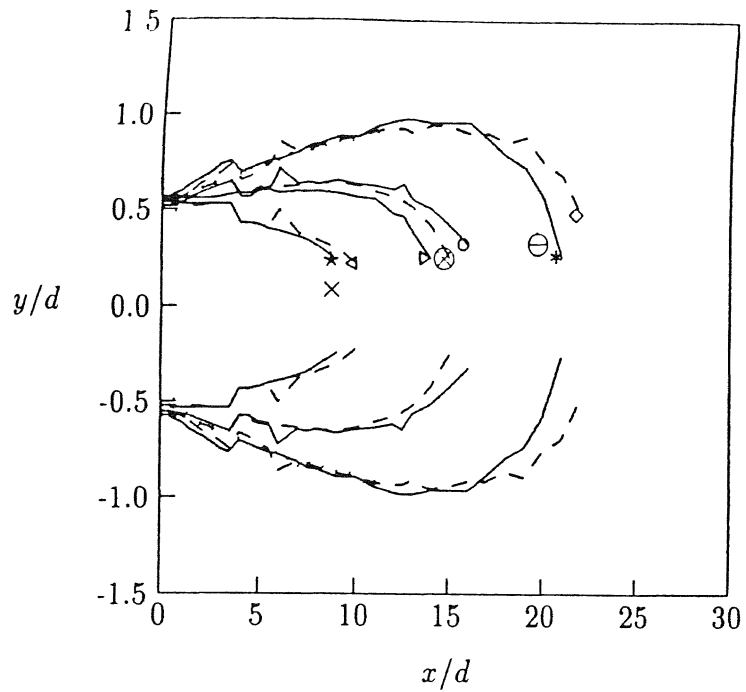


Fig. 4.5 Effect of initial inertia on the iso-Mach lines : $M_e = 0.2$: $\times f = 0.75$, $\blacktriangleright f = 0.50$, $\ominus f = 0.35$ $M_e = 0.6$: $\star f = 0.75$, $\otimes f = 0.50$, $*$ $f = 0.35$ $M_e = 1.0$: $\triangleleft f = 0.75$, $\circ f = 0.50$, $\diamond f = 0.35$

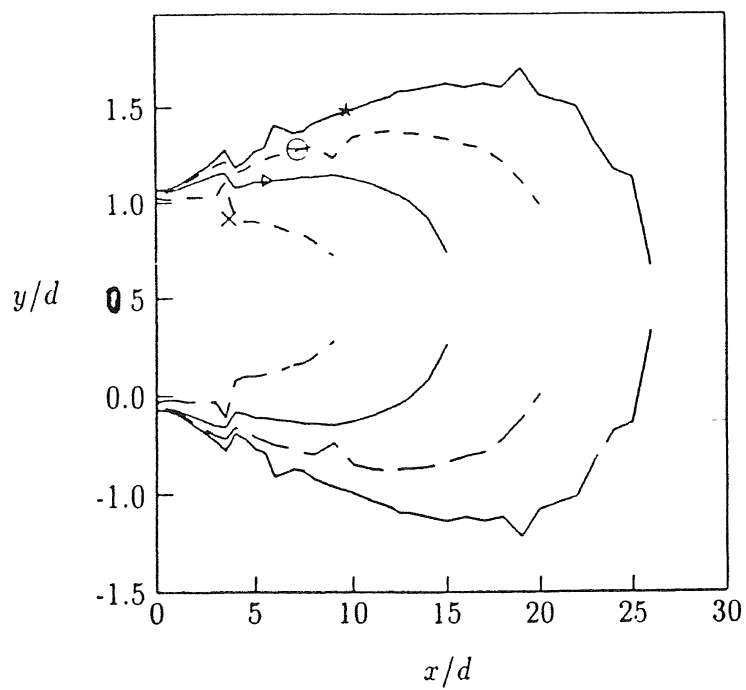


Fig. 4.6 Spatial extent of compressible zones : $\times M_e = 0.4$ $\blacktriangleright M_e = 0.6$, $\ominus M_e = 0.8$, and $* M_e = 1.0$.

it is found to increase linearly with increasing non-uniformity of the initial velocity profile. From Fig. 4.7, it is seen that for the same fraction of the centreline Mach number distribution (when normalized with nozzle exit Mach number), the lower Mach number jet decays faster compared to higher Mach number jet.

This is due to the lower inertia of the lower Mach number jet which enhances the mixing characteristics due to higher entrainment, compared to higher Mach number jet. This is defined as *inverse inertia-entrainment* relationship.

The *iso-spread lines* defined as contours in the space that have the same fraction b of the centre line Mach number M_c are shown in Fig. 4.8, for $M_e = 0.4$. In this figure the isospreads b range from 1.0 to 0.2. The spread $b = 1.0$ refers to the lateral extent of the potential core in the potential core zone, and the centreline in the transition as well as the fully developed regions. The spread $b=0.5$ is the half velocity width. There exists two distinct zones in this figure ; the underdeveloped zone (*upto about 10.0d*) where the isospread $b=0.99$ converges, and the developed zone (*beyond 10.0d*) where the isospread diverges. The general feature of the isospreads in the developed region on an average is linear. The Mach number along these isospreads with respect to the same fraction of the jet Mach number follow the centre line decay as shown in Fig. 4.7. Thus, *the centre line Mach number decay may be treated as the representative of the decay of the entire jet flow field.*

The half velocity width that represents the spreading characteristics of the jet has been compared for different jet exit Mach numbers in Fig. 4.9. The half velocity width spread is on an average linear with saturation locations (corresponds to the local peak) as reported by Laufer and Zhang (1983) [67].

The scatter observed in Fig 4.9 may be due to the following factors:

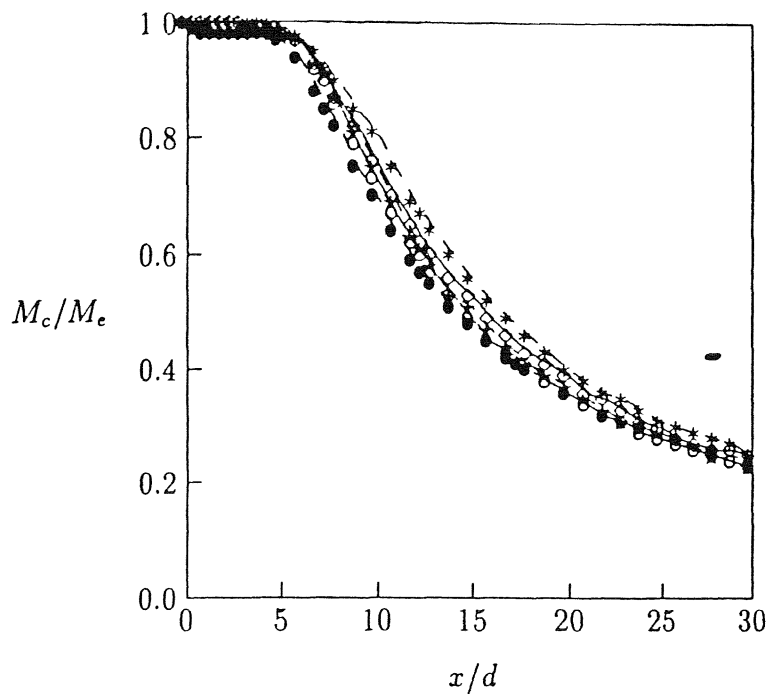


Fig. 4.7 Comparison of centreline Mach number decay for different M_e • $M_e = 0.2$ ◦ $M_e = 0.4$, * $M_e = 0.6$, ◇ $M_e = 0.8$, and + $M_e = 1.0$.

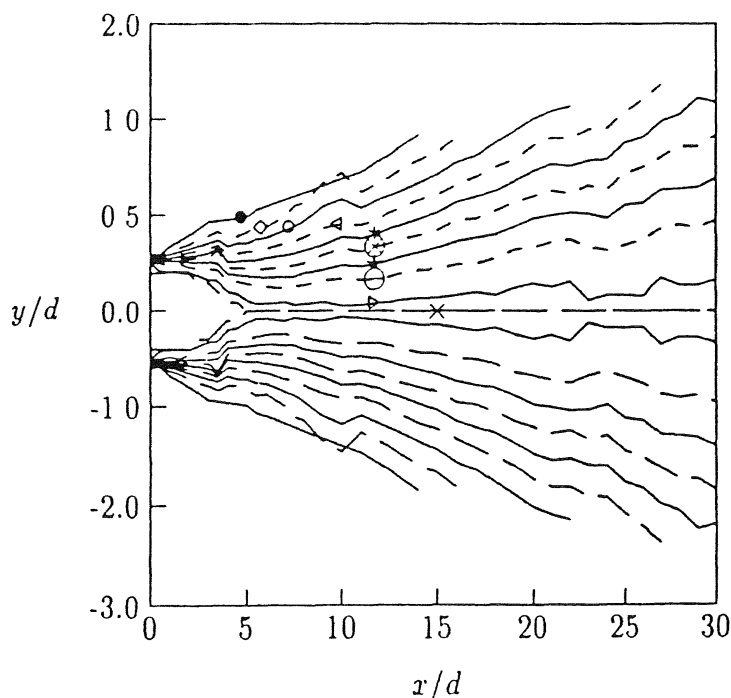


Fig. 4.8 Iso-spreads for various fractions b of centreline Mach number M_c with $M_e = 0.4$
 $\times b = 1.00$, ◇ $b = 0.99$, ◇ $b = 0.90$, * $b = 0.80$, ⊗ $b = 0.70$, + $b = 0.60$, ▲ $b = 0.50$, ◇ $b = 0.30$ and • $b = 0.20$.

1. Initial instability at the nozzle lip.
2. Behaviour of the tunnel inherent characteristics for different Mach numbers.
3. Due to acoustic feedback either from the probe or other sources.

Repeatability of experiments confirm to similar behaviour of the half velocity width with jet Mach numbers.

The half velocity width was found to be a convenient length scale to collapse velocity distribution and other turbulent characteristics. A cross plot of half velocity width with iso-Mach lines reveals an interesting feature of this useful length scale. Referring to Fig. 4.4, the contour corresponding to $b = 0.5$ is found to intersects the iso-Mach lines at the zero gradient band. It would imply that this convenient length scale has distinct physical significance, namely that the *half velocity width demarcates the jet flow field into zones of dominance of inertial and viscous forces. The region above the half velocity width is the zone of dominance of the viscous forces over the inertia forces, and the region below the width is the zone of dominance of inertia forces over the viscous forces.*

However in the literature, half velocity width defined from the jet centre line was found to be a suitable length scale to obtain collapse of velocity and other quantities only in the fully developed region. Various scales have been used for collapse of the velocity distribution in the underdeveloped region. Comparison of the iso-Mach lines for different M_e shown in Fig. 4.5 reveal that the iso-Mach lines collapse in the positive gradient zone. From this it may be inferred that the viscous dominant zones collapse irrespective of the jet Mach number, while the negative gradients exhibit the inertial effect. This is an important observation since the zone encompassed by the length

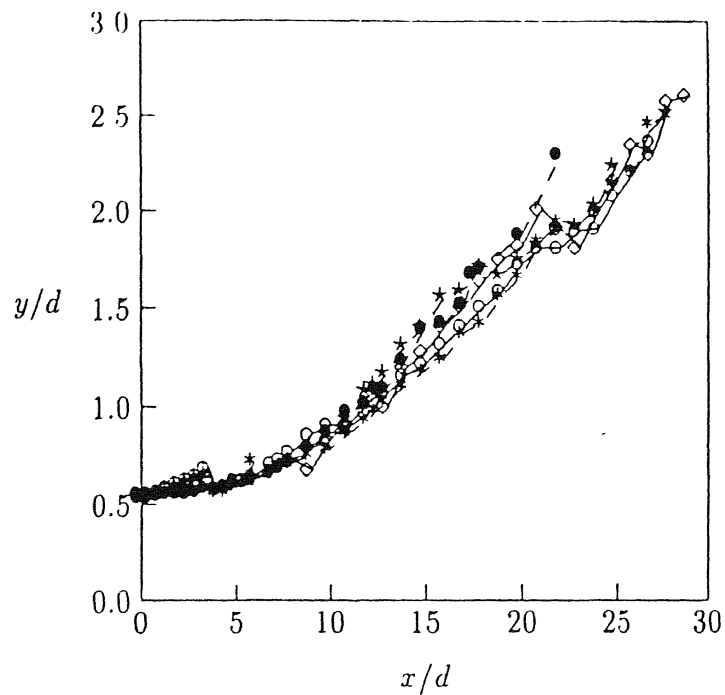


Fig. 4.9 Comparison of half velocity width $b = 0.5$ for different M_e : • $M_e = 0.2$, ○ $M_e = 0.4$, ★ $M_e = 0.6$, □ $M_e = 0.8$ and * $M_e = 1.0$.

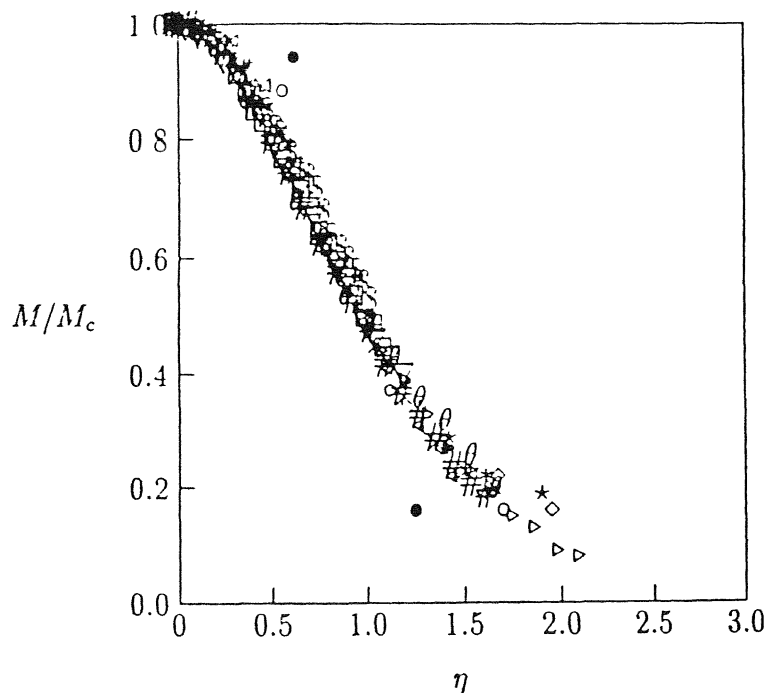


Fig. 4.10 Complete similarity of velocity in the underdeveloped and the developed region for $M_e = 0.4$: $x =$ • $0.5d$, ○ $1.0d$, ★ $2.0d$, □ $3.0d$, * $4.0d$, △ $5.0d$, × $6.0d$, θ $8.0d$, ▽ $11.0d$, # $14.0d$, ∇ $19.0d$, □ $25.0d$ and § $30.0d$

parameter $b = 0.5$ would imply *the inertial dominant zone* of the jet flow field.

At this juncture, the existence of a unique length scale for normalizing the length parameters is evident. Defining the non-dimensional length parameter (excluding the inviscid zone) as

$$\eta = \frac{(r - r_{b=1.0})}{(r_{b=0.5} - r_{b=1.0})} \quad (3)$$

and taking the local axis for similarity along $b = 1.0$, collapse of the Mach number distribution profiles were obtained starting from the nozzle exit, of course excluding the potential core region.

The similarity of the Mach number distribution based on the proposed length scale η is shown in Fig. 4.10, for $M_e = 0.4$. Since the potential core is excluded from similarity consideration, it may be concluded that *similarity may be attained only in the mixing region of the flow field*. In Fig. 4.11, the similar profiles for the wide range of subsonic to correctly expanded sonic obtained with the length scale are plotted. From Fig. 4.10 and 4.11, it is evident that the proposed scale η results in complete Mach number similarity for the jet field right from the nozzle exit. Further more, the resulting similarity is independent of the jet Mach number M_e .

The Mach number similarity curve in Figs. 4.10 and 4.11 exhibit a normal distribution and is given

by the following relation

$$\frac{M}{M_c} = e^{-0.5 \times (\frac{\eta}{\sigma})^2} \quad (4)$$

Based on the nondimensional length scale η , the normal probability distribution for $\sigma = 0.85$ is found to closely match with the present experimental results.

From these results, it may be concluded that *freejets with jet Mach numbers from incompressible to compressible correctly expanded sonic level are completely similar and the similarity profile obey normal distribution.*

The scatter seen in the similarity profile may be due to the inaccuracy in determining the lateral extent of the potential core, and also due to the inaccuracies in the measurement of very low pitot pressures.

4.1.3 Iso-Shear

The effect of the penetration of the high shearing action at the jet edge into the flow field may be seen from the constant fraction contour of S , defined as

$$S = -\frac{dM}{dy} \frac{d}{M_e} \quad (5)$$

where S is called the normalized shear. Constant fraction contours of the shear S , for $M_e = 0.4$ is shown in Fig. 4.12. Close to the nozzle exit there are two lobes with the same value of S . The inner lobe is formed by the faster moving shear layer which is resultant of the initial inertia, while the outer lobe is formed by the slower moving shear layer carrying the entrained mass. The outer lobe being swept away from the inner lobe is also evident from this figure. Each lobe has a peak, where the tangent is parallel to the radial direction. Further downstream, the shear layers fragment indicating the random nature of mixing. Similar observations were reported by Wynanski and Fiedler (1970) [103] for plane mixing layers and by Hussain and Clark (1981) [52] for free jets. The half velocity width demarcates the inertia dominant zone (*the inner lobe*) and the viscous dominant zone (*the outer lobe*). This further re-iterates the argument on the

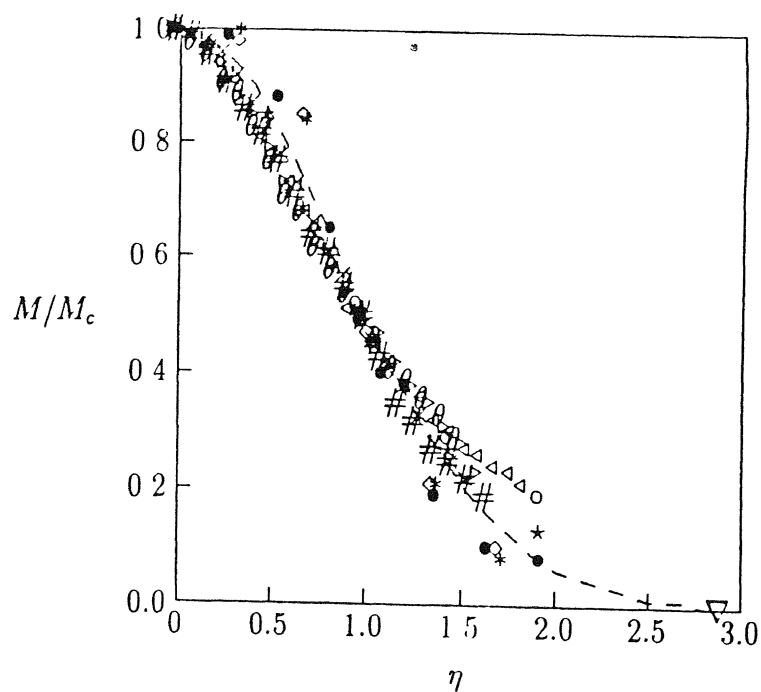


Fig. 4.11 Complete similarity of velocity in the *underdeveloped and the developed region* for subsonic to correctly expanded sonic jet Mach numbers : $M_e = 0.2$ $x = \bullet$ $2.0d$, $\triangleleft 15.0d$, $M_e = 0.4$ $x = \circ$ $2.0d$, $\times 15.0d$, $M_e = 0.6$ $x = \star$ $2.0d$, $\theta 15.0d$, $M_e = 0.8$ $x = \diamond$ $2.0d$, $\triangleright 15.0d$, $M_e = 1.0$ $x = *$ $2.0d$, $\# 15.0d$, $-\nabla-\sigma = 0.85$

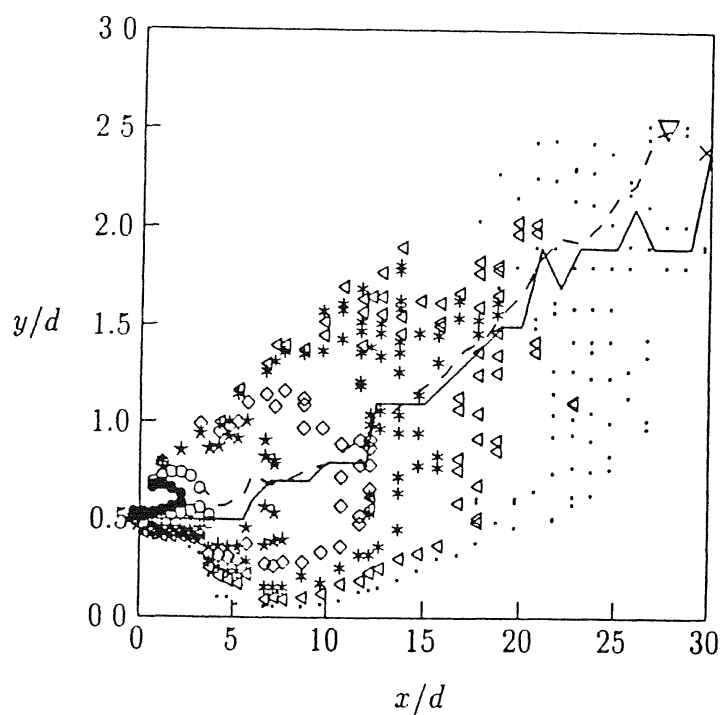


Fig. 4.12 Representation of shear : $S = \bullet 0.30$, $\circ 0.20$, $\star 0.09$, $\diamond 0.05$, $*$ 0.03 , $\triangleleft 0.02$, $\cdot 0.01$ and $-\nabla-$ $b = 0.5$, $-\times-$ R . $M_e = 0.4$

physical significance of the half velocity width discussed earlier.

4.1.4 Volume flow rate distribution

The jet field is entrainment dominated and the principle of conservation of mass does not hold. The domain in the flow field that conserves the same amount of initial volume flow rate is represented by the contour $q = 1.0$ in Fig. 4.13 for $M_e = 0.2$ and 1.0. The geometry of this contour is similar to that of a straight subsonic diffuser. The combination of entrainment, the relief effect and the initial inertia results in the *expansion* of the initial volume of the exit mass. This diffuser may be termed as *virtual diffuser*, since it is a measure of expansion of the jet into the surroundings. Interestingly, in a complex and turbulent domain of the jet flow field, the virtual diffuser shows a geometrically linear behaviour, which seems to be almost independent of jet Mach number.

The total volume flow rate given by

$$\frac{Q}{Q_e} = \frac{2 \int_{y=0}^{y=\infty} y M(y) dy}{r_e^2 M_e} \quad (6)$$

, computed upto 10 – 12% of the jet exit Mach number. The entrained volume flow rate is shown in Fig. 4.14, obey the following variation

$$\frac{(Q - Q_e)}{Q_e} = C \frac{x}{d} \quad (7)$$

From the results of this investigation, it is found that *C is almost independent of incompressible and compressible jet Mach numbers* of the present study.

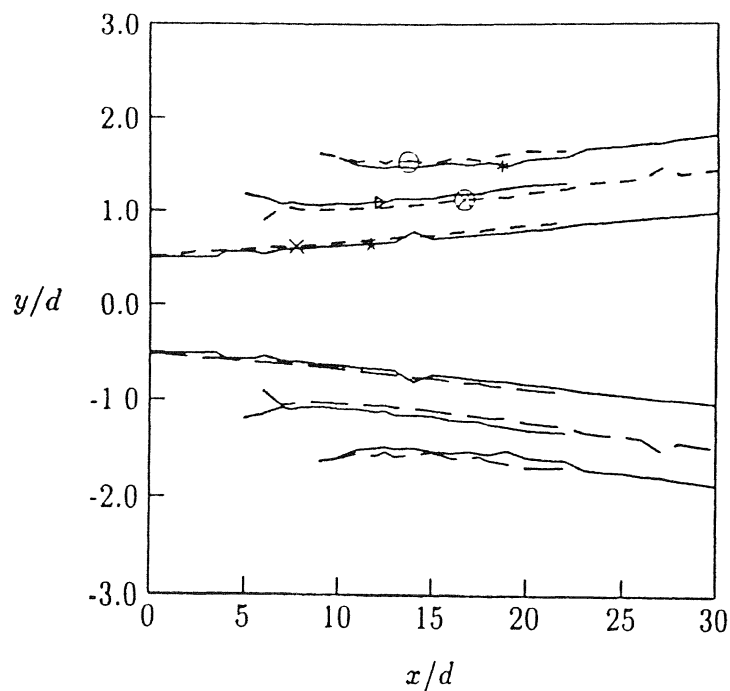
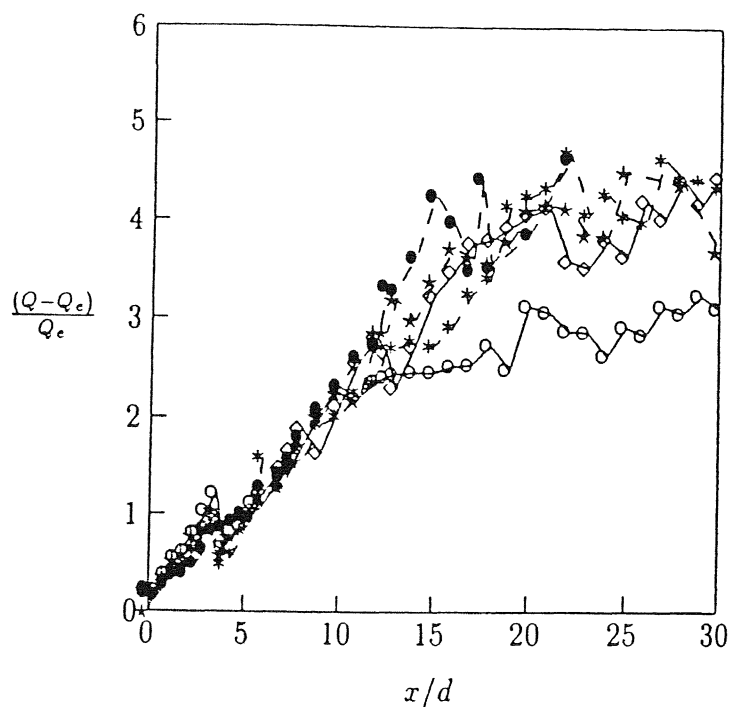


Fig. 4.13 Comparison of iso-volume flow rate : $q = 1 \times M_e = 0.2$, $\star M_e = 1.0$, $q = 2 \diamond M_e = 0.2$, $\otimes M_e = 1.0$, $q = 3 \ominus M_e = 0.2$, $*$ $M_e = 1.0$.



CENTRAL LIBRARY
I.I.T., KANPUR
Loc. No. A121745

Fig. 4.14 Comparison of entrained volume flow rate for different M_e : $\bullet M_e = 0.2$, $\circ M_e = 0.4$, $\star M_e = 0.6$, $\diamond M_e = 0.8$ and $*$ $M_e = 1.0$.

4.1.5 Coherent structures

The large-scale coherent structures in the jet flow field are defined on the basis of coherent vorticity, Hussain (1983) [50]. These structures are lumps of rotating fluid mass distributed in the jet field and have interesting characteristics, namely, they are spatially non overlapping with each structure having independent domain and boundary. Contours of equal radial rate of volume flow rate dQ/dy plotted in Fig. 4.15 display similar interesting features. The mean structure of the jet flow field shown in this figure also exhibits generation and degeneration of coherent structures that results from pairing, tearing and shearing action. From this figure, it is seen that the lateral extent of the coherent structures is of the order of magnitude of the nozzle exit diameter.

The linear step wise increasing half velocity width upto saturation point followed by a dip may be due to the tearing or degeneration of the coherent structures as evident from Fig. 4.15. By taking equal contours of dQ/dy coherent mean structures in the near field of the nozzle exit cannot be plotted as $dQ/dy = 0$.

To obtain these structures in the near field, a further refinement was carried out. Change of volume flow rate at a given radial location given by

$$g = \frac{\Delta Q}{Q_e} = \frac{2 \int_{y=0.0}^{y=y_a} y M(y) dy}{r_e^2 M_e} - \frac{2 \int_{y=0.0}^{y=y_b} y M(y) dy}{r_e^2 M_e} \quad (8)$$

is plotted in Fig. 4.16, for free and impinging jet field, where y_a and y_b are the radial locations. As seen from this figure, the value of g increases and then decreases. The increase of change of volume flow rate at a radial location increases radially upto a definite radial location and then decreases. The increase signifies the direction of

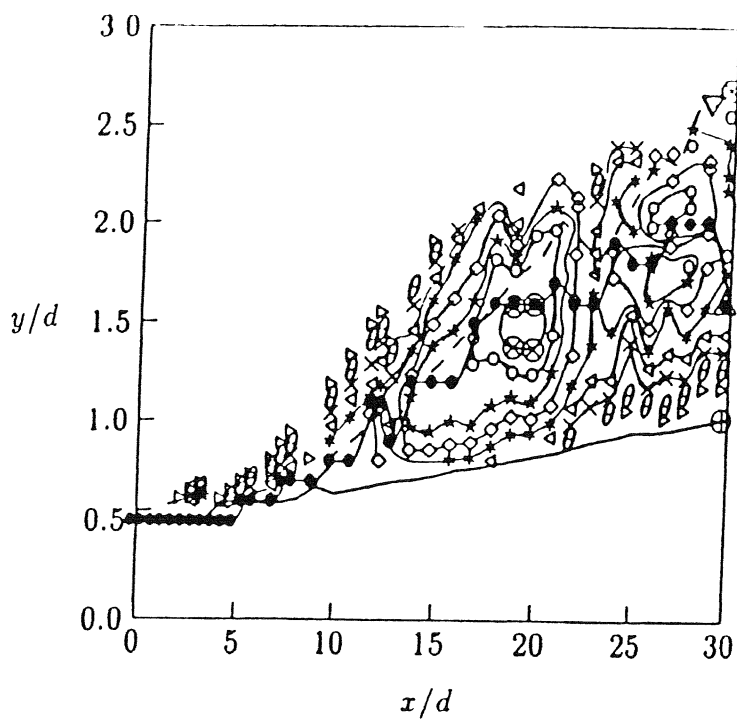


Fig. 4.15 Spatial rate of change of entrained volume flow rate : $\otimes 0.29$, $\circ 0.28$, $\star 0.27$, $\diamond 0.26$, $*$ 0.25 , $\triangleleft 0.24$, $\times 0.23$, $\theta 0.22$, $\triangleright 0.21$, $\bullet R$, and $-- b = 0.5$, $oplus q = 1$.

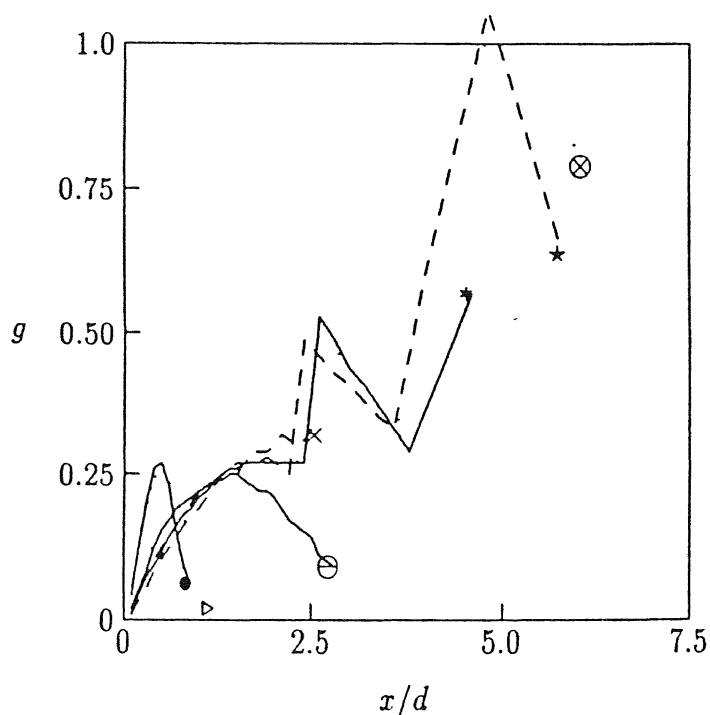


Fig. 4.16 Variation of g for free and impinging jets : $M_e = 1.0$ freejet $\bullet 2.0d$, $\times 26.0d$, impinging jet $D_w = 25.0$, $\triangleright 5.0d$, $\ominus 19.0d$, $\star 22.5d$, $\otimes 23.5d$ and $* 24.0d$.

movement of the structure along the flow direction, while the decrease signifies the direction of movement opposite to that of the flow direction. The direction of the structure is effectively counter-clockwise. Further, it can be seen that for freejets, there is one peak along the radial direction, whereas impinging jets exhibit more than one peak. The radial location where the change is maximum is denoted by R .

Contours of constant g shown in Fig. 4.17 reveal the mean coherent structures in the entire jet field. The first structure is observed at about $4.0d$, the second structure extends upto about $12.0d$, the third upto about $22.0d$ and further downstream growth and degeneration of the structure takes place. From these results R may be visualized as the coherent structure centre, where the mass concentration is maximum. This fact may also be inferred from Fig. 4.15.

The radial locations of R for different M_e is presented in Fig. 4.18. It is seen from this figure that the *radial location of R is independent of the jet exit Mach number* as shown in Fig. 4.18. Fig. 4.19 shows the iso-Mach lines, half velocity width, initial volume flow rate, and the location of the flow reversal denoted by R . Some of the interesting observation are that the contour formed by R is stepwise linear, and the linear portion of R lie on the zero gradient iso-Mach lines as in Fig. 4.19 . Comparing Fig. 4.3 and Fig. 4.19, it may be concluded that *the axial extent of the linear portion of R correspond to the iso-Mach points*, the root of the present investigation.

4.1.6 Conclusions

From the geometric mean structure of incompressible and compressible subsonic and correctly expanded sonic freejets several interesting conclusions have been drawn. The present work explains the physics of many vital characteristics of the jet, and also

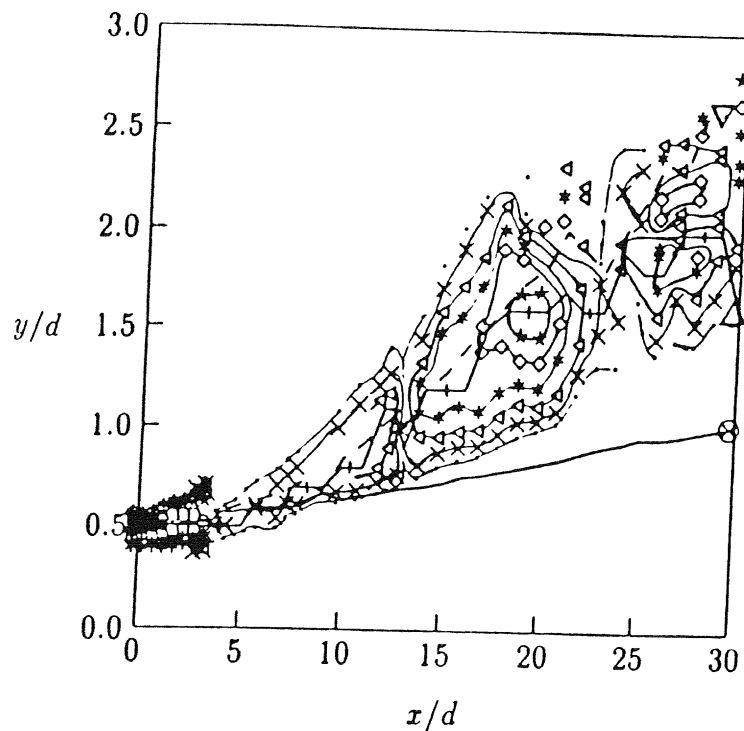


Fig. 4.17 Change of volume flow rate at a radial location : • 0.33, ○ 0.31, ★ 0.29, ◇ 0.28, * 0.27, △ 0.26, × 0.25, · 0.24, and --- $b = 0.5$, $\otimes q = 1.0$, - R .

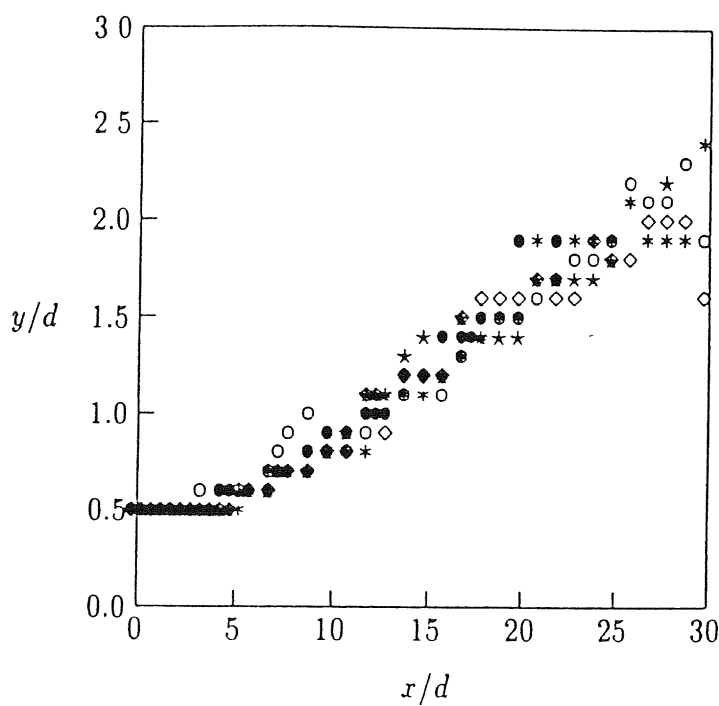


Fig. 4.18 Radial location of volume flow rate change (max): • $M_e = 0.2$, ○ $M_e = 0.4$, ★ $M_e = 0.6$, ◇ $M_e = 0.8$ and * $M_e = 1.0$.

defines new parameters based on the geometric structure to achieve similarity of free jets. The highlights of the results in this chapter are

- A universal length scale proposed, results in complete similarity of the velocity (Mach number) distribution encompassing the underdeveloped and the developed region of the jet flow field, for the entire range of parameters of the study.
- The velocity (Mach number) distribution obeys the normal distribution for $\sigma = 0.85$.
- The significance of half velocity width is that it demarcates the jet field into zones of dominance of viscous and inertia forces.
- Normalizing the field by the half width implies normalization by the inertial dominant zone in the mixing region of the jet flow field.
- The centre line velocity (Mach number) decay is the representative decay for the entire jet field.
- The negative and the positive gradients of the iso-Mach lines correspond to the inertial dominant and the viscous dominant fronts in the mixing region, respectively.
- The virtual diffuser is a measure of expansion of the jet. Further the expansion is due to the combined action of entrainment and the relief effect over the inertial effect of the jet.
- Higher entrainment rate is observed in the initial region compared to the developed region, as expected.

- It is possible to obtain the mean coherent structure from the mean properties based on two methods.
 1. contours of equal radial gradient of the volume flow rate.
 2. contours of equal change of volume flow rate at a radial location.

4.2 Pressure based approach

In this section, a method has been proposed to understand the freejet characteristics from the measured pressures. The jet exit pressure conditions correspond to exit Mach numbers analyzed in the previous section. The highlight of this section is the choice of a pressure scale and the corresponding length scale. The normalized gauge pressure is defined by the following equation.

$$P_g = (P/P_a - 1.0)/(P_s/P_a - 1.0) \quad (9)$$

The above equation is equivalent to the measured gauge pressures normalized by the gauge pressure of the settling chamber. The measured gauge pressure is chosen as a parameter for the analysis of the jet field in terms of isobars and iso-pressure-spreads.

4.2.1 Isobars

Various fractions f of the normalized exit gauge pressures P_g constructed are shown in Fig. 4.20. As expected, the isobars also exhibit positive and negative gradients like iso-Mach lines. The positive gradient isobars are due to the expansion of the higher pressure potential into the stagnant atmosphere, whereas the negative gradient

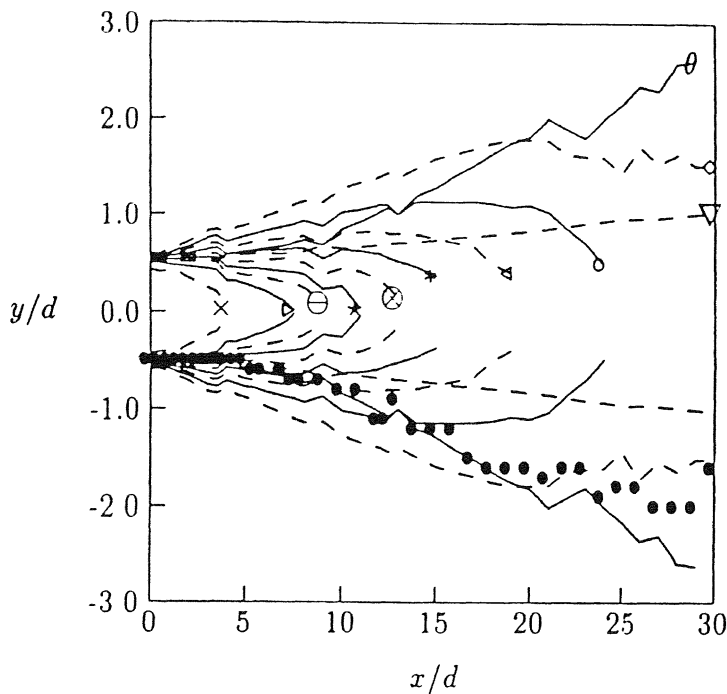


Fig. 4.19 Iso-Mach lines for various fractions f of exit Mach number : $-\theta$ $b = 0.5$, $--\nabla$ $q = 1.0$, $\bullet R$, $\times f = 0.99$, $\triangleright f = 0.90$, $\ominus f = 0.80$, $\star f = 0.70$, $\otimes f = 0.60$, $* f = 0.50$, $\triangleleft f = 0.40$, $\circ f = 0.30$, $\diamond f = 0.20$

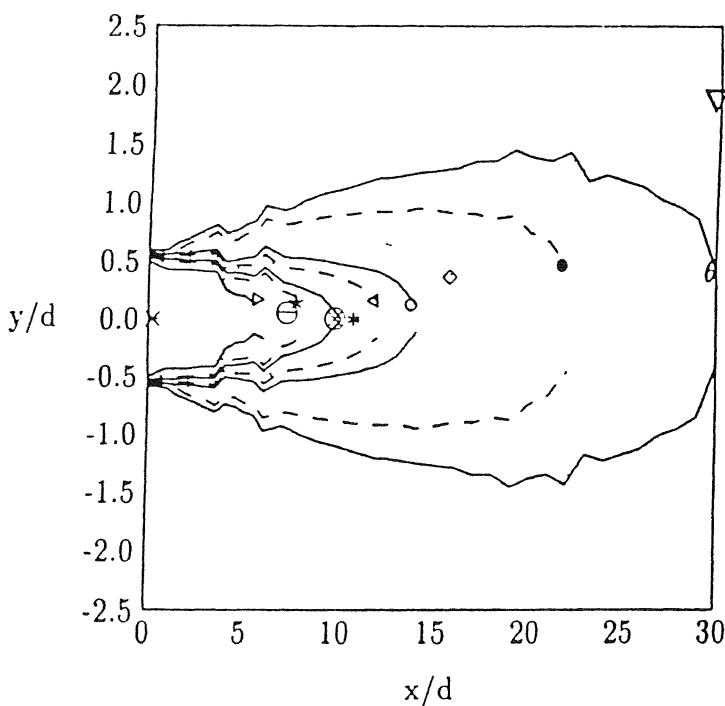


Fig. 4.20 Isobars and half pressure width for $M_e = 1.0$: $\times f = 1.0$, $\triangleright f = 0.90$, $\ominus f = 0.80$, $\star f = 0.70$, $\otimes f = 0.60$, $* f = 0.50$, $\triangleleft f = 0.40$, $\circ f = 0.30$, $\diamond f = 0.20$, $\bullet f = 0.10$, $\theta f = 0.05$, and $.. \nabla$. $b = 0.5$

isobars represent the contraction of the isobars into the jet field. In the near field, the contraction of the isobars is due to retention of high pressure potential, whereas in the far field it is due to the combined effect of high pressure potential and decrease of relative pressure gradient between the jet potential and the surrounding stagnant atmosphere.

Comparison of the isobars for different Mach numbers is shown in Fig. 4.21. Contrary to the iso-Mach lines, the iso-bars for a given fraction of the exit pressure collapse in the negative as well as positive gradient zones. This implies that for the range of exit Mach numbers studied, the isobaric contraction begins at about the same lateral and axial extent in the jet flow field.

4.2.2 Iso-pressure-spreads

The normalized centre line gauge pressure is given by the following relation.

$$P_C = (P_c/P_a - 1.0)/(P_s/P_a - 1.0) \quad (10)$$

The decay of P_C for different jet exit Mach numbers is shown in Fig. 4.22. The centre line gauge pressure for lower jet Mach number decays faster compared to higher jet Mach number. Fractions of the centreline pressure spreads denoted by b are defined as iso-pressure-spreads. In Fig. 4.23, these fractions varying from $b = 1.0$ to $b = 0.1$ are shown for exit Mach number conditions $M_e = 1.0$. Similar to iso-spreads, the centre line pressure decay is a representative decay along the pressure iso-pressure-spreads in the jet field.

Choosing the local axis on $b = 1.0$ iso-pressure spreads (*as in iso- Mach-spreads*)

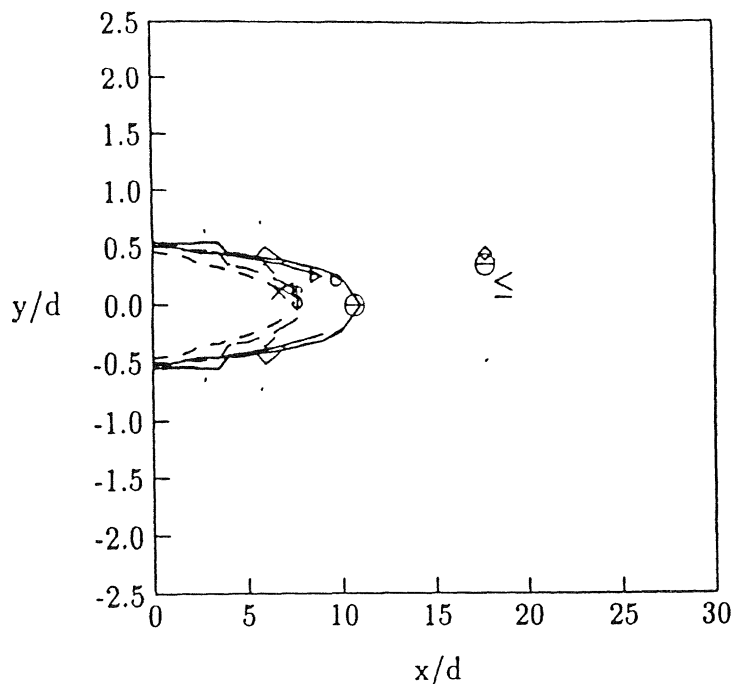


Fig. 4.21 Comparison of isobars for jet Mach numbers ranging from subsonic to correctly expanded sonic freejets : $\bullet M_e = 0.2 \times f = 0.75$, $\blacktriangleright f = 0.50$, $\ominus f = 0.15$, $M_e = 0.6 \triangle f = 0.75$, $\circ f = 0.50$, $\diamond f = 0.15$, $M_e = 1.0 \$ f = 0.75$, $\ominus f = 0.50$, $\leq f = 0.15$.

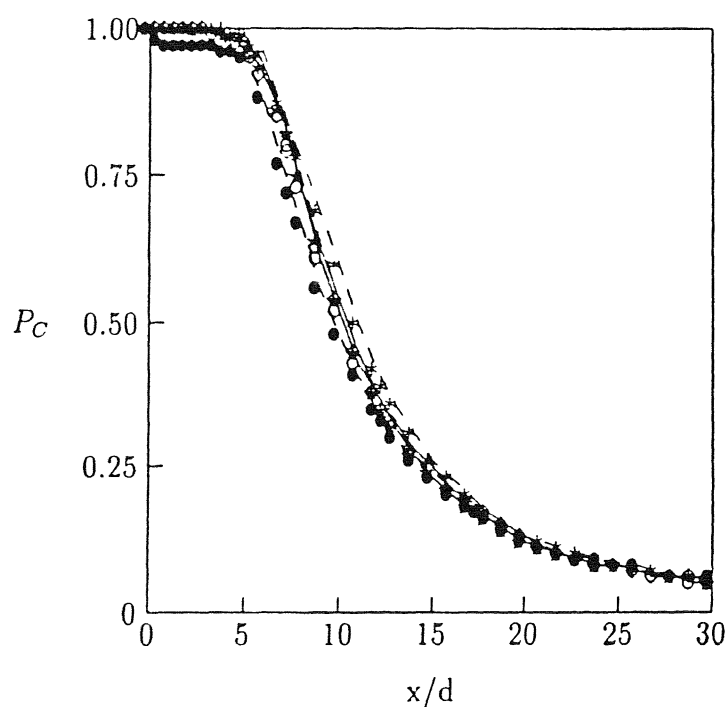


Fig. 4.22 Centreline pressure decay : $\bullet M_e = 0.2$, $\circ M_e = 0.4$, $\star M_e = 0.6$, $\diamond M_e = 0.8$ and $\ast M_e = 1.0$.

and redefining the length scale in terms of pressure width as

$$\eta = \frac{r - r_{b=0.5}}{r_{b=0.5} - r_{b=1.0}} \quad (11)$$

and the proposed pressure scale as

$$P_S = \frac{P_g}{P_C} \quad (12)$$

complete similarity of the jet pressure field has been obtained. The similarity profile is shown in Fig. 4.24 for jet Mach number 0.4. It is interesting to note that the proposed scales result in complete similarity of the jet pressure field right from the nozzle exit.

Pressure similarity upto correctly expanded sonic exit Mach numbers are shown in Fig. 4.25. The deviation in the initial region from the farfield region observed in the figures may due to the error in determining the isospread $b = 1.0$.

4.2.3 Conclusions

In this part, a new approach based on the measured pressure has been adopted to study the free jets . The highlights of the analysis are the following:

- Complete similarity of the pressure distribution for free shear flows has been obtained with the proposed pressure scale and the corresponding length scale.
- The half pressure width demarcates the isobars into zones of isobaric expansion and isobaric contraction.
- The isobars of equal fraction of the exit gauge pressure exhibit positive as well as negative gradients. The positive gradient corresponds to the isobaric expansion

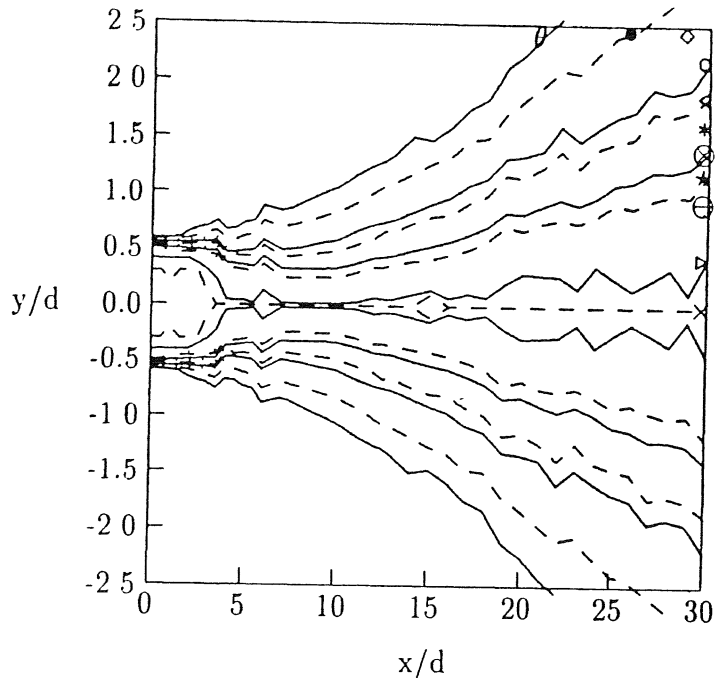


Fig. 4.23 Iso-pressure spread lines for $M_e = 1.0$: $\times b = 1.0$, $\triangleright b = 0.99$, $\ominus b = 0.90$, $\star b = 0.80$, $\otimes b = 0.70$, $*$ $b = 0.60$, $\triangleleft b = 0.50$, $\circ b = 0.40$, $\diamond b = 0.30$, $\bullet b = 0.20$, and $\theta = 0.10$.

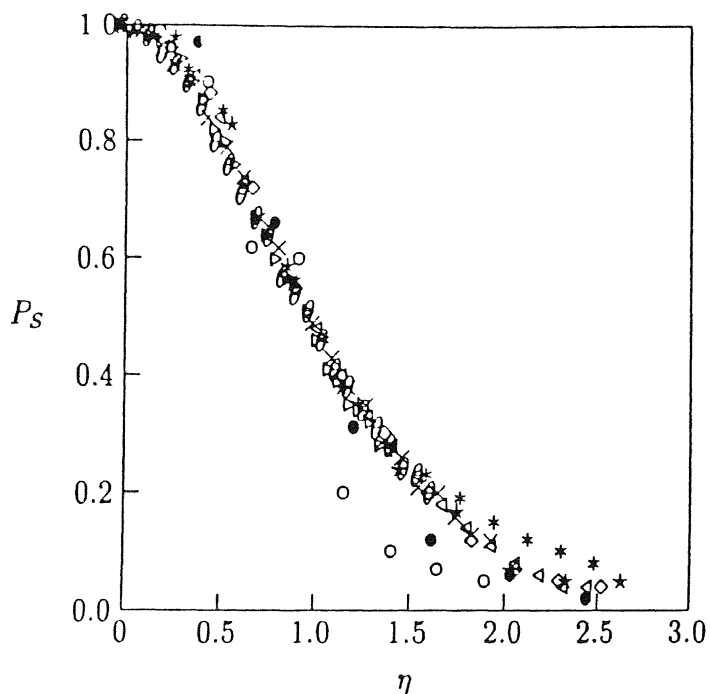


Fig. 4.24 Complete similarity of freejet field pressure distribution for $M_e = 0.4$: $\bullet 2.5d$, $\circ 3.5d$, star $4.5d$, $\diamond 6.0d$, $*$ $9.0d$, $\triangleleft 14.0d$, $\times 20.0d$, $\theta 25.0d$, and $\triangleright 30.0d$.

of the higher pressure potential into the stagnant atmospheric surrounding. The negative gradients exhibit isobaric contraction. In the near field this is due to concentration of higher pressure potential, whereas in the far field this is due to relative decrease of the pressure potential with respect to the stagnant atmosphere.

- Complete pressure similarity exists for jet exit conditions from subsonic to correctly expanded sonic conditions.

4.3 Comparative studies

In this section, comparative study between Mach number approaches and pressure approaches has been discussed.

Comparison of the centre line Mach number decay and centre line gauge pressure decay is shown in Fig. 4.26 . At any axial location downstream of the potential core, the pressure decay is below the Mach number decay, as expected. The centre line decay of pressure and Mach number in this figure further substantiates that the inertial effect is obvious through Mach number representation. The half velocity and the half pressure widths have been compared in Fig. 4.27 for free jet. This figure shows that the meaningful half pressure width for the range of Mach numbers studied, is significantly lower than the corresponding meaningful half velocity width.

The pressure similarity and velocity similarity for the free jet are similar as seen from Fig. 4.28, and exhibit normal distribution. This implies that the jet maintains the same similarity, whether the distribution is the basic flow quantity, namely, the measured pressure or the derived quantity, namely the Mach number.

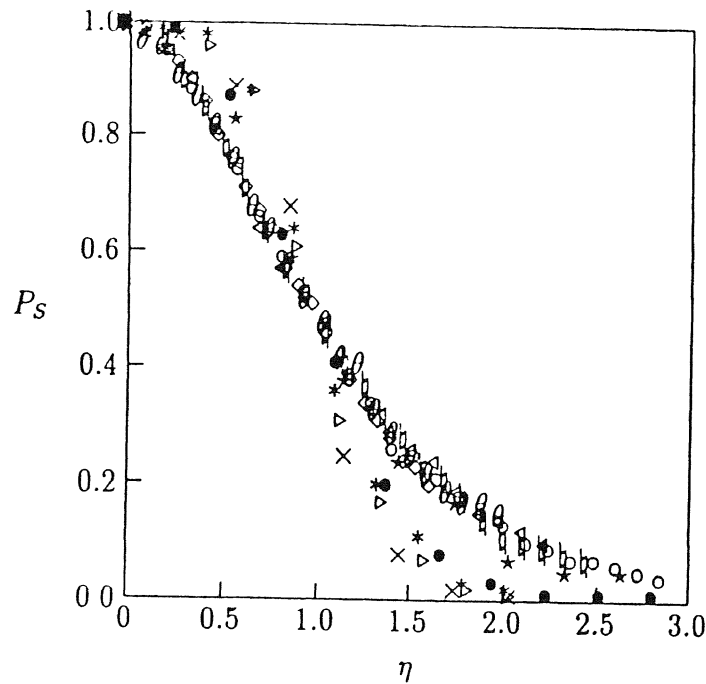


Fig. 4.25 Complete similarity of freejet field pressure distribution for subsonic to correctly expanded sonic jets : $M_e = 0.2 \bullet 2.5d$, $\circ 15.0d$, $M_e = 0.4 \star 4.5d$, $\diamond 25.0d$, $M_e = 0.6 * 4.0d$, $\triangleleft 16.0d$, $M_e = 0.8 \times 2.5d$, $\theta 20.0d$, and $M_e = 1.0 \triangleright 4.0d$, $\sharp 20.0d$.

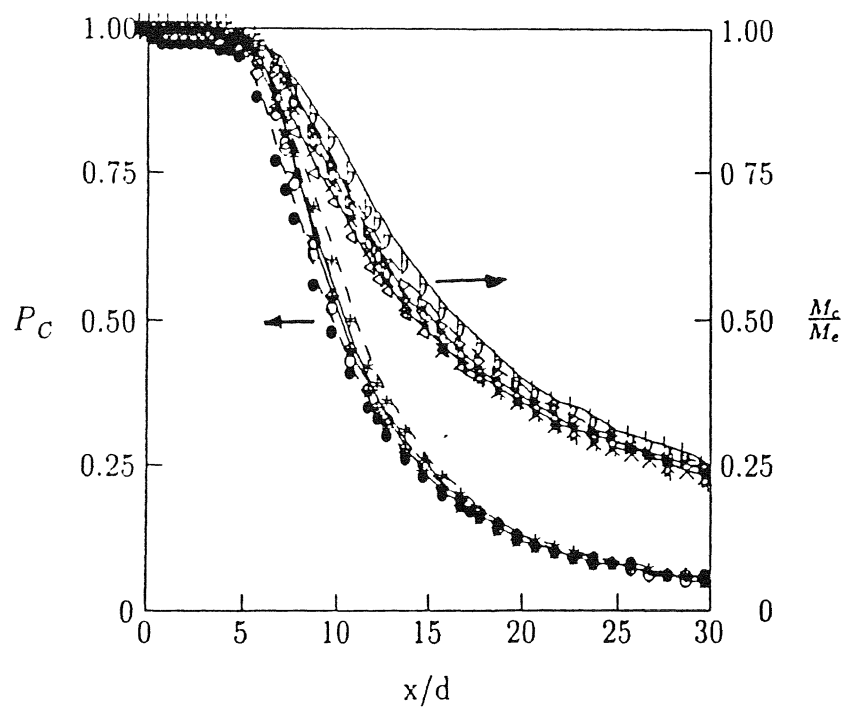


Fig. 4.26 Comparison of centreline pressure decay and Mach number decay : Centre line pressure : $\bullet M_e = 0.2$, $\circ M_e = 0.6$, $\diamond M_e = 0.8$, $\star M_e = 1.0$, Centre line Mach number : $\triangleleft M_e = 0.2$, $\times M_e = 0.4$, $\sharp M_e = 0.6$, $\triangleright M_e = 0.8$, $\flat M_e = 1.0$.

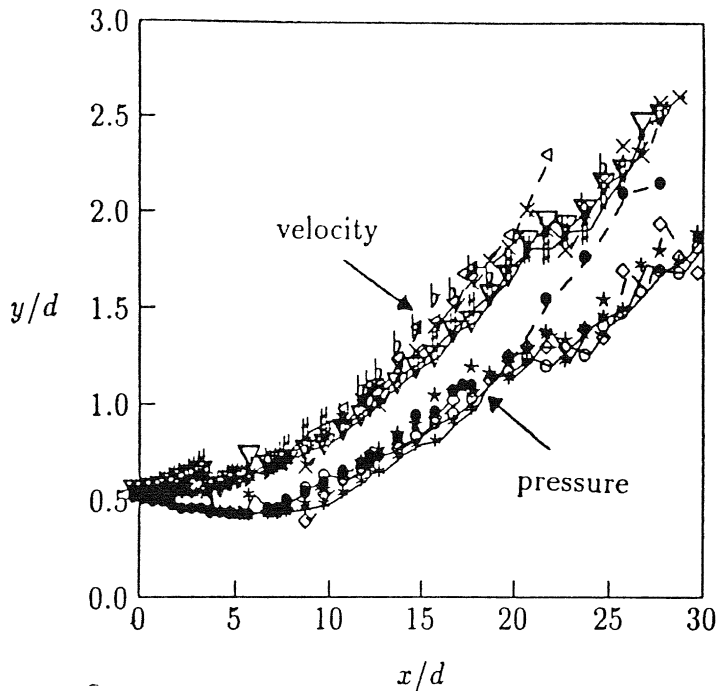


Fig. 4.27 Comparison of half pressure widths and velocity widths for freejets : pressure width : • $M_e = 0.2$, ○ $M_e = 0.4$, ★ $M_e = 0.6$, ◇ $M_e = 0.8$, * $M_e = 1.0$ velocity width : ▲ $M_e = 0.2$, # $M_e = 0.4$, ▽ $M_e = 0.6$, × $M_e = 0.8$, ∇ $M_e = 1.0$

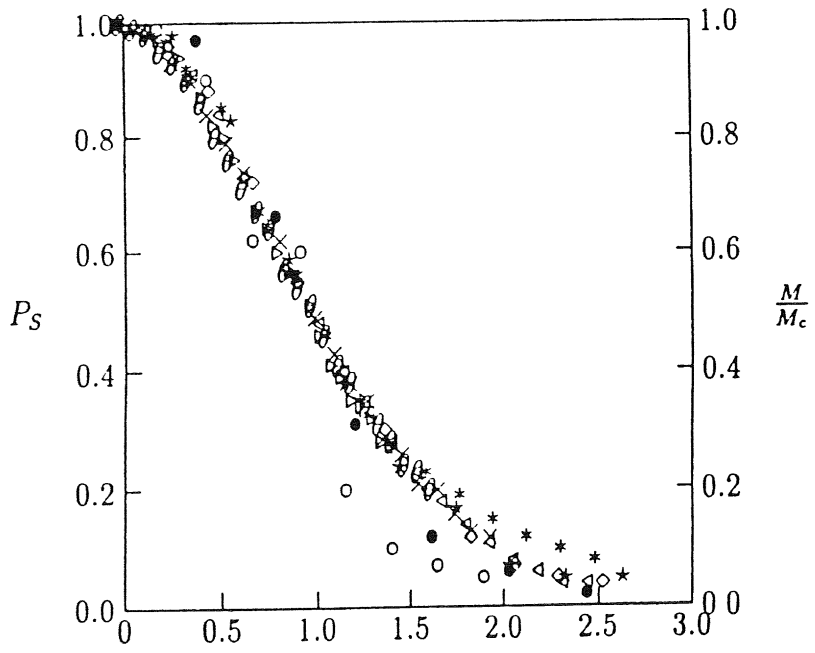


Fig. 4.28 Comparison of pressure and velocity similarity for freejets : pressure similarity : $M_e = 0.2 \bullet 15.0d$, $M_e = 0.4 \circ 17.0d$, $M_e = 0.6 \star 16.0d$, $M_e = 0.8 \diamond 15.0d$, $M_e = 1.0 *$ 20.0d velocity similarity : $M_e = 0.2 \triangleleft 12.5d$, $M_e = 0.4 \times 12.5d$, $M_e = 0.6 \# 12.5d$, $M_e = 0.8 \triangleright 12.5d$, $M_e = 1.0 \# 12.5d$

4.3.1 Concluding remarks

Comparative study between the Mach number based approach and the pressure based approach reveal the following.

- the half pressure width with respect to the local coordinate system for free flows are significantly lower than the half velocity width.
- the pressure similarity and the velocity similarity are similar for freejets.
- the comparison of the same fraction of isobars for different exit Mach numbers, exhibit collapse in the negative as well as the positive gradient zones, contrary to the iso-Mach lines which shows the inertial effect. This implies that the expansion and contraction of the isobars of the same fraction are independent of the initial exit conditions.

Chapter 5

Normal Impinging Jets

A jet impingement is said to be normal when the impingement plane is normal to the jet axis. The schematic of the various zones of normal impinging jet is shown in Fig. 5.1. The impinging jet field is divided into three zones: a) freejet zone, which has the characteristics of a freejet issuing into quiescent ambient surroundings b) impingement zone, the zone just above the surface of the impingement plane and c) walljet zone, the zone where the flow deflects radially outward due to the presence of the wall.

In the first part of this chapter, the effect of the wall on the impinging jet field is analyzed based on the Mach number. In the second part, the effect of the wall on the impinging jet field and the jet field on the wall surface pressure distribution is analyzed based on the measured gauge pressure. The impinging jet studies have been carried out for exit Mach numbers ranging from low subsonic of 0.2 to correctly expanded sonic, in steps of 0.2. Further, the freejet characteristics has been compared with the impinging jet characteristics.

5.1 Mach number based approach

In this section, the impinging jet field has been analyzed on the basis of iso-Mach lines, iso-shear and volume flow rate distribution. These characteristics have been compared with those of the freejet characteristics. The pitot pressure measurements have been carried out in the impinging jet field for the different exit conditions of the present study and various nozzle to wall distances.

5.1.1 Iso-Mach lines

The iso-Mach lines shown in Fig. 5.2 are for $D_w = 7.5$ and $M_e = 0.2$. The fractions of exit Mach number shown are from $f = 0.99$ to 0.2 . The iso-Mach lines have negative as well as positive gradients similar to that of freejet field characteristics. However, mild oscillations in the gradients are observed. These oscillations may be due to interaction between the oncoming and reflected pressure waves from the wall that triggers the shear layers at the nozzle exit periodically. In Fig. 5.3, the iso-Mach lines of the impinging jet field have been shown for wall at the far field location of $D_w = 30$ and exit Mach number $M_e = 1.0$. The fractions f vary from 0.99 to 0.2 . It is seen from these results that the inertia dominant zone of the impinging jet field is not significantly influenced by the wall, however the lower fractions of f corresponding to the viscous dominant zone are influenced considerably by the periodic oscillations triggered at the nozzle exit shear layer. In Fig. 5.4 iso-Mach lines, with three fractions of $f = 0.75, 0.5$ and 0.35 of the impinging jet field with wall at $D_w = 5.0, 10.0, 15.0, 20.0, 25.0$ and 30.0 have been compared with the freejet for $M_e = 0.8$. The lateral spread of the iso-Mach lines of the impinging jet field is observed to be lower than that of the freejet in the viscous

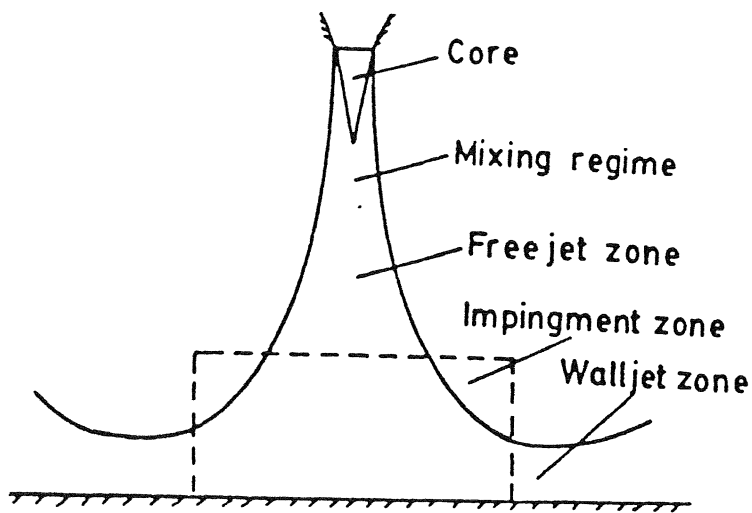


Fig. 5.1 Characteristic features of impinging jet :

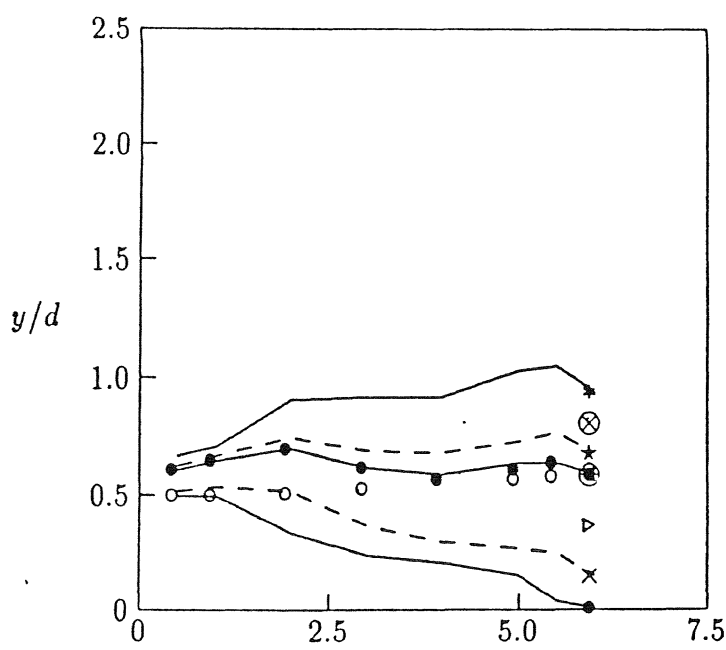


Fig. 5.2 Impinging jet with wall at $D_w = 7.5$ for $M_e = 0.2$: Iso-Mach lines $\# f = 0.99$, $\times f = 0.90$, $\triangleright f = 0.70$, $\ominus f = 0.50$, $\star f = 0.40$, $\otimes f = 0.30$, $*$ $f = 0.20$, half velocity width $\bullet b = 0.50$ and iso-volume flow rate lines $\circ q = 1.0$.

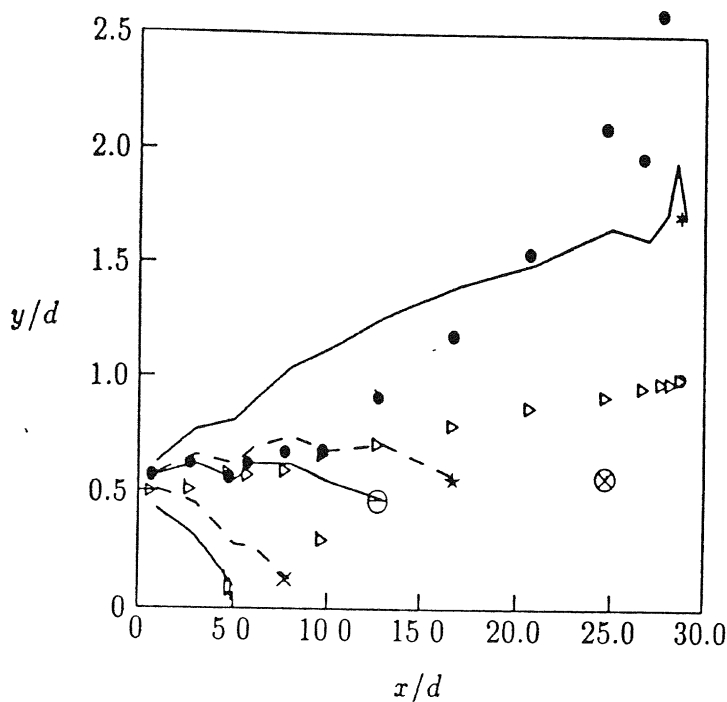


Fig. 5.3 Impinging jet with wall at $D_w = 30.0$ for $M_e = 1.0$: Iso-Mach lines $\# f = 0.99$, $\times f = 0.90$, $\triangleright f = 0.70$, $\ominus f = 0.50$, $\star f = 0.40$, $\otimes f = 0.30$, $* f = 0.20$, half velocity width $\bullet b = 0.50$ and iso-volume flow rate lines $\circ q = 1.0$.

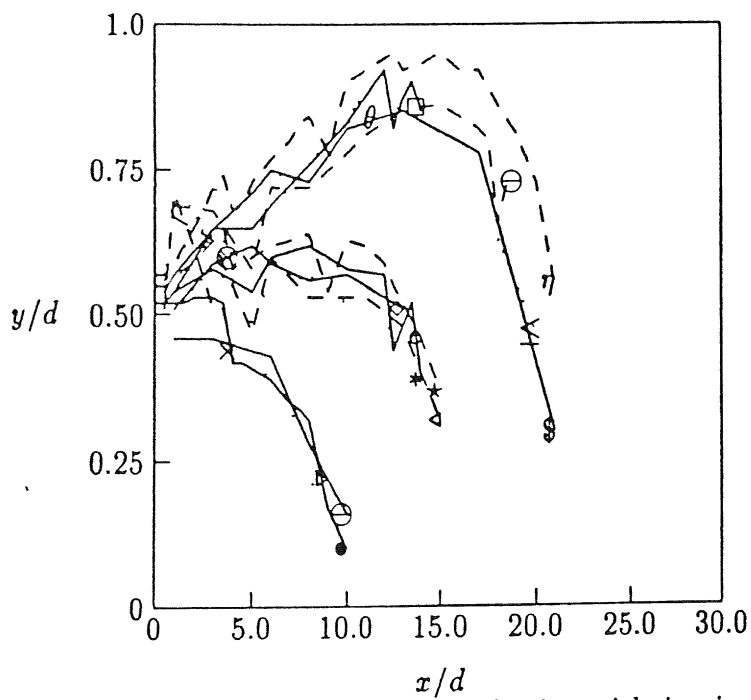


Fig. 5.4 Comparison of Iso-Mach lines of freejet with impinging jets at various wall locations for $M_e = 0.8$: freejet $\bullet f = 0.75$, impinging jet $D_w = \times 5.0$, $\triangleright 10.0$, $\ominus 30.0$, freejet \star , impinging jet $f = 0.5$, $\ominus 5.0$, $\star 15.0$, $\triangleleft 20.0$, $\circ 25.0$, $\diamond 30.0$, freejet η , impinging jet $f = 0.35$, $\theta 12.5$, $\square 15.0$, $\ominus 20.0$, ≤ 25.0 and $\$ 30.0$.

dominant zone. This is due to the fact that at any location the pitotprobe records higher value in the freejet field compared with impinging jet, since in the impinging jet field the streamlines reaching the pitot probe has more obliqueness.

From the above results it may be summarized that, the effect of the wall on the impinging jet are :

1. The impinging jet field has positive as well as negative gradient iso-Mach lines, and the physical significance of these gradients such as; dominance of viscous and inertia zones and the axial limit on penetration of the jet edge viscous effects on the impinging jet field are valid.
2. Mild oscillations are observed in the viscous dominant zone near the nozzle exit due to periodic tripping of the shear layers.
3. The iso-Mach lines in the impinging jet field have lower lateral extent due to higher radial component in the impinging field compared with the freejet field.

5.1.2 Iso-Mach spreads

In Fig. 5.5, the freejet decay for $M_e = 0.6$ has been compared with the decay of the jet at various wall locations $D_w = 2.5, 5.0, 7.5, 10.0, 12.5, 15.0, 20.0, 25.0$ and 30.0 . The impinging jet decay is found to be similar to that of the freejet.

This figure shows that the decay of the freejet zone in the impinging jet field is not influenced by the wall locations. This is due to the inertia dominance at the centre line in the jet field. Since the impinging jet is an axi-symmetric one, whatever be the influence of the wall on the jet, it is felt only along the radial direction and

that too close to the wall. Therefore, the jet centreline propagates along that of the corresponding freejet till it hits the wall. This aspect is clearly reflected by the close agreement between the freejet and the impinging jet decay shown in Fig. 5.5. The iso-spreads in the impinging jet field is shown in Fig. 5.6 for $M_e = 0.6$ at $D_w = 30$. The fractions b of the centre line iso-spreads vary from 1.0 to 0.2. From this figure, it is once again seen that the effect of the wall is seen in the form of oscillatory nature of the isospreads in the vicinity of the wall.

The half velocity width as a length scale is useful to study the growth of the freejet. The half velocity width in the impinging jet field has been compared with that of the freejet for $M_e = 0.2$ at various wall locations $D_w = 2.5, 5.0, 7.5, 10.0$ and 12.5 in Fig. 5.7. The influence of the wall is seen right from the nozzle exit for this near field impingement.

In Fig. 5.8, the freejet half velocity width and the impinging jet half velocity width have been compared for $M_e = 0.6$ and $D_w = 2.5, 5.0, 7.5, 10.0, 12.5, 15.0, 20.0, 25.0$ and 30.0 . From this figure, it is evident that at all Mach numbers of the present study, the half width of the free and impinging jet are almost identical except near the region adjacent to the wall.

In Figures 5.9, the half velocity widths has been compared for the Mach numbers ranging from 0.2 to 1.0 in steps of 0.2, and various wall locations $D_w = 2.5, 5.0, 7.5, 10.0, 12.5, 15.0, 20.0$ and 25.0 . For near field impingement of $D_w < 7.5$, the half width shows some oscillations, but as the wall is progressively moved away from the nozzle exit the oscillations subside for all the Mach numbers as seen from these figures. This may be due to the combined effect of large entrainment near the nozzle exit and the instabilities triggered by the wall. From these results it is seen that the behaviour is

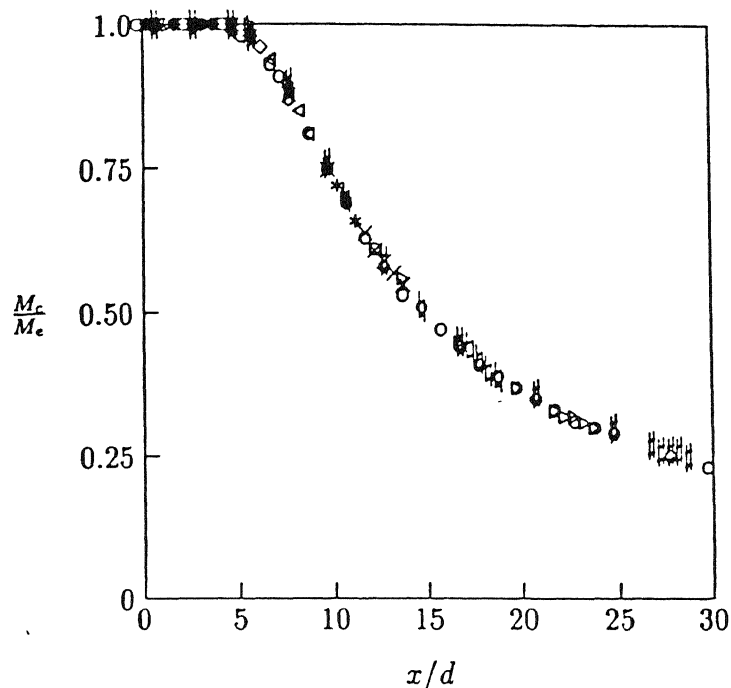


Fig. 5.5 Centre line decay of freejet compared with impinging jet centre line decay at various wall locations : $M_e = 0.6$ \circ free, $D_w = \star 2.5$, $\bullet 5.0$, $\diamond 7.5$, $\triangleleft 10.0$, $\ast 12.5$, $\times 15.0$, $\# 20.0$, $\triangleright 25.0$ and $\# 30.0$.

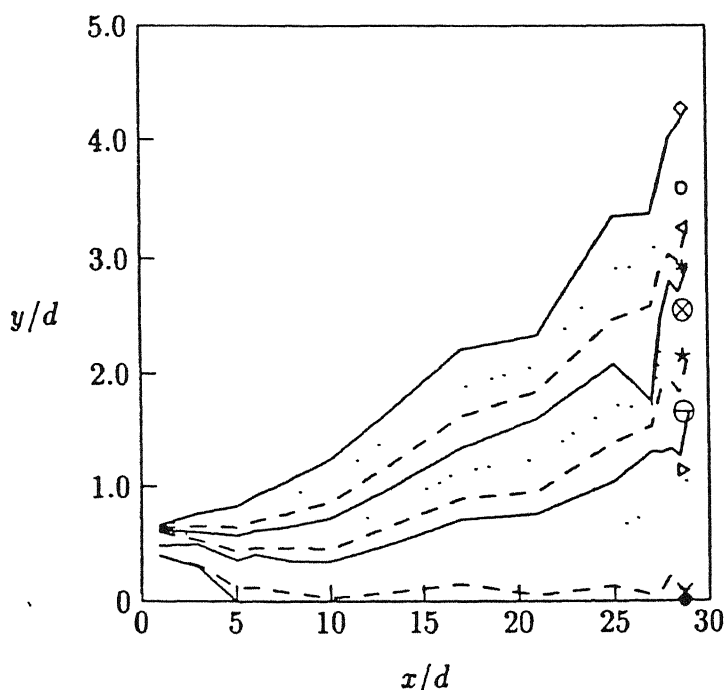


Fig. 5.6 Impinging jet iso-spread lines with wall at $D_w = 30$ for $M_e = 0.6$ $\bullet b = 1.0$, $\times b = 0.99$, $\triangleright b = 0.90$, $\ominus b = 0.80$, $\star b = 0.70$, $\otimes b = 0.60$, $\ast b = 0.50$, $\triangleleft b = 0.40$, $\circ b = 0.30$ and $\diamond b = 0.20$.

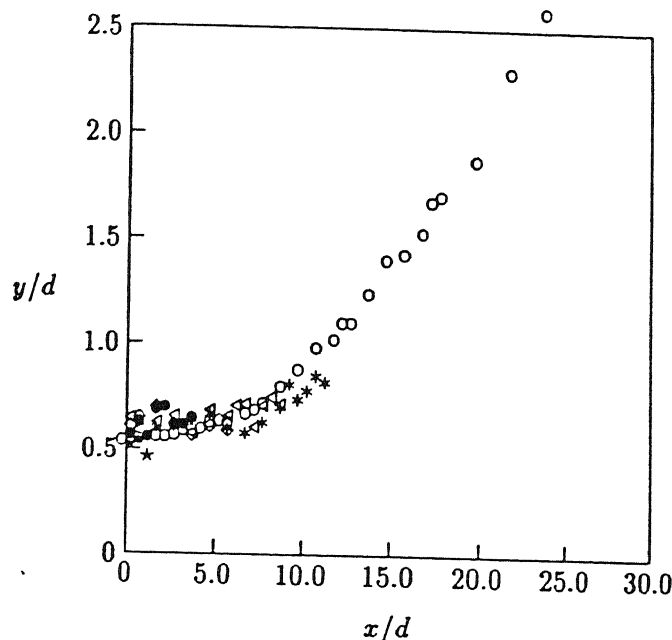


Fig. 5.7 Comparison of half velocity widths between freejet and impinging jets at various wall locations : freejet $\circ M_e = 0.2$, impinging jet $D_w = \star 2.5, \bullet 5.0, \diamond 7.5, \triangleleft 10.0, \ast 12.5$.

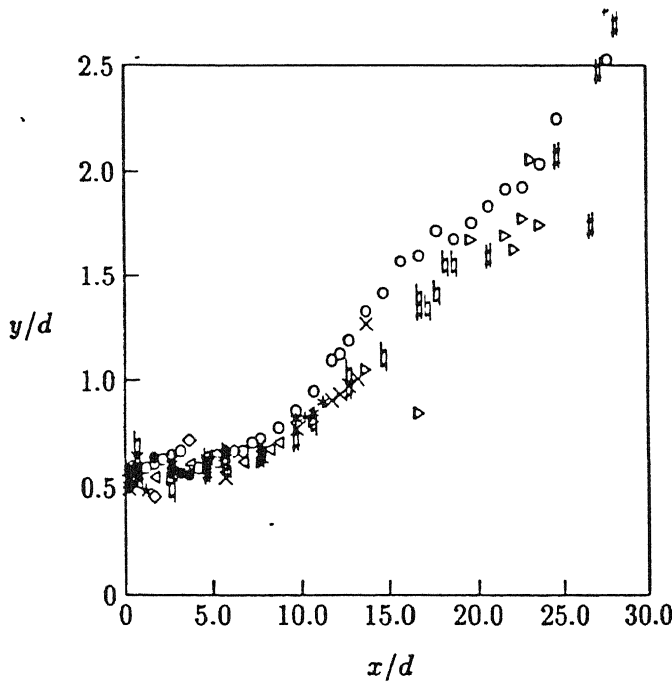


Fig. 5.8 Comparison of half velocity widths between freejet and impinging jets at various wall locations : freejet $\circ M_e = 0.6$, impinging jet $D_w = \star 2.5, \bullet 5.0, \diamond 7.5, \triangleleft 10.0, \ast 12.5, \times 15.0, \triangleright 25.0$, and $\# 30.0$.

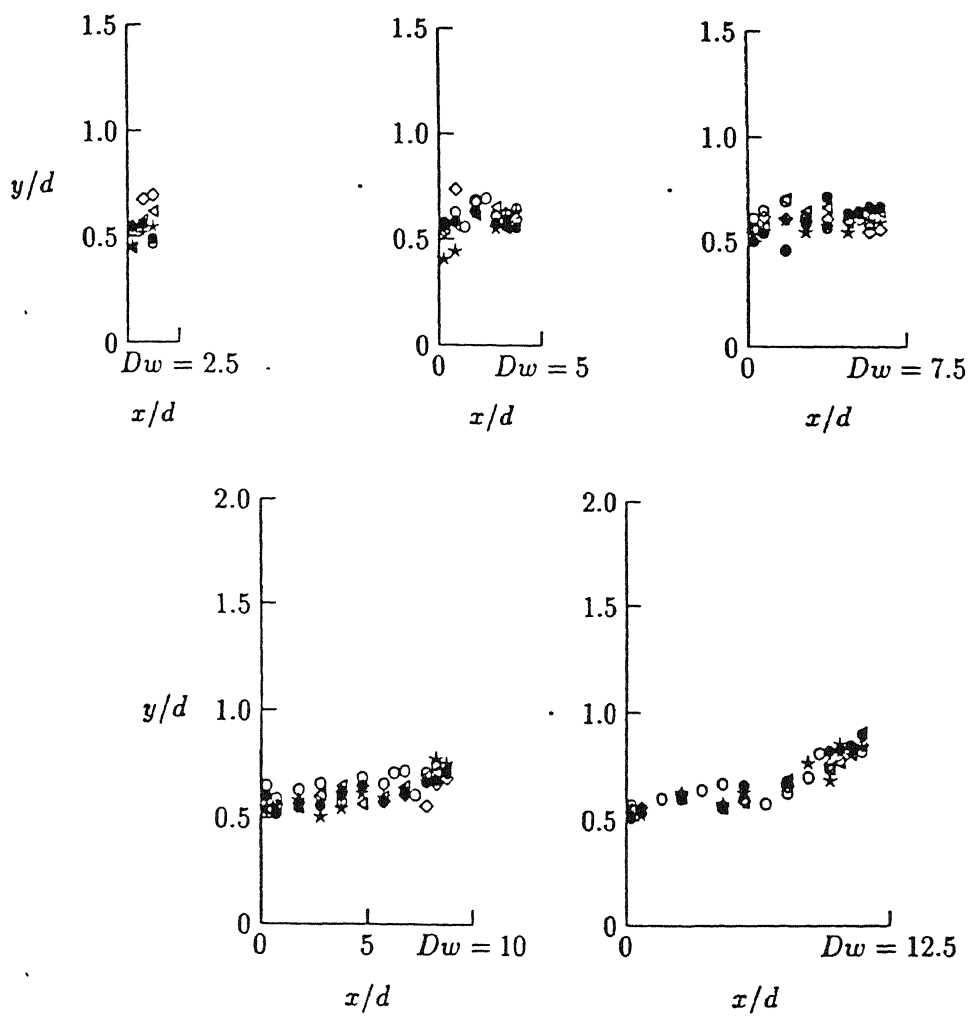


Fig. 5.9 . . .

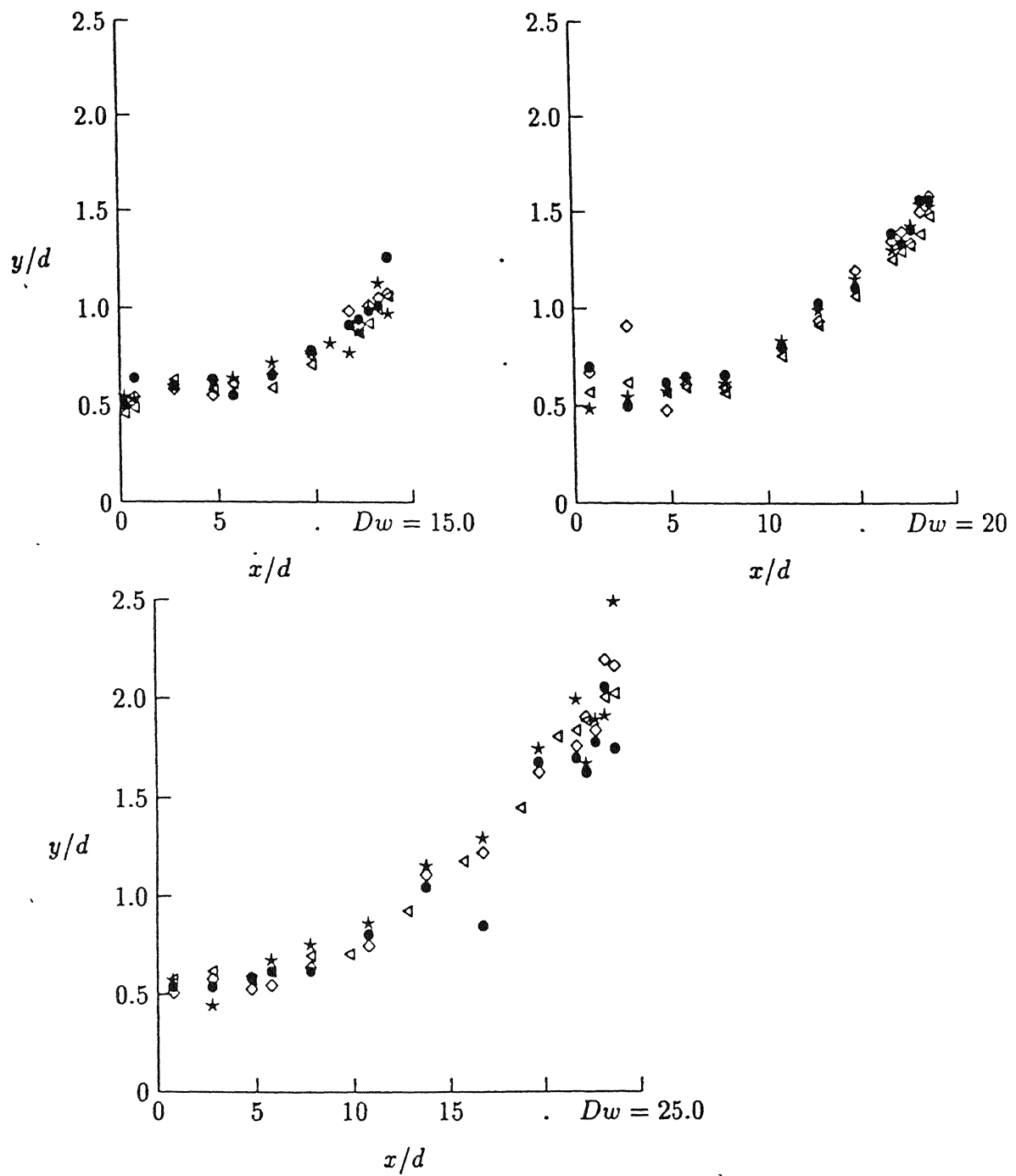


Fig. 5.9 Comparison of half velocity widths at various wall locations : $\circ M_e = 0.2$, $\star M_e = 0.4$, $\bullet M_e = 0.6$, $\diamond M_e = 0.8$, $\triangleleft M_e = 1.0$.

almost independent of the jet Mach number.

Complete similarity of the free shear flow has been reported for free jets in the underdeveloped and the developed region of the flow field by a suitable definition of the length scale given by eqn. (3). This length scale proposed for complete similarity has been applied to the impinging jet field. In Figs. 5.10 and 5.11, similarity in the freejet field has been compared with the impinging jet field for various wall locations.

As seen from these results, complete similarity is exhibited for the impinging jet field also. The similarity achieved is independent of the wall location. Like freejet similarity, the impinging jet similarity also exhibits a normal distribution. The reason for the scatter is same as that for the freejet and also due to the influence of the wall on the impinging jet field.

5.1.3 Iso-shear

The jet field is an entrainment dominated flow field as a result of the action-reaction principle leading to penetration of the surrounding mass into the flow field. The penetration of the surrounding mass is not only responsible for retarding the moving fluid mass, but it also enhances the mixing. In addition to the above phenomena, the consequence of impingement are reingestion, excitation of the shear layers due to reflection of the downstream pressure waves, reversal of the axial velocity due to rebounding of the structures, and enhancement of the radial velocity. To assimilate these phenomena, constant shear surfaces given by eqn (5) are constructed for the impinging jet field for various wall locations. Figs. 5.12-5.14 show iso-shear surfaces denoted by S with jet exit Mach numbers $M_e = 0.2$ and 1.0 for freejet field and the impinging jet field. For comparative analysis between freejet and the impinging jet fields two values of $S =$

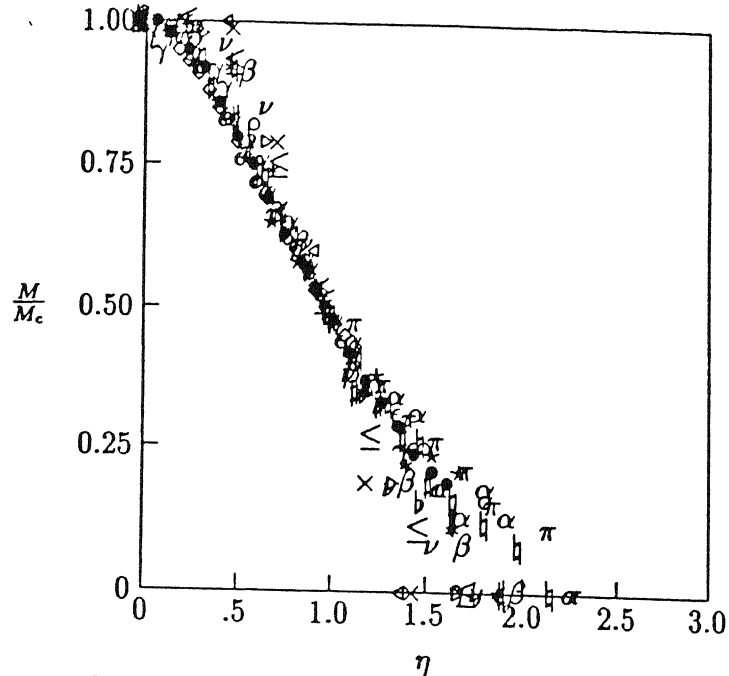


Fig. 5.10 Complete similarity of freejet and impinging jet field for $M_e = 0.4$: freejet $\circ 2.5d \star 7.0d \bullet 14.0d \diamond 24.0d$ impinging jet $D_w = 2.5 x = \triangleleft 1.0d, D_w = 5.0 x = * 3.5d, D_w = 7.5 x = \times 2.0d, \# 6.5d, D_w = 10.0 x = \triangleright 2.0d, \# 8.5d, D_w = 12.5 x = \flat 3.0d, \pi 10.0d, D_w = 15.0 x = \leq 3.0d, \alpha 12.5d, D_w = 20.0 x = \nu 3.0d, \epsilon 17.0d, D_w = 25.0 x = \beta 3.0d, \gamma 22.0d$.

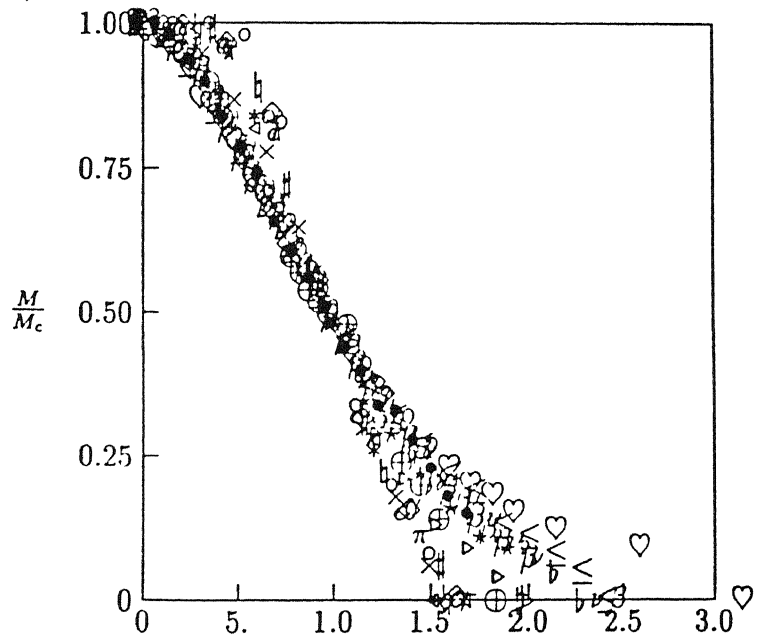


Fig. 5.11 Complete similarity of freejet and impinging jet field for $M_e = 1.0$: freejet $\circ 3.0d \star 7.0d \bullet 14.0d \diamond 23.0d$ impinging jet $D_w = 2.5 x = \triangleleft 1.5d, D_w = 5.0 x = * 2.0d, \times 4.0d, D_w = 7.5 x = \# 2.0d, \triangleright 5.5d, D_w = 10.0 x = \# 2.0d, \flat 8.0d, D_w = 12.5 x = \pi 3.0d, \leq 10.0d, D_w = 15.0 x = \alpha 3.0d, \nu 13.0d, D_w = 20.0 x = \epsilon 3.0d, \beta 19.0d, D_w = 25.0 x = \gamma 3.0d, \heartsuit 22.0d, D_w = 30.0 x = \diamond 3.0d, \oplus 25.0d$.

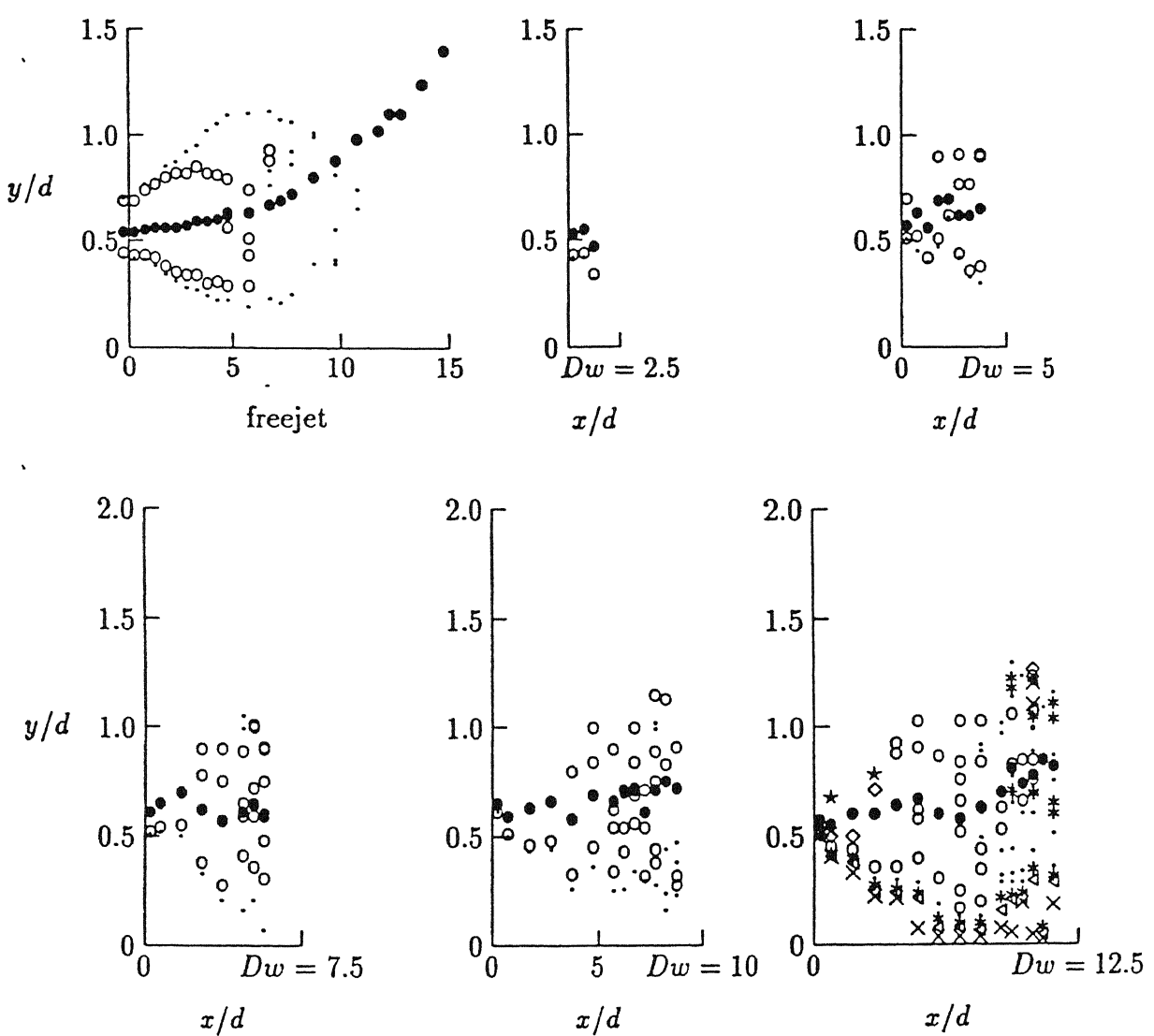


Fig. 5.12 Shear representation at various wall distances for $M_e = 0.2$: $S = \star 0.30, \diamond 0.20, \circ 0.09, \cdot 0.05, * 0.03, \triangleleft 0.02, \times 0.01$ and $\bullet b = 0.5$.

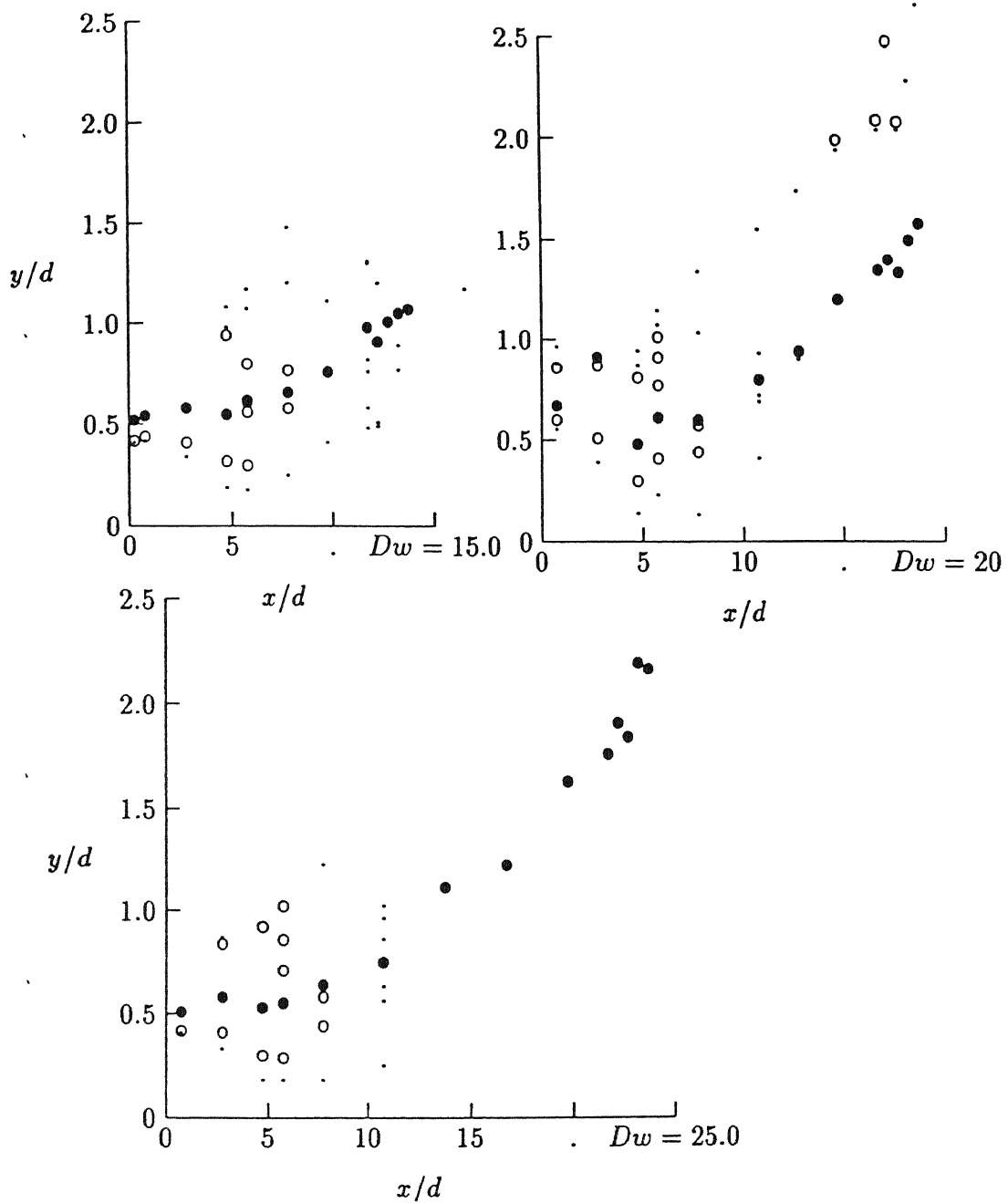


Fig. 5.13 Shear representation at various wall distances for $M_e = 1.0$: $S = \star 0.30, \diamond 0.20, \circ 0.09, \cdot 0.05, * 0.03, \triangleleft 0.02, \times 0.01$ and $\bullet b = 0.5$.

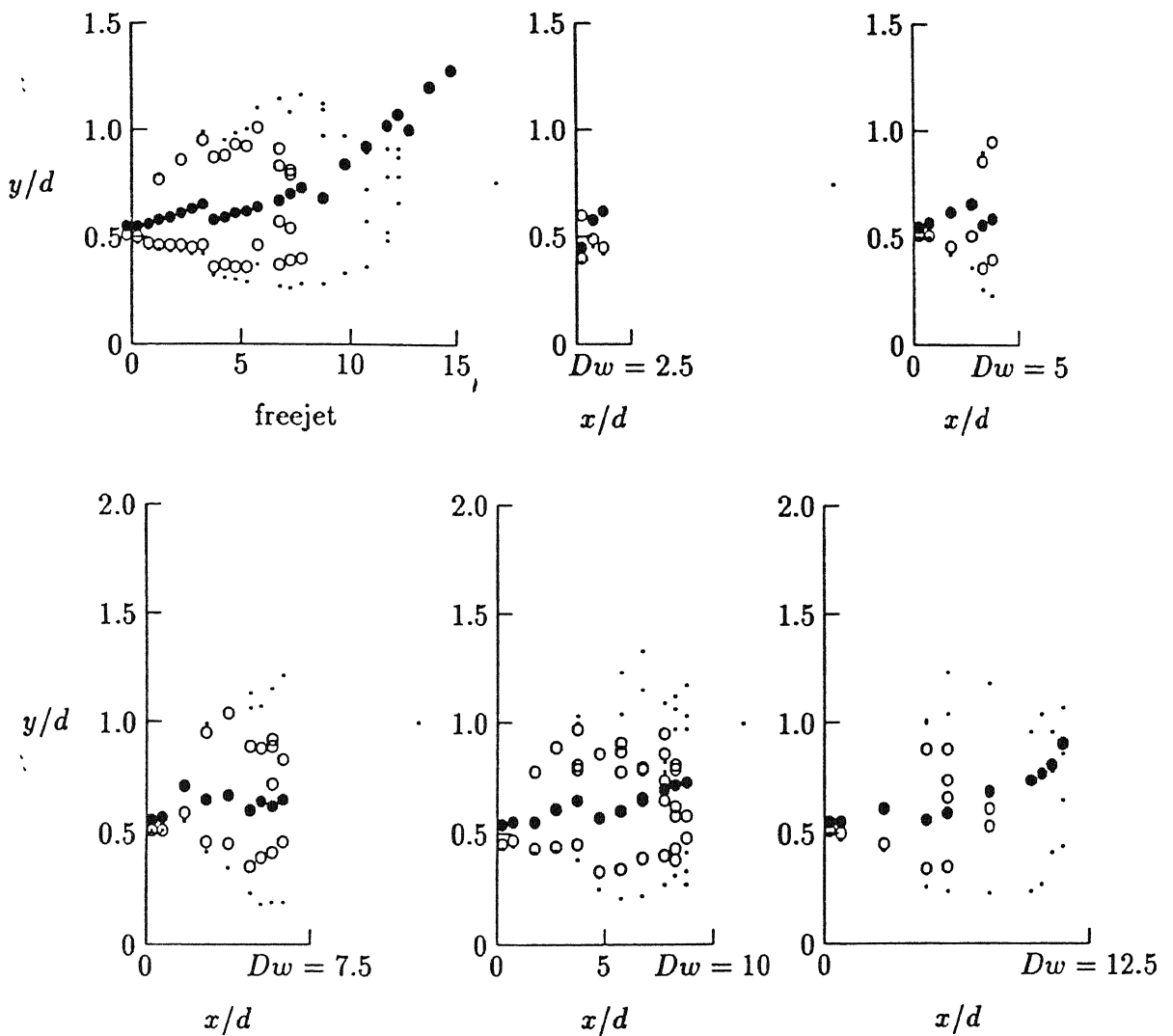


Fig. 5.14 Shear representation at various wall distances for $M_e = 0.8$: $S = \star 0.30, \diamond 0.20, \circ 0.09, \cdot 0.05, \ast 0.03, \triangleleft 0.02, \times 0.01$ and $\bullet b = 0.5$.

0.09 and 0.05 are chosen

The freejet shear surfaces exhibit uniform pattern, whereas the impinging jet exhibits oscillations with increasing wall distances upto $D_w = 5$. For $7.5 < D_w < 12.5$ the shear surfaces exhibit lateral as well as longitudinal stretching. The lateral stretching may be due to the relief effect in the radial direction, whereas the longitudinal stretching may be due to the interaction of the oncoming pressure waves from the wall causing severe oscillations at higher frequency which cannot be detected with pitot probe, thereby making the pitot probe to measure a higher pressure compared to a freejet field under similar conditions. The periodic excitation of the shear layers might also contribute to the stretching of the shear layers. For far field locations of the wall, the effect of interaction of the oncoming and the reflected pressure waves becomes weaker that its effect on the jet structure also becomes marginal, hence the interaction of the wall on the shear layers diminishes progressively as the wall distance increases, as seen from results shown in Figs. 5.12 to 5.14.

5.1.4 Volume flow rate distribution

The diffusion of free jets may be expressed in terms of the initial volume flow rate although free jet flow is an entrainment dominated flowfield. In Fig. 5.15, the iso-volume flow contours in the impinging jet are compared with that of the freejet field for $M_e = 0.6$ at various wall locations $D_w = 5.0, 7.5, 10.0, 15.0, 20.0, 25.0$ and 30.0 . As seen from these results, the iso-volume flow contour $q = 1.0$ of the freejet field is not affected by the presence of the wall. This may be due to the maximal inertia at the jet centre line. On progressing laterally towards the viscous dominant zone, the multiples of the iso-volume flow contours exhibit oscillations triggered at the nozzle exit.

5.1.5 Coherent structures

The mean coherent structures are obtained by constructing surfaces of equal values of g given by eqn (8). The location of maximum g value closer to the lateral axis was defined to be the flow reversal location and represented by R . In Fig. 5.16 the impinging jet flow reversal locations have been compared with the freejet for $M_e = 0.4$, and for $M_e = 0.6$ in Fig. 5.17. In the impinging jet field shown in Fig. 5.16, the flow reversal location occurs close to the jet axis for $D_w = 15.0, 20.0$ and 25.0 . The oscillations observed in the impinging jet field are also re-iterated by the variations in R seen from these results. In Fig. 5.17, it is seen that the earlier flow reversal locations near the jet axis occurs for $D_w = 15.0, 25.0$ and 30.0 . The reversal of the flow in the lateral direction may be due to the inviscid-viscous interaction at the wall resulting in reversal of the axial velocity and structure rebounding phenomena, compared to the freejet. The flow visualization pictures of Landreth and Adrian [65] also show flow reversal occurring close to the jet axis near the wall.

In Figs. 5.18-5.20, the mean coherent structures are shown along with the flow reversal locations. In Fig. 5.18, the structures are shown for $M_e = 0.2$ at $D_w = 7.5$. The reversal location passes through the centre of the structure in this figure, and however exhibit periodic oscillations which is inherent nature of the impinging jet field. In Fig. 5.19, the tendency of the flow to move close to the wall is seen. Near the wall oscillatory nature of the structures exhibit the periodic growth of the structure. Fig. 5.20 also exhibit similar nature, but higher energy of the jet for $M_e = 1.0$ at $D_w = 20$ exhibit higher lateral spread, compared to the lower energy jet with $M_e = 0.4$ at $D_w = 20$.

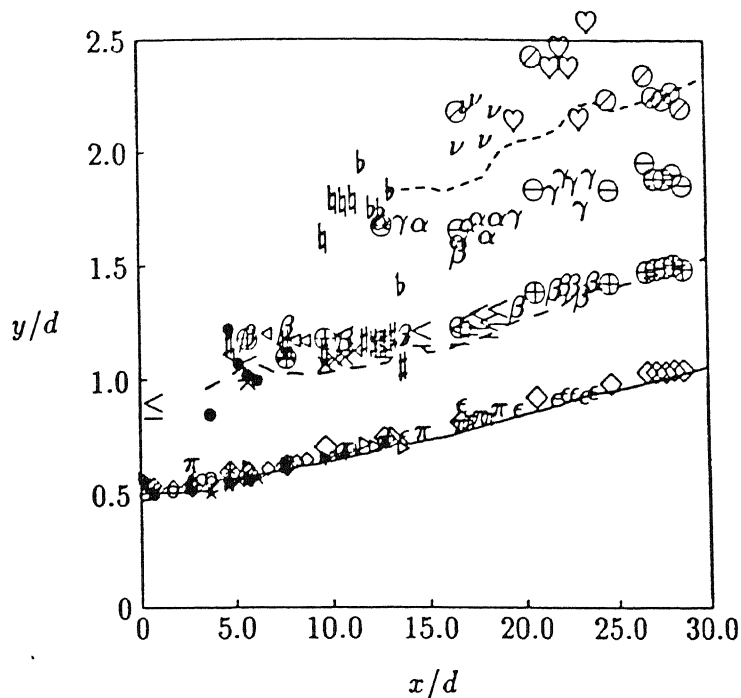


Fig. 5.15 Comparison of iso-volume flow rate for different wall locations ; freejet : solidline $q = 1$, dash $q = 2$, dots $q = 3$, dash $q = 4$, impinging jet $D_w = 5.0 \circ q = 1.0$, $D_w = 7.5 \star q = 1.0$, $\bullet q = 2.0$, $D_w = 10.0 \diamond q = 1.0$, $\triangleleft q = 2.0$, $D_w = 12.5 * q = 1.0$, $\times q = 2.0$, $\# q = 3.0$, $D_w = 15.0 \triangleright q = 1.0$, $\# q = 2.0$, $\flat q = 3.0$, $D_w = 20.0 \pi q = 1.0$, $\leq q = 2.0$, $\alpha q = 3.0$, $\nu q = 4.0$, $D_w = 25.0 \epsilon q = 1.0$, $\beta q = 2.0$, $\gamma q = 3.0$, $\heartsuit q = 4.0$, $D_w = 30.0 \diamondsuit q = 1.0$, $\oplus q = 2.0$, $\ominus q = 2.0$, $\ominus q = 3.0$ and $\ominus q = 4.0$.

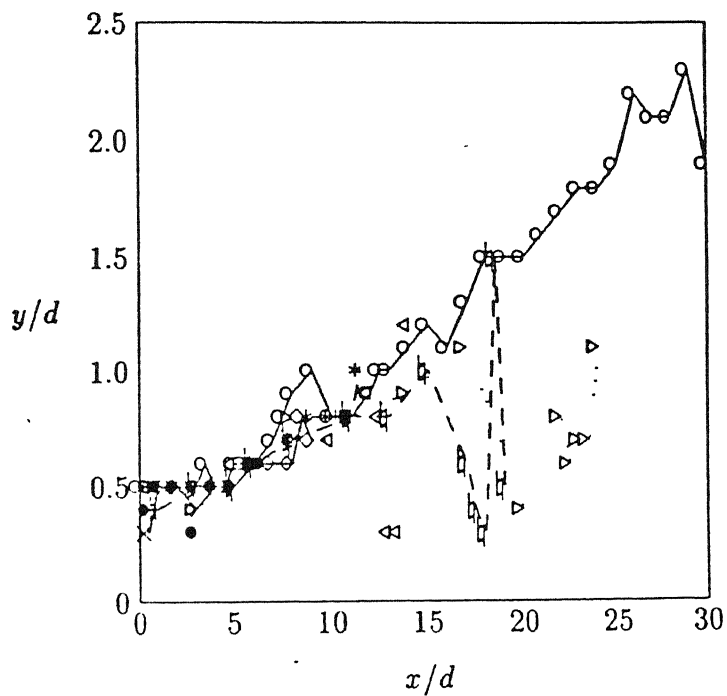


Fig. 5.16 Comparison of impinging jet flow reversal location R with freejet $M_e = 0.4$: \circ freejet, impinging jet $D_w = \times 2.5$, $\cdot 5.0$, $\bullet 7.5$, $* 12.5$, $\triangleleft 15.0$, $\# 20.0$, and $\triangleright 25.0$.

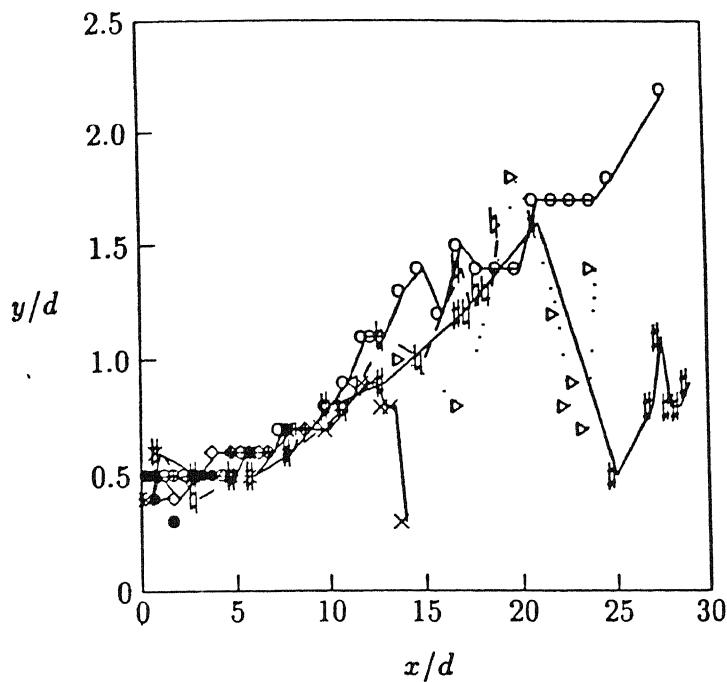


Fig. 5.17 Comparison of impinging jet flow reversal location R with freejet $M_e = 0.6$: \circ freejet, impinging jet $D_w = \cdot 2.5$, $\bullet 5.0$, $\diamond 7.5$, $*$ 10.0 , $\triangleleft 12.5$, $\times 15.0$, $\# 20.0$, and $\triangleright 25.0$.

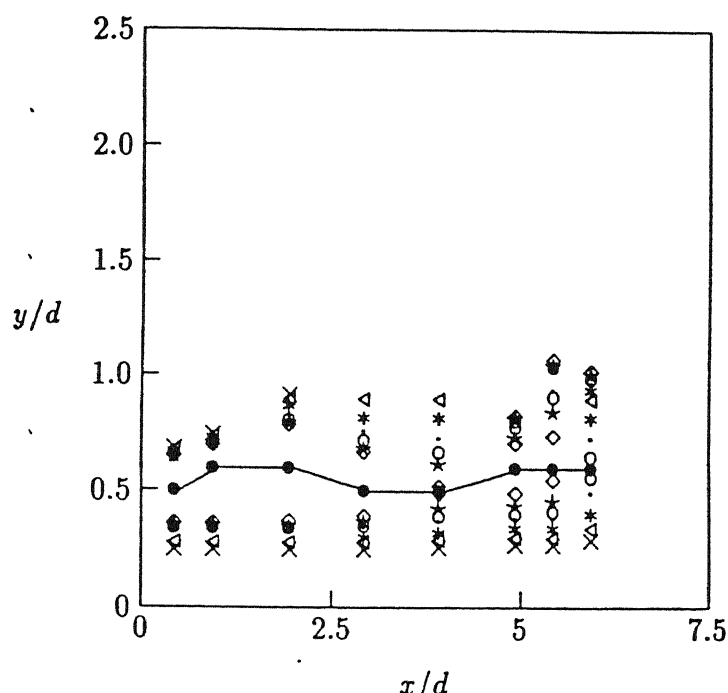


Fig. 5.18 Mean coherent structures $M_e = 0.2$: $D_w = 7.5$ $g = \diamond 0.25$, $\star 0.24$, $\circ 0.23$, $\cdot 0.22$, $* 0.20$, $\triangleleft 0.18$, $\times 0.16$, and $\bullet R$.

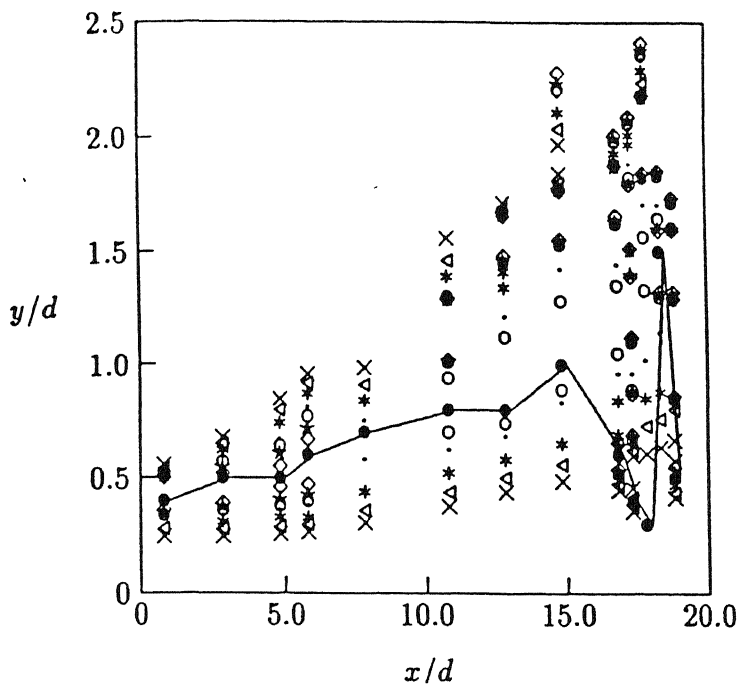


Fig. 5.19 Mean coherent structures $M_e = 0.4$: $D_w = 20.0$ $g = \diamond 0.25, \star 0.24, \circ 0.23, \cdot 0.22, * 0.20, \triangleleft 0.18, \times 0.16$, and $\bullet R$.

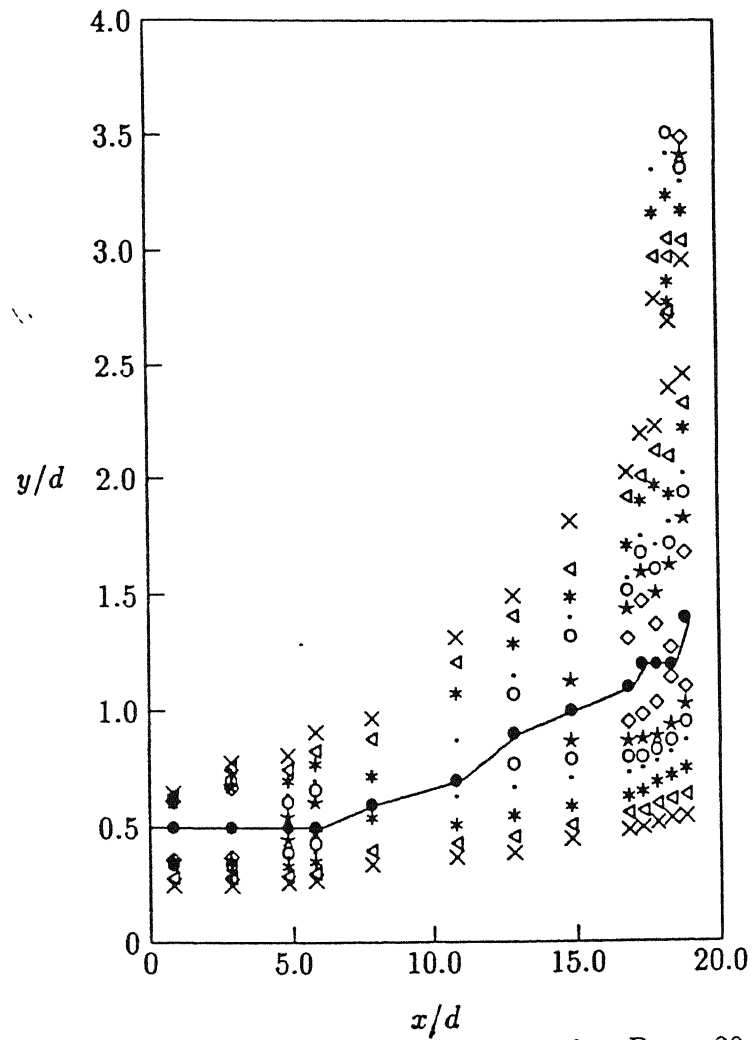


Fig. 5.20 Mean coherent structures $M_e = 1.0$: $D_w = 20.0$ $g = \diamond 0.25, \star 0.24, \circ 0.23, \cdot 0.22, * 0.20, \triangleleft 0.18, \times 0.16$, and $\bullet R$.

5.1.6 Conclusions

- The decay of the jet is not altered by the presence of the wall.
- The iso-Mach lines have positive as well as negative gradients when the wall is in the far field, but for near field impingement the iso-Mach lines are with periodically alternating gradients. This is a result of the excitation of the shear layer at the nozzle exit due to the reflected acoustic waves.
- In the near field, the half width shows oscillatory nature, and has higher width compared to freejet upto around 7.5d. The half width also exhibit an orderly behaviour for all the Mach numbers of the present study, in the far field impingement cases.
- The iso-Mach lines of the impinging jet field having lower fractions of the exit Mach number occur at lower lateral extent as compared to iso-Mach lines of freejet having the same fraction as well as exit Mach number.
- The impinging jet also exhibits complete similarity of the velocity distribution similar to that of the free jet in the underdeveloped region as well as developed region. Similarity represents normal distribution variation in the mixing region.
- The iso-volume contour of the initial volume flow is not influenced by the impingement, but the iso-volume contour of multiples of the initial volume show higher volume in space as compared to the freejet.
- The constant property shear surfaces of impinging jets exhibit longitudinal as well as lateral stretching, compared to free jets.

- Near field impingement has greater stretching of shear layers compared to far field impingement.
- The growth of the structures near the wall is evident from the oscillatory nature of the flow reversal locations.
- The interaction between the primary and secondary structure results in the reversal of the axial velocity.

5.2 Pressure based approach

In this section, the impinging jet field has been analyzed based on the measured gauge pressures. The wall surface pressures have also been analyzed based on the measured pressures and a force scale has been identified to achieve similarity of the force field for normal impingement over a wide range of subsonic to correctly expanded sonic Mach numbers.

5.2.1 Impinging jet field

The emphasis of the present study has been to investigate the variation of the parameters of freejet when a wall is placed in the jet field at various locations for the same exit gauge pressure conditions. The centreline gauge pressure decay is shown in Fig. 5.21 for a representative jet exit Mach number. In this figure the centre line pressure decay of the freejet has been compared with that of impinging jet for various wall locations and are observed to follow the freejet decay.

Fractions of the exit gauge pressure at wall locations $D_w = 7.5$ for exit Mach number

$M_e = 0.2$, $D_w = 20.0$ for exit Mach number $M_e = 0.4$, and $D_w = 30.0$ for exit Mach numbers $M_e = 0.8$ are shown in Figs. 5.22, 5.23 and 5.24, respectively. The negative and positive gradient isobars have physical significance as that in the freejet, but the field is governed by oscillations. In these figures, the half gauge pressure width for wall locations do not demarcate the negative and positive gradients. The effect of the reflected pressure waves from the wall is seen to push the isobar contours upstream (Fig. 5.23). For the far field impingement, the effect of the wall on the jet field isobars is minimal (Fig. 5.24). Further, the half pressure width demarcates the flow field in the far field impinging jets into the expansion and contraction zones as described earlier. These observations are almost the same for all exit Mach numbers of the present study.

Comparison of three fractions of isobars between impinging jets and freejets in Fig 5.25 reveal oscillations in the impinging jet pressure field. The higher fraction isobar exhibit similarity between free and impinging jets due to higher potential, while the lower fraction isobar $f = 0.15$ is influenced significantly by the reflecting pressure waves.

As the half pressure width has physical significance, the impinging jet field pressure width at various wall locations has been compared with the freejet for exit Mach number $M_e = 0.6$ in Fig. 5.26. Near the potential core zone, the half width converges and then diverges. In the diverging portion of the field, the freejet half pressure width is seen to be higher than that of the impinging jet. In the near field considerable oscillations are observed due to the excitation of the shear layer by the wall. Further downstream, the reduction of the pressure width compared to the freejet may be due to the interaction of the downstream pressure waves and the pressure waves reflected from the wall in the upstream direction, and due to the radial component of the flow introduced by

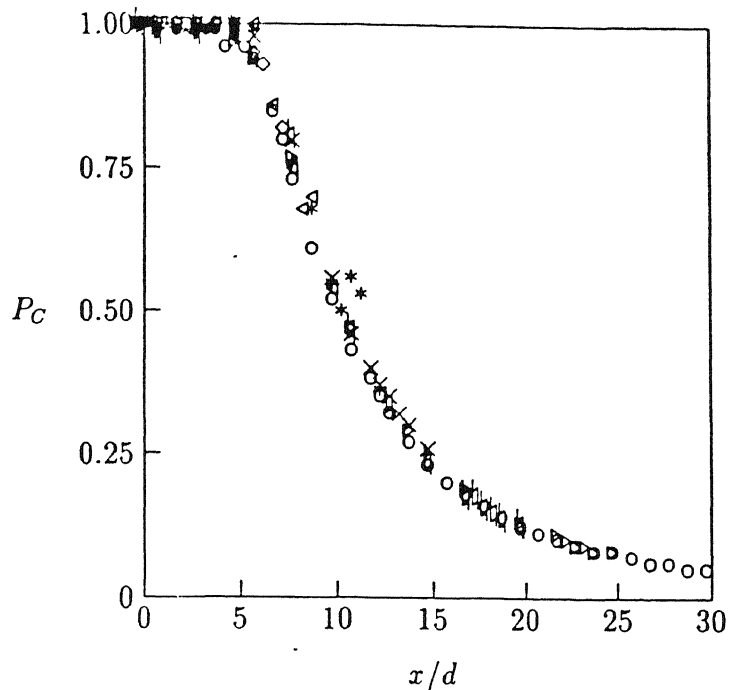


Fig. 5.21 Pressure of freejet compared with impinging jet at various wall locations for $M_e = 0.4$: \circ freejet, \star 2.5, \bullet 5.0, \diamond 7.5, \triangleleft 10.0, $*$ 12.5, \times 15.0, \sharp 20.0 and \triangleright 25.0.

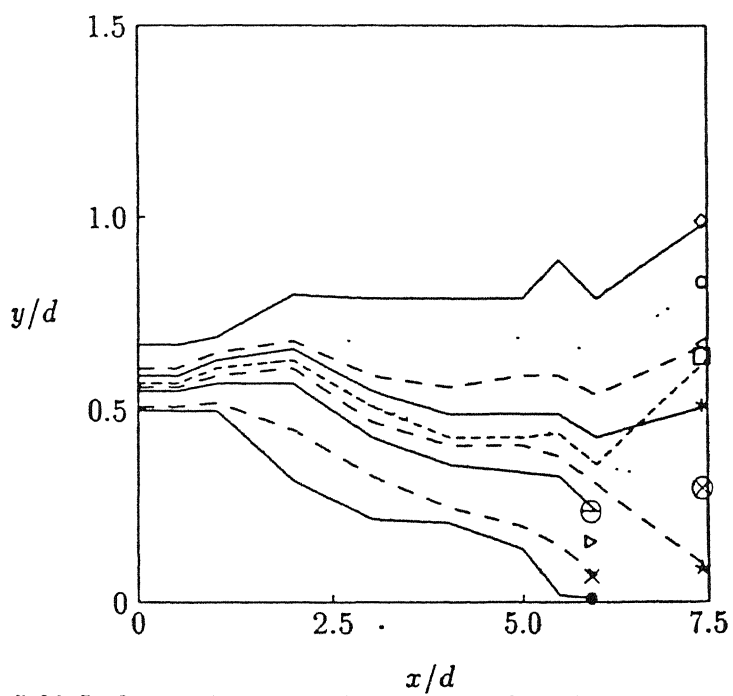


Fig. 5.22 Isobars of various fractions and half pressure width for $M_e = 0.2$ with wall at $D_w = 7.5$: $f = \bullet 0.99, \times 0.90, \triangleright 0.80, \ominus 0.70, \star 0.60, \ominus 0.70, * 0.40, \triangleleft 0.30, \circ 0.20, \diamond 0.10$ and $\square b = 0.5$.

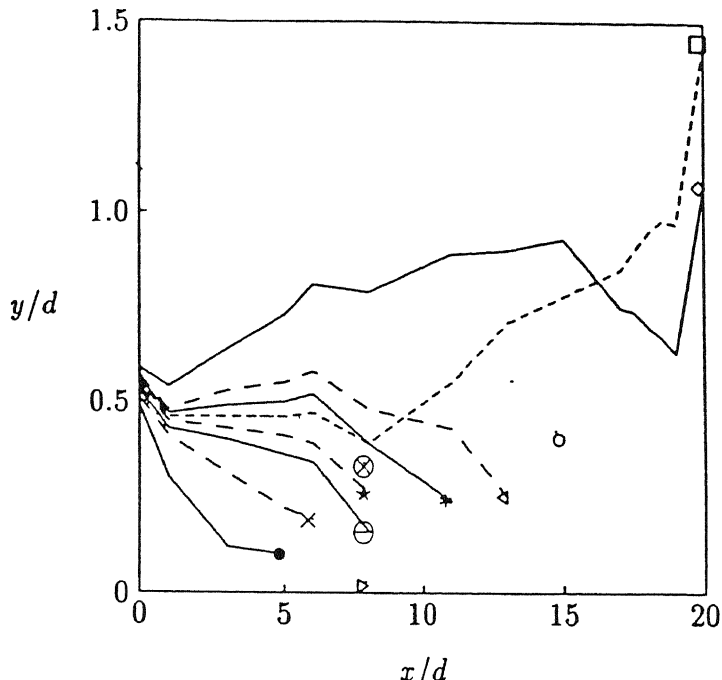


Fig. 5.23 Isobars of various fractions and half pressure width for $M_e = 0.4$ with wall at $D_w = 20.0$: $f = \bullet 0.99, \times 0.90, \triangleright 0.80, \ominus 0.70, \star 0.60, \ominus 0.70, *$ 0.40, $\triangleleft 0.30, \circ 0.20, \diamond 0.10$ and $\square b = 0.5$.

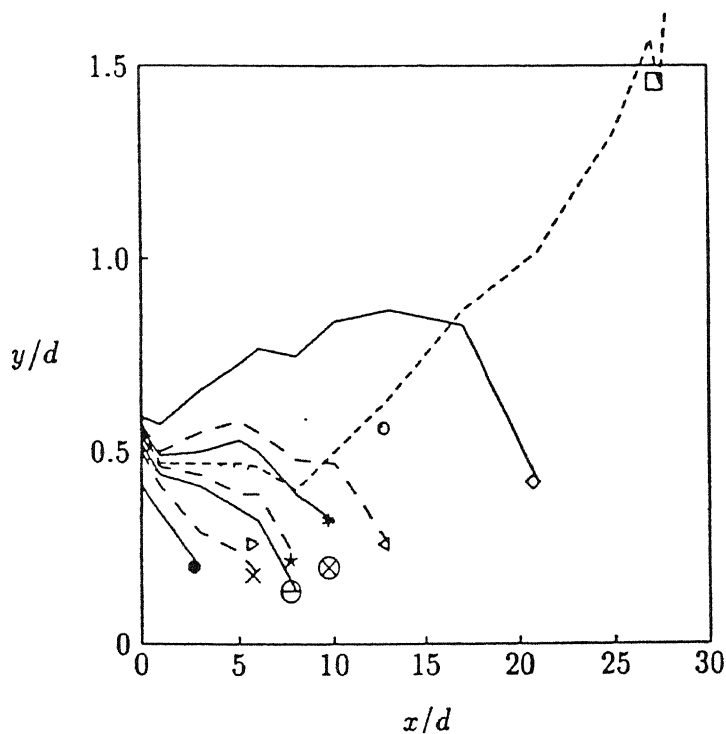


Fig. 5.24 Isobars of various fractions and half pressure width for $M_e = 0.8$ with wall at $D_w = 30.0$: $f = \bullet 0.99, \times 0.90, \triangleright 0.80, \ominus 0.70, \star 0.60, \ominus 0.70, *$ 0.40, $\triangleleft 0.30, \circ 0.20, \diamond 0.10$ and $\square b = 0.5$.

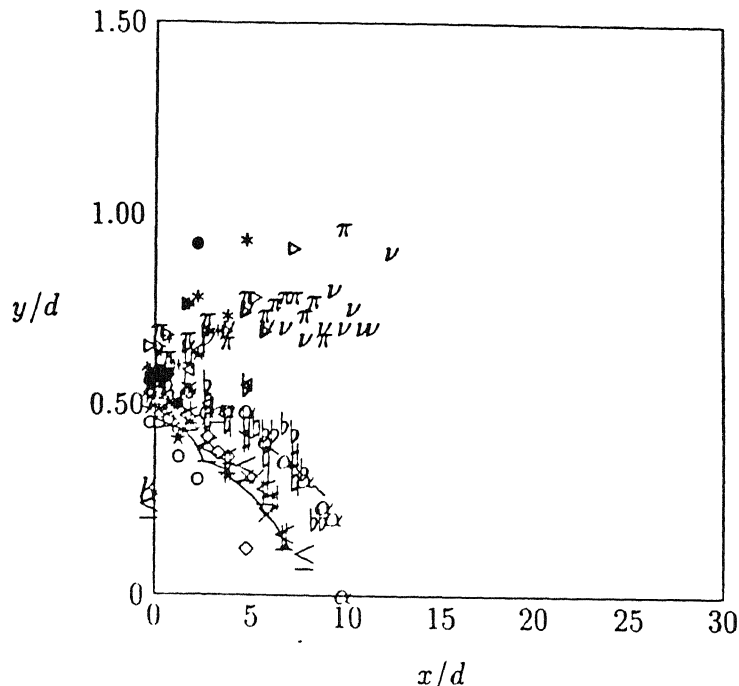


Fig. 5.25 Comparison of iso-bars of various fractions of freejet and impinging jet:freejet
: solidline $f = 0.75$, dash $f = 0.50$, dots $f = 0.15$, impinging jet $D_w = 2.5$ $f = \circ 0.75$, $\star 0.50$, $\bullet 0.15$, $D_w = 5.0$ $f = \diamond 0.75$, $\triangleleft 0.50$, $*$ 0.15 , $D_w = 7.5$ $f = \times 0.75$, $\ddagger 0.50$, $\triangleright 0.15$, $D_w = 10.0$ $f = \# 0.75$, $\flat 0.50$, $\pi 0.15$, $D_w = 12.5$ $f = \leq 0.75$, $\alpha 0.50$, $\nu 0.15$.

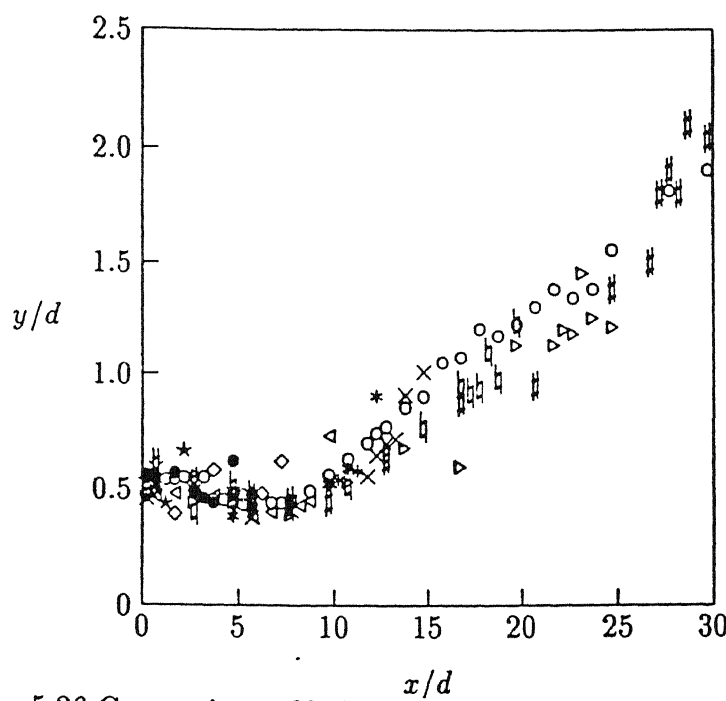


Fig. 5.26 Comparison of half pressure widths between freejet and impinging jets $M_e = 0.6$
: \circ freejet, impinging jet, $D_w = \star 2.5$, $\bullet 5.0$, $\diamond 7.5$, $\times 15.0$, $\ddagger 20.0$, $\triangleright 25.0$ and $\# 30.0$.

the presence of the wall. Applying the length scale eqn. (11) and the pressure scale eqn.(12) proposed for freejets, complete similarity of the measured gauge pressures in the underdeveloped and developed region of the flow for freejet and impinging jet field with wall at $D_w = 2.5, 5.0, 7.5, 10.0, 12.5, 15.0, 20.0, 25.0$ and 30.0 is observed for jet exit Mach number $M_e = 0.6$ in Fig. 5.27. In this aspect, the impinging jet and free jet are similar for the jet exit Mach numbers of the present study. Pressure similarity is also found to follow the normal distribution.

5.2.2 Wall surface distribution

The impinging pressure field influences the gauge pressures on the wall surface and divides the surface pressure fields into two distinct zones: a) positive pressures and b) oscillating pressures. The wall pressure are normalised with the exit pressures given by the equation

$$P_w = (P/P_a - 1.0)/(P_s/P_a - 1.0) \quad (13)$$

The distribution of P_w for different wall locations is shown for jet Mach number $M_e = 0.4$ in Fig. 5.28. The positive pressure corresponds to the impact zone, and the region of initiation of the separation. Secondary vortex structures are initiated in this region due to the interaction of the primary structures with the wall. These secondary structures grow and propagate in the radial direction resulting in mild oscillation between positive and negative wall surface pressures. In the oscillatory pressure zones, the minimum pressure point corresponds to ground vortex core position, while the maximum pressure point corresponds to the ground vortex penetration point, and the zero pressure corresponds to the ground vortex separation point as reported by

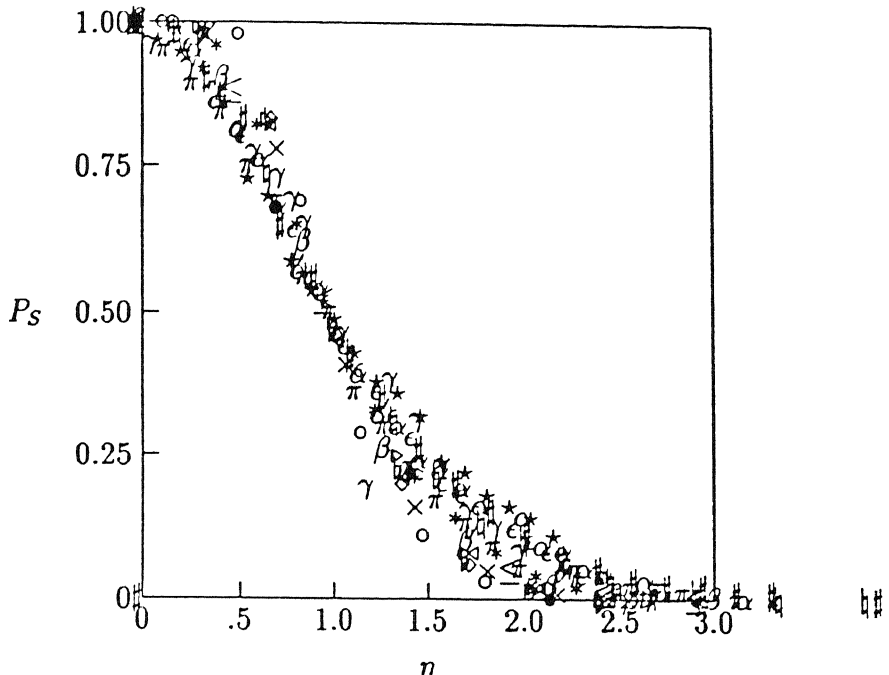


Fig. 5.27 Complete similarity of freejet and impinging jet field for $M_e = 0.6$: freejet \circ
 $3.0d \star 17.0d$ impinging jet $D_w = 2.5 x = \bullet 1.5d, D_w = 5.0 x = \diamond 3.0d, D_w = 7.5 x = \triangleleft 3.0d, * 6.5d, D_w = 10.0 x = \times 3.0d, \# 8.0d, D_w = 12.5 x = \triangleright 3.0d, \# 10.0d, D_w = 15.0 x = \triangleright 3.0d, \pi 13.0d, D_w = 20.0 x = \leq 3.0d, \alpha 17.0d, D_w = 25.0 x = \nu 3.0d, \epsilon 20.0d, D_w = 30.0 x = \beta 3.0d, \gamma 27.0d$.

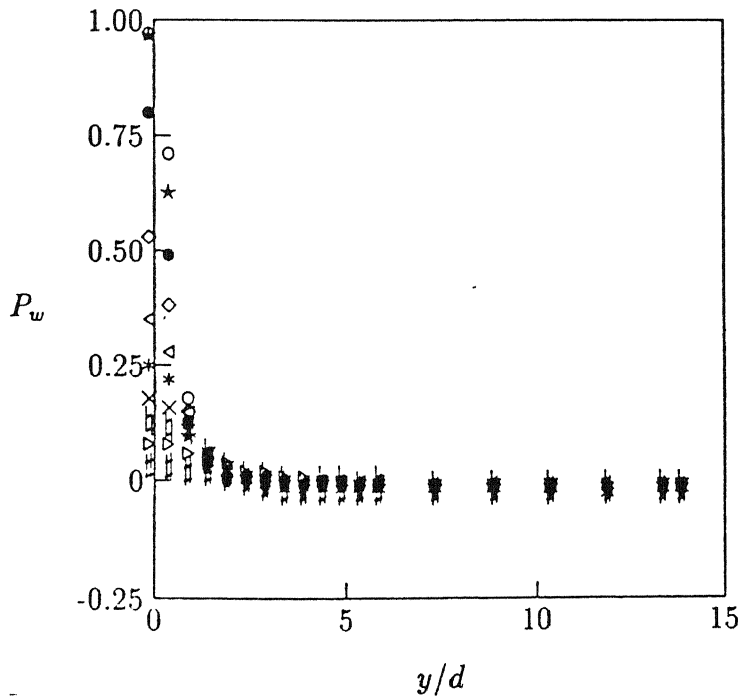


Fig. 5.28 Gauge wall pressure normalised with settling chamber pressure for $M_e = 0.4$ °
 2.5d, ★ 5.0d, • 7.5d, ◊ 10.0d, ▲ 12.5d, * 15.0d, × 17.5d, # 20.0d, ▽ 25.0d and # 30.0d.

Knowles (1991) [61].

In Fig. 5.29, fractions of the positive wall pressures normalized with exit pressure are plotted for different wall locations and $M_e = 0.6$. The influence of the wall locations are evident for lower fractions $f = 0.2, 0.1, 0.07$ as these have positive gradients upto a definite axial location of the wall, and further switch to negative gradient downstream. This implies that the influence of the wall on lower fractions extend only upto a definite downstream location, beyond which the wall does not cause the flow to deflect. In the near field, the dominance of the pressure potential of the jet is evident for fractions upto about $f = 0.4$. Comparison of various fractions of the positive wall pressure are shown for different wall locations and exit conditions in Fig. 5.30. The influence of the exit conditions on the locations in space for same fraction of the exit pressures are only marginal, although the effect of initial pressure potential is evident. Near field impingement at about $2.5d$ exhibits inertia resulting in a narrow zone for higher Mach number compared to lower Mach number.

The half pressure width of the wall surface pressures has been plotted in Fig. 5.31. Interestingly, the spatial location of the wall pressure half width are almost the same over a wide range of exit pressure conditions upto correctly expanded sonic level and wall axial locations. Normalising P_w by the maximum centreline gauge pressure complete similarity of positive wall pressures at various wall locations has been obtained. The results are shown in Fig. 5.32. In Fig. 5.33, the similarity of wall pressures has been compared for various axial locations of the wall and exit conditions. They obey normal-distribution. From these results, it looks like that the parameter used for similarity makes the similarity profile independent of the parameters of the present study.

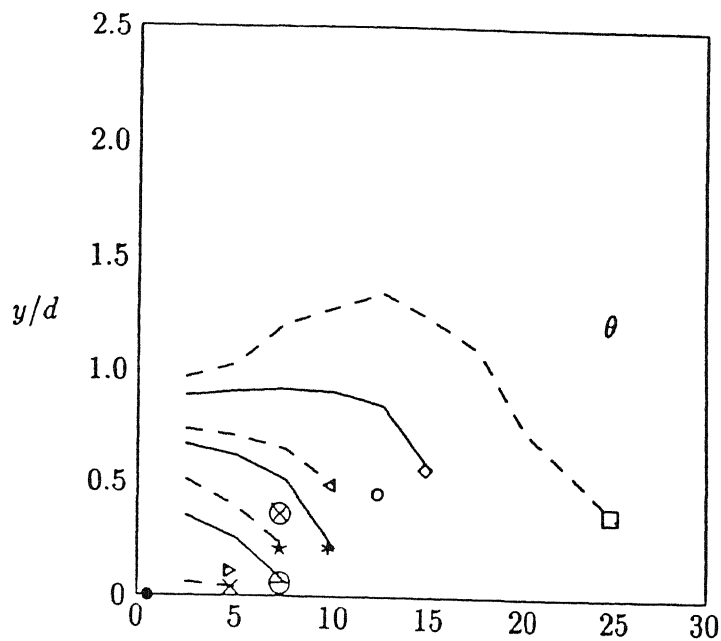


Fig. 5.29 Wall isobars of various fractions $M_e = 0.6$: • $f = 1.0$, × $f = 0.95$, ▽ $f = 0.90$, ◻ $f = 0.80$, ★ $f = 0.70$, ⊗ $f = 0.6$, * $f = 0.50$, △ $f = 0.4$, ○ $f = 0.30$, ◇ $f = 0.2$, □ $f = 0.1$ and θ $f = 0.07$.

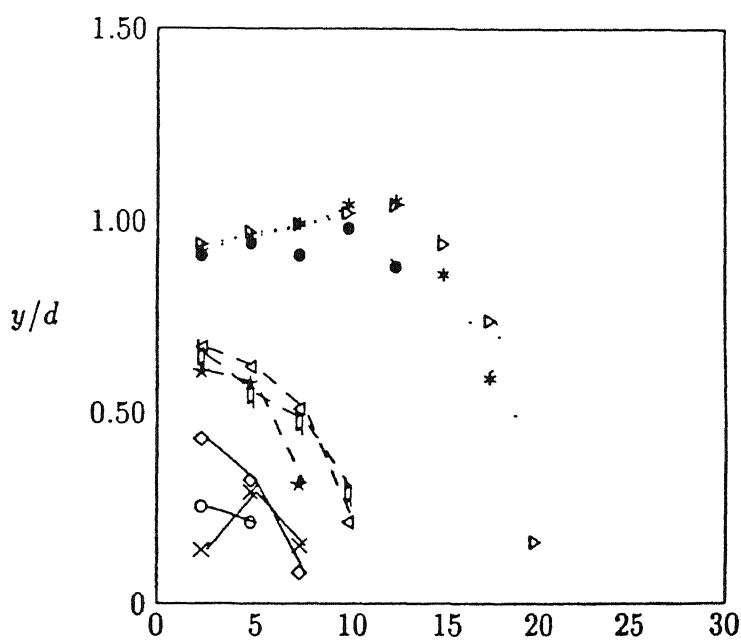


Fig. 5.30 Comparison of wall isobars of various fractions : $M_e = 0.2$ ◦ $f = 0.75$, ★ $f = 0.50$, • $f = 0.15$, $M_e = 0.6$ ◇ $f = 0.75$, △ $f = 0.50$, * $f = 0.15$, $M_e = 1.0$ × $f = 0.75$, # $f = 0.50$, □ $f = 0.15$.

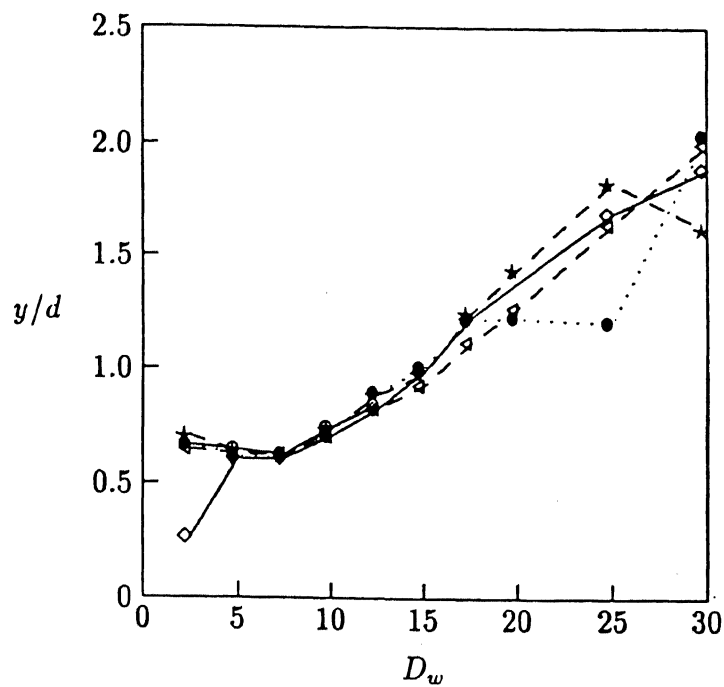


Fig. 5.31 Comparison of half pressure width for jet Mach numbers : $\circ M_e = 0.2$, $\star M_e = 0.4$, $\bullet M_e = 0.6$, $\diamond M_e = 0.8$, and $\triangleleft M_e = 1.0$.

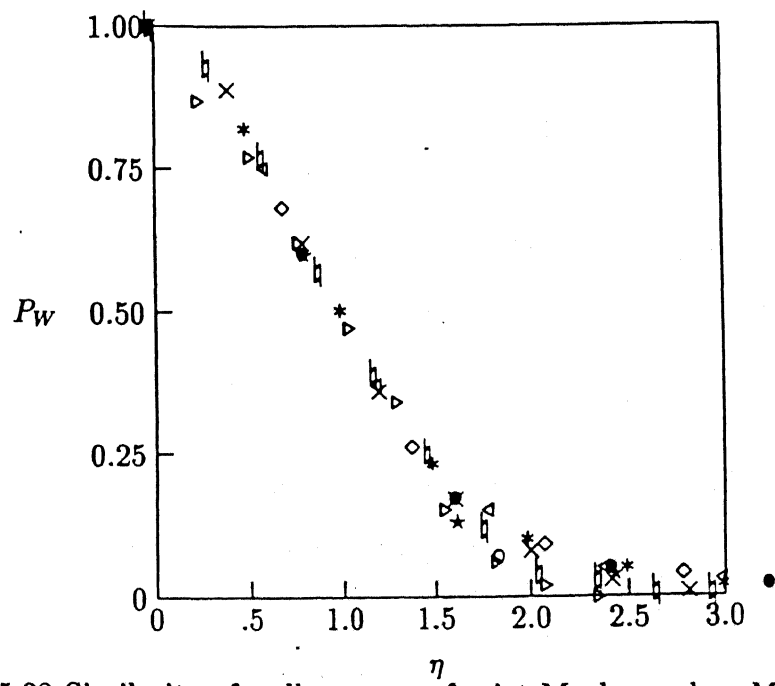


Fig. 5.32 Similarity of wall pressures for jet Mach number $M_e = 0.8$: $\circ 2.5d$, $\star 5.0d$, $\bullet 7.5d$, $\diamond 10.0d$, $\triangleleft 12.5d$, $\ast 15.0d$, $\times 17.5d$, $\sharp 30.0d$.

In Fig. 5.34 comparison of the normalised force given by eqn

$$F_N = \frac{2 \int_{y=0}^{y=p_f} y P(w) dy}{r_e^2 P_e} \quad (14)$$

for various exit pressure conditions has been made. The normalised force has been computed upto 10% of the initial exit pressure. The curves follow a definite behaviour for various wall locations and exit gauge pressures, and nearly collapse. Thus with the proposed force scale, similarity of the wall surface forces has been established for a wide exit pressure conditions upto correctly expanded sonic level and wall axial locations. The zone of the influence of positive pressure for the same fraction p_f of the initial exit pressure P_e is shown in Fig. 5.35. The zone of influence of positive pressures are also similar for the present range of exit conditions upto correctly expanded sonic level.

From Figs. 5.34 and 5.35, it may be concluded that by conducting experiments with one Mach number for various wall locations, it is possible to infer the load that will act on the wall for any other Mach number of interest from these plots.

5.2.3 Conclusions

The analysis of the impinging pressure field leads to the following conclusions.

- Like the freejet pressure field, the impinging jet pressure field and wall surface pressures also exhibit similarity, and are identical. They also obey normal distribution variation
- The pressure scales and the length scales proposed are valid for both freejet regime or impinging jet regime.

- The wall influences the lower fraction isobars, their lateral width is lower than that of the freejet.
- The wall half pressure width are similar for all exit conditions upto correctly expanded sonic levels.
- The proposed force scale results in the similarity of forces on the wall for exit pressure conditions upto correctly expanded sonic level.
- The zone of influence of positive pressures also exhibit similarity for the present exit conditions.

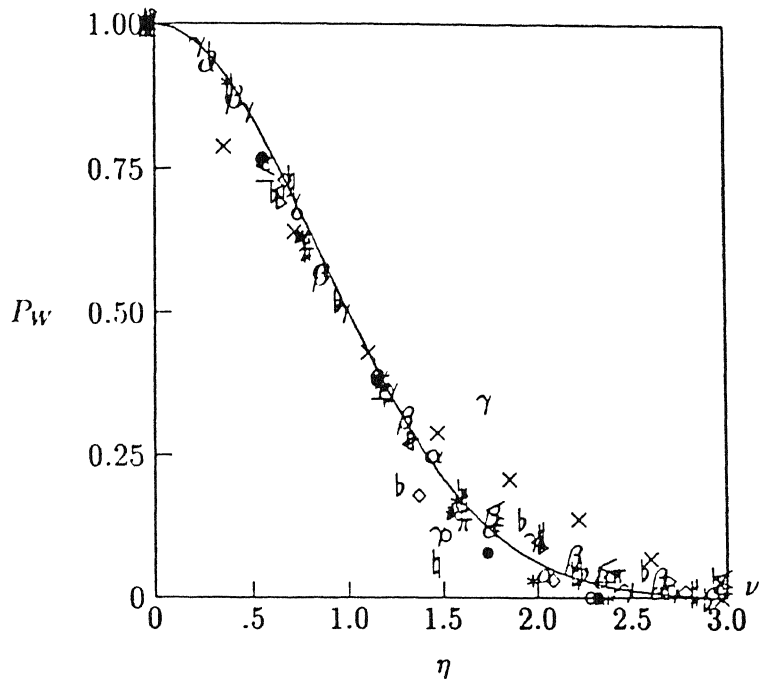


Fig. 5.33 Comparison of similarity of wall pressures for jet Mach numbers : $M_e = 0.2$ $D_w = \diamond 5.0, \star 7.5, \bullet 12.5, M_e = 0.4 D_w = \diamond 2.5, \triangleleft 10.0, * 17.5, \times 25.0, M_e = 0.6 D_w = \# 2.5, \triangleright 10.0, \# 17.5, \flat 30.0, M_e = 0.8 D_w = \pi 5.0, \leq 12.5, \alpha 25.0, M_e = 1.0 D_w = \nu 5.0, \epsilon 12.5, \beta 17.5, \gamma 30.0$ and $- \sigma = 0.86$.

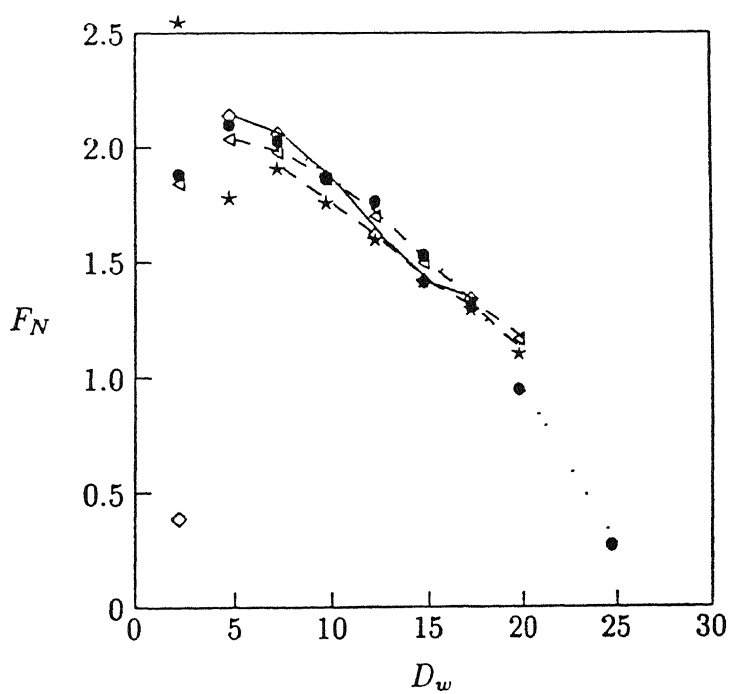


Fig. 5.34 Normalised force coefficient variation (computed upto 10 % of settling chamber pressure) $M_e = 0.4$, $\bullet M_e = 0.6$, $\diamond M_e = 0.8$, and $\blacktriangle M_e = 1.0$.

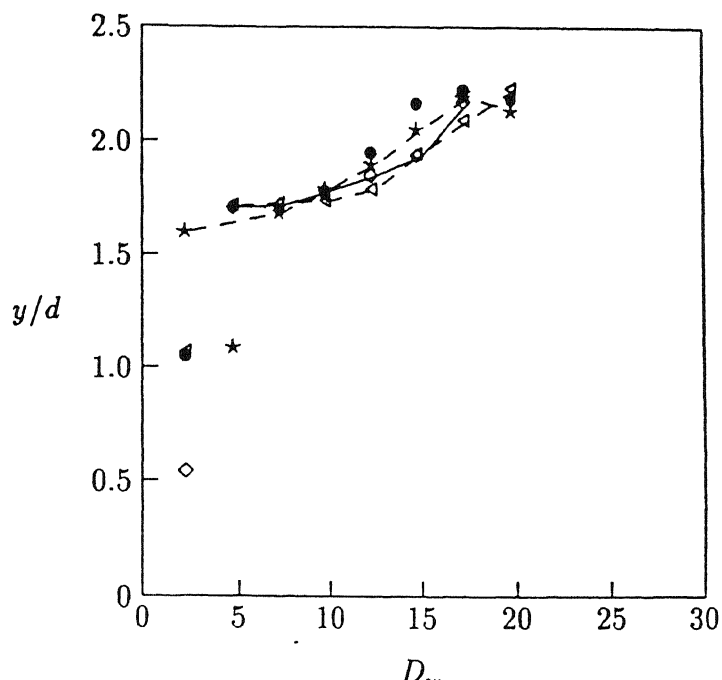


Fig. 5.35 Zone of influence of positive pressure (radial extent upto 10 % of settling chamber pressure) $\star M_e = 0.4$, $\bullet M_e = 0.6$, $\diamond M_e = 0.8$, and $\triangleleft M_e = 1.0$.

Chapter 6

Flat Plate and Radial walljet Flow

Free and bounded shear flows occur in various flow fields of practical interest either *independently* as in jets and boundary layer flows, or *together* as in walljet flows or *in succession* as in impinging jets or backward facing step flows. The inherent characteristic of free shear flows is the phenomena of entrainment as a consequence of viscous action. For bounded shear flows the entrainment is absent. Similarity of velocity profiles are applicable only in the mixing region as discussed in chapters 4 and 5. The proposed scales for jets are applied to flat plate boundary layer and walljet flow field in this chapter.

6.1 Velocity based approach

In this section the boundary layer flow and the walljet flow have been investigated based on the velocity. The parametric study carried out for freejets, namely, the iso-velocity and iso-spread have been applied to flow over a flat plate. Similar investigation

for the walljet flow field is also carried out.

6.1.1 Flow over flat plate

The thin region adjacent to the plate where viscous forces are predominant is known as *boundary layer*. A representation of the measured velocity profile at various stations in the boundary layer along the plate is shown in Fig. 6.1. The edge of the boundary layer taken to be approximately equal to the free stream velocity ($b = 1.0$) and the half velocity width ($b = 0.5$) are also shown in this figure.

The normalised velocity distribution for $Re = 1.76 \times 10^5$, based on the length of the plate, is shown in Fig. 6.2 at the measured locations . The iso-Mach and the iso-spread lines in the flat plate boundary layer are the same, and is shown in Fig. 6.3 for various fractions ranging from $f = 1.0$ to $f = 0.2$. From this figure it is seen that the isospread lines from $b = 0.2$ to 0.5 change their slope from positive to negative as the flow proceeds from the leading edge in the downstream direction. Also, it is seen that all the isospread lines from $b = 0.5$ to 1.0 have only positive slope. Therefore the isospread line with $b = 0.5$ may be visualized as something similar to the half width in the freejet field. Hence, it may also be visualized that the flow zone below $b = 0.5$ line may be considered as viscous dominant and that above may be treated as inertia dominant. However, it should be realized that close to the leading edge where the boundary layer just starts growing the entire flow field behaves as if it is inertia dominated.

In other words even in the boundary layer, *the half velocity width demarcates the boundary layer region into viscous and inertia dominant zones*. Normalising the length parameter by the half velocity width implies normalising by the inertia dominant zone.

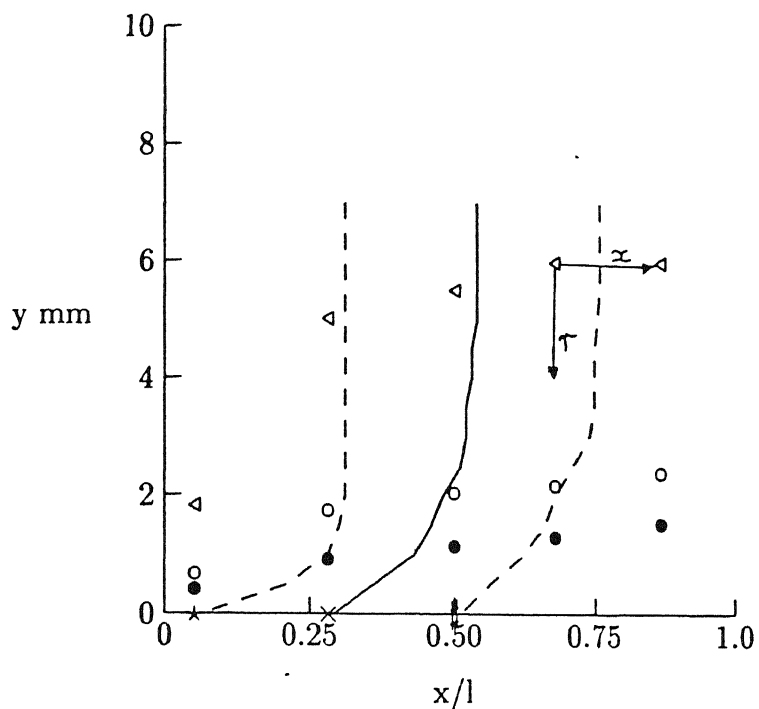


Fig. 6.1 Characteristics of boundary layer on flat plate : \triangle freestream velocity or pressure denoted by $b = 1.0$, \bullet half velocity width, \circ half pressure width. locations of measurements at $\star x/l = 0.06$, $\times x/l = 0.29$, $\# x/l = 0.51$.

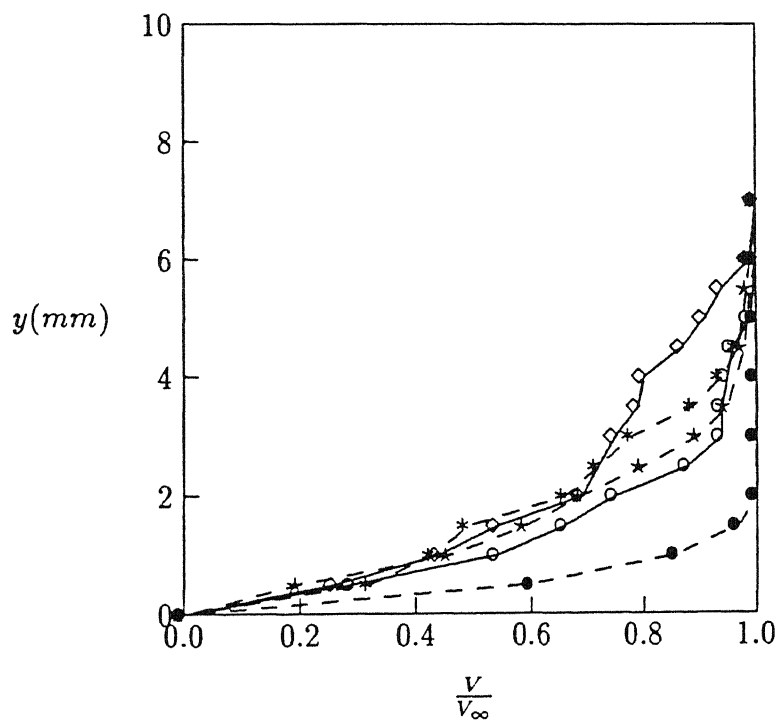


Fig. 6.2 Normalised velocity distribution in the boundary layer over a flat plate : at $\bullet x/l = 0.06$, $\circ x/l = 0.29$, $\star x/l = 0.51$, and $* x/l = 0.88$.

The length parameter of the velocity distribution in the boundary layer when represented in terms of η given by the eqn(3) results in a self similar velocity profiles within the boundary layer. The self-similar velocity profiles within the boundary layer is shown in Fig. 6.4.

The present results show complete similarity excluding the point of initiation of the boundary layer, therefore the leading edge of the flat plate may be defined as the *origin of similarity*. This length scale η is of important significance as it is independent of the free stream velocity, kinematic viscosity and the length along the plate.

An important conclusion arrived from the above analysis is that , *the length scale which is applicable to free jets to obtain complete similarity of velocity profiles shows complete similarity of the velocity profiles in the flat plate boundary layer flows, which is a bounded shear flow.*

6.1.2 Radial wall jet

The characteristics of radial wall jet shown in Fig. 6.5 is the experimentally measured representation of the present study. Wall jet consists of free shear flow in the outer region and bounded shear flow in the inner region close to the wall surface. There are two half velocity widths $b = 0.5$ in the radial wall jet, one in the inner region similar to flow over flat plate and the other in the outer region similar to free jet flows. The contour corresponding to $b = 1.0$ is the maximum velocity in the radial wall jet. The velocity distribution taken from Rajaratnam (1976,p 234) [85] is shown in Fig. 6.6. The Reynolds number of the radial wall jet is based on the kinematic momentum flux, and has a value 1.96×10^5 . The kinematic momentum flux was calculated by Poreh *et. al.* (1967) [83] assuming that the effective area of the jet due to contraction was

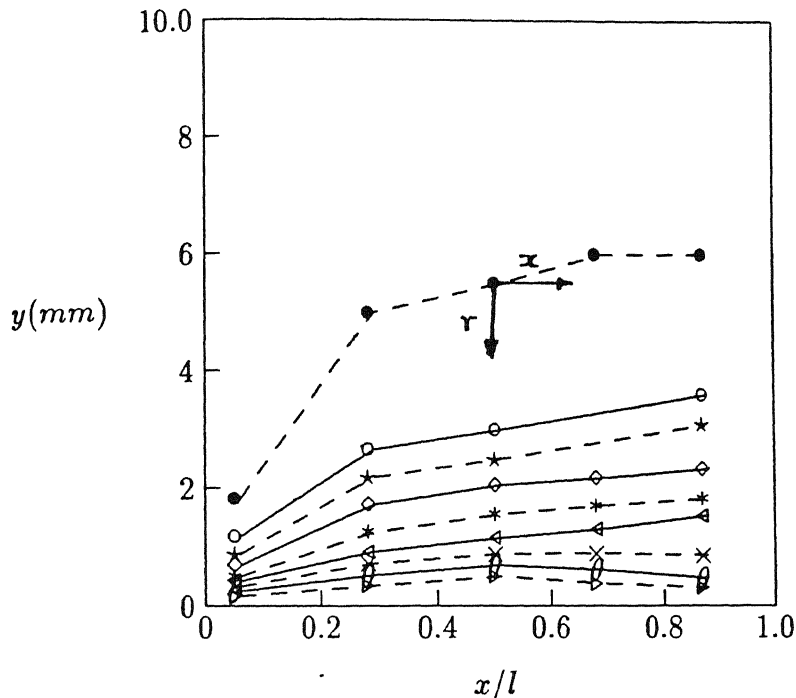


Fig. 6.3 Iso-velocity (iso-spread) lines in the boundary layer over flat plate : $f = 1.0$, \circ $f = 0.90$, \star $f = 0.60$, \diamond $f = 0.70$, $*$ $f = 0.60$, \triangleleft $f = 0.50$, \times $f = 0.40$, θ $f = 0.30$, and \triangleright $f = 0.20$.

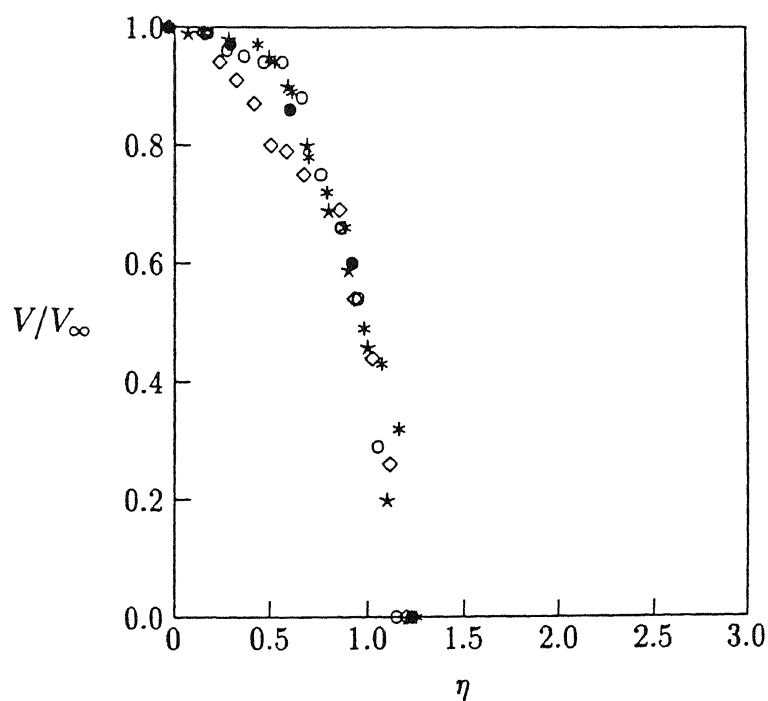


Fig. 6.4 Complete similarity of velocity distribution within the boundary layer over flat plate : \bullet $x/l = 0.06$, \circ $x/l = 0.29$, \star $x/l = 0.51$, \diamond $x/l = 0.69$, and $*$ $x/l = 0.88$.

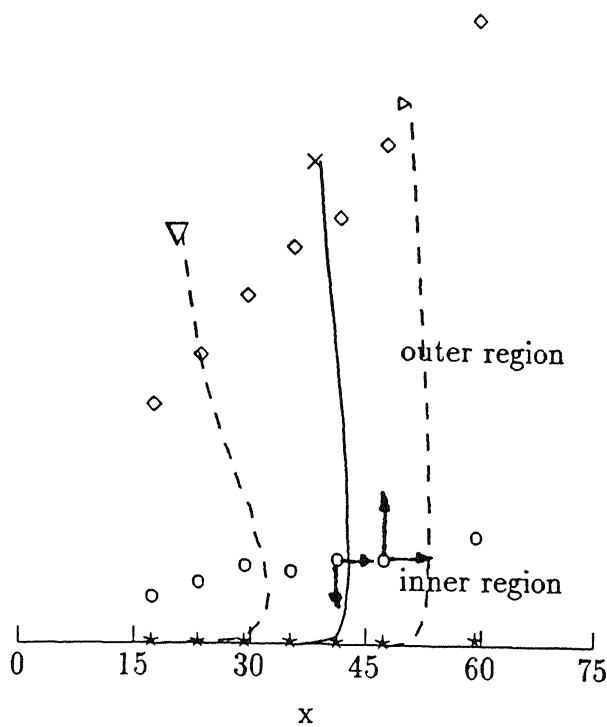


Fig. 6.5 Characteristics of radial wall jet : velocity profiles at at $x = 18$ in. ∇ , $x = 36$ in. \times , $x = 48$ in. \blacktriangleright , \diamond $b = 1.0$, inner region half velocity width \star $b = 0.50$, outer region half velocity width \diamond $b = 0.50$.

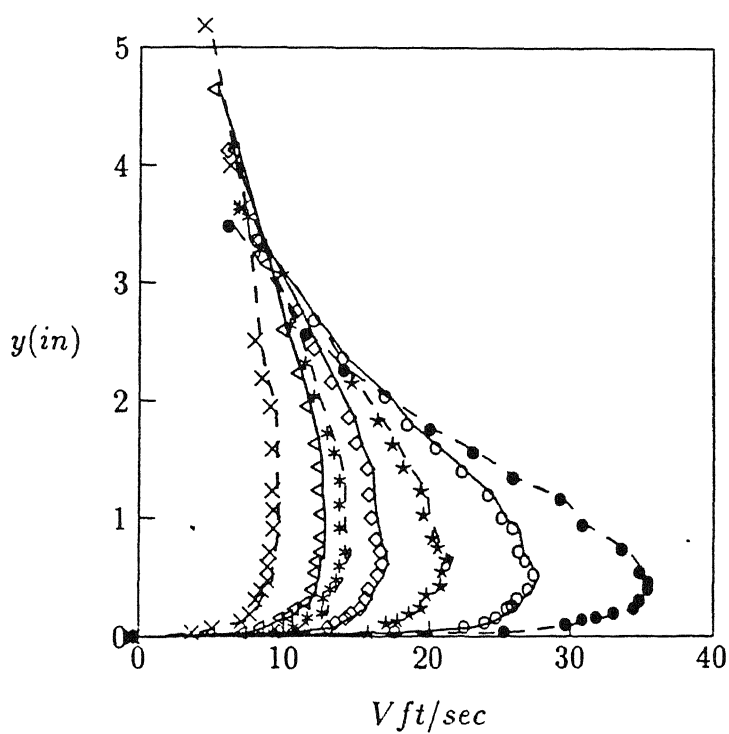


Fig. 6.6 Velocity distribution in the impinging radial wall jet reported by Tsuei(1962). Data replotted from Rajaratnam (1976) \bullet $x = 18$ in., \circ $x = 24$ in., \star $x = 30$ in., \diamond $x = 36$ in., \blacktriangleleft $x = 42$ in., \blacktriangleright $x = 48$ in. , and \times $x = 60$ in..

0.611 of the orifice area. The iso-Mach line representation for the radial wall jet is shown in Fig. 6.7. The iso-spread lines shown in Fig. 6.8 indicate two different types of similarity in the inner and outer regions, as expected. Again, following the similar procedure as in free and bounded shear flows, the local axis to obtain similarity is taken to be $b = 1.0$. Complete similarity in the inner and the outer regions of the wall jet is shown in Figs. 6.9 and 6.10, respectively using the length scale given by eqn(3) .

The advantage of the choice of this co-ordinate system renders complete similarity with only one velocity scale and two length scales, as compared to partial similarity with two velocity and two length scales reported by Glauert (1956) [38] in the radial wall jet region. Further, in the present approach the length scales are also independent of the constant α as in Glauert profile for radial wall jets.

The above results imply that the general length scale η to obtain similarity is also applicable when free shear and bounded shear flows coexist. Hence this scale may be called as the *universal* length scale.

Comparison of the similarity of velocity distribution between the free jet and the outer radial wall jet in Fig. 6.11 indicate complete structural similarity of the velocity profiles and it obeys normal distribution. Bounded shear flows, as in the case of boundary layer over flat plate and the inner region of the radial wall jet are devoid of the entrainment phenomena unlike free shear flows. Fig. 6.12 shows complete structural similarity between the boundary layer flows over a flat plate and inner region of radial wall jet. Comparison between the normal distribution curve in this figure and bounded shear flows, emphasises the effect of entrainment on the similarity of the velocity profiles. The nature of the bounded similarity is governed (approximately) by

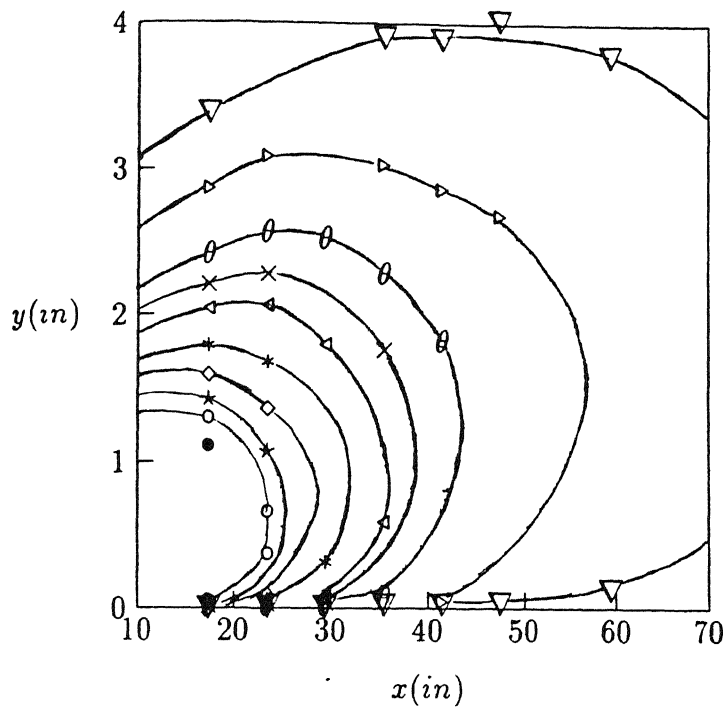


Fig. 6.7 Iso-velocity lines in the radial walljet field : • $V = 30.0 \text{ ft/sec}$, ○ $V = 27.0$, * $V = 25.0$, ◇ $V = 23.0$, * $V = 20.0$, ▲ $V = 17.0$, × $V = 15.0$, θ $V = 13.0$, ▲ $V = 10.0$ and ▽ $V = 7.0$.

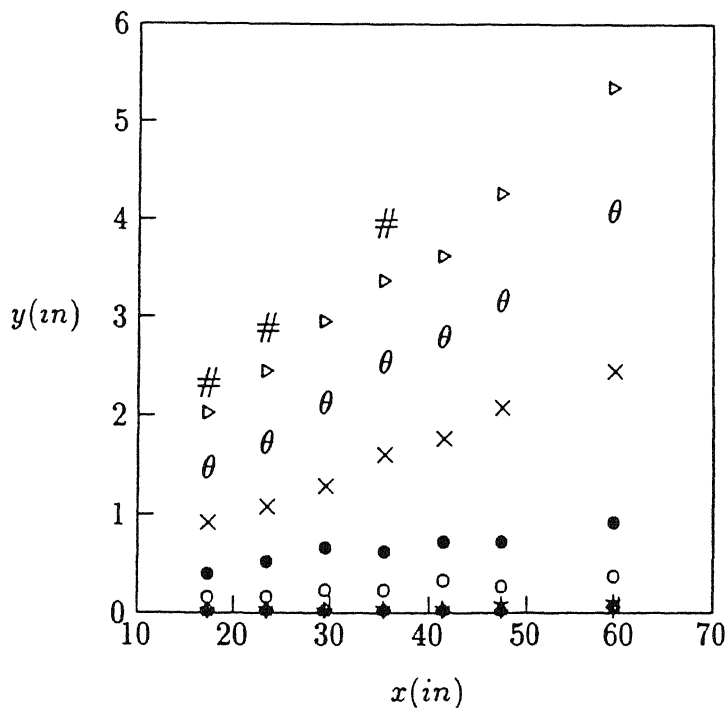


Fig. 6.8 Iso spread lines in the radial walljet field : maximum velocity : • $b = 1.0$ inner region : ○ $b = 0.90$, * $b = 0.70$, ◇ $b = 0.50$, * $b = 0.20$, outer region : b = 0.90, θ $b = 0.70$, ▲ $b = 0.50$ and # $b = 0.40$.

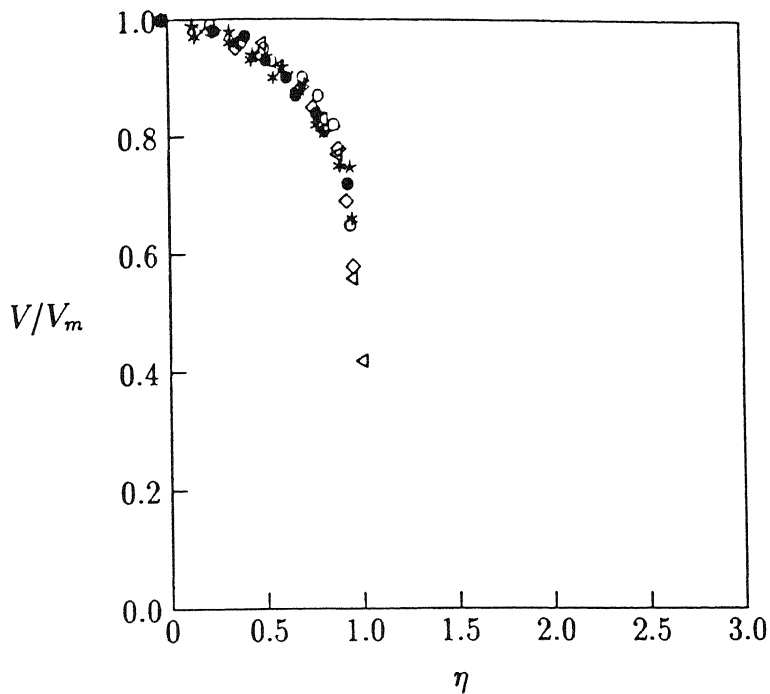


Fig. 6.9 Complete similarity of velocity distribution in the inner region of the radial wall jet : $x = (\text{in.})$: \bullet 18 , \circ 24 , \star 30, \diamond 36, $*$ 42, and \triangleleft 60.

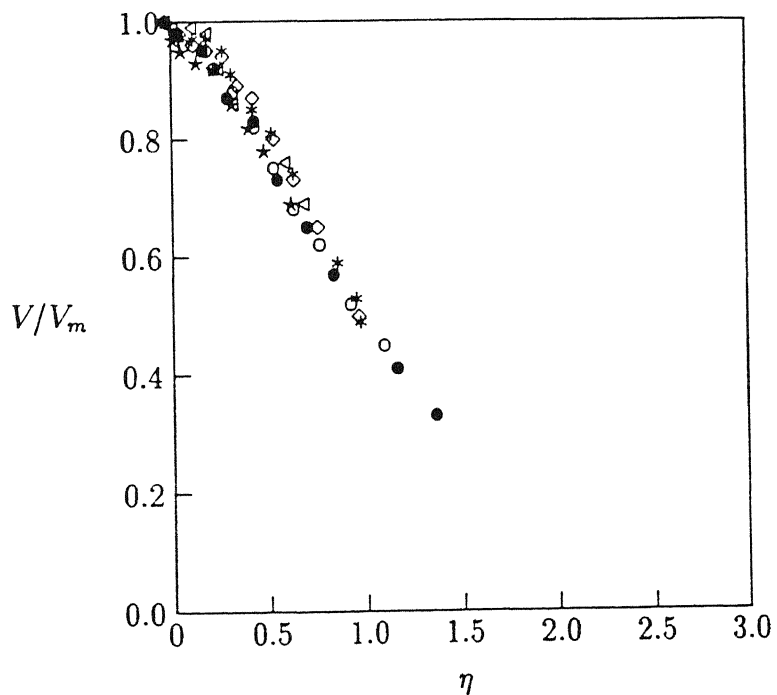


Fig. 6.10 Complete similarity of velocity distribution in the outer region of the radial wall jet : $x = \bullet$ 18 in. , \circ 24 in., \star 30 in., \diamond 36 in., $*$ 42 in., and \triangleleft 60 in..

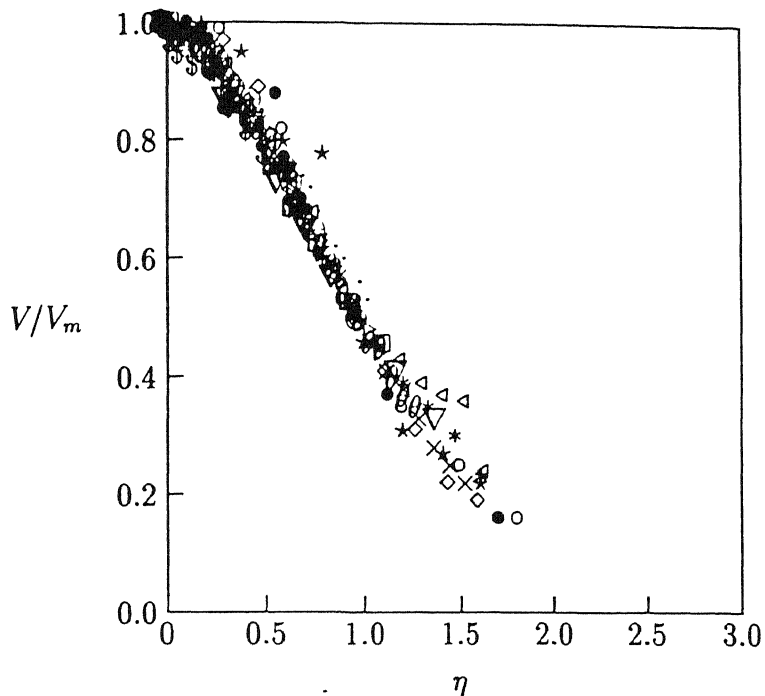


Fig. 6.11 Comparison of similarity between freejet and the outer region of radial walljet : freejet $x =$: • 1.0d, ○ 2.5d, ★ 3.5d, ◇ 5.0d, × 7.5d, ▽ 10.0d, × 15.0d, θ 20.0d, ▷ 25.0d, - 30.0d. walljet $x =$ (in.) : ▽ 18, □ 24, \$ 30, ≤ 42, and ♣ 60.

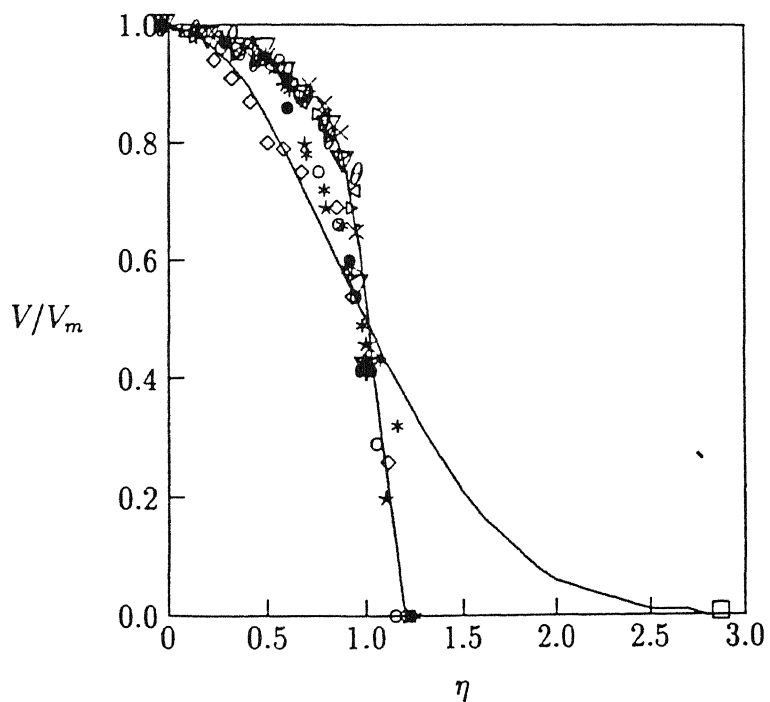


Fig. 6.12 Similarity comparison between freeshear flow (freejet and outer region of radial walljet) and bounded shear flow (inner region of walljet and flat plate boundary layer) : free shear flow - □ normal distribution bounded shear flow - fifth order polynomial variation superimposed on the markers flat plate boundary layer $x/l =$: • 0.06, ○ 0.29, ★ 0.51, ◇ 0.69, × 0.88. inner region of walljet $x =$: ▽ 18, × 24, θ 30, ▷ 36, · 42, ∇ 60.

the following equation

$$\frac{V}{V_m} = 1.0 - 0.439\eta + 3.52\eta^2 - 11.73\eta^3 + 15.65\eta^4 - 7.48\eta^5 \quad (15)$$

These results makes it clear that, *the fifth order polynomial similarity variation of bounded shear flows switches to normal-probability variation in the case of free shear flows, indicating that entrainment induces thorough mixing resulting in normal distribution.*

6.1.3 Concluding remarks

The highlights of the study on bounded shear and the blend of free and bounded shear flows are:

- The length scale η which ensures complete similarity of velocity profiles in free shear flows is also applicable to bounded shear flows.
- Appropriate choice of the co-ordinate system renders the length scale to be independent of the flow variables such as viscosity, velocity and characteristics length of the boundary.
- Both in free shear and bounded shear flows, the negative gradient of the iso-Mach lines correspond to the dominance of the inertial effect region of the flow, whereas the positive gradient correspond to the dominance of the viscous effect region of the flow.
- The half velocity width which demarcates the mixing zone of the free jets into two distinct regions; *the zones of dominance of the inertial and the viscous effects*, and retains its physical significance even in bounded shear flows.

- In the case of radial walljets, similarity of velocity in the inner zone is almost identical to bounded shear flow, while the similarity in the outer zone exhibits normal distribution.
- With the choice of local co-ordinate system at the maximum velocity of the radial wall jet, there is only one velocity scale and two length scales; one in the inner region and the other in the outer region, for the walljet flow field.
- The point of initiation of boundary layer growth over a flat plate may be defined as the origin of similarity.

6.2 Pressure based approach

In this section, the pressure scale proposed for freejets are applied to the boundary layer of flow over a flat plate.

6.2.1 Flow over a flat plate

The free stream pressure boundary is also represented as $b = 1.0$ in Fig. 6.1. Complete similarity with the pressure scale P_S given by eqn (12), and choosing η given by eqn (11) is shown in Fig. 6.13. This implies that pressure scales applied for freejets are also valid for bounded shear flows, namely, the boundary layer of flow over a flat plate.

6.3 Comparative studies

In the case of flow over a flat plate, the half pressure width is lower than the half velocity width with respect to the local axis, shown in Fig. 6.1. This aspect was also observed for freejets, where the half velocity width is higher than the half pressure width. Thus irrespective of the nature of the flow, i.e. free shear or bounded shear flow, the half pressure width is lower than that of the half velocity width, as expected.

The pressure similarity and the velocity similarity for flow over a flat plate has been compared in Fig. 6.14. They exhibit good agreement. Hence, by proper choice of appropriate length scales for pressure or velocity and the local axis, complete pressure or velocity similarity in the boundary layer may be achieved. In Fig. 6.15, the pressure similarity for freejet and flat plate has been compared. The effect of the boundary preventing the entrainment is seen from this figure. The bounded flow exhibits a fifth order polynomial variation which becomes a normal-distribution on removal of the boundary.

6.3.1 Concluding remarks

The highlights of the comparative study are the following:

- The half pressure width with respect to the local coordinate system for free as well as bounded shear flows are significantly lower than the half velocity width.
- The pressure similarity and velocity similarity are similar for bounded shear flows.
- The effect of entrainment is evident from the pressure similarity between free and bounded shear flows. Entrainment is seen to induce thorough mixing, thereby

resulting in normal-distribution of the free shear pressure similarity compared to the bounded pressure similarity.

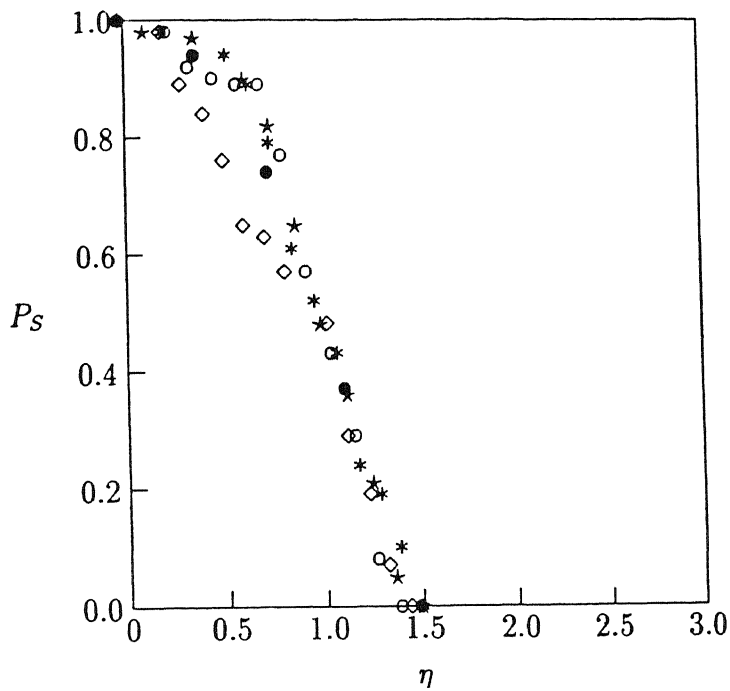


Fig. 6.13 Complete similarity of the pressure distribution for the boundary layer over a flat plate : $x/l = \bullet 0.06, \circ 0.29, \star 0.51, \diamond 0.69$, and $\times 0.88$.

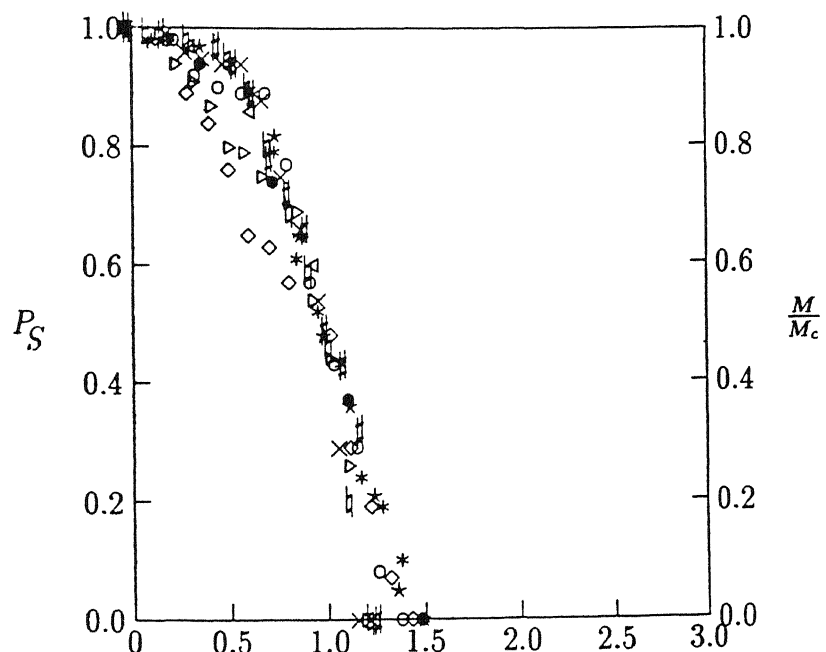


Fig. 6.14 Comparison between pressure and velocity similarity for flat plate : pressure : $x/l = \bullet 0.06, \circ 0.29, \star 0.51, \diamond 0.69, \times 0.88$, velocity : $x/l = \triangleleft 0.06, \times 0.29, \sharp 0.51, \triangleright 0.69, \# 0.88$.

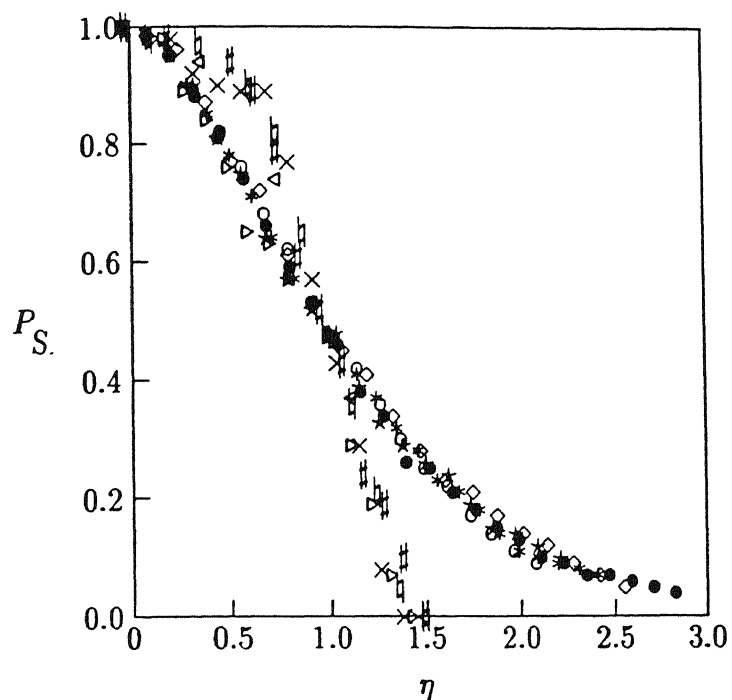


Fig. 6.15 Comparison of pressure similarity for freejet and flat plate : freejet : $M_e = 0.2 \bullet 15.0d, M_e = 0.4 \circ 17.0d, M_e = 0.6 \star 16.0d, M_e = 0.8 \diamond 15.0d, M_e = 1.0 \# 20.0d$, flat plate : $x/l = \square 0.06, \times 0.29, \# 0.51, \triangleright 0.69$, and $\# 0.88$.

Chapter 7

Underexpanded Freejets

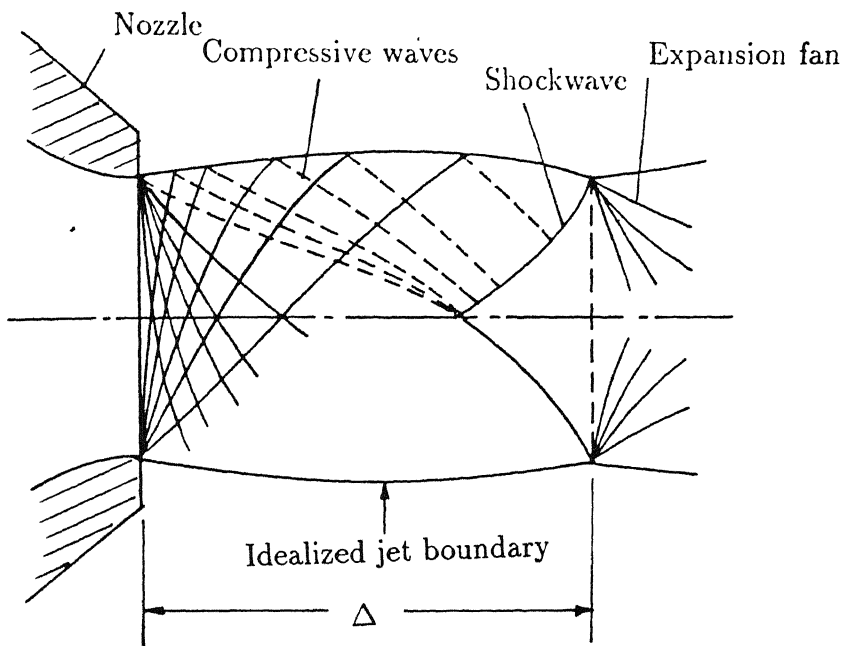
The complexities of freejets increases as the underexpansion level increases due to the presence of cellular wave structures in the potential core. In this chapter, the cellular wave structure of the underexpanded jets are analyzed based on the visualization with Schlieren technique, and the measured static pressure and pitot (gauge) pressure. The mixing zone has been analyzed based on the pitot (gauge) pressures. The underexpanded jet flow field has been compared with correctly expanded sonic jet.

7.1 Flow visualization

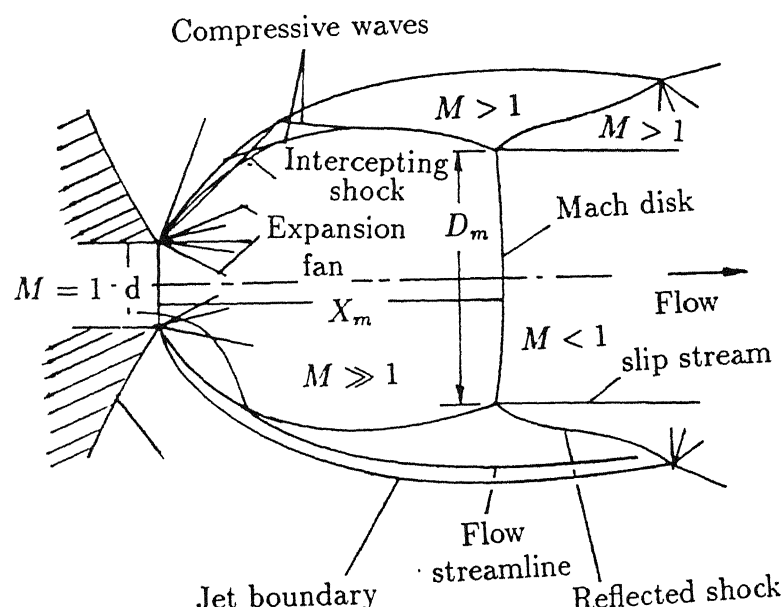
Schlieren technique is a non-intrusive flow visualization technique suitable to study flow structures where density gradients exists. In flow fields like the one in the underexpanded jets with non-simple wave structure, the pressure measurements cannot be taken as correct representation of the flow properties. Under such situations, the flow visualization is proved to be a boon to get a proper understanding of the complex

flow phenomenon. The underexpanded freejet has high density gradient zones in the potential core region and has the form of (bead like) cellular structure. The density gradients in the potential core region arise due to incorrect expansion. The incorrect expansion for a sonic nozzle is when the static pressure at the exit is higher than the ambient pressure, known as underexpansion. Various degrees of underexpansion may be achieved by controlling the pressure ratio P_s/P_a . When the pressure ratio P_s/P_a is increased beyond the critical value, the jet expands into the ambient surroundings with Prandtl-Meyer expansion fans originating from the nozzle exit. These fans reflect from the free jet boundary as compressive waves, the pressure gradients rise due to these compression waves and cause inward diffusion of the mixing region and narrowing of the cell as shown in Fig 7.1a. Further downstream, if the underexpansion level is considerable, these reflected waves coalesce to form conical oblique shocks as shown in the figure. These oblique shocks on impingement with free boundary reflect back as expansion fan, and the cycle repeats. This phenomenon extends upto the axial distance where the axial velocity becomes subsonic. For further increase of the pressure ratio P_s/P_a , the expansion fan becomes highly powerful to cause an intercepting shock as shown in Fig. 7.1b. The shocks formed ahead of the conical shock wave are called barrel shocks because of their shapes. For high levels of underexpansion the barrel shocks consist of a normal shock wave known as Mach disc, with the flow behind the Mach disc being subsonic.

In Figs. 7.2 (photographs), the cellular structure of the potential core region visualized with Schlieren method has been shown for four levels of underexpansion, namely, $Pr = 1.2, 1.5, 2.0$ and 2.25 . In these photographs, bead like cellular structures are clearly seen. There are number of beads, which reduce in length as well as diameter



a) moderately underexpanded



b) highly underexpanded.

Fig. 7.1 Characteristics of underexpanded sonic jets a) moderately underexpanded b)
highly underexpanded.

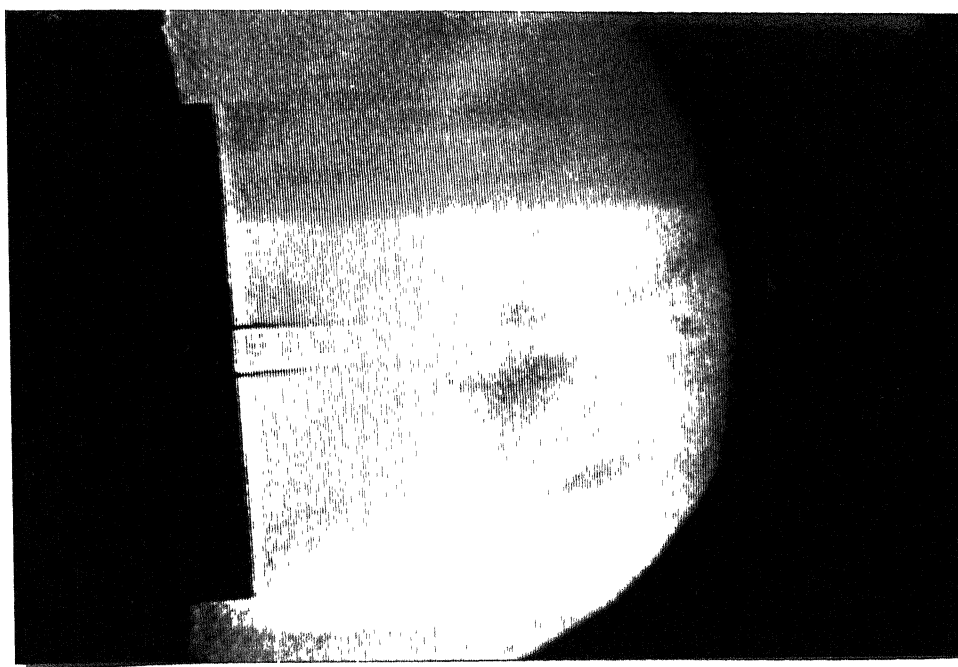


Fig. 7.2a Schlieren photograph of freejet $Pr = 1.2$

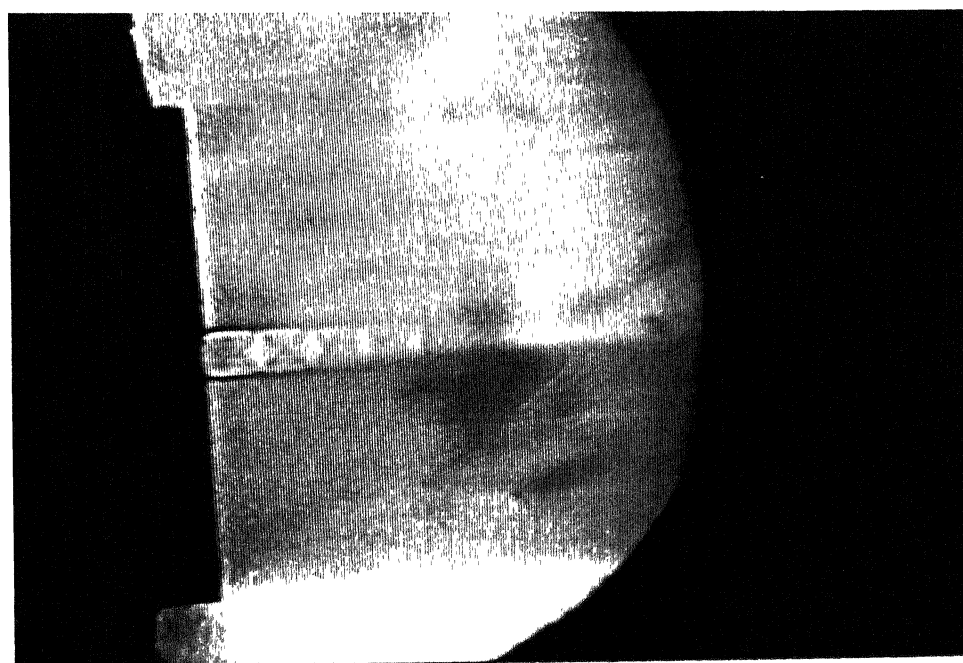


Fig. 7.2b Schlieren photograph of freejet $Pr = 1.5$

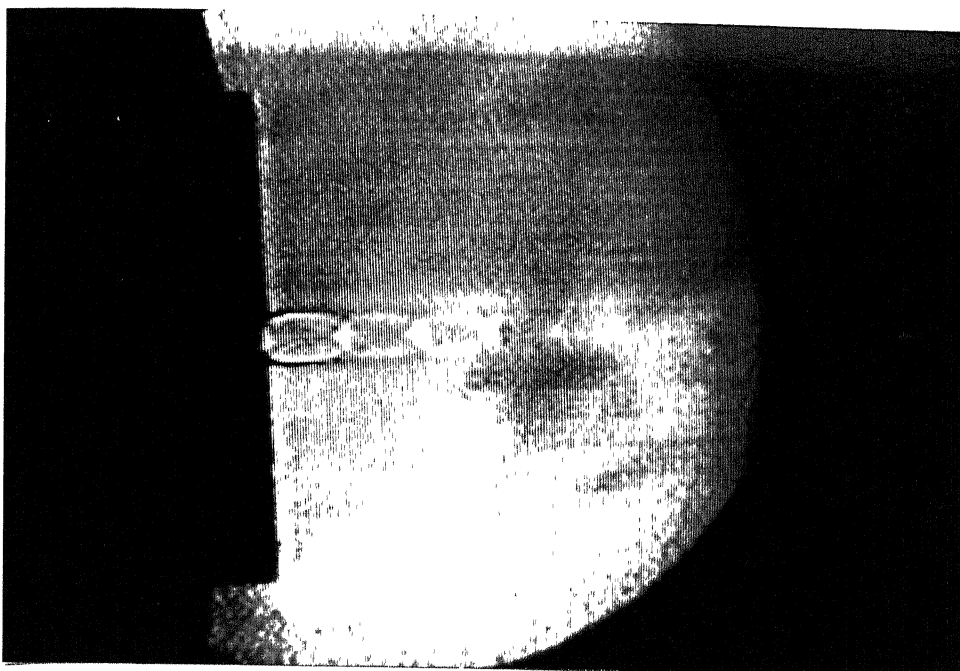


Fig. 7.2c Schlieren photograph of freejet $Pr = 2.0$

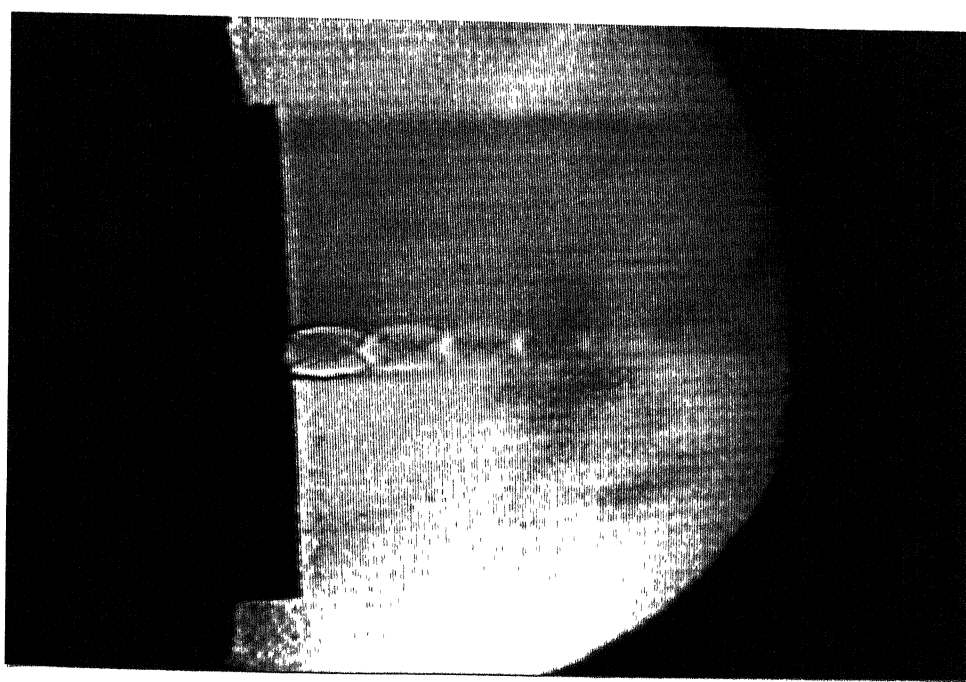


Fig. 7.2d Schlieren photograph of freejet $Pr = 2.25$

due to inward diffusion of the mixing region into the potential core, as seen from the photographs. As the underexpansion level is increased from $Pr = 1.2$ to 2.25 with the following intermediate values $Pr = 1.5$ and 2.0, the following observations are noted with increase of underexpansion levels.

1. The length of the individual cells increase
2. The diameter of the individual cells also increase
3. The expansion and compression waves become stronger and sharp gradients are observed in the potential core region

Even though the degree of underexpansion is seen to influence the wave pattern in the core region of the jet, it is difficult to observe the extent of the potential core from these visualization. For identifying the extent of the potential core it is essential to carry out actual pressure measurements.

7.2 Pressure based analysis

7.2.1 Potential core

By normalizing the measured pitot pressure (gauge) with the correctly expanded sonic gauge pressure, the nondimensionalized pressure is written in the following form.

$$P_* = (P_s/P_a - 1)/(P_s/P_{a_{correct}} - 1) \quad (16)$$

The variation of P_* along the jet axis is shown in Fig. 7.3-7.6 , for $Pr = 1.2, 1.5, 2.0$ and 2.25 along with the static pressure P_{st} for various levels of underexpansion. The

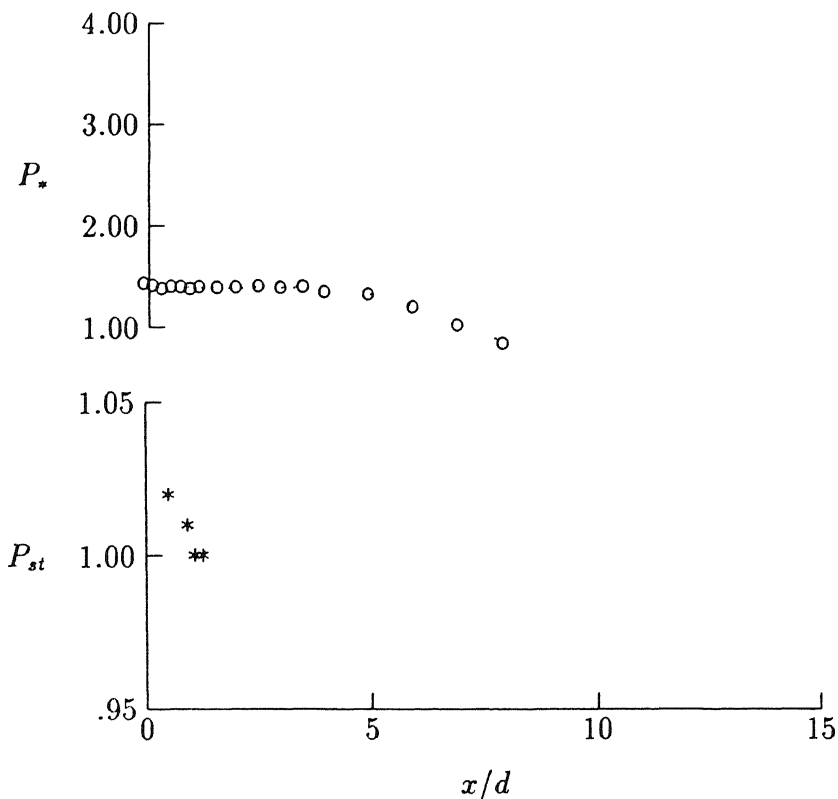


Fig. 7.3 Potential core : freejet $Pr = 1.2$ o mean pressure * static pressure

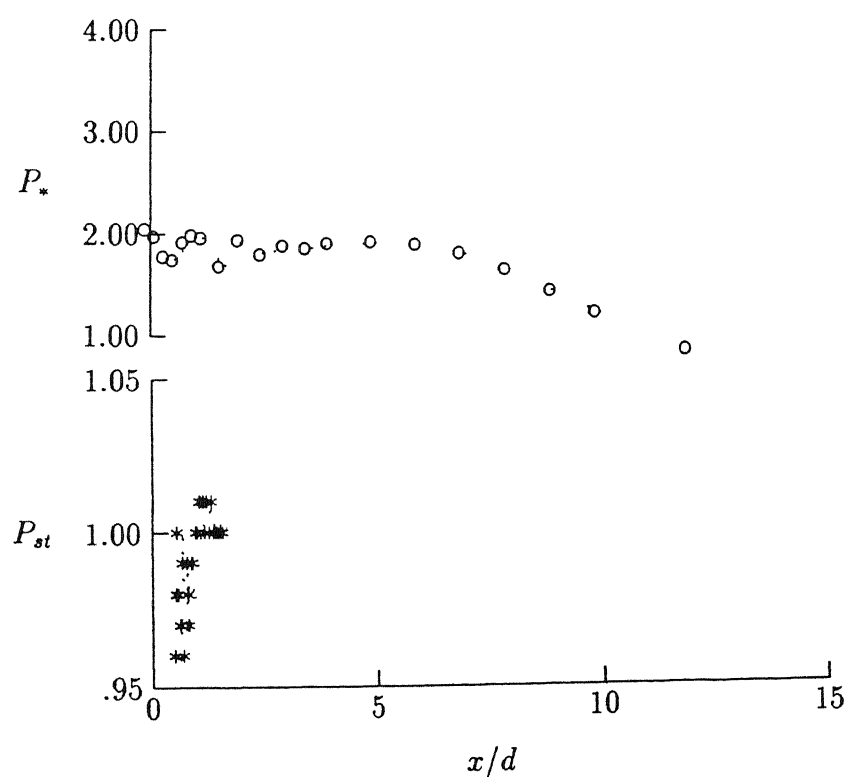


Fig. 7.4 Potential core : freejet $Pr = 1.5$ o mean pressure * static pressure

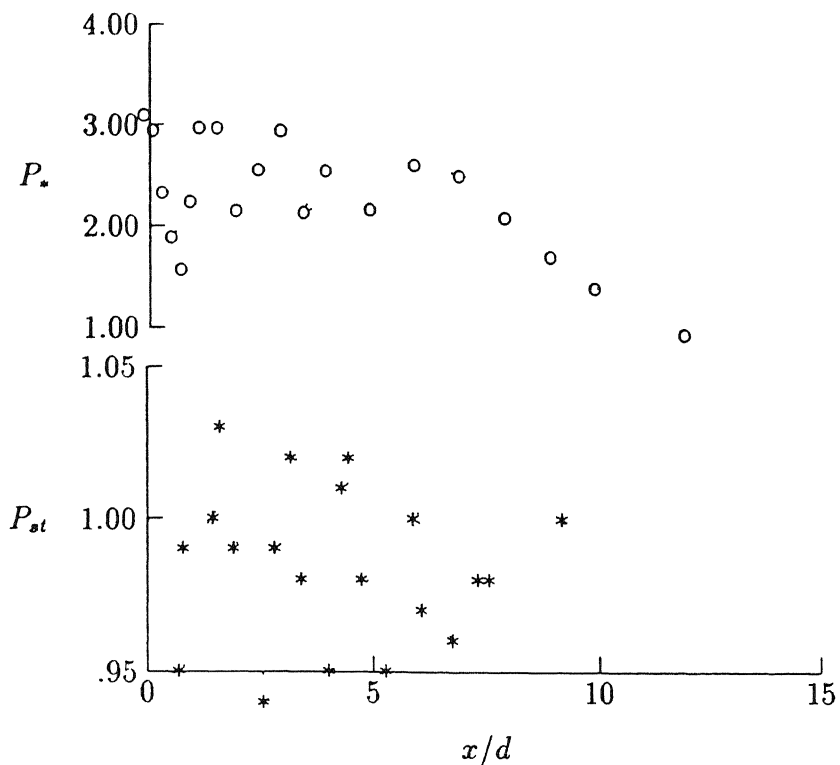


Fig. 7.5 Potential core : freejet $Pr = 2.0$ o mean pressure * static pressure

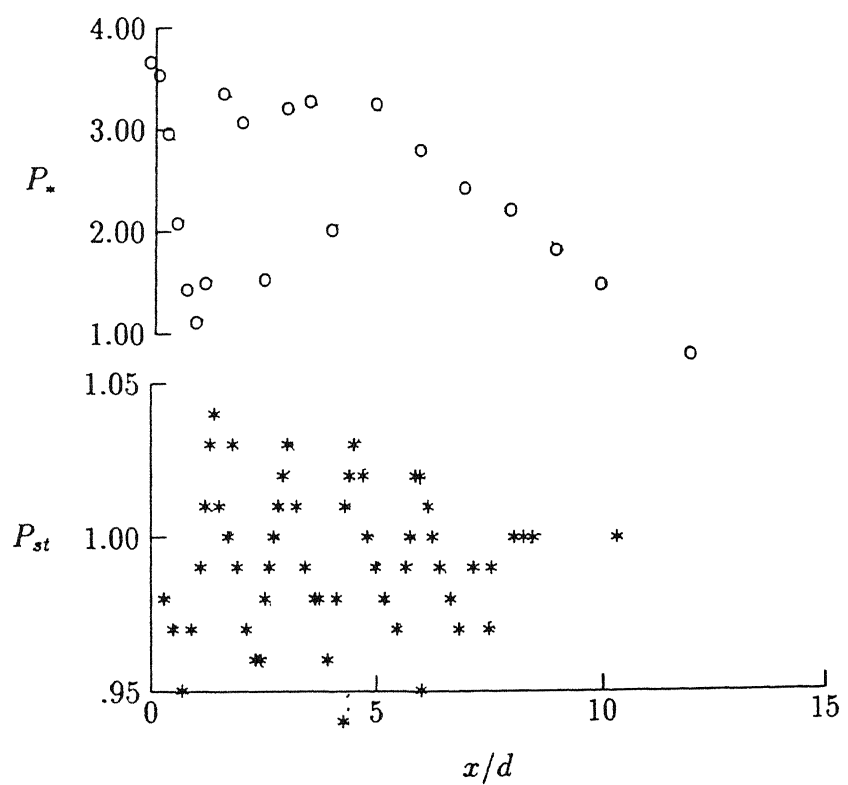


Fig. 7.6 Potential core : freejet $Pr = 2.25$ o mean pressure * static pressure

variation of the pitot and static pressure change from smooth to alternating pattern, indicating the presence of compression and expansion waves in the potential core at higher levels of underexpansion. Behind a shock, the static pressure rises whereas the total pressure drops. This trend is observed for levels of underexpansion greater than 1.2. Further the length of the potential core shows an insignificant variation with the levels of underexpansion.

7.2.2 Decay

The centreline decay of underexpanded jets in terms of P_* is shown in Fig. 7.7 for various levels of underexpansion. The centreline decay for correctly expanded sonic jet is also shown for comparison. With increasing levels of underexpansion, the amplitude of the variation of the centreline pressure increases. The choice of the parameter P_* , determines the axial extent of the potential core. When $P_* = 1$, the flow is assumed to be correctly expanded and sonic. The initiation of the subsonic zone from the wave dominated initial zone occurs at larger axial distances with the higher levels of underexpansion. The presence of the wave cells cause higher rate of decay due to faster dissipation of the energy compared to correctly expanded sonic jet. The decay of centreline pressure P_C (eqn (10)) and is shown in Fig. 7.8. Through this representation, it is shown that with respect to the initial pressure potential jet at the higher level of underexpansion decays earlier than the lower level of underexpansion.

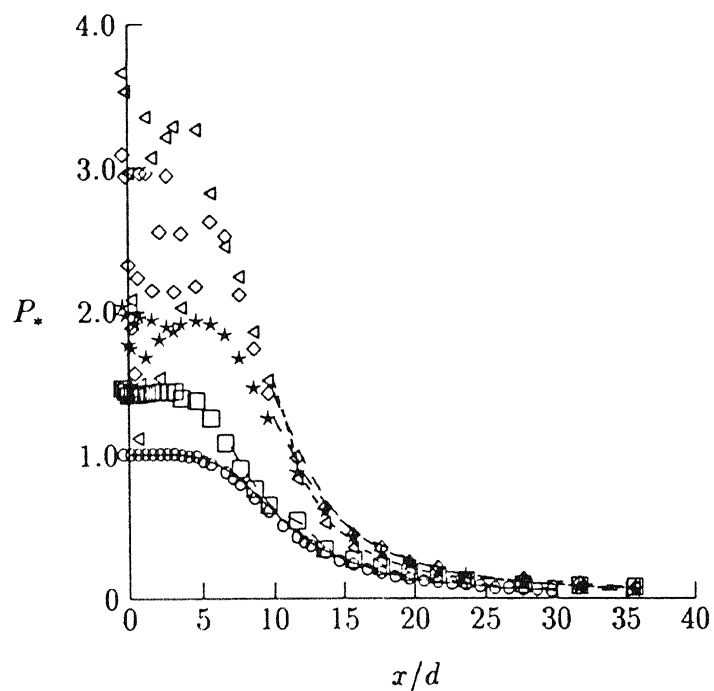


Fig. 7.7 Decay of centre line pressure for sonic jet : $\circ Pr = 1.0$, $\square Pr = 1.2$, $\star Pr = 1.5$,
 $\diamond Pr = 2.0$, and $\triangle Pr = 2.25$.

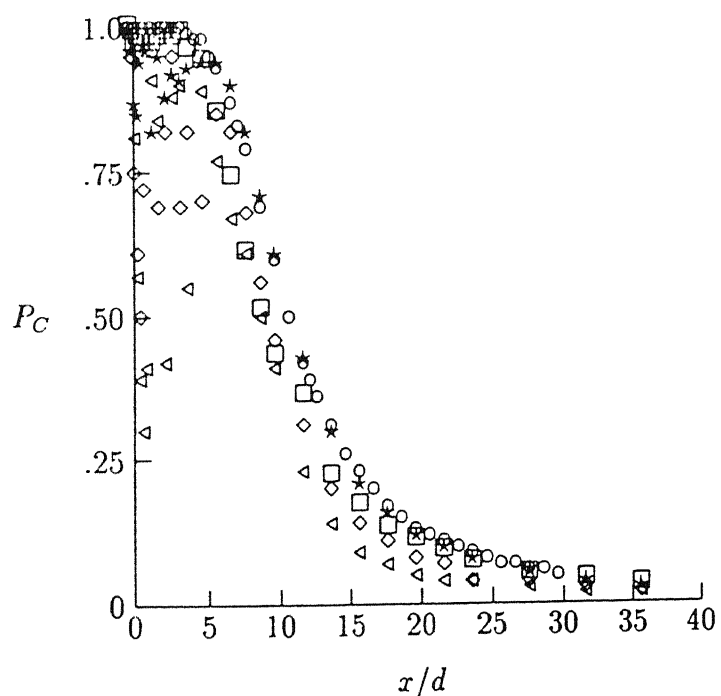


Fig. 7.8 Decay of centre line pressure for sonic jet : $\circ Pr = 1.0$, $\square Pr = 1.2$, $\star Pr = 1.5$,
 $\diamond Pr = 2.0$, and $\triangle Pr = 2.25$.

7.2.3 Isobars

In Fig. 7.9, the isobars are shown for underexpansion level $Pr = 1.5$ with $P_* \leq 1$. $P_* \leq 1$ represents the correctly expanded sonic to subsonic regime excluding the potential core in the jet field. The isobars exhibit positive as well as negative gradients as described for subsonic to correctly expanded jet. The half pressure width is observed not to demarcate at the zero gradient isobar, this may be due to lateral expansion of the field caused by the cellular structure of the potential core. This nature is similar for all the levels of underexpansion, as also seen from Fig. 7.10. Figure 7.11 shows isobars for two fractions of exit pressure ($f = 0.5$ and $f = 0.07$), for various levels of underexpansion of the present study. With increased levels of underexpansion, the lateral extent of the isobars increases due to increase in the size of the cellular wave structure laterally as well as longitudinally. Although, the effect of underexpansion is predominant for various isobars, the half pressure width is only marginally affected by the levels of underexpansion as compared with correctly expanded flow as in Fig. 7.12.

7.2.4 Shear

Based on contours of equal values of S given by the eqn (5), shear surfaces of constant properties has been constructed for underexpanded freejets. The shear layers for the subsonic field of the underexpanded jets are shown in Fig. 7.13 for under expansion level $Pr = 2.0$. The effect of the cellular wave structure of the potential core on the shear layers of the mixing zone is seen in this figure as distortion of the regular pattern for S compared to that for correctly expanded jets.

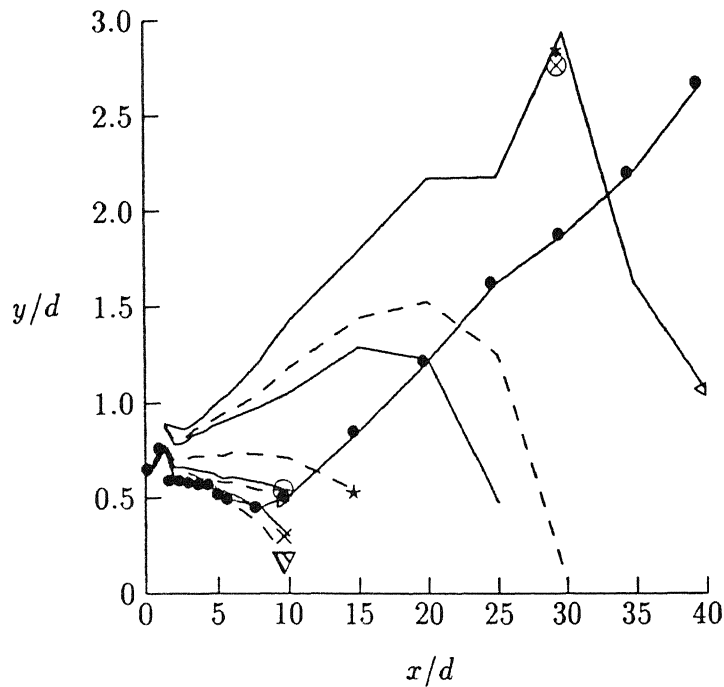


Fig. 7.9 Isobars and half pressure width : $Pr = 1.5$ $\nabla 1.0$, $\times 0.80$, $\triangleright 0.60$, $\ominus 0.50$, $\star 0.30$, $\otimes 0.10$, $*$ 0.07, $\triangleleft 0.03$, and $\bullet b = 0.5$.

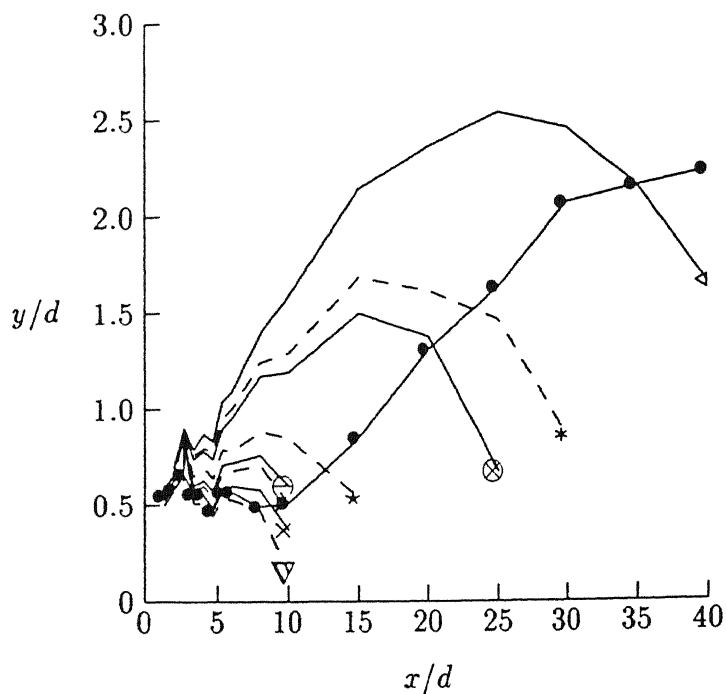


Fig. 7.10 Isobars and half pressure width : $Pr = 2.0$ $\nabla 1.0$, $\times 0.80$, $\triangleright 0.60$, $\ominus 0.50$, $\star 0.30$, $\otimes 0.10$, $*$ 0.07, $\triangleleft 0.03$, and $\bullet b = 0.5$.

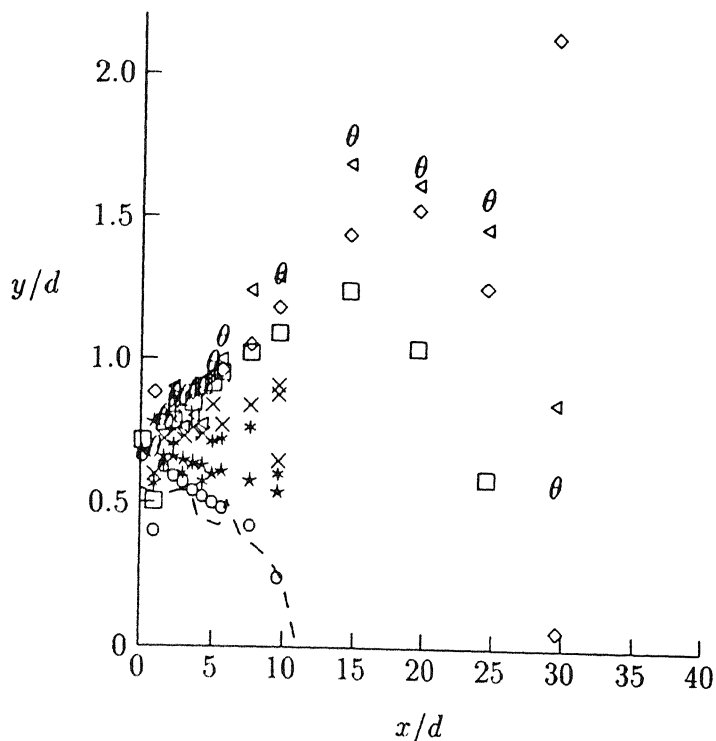


Fig. 7.11 Comparison of isobars for sonic jets : dash $f = 0.50$, dotted $f = 0.07$, $Pr = 1.2$: $\circ 0.50$, $\square 0.07$, $Pr = 1.5$: $*$ 0.50 , $\diamond 0.07$, $Pr = 2.0$: $*$ 0.50 , $\triangle 0.07$, and $Pr = 2.25$: $\times 0.50$, $\theta 0.07$.

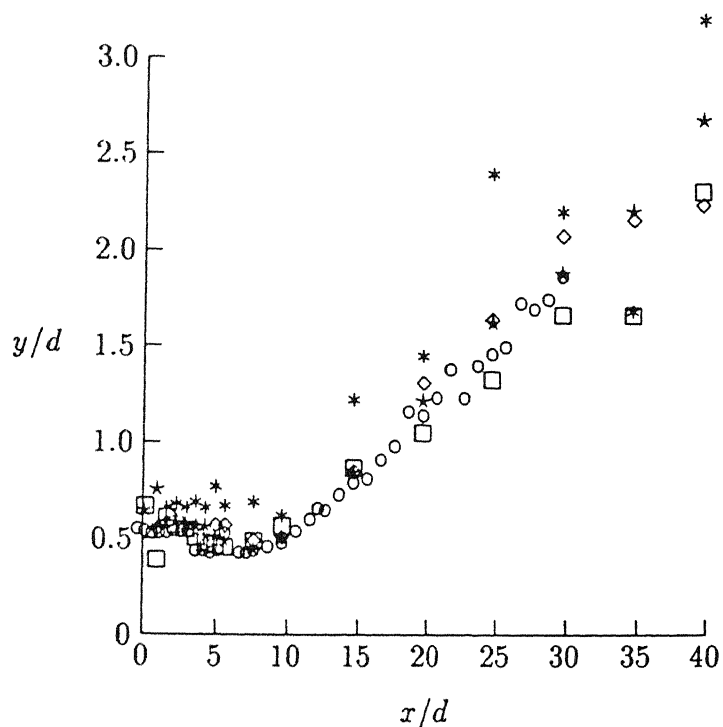


Fig. 7.12 Comparison of half pressure widths : $\circ Pr = 1.0$, $\square Pr = 1.2$, $\star Pr = 1.5$, $\diamond Pr = 2.0$, and $*$ $Pr = 2.25$.

7.2.5 Similarity

Complete similarity of pressure field was reported for freejets by suitable definition of the pressure and the length scale given by eqns 12 and 11, resp.. Defining the pressure scale for the mixing (*correctly expanded sonic to subsonic*) regime of the underexpanded flow as

$$P_{S*} = (P/P_a - 1)/(P_s/P_{a_{correct}} - 1) \quad (17)$$

and the half pressure width given by the eqn (11) complete similarity of the pressure profiles is shown in Fig. 7.14. The comparison f similarity at different levels of underexpansion of the present study shows that all the curves collapse when the above scales are used.

7.3 Conclusions

- The cellular wave structure of freejets increase in lateral as well longitudinal extent with increase of the level of underexpansion.
- The length of the potential core consisting of cellular wave structures are nearly the same for levels of underexpansion from $Pr = 1.5$ to 2.25.
- The decay of the sonic jet with respect to the initial pressure occurs earlier for higher levels of underexpansion as compared to the correctly expanded sonic jet due to dissipation of energy through the cellular wave structure.
- The level of underexpansion influences the isobars of the same value by causing a lateral outward shift.

- The half pressure width does not demarcate the positive and negative gradient isobars for higher levels of underexpansion of sonic jets unlike in the case of subsonic to correctly expanded sonic jets.

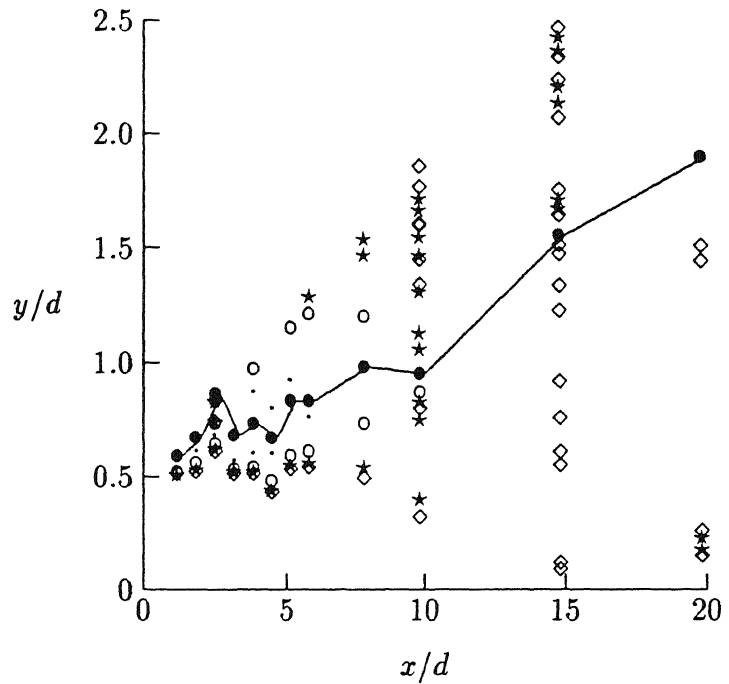


Fig. 7.13 Representation of shear : $Pr = 2.0$, $S = \cdot 0.20$, $\circ 0.09$, $\star 0.05$, $\diamond 0.03$, and $\bullet b = 0.5$.

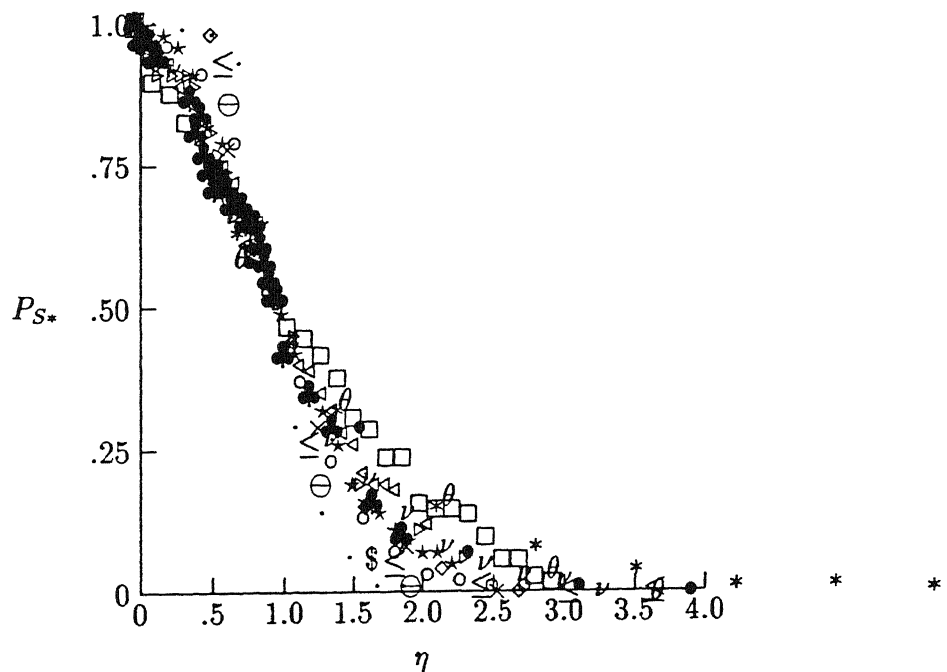


Fig. 7.14 Comparison of pressure similarity of sonic jet : $Pr = 1.0 : \cdot 3.5d$, $\circ 5.5d$, $\star 18.0d$, $Pr = 1.2 : \diamond 2.66d$, $\ast 4.0d$, $\triangleleft 25.0d$, $Pr = 1.5 : \times 2.66d$, $\theta 4.0d$, $\triangleright 30.0d$, $Pr = 2.0 : \bullet 4.0d$, $\nu 8.0d$, $\square 15.0d$, $Pr = 2.25 : \$ 2.0d$, $\ominus 2.7d$, $\leq 4.0d$, $\clubsuit 40.0$.

Chapter 8

Underexpanded Normal Impinging Jets

In this chapter, the effect of the wall on the impinging jet field and the jet field on the wall has been investigated for various levels of underexpansion and nozzle-wall distance. A flat plate when placed in the potential core region of the underexpanded freejet field modifies the cellular wave structure. Schlieren flow visualization technique has been applied to study the impinging cellular shock structure in the first part. In the second part of this chapter, the impinging field and the wall surface distribution has been analyzed based on the measured pressure. The effect of underexpansion has been compared with correctly expanded impinging jets.

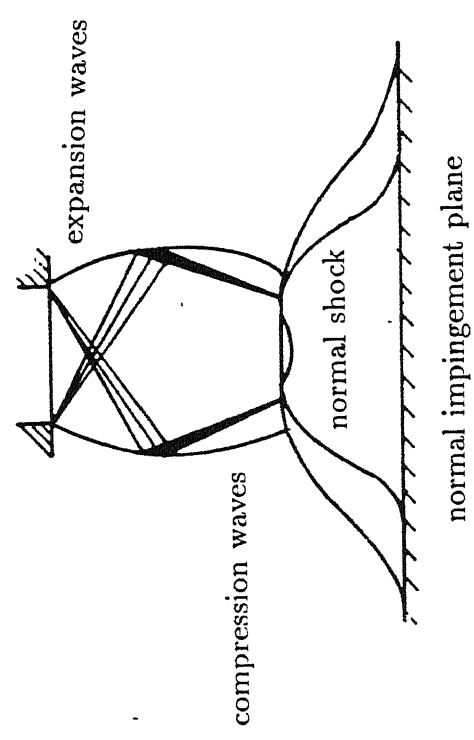


Fig. 8.1 Characteristics of cellular wave structure on normal impingement of underexpanded jet

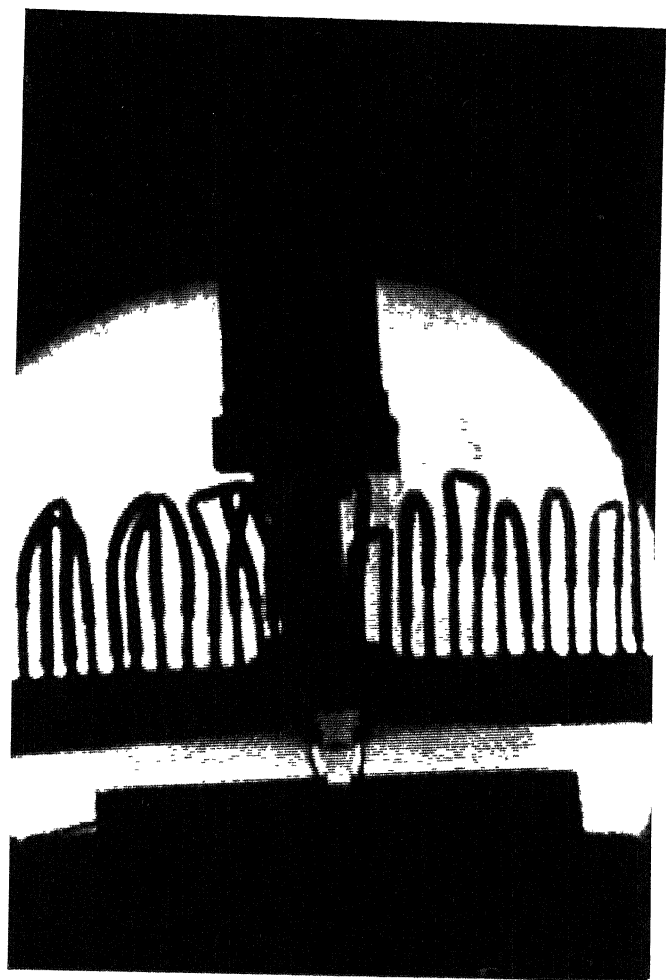


Fig. 8.2 Schlieren photograph of normal impinging jet $D_w = 1.0$ and $Pr = 2.0$

8.1 Flow visualization

The impinging flow field having a single cellular structure may be divided into two zones : a) region upstream of the shock waves produced by the plate and b) impingement flow region between the standoff shock wave and wall as shown in Fig. 8.1. In the region upstream of the standoff shock expansion fans originate from the nozzle exit and reflect from the free boundary as compressive waves. These waves coalesce for higher levels of underexpansion to form reflected oblique shocks, which merge at the end of the standoff shocks known as triple point lying inward to the intersection of the jet boundary and the walljet boundary. Below the standoff shock, the flow is subsonic and accelerates through an expansion fan at the triple point into the wall jet region. The walljet region may have alternating compressive and expansion waves followed by the viscous walljet region.

The Schlieren pictures of the impinging cellular wave structure show the effect of the wall on the freejet potential core cellular structure. The study has been carried out with the wall placed at different axial locations in the jet field with distances greater than the first single cell.

The impinging shock structure with $D_w = 1.0$ and $Pr = 2.0$ and 2.25 are shown in Figs. 8.2 and 8.3, respectively. As shown in the schematic representation of Fig. 8.1, the plate shock is parallel to the wall. This shock demarcates the impinging field into two regions; upstream of the shock consisting of expansion and compressive waves, and downstream of the shock which is a subsonic zone bounded by the wall. The boundaries of the walljet region are also seen in these figures.

The qualitative picture of the impinging jet flow field when the wall is placed normal

to the jet axis at a distance $D_w = 2.5$ is given in Figs. 8.4 to 8.6, for three levels of underexpansion; $P_e/P_a = 1.5, 2.0$ and 2.25 , respectively. Here again, all the flow field features observed in the near field impingement are clearly seen. Further, the influence of the level of underexpansion, resulting in the modification of the wave strength and the jet boundary are clearly seen from the pictures. For instance, the first cell just downstream of the nozzle gets stretched considerably when the P_e increases from 1.5 to 2.0 . The stretching is both in axial and radial directions. Also the expansion fan at the nozzle lip becomes more powerful with increase of underexpansion level. For further increase in Pr from 2.0 to 2.25 there is no visible change in the first cell structure except the strength of waves become higher, as seen as much darker in the picture. The stand-off shock gets pushed closer to the wall as the level of underexpansion increases. This may be due to the longitudinal stretching of the cell.

The plate shock strength increases with increasing level of underexpansion, but decreases with the increase of D_w . As the wall is moved away from the nozzle exit, the plate shock moves along with the wall in the axial direction. The present results are in good agreement with the structure reported by Iwamoto [57].

Figs. 8.7 to 8.9 show their flow structure with $D_w = 4.0$ for $Pr = 1.2, 2.0$ and 2.25 , respectively. Here again the increase in Pr from 1.2 to 2.0 results in considerable stretching of the cells. Also the cell boundaries becomes well defined with increase of underexpansion level. However, as the number of cells becomes more the Schlieren picture clarity becomes poor as expected, since the flow Mach number falls on progressing away from the nozzle exit.

For lower level of underexpansion, $Pr = 1.2$ the standoff shock is weaker as compared to higher levels of underexpansion of $Pr = 2.0$ and 2.25 . In the impinging jet

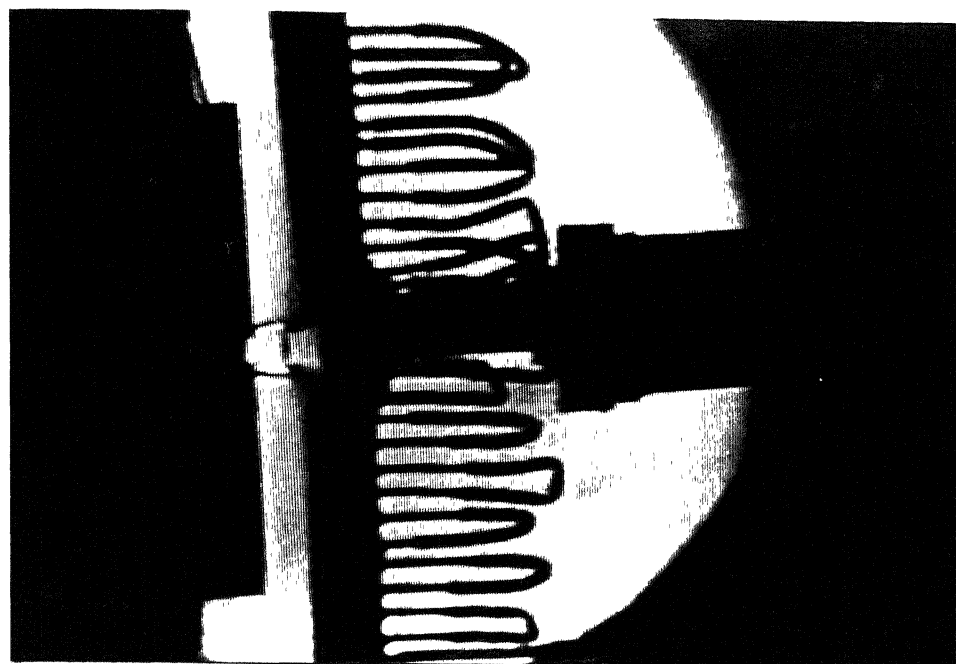


Fig. 8.3 Schlieren photograph of normal impinging jet $D_w = 1.0$ and $Pr = 2.25$

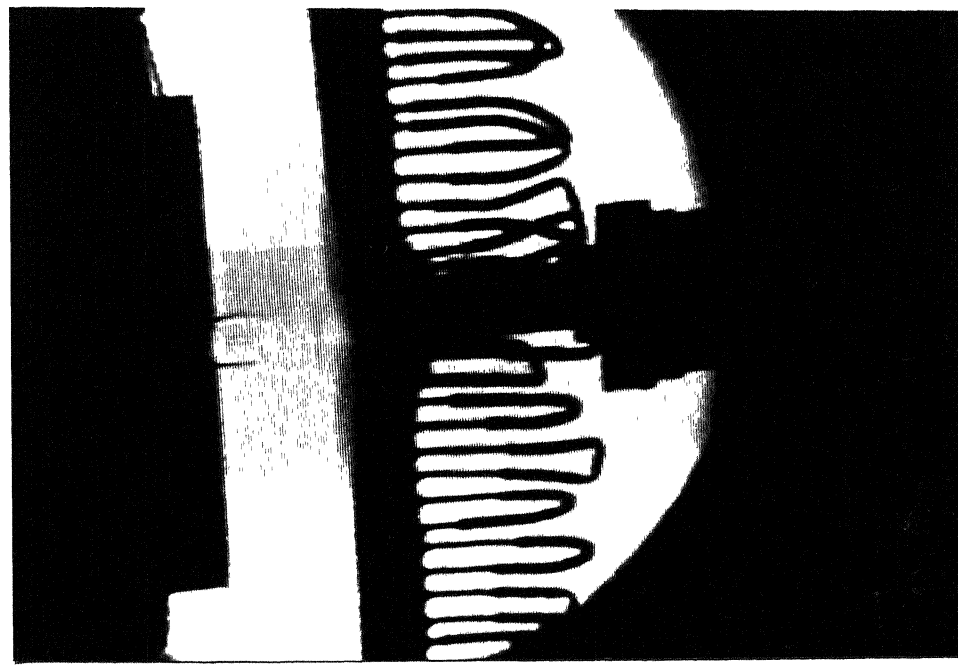


Fig. 8.4 Schlieren photograph of normal impinging jet $D_w = 2.5$ and $Pr = 1.5$

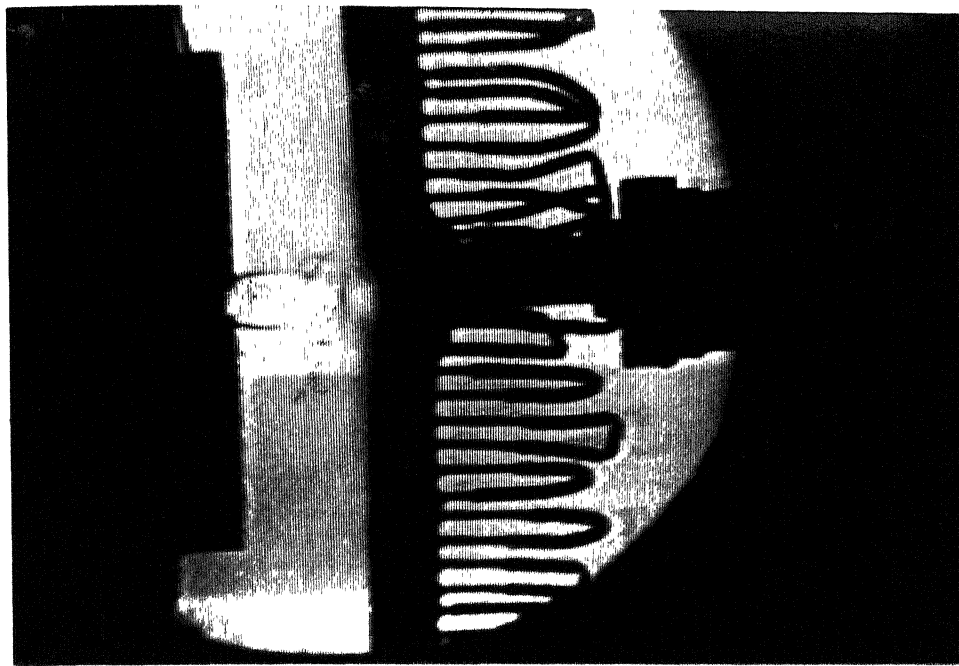


Fig. 8.5 Schlieren photograph of normal impinging jet $D_w = 2.5$ and $Pr = 2.0$

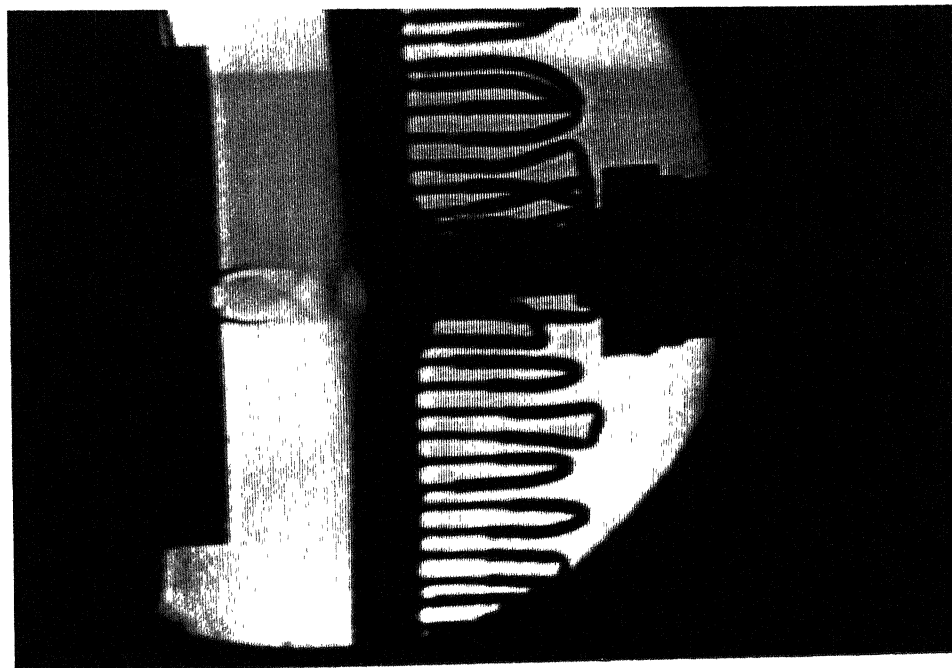


Fig. 8.6 Schlieren photograph of normal impinging jet $D_w = 2.5$ and $Pr = 2.25$

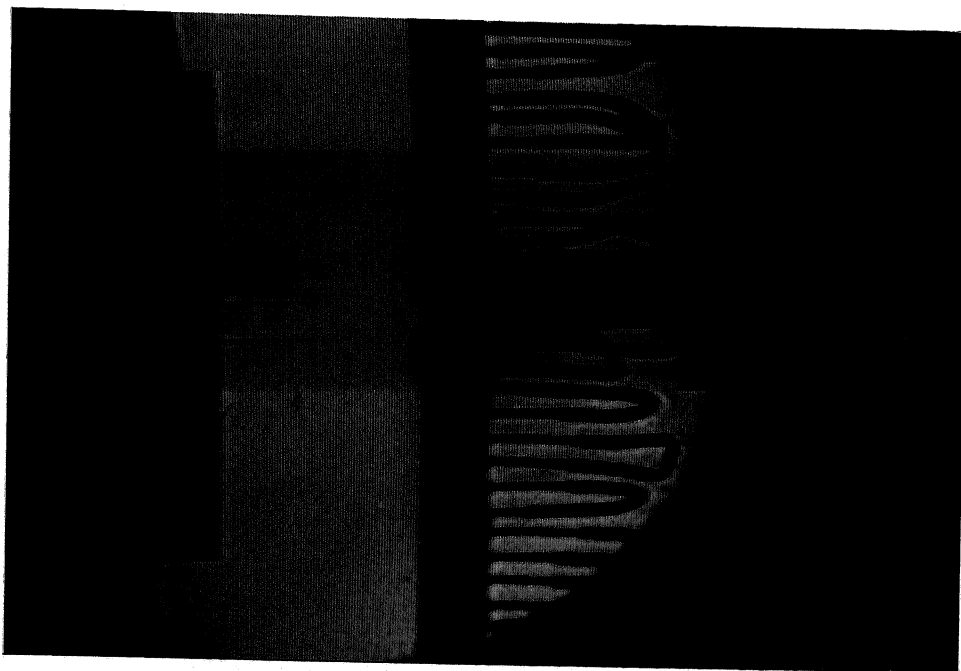


Fig. 8.7 Schlieren photograph of normal impinging jet $D_w = 4.0$ and $Pr = 1.2$

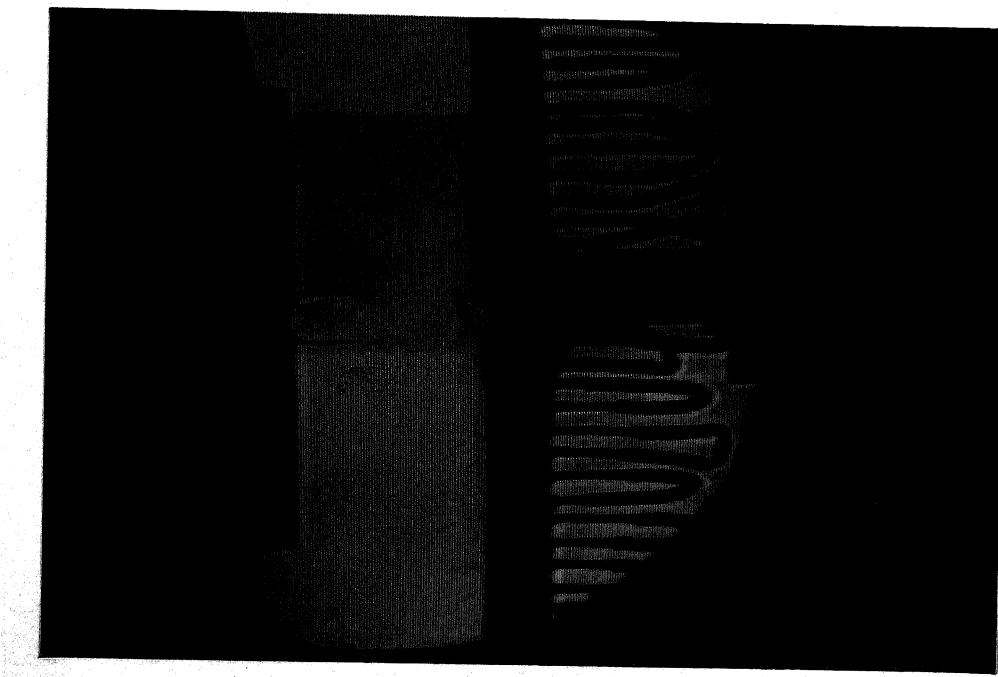


Fig. 8.8 Schlieren photograph of normal impinging jet $D_w = 4.0$ and $Pr = 2.0$

field the complete cells maintain the same characteristics as that of the freejet. It was also observed that beyond the potential core of the underexpanded jets, the wall does not influence the structure of the freejet cellular structure.

Fig. 8.10 gives the flow field for pressure ratio 2.25 when $D_w = 5.0$. From this it is evident that the cells adjacent to the walls are getting adjusted whereas those away from the wall are influenced insignificantly. It is also observed that beyond the potential core of the underexpanded jets, the wall does not influence the structure of the freejet cellular structure.

8.2 Impinging jet field

8.2.1 Decay

The centre line decay of P_* in the impinging jet field is compared with freejet field at different wall locations in Fig 8.11 for $Pr = 2.0$. The pressure waves reflected from the wall triggers the shear layers at the nozzle exit causing oscillations in the jet field upto about 5.0d, beyond which the impinging jet decays similar to that of the freejet. This observation was consistent for all the levels of underexpansion of the present study.

8.2.2 Isobars

From the measurements in the impinging jet field and the wall surface pressures, various fractions of the exit pressure are shown for two levels of underexpansion $Pr = 1.2$ and $Pr = 2.0$ with wall at $D_w = 8$, in Figs. 8.12 and 8.13. With increase in the levels of underexpansion from 1.2 to 2.0, the spread near the wall increases and the contour

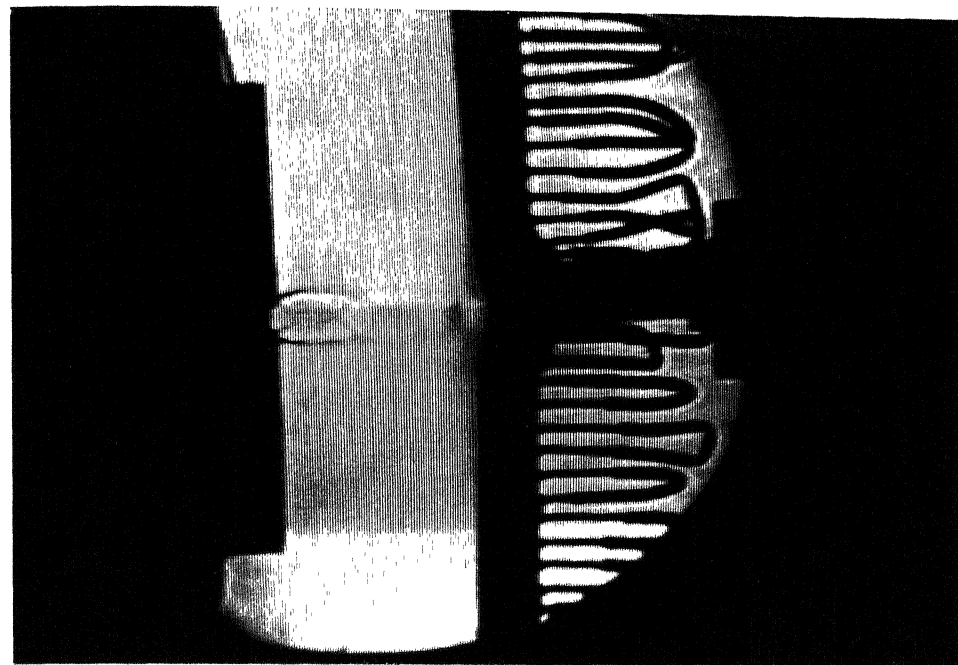


Fig. 8.9 Schlieren photograph of normal impinging jet $D_w = 4.0$ and $Pr = 2.25$

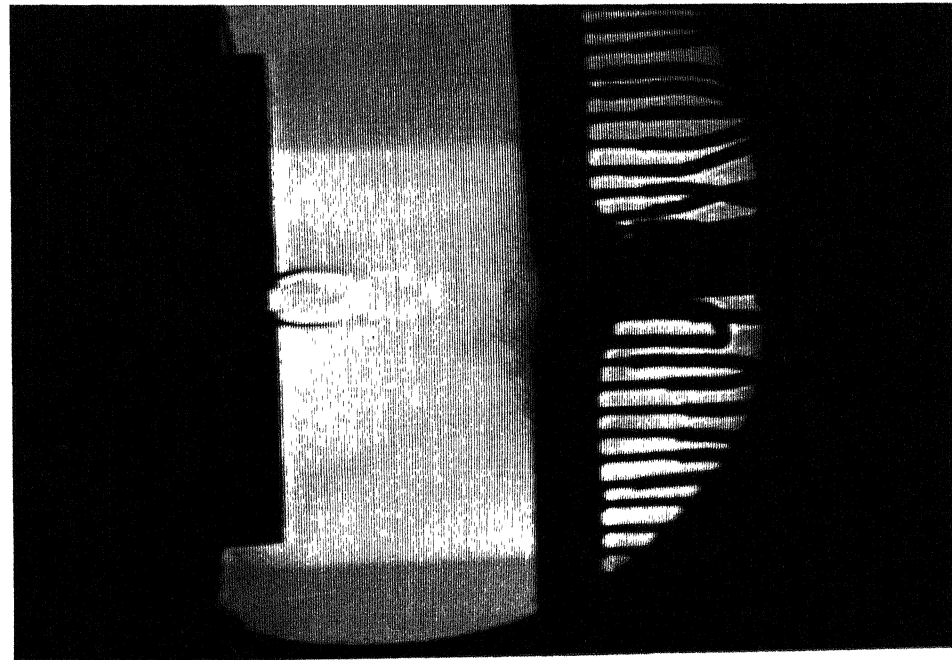


Fig. 8.10 Schlieren photograph of normal impinging jet $D_w = 5.0$ and $Pr = 2.25$

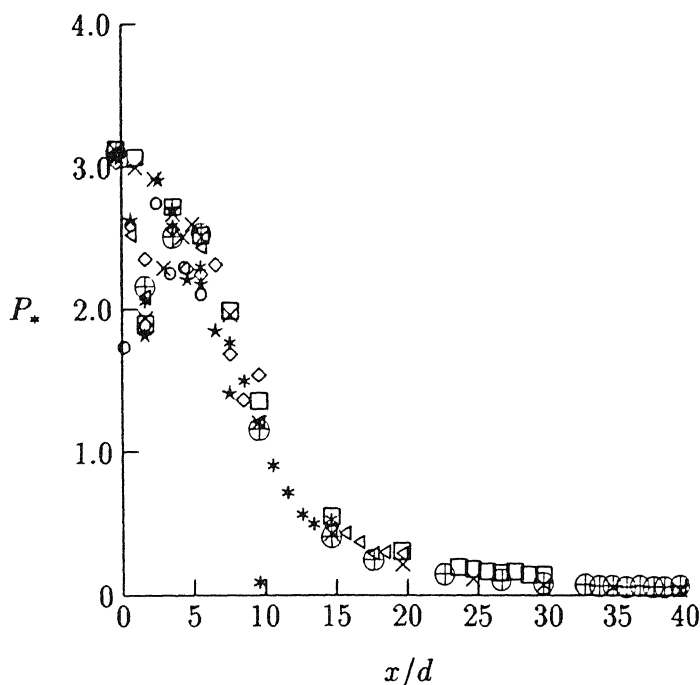


Fig. 8.11 Decay of centre line gauge pressure for sonic jet at $Pr = 2.0$ \times freejet, impinging jet at $D_w = \circ 6, \star 8, \diamond 10, * 15, \triangleleft 20, \square 30$ and $\oplus 40$.

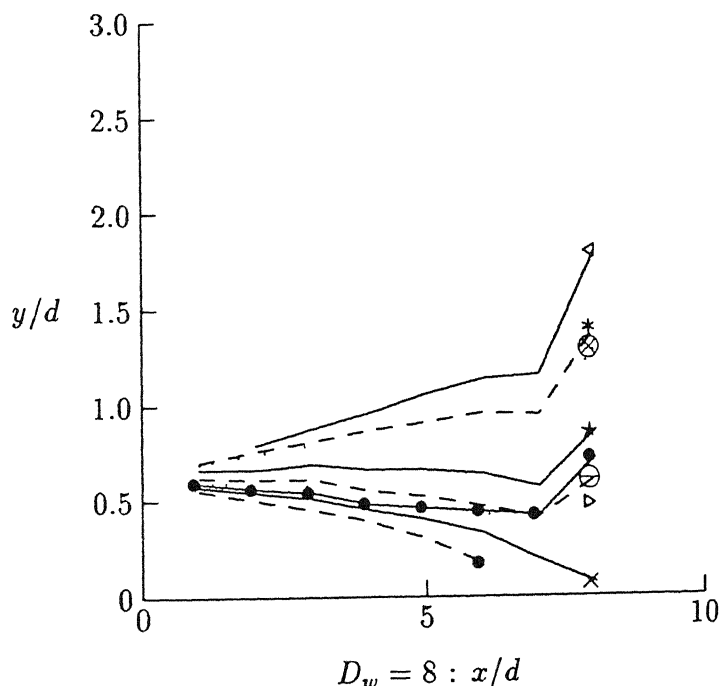


Fig. 8.12 Isobars and half pressure width $Pr = 1.2$ with $D_w = 8$: $\bullet 1.00, \times 0.80, \triangleright 0.60, \ominus 0.50, \star 0.30, \otimes 0.10, * 0.07, \triangleleft 0.03$ and $- \bullet - b = 0.5$.

$P_* = 1$ and its lower fractions shift outward laterally. As the wall is moved away from the nozzle exit to $D_w = 20$ (in Fig. 8.14), mild oscillations in the half pressure width is observed. This may be due to the reflection of the acoustic waves from the plate causing tripping of the shear layers at the nozzle exit.

The half pressure width at various wall locations has been compared locations with that of the freejet for $Pr = 2.0$ in Fig. 8.15. From these results it is seen that the wall locations influence the half pressure width when the wall is close to the nozzle exit for $D_w < 15$. From the results shown in Fig. 8.14 and 8.15, it can be inferred that the combination of wall distance and level of underexpansion dictates the nature and the location of oscillations of half pressure width. For some combination of the parameters the half pressure width oscillations are in the far field ($x/d > 10$) and for some other combination the half pressure width are in the near field ($x/d < 10$).

In Figs. 8.16 - 8.19, the fractions of the isobars of the impinging jet field for $Pr = 1.2, 1.5, 2.0$ and 2.25 have been compared with the corresponding freejet isobars. At lower value of $Pr = 1.2$ (Fig. 8.16), comparison of the freejet isobar and the impinging jet isobars show no difference between the two fields. As the level of underexpansion is increased to $Pr = 1.5$ (Fig. 8.17), the lower fractions f of the impinging jet field show mild variation as compared to the freejet. With increasing levels of underexpansion to $Pr = 2.25$ as in Fig. 8.18, with an intermediate level at $Pr = 2.0$ as in Fig. 8.19, the oscillations in the impinging jet field increase. This may be due to the stronger tripping of shear layers at the nozzle exit.

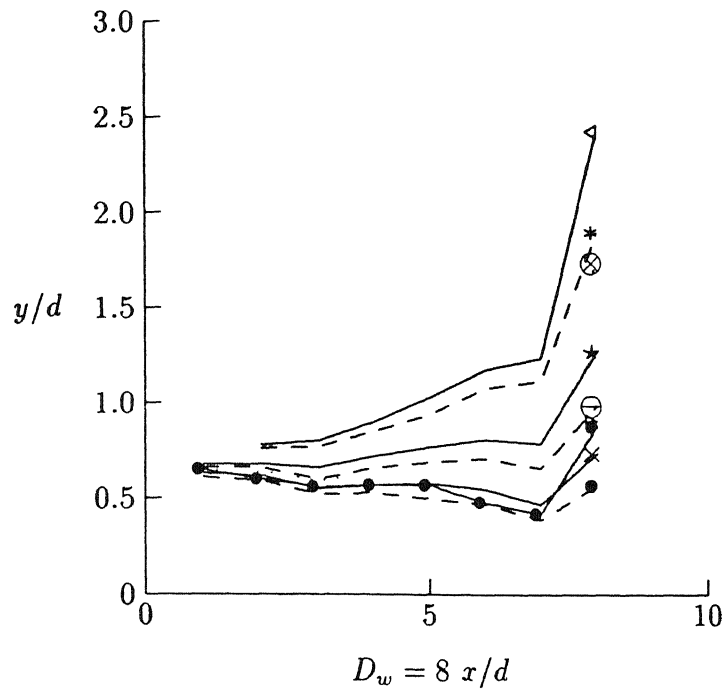


Fig. 8.13 Isobars and half pressure width $Pr = 2.0$ with $D_w = 8$: • 1.00, × 0.80, ▷ 0.60, ⊖ 0.50, ★ 0.30, ○ 0.10, * 0.07, ▲ 0.03 and – ● – $b = 0.5$.

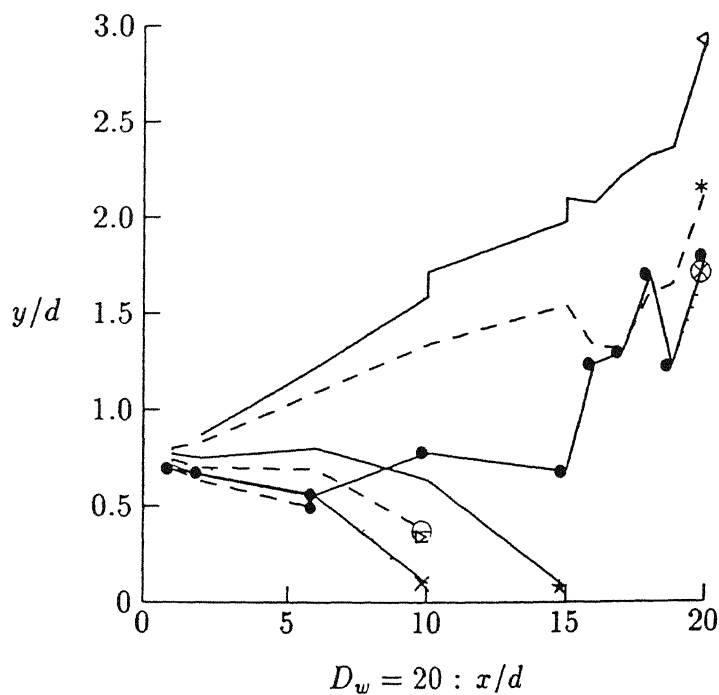


Fig. 8.14 Isobars and half pressure width $Pr = 1.5$ with $D_w = 20$: • 1.00, × 0.80, ▷ 0.60, ⊖ 0.50, ★ 0.30, ○ 0.10, * 0.07, ▲ 0.03 and – ● – $b = 0.5$.

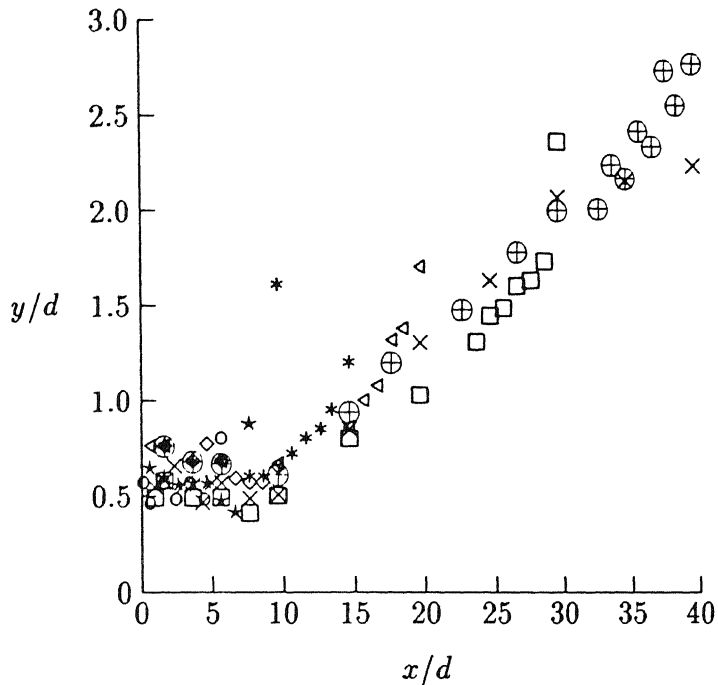


Fig. 8.15 Comparison of half pressure widths $Pr = 2.0$: \times freejet, impinging jet : \circ 6, \star 8, \diamond 10, $*$ 15, \triangleleft 20, \square 30, and \oplus 40.

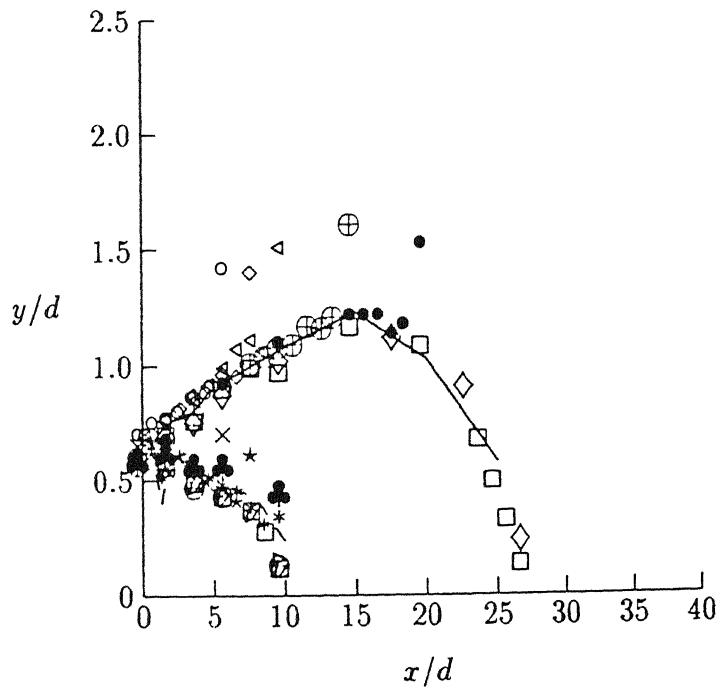


Fig. 8.16 Comparison of isobars for sonic jet $Pr = 1.2$ at various wall locations : freejet dash $f = 0.50$, dotted $f = 0.07$ impinging jet : $D_w = 6 \times f = 0.50$, $\circ f = 0.07$, $D_w = 8 \star f = 0.50$, $\diamond f = 0.07$, $D_w = 10 * f = 0.50$, $\triangleleft f = 0.07$, $D_w = 15 \square f = 0.50$, $\oplus f = 0.07$, $D_w = 20 \triangleright f = 0.50$, $\bullet f = 0.07$, $D_w = 30 \nu f = 0.50$, $\square f = 0.07$, and $D_w = 40 \ominus f = 0.50$, $\clubsuit f = 0.30$, $\diamondsuit f = 0.07$.

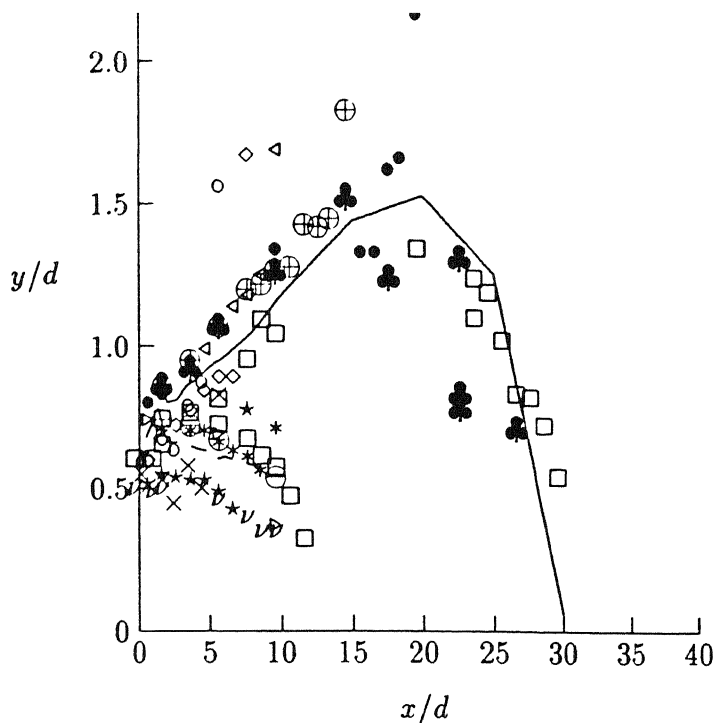


Fig. 8.17 Comparison of isobars for sonic jet $Pr = 1.5$ at various wall locations : freejet dash $f = 0.50$, dotted $f = 0.07$ impinging jet : $D_w = 6 \times f = 0.50$, $\circ f = 0.07$, $D_w = 8 \star f = 0.50$, $\diamond f = 0.07$, $D_w = 10 * f = 0.50$, $\triangleleft f = 0.07$, $D_w = 15 \square f = 0.50$, $\oplus f = 0.07$, $D_w = 20 \triangleright f = 0.50$, $\bullet f = 0.07$, $D_w = 30 \nu f = 0.50$, $\square f = 0.07$, and $D_w = 40 \ominus f = 0.50$, $\clubsuit 0.07$.

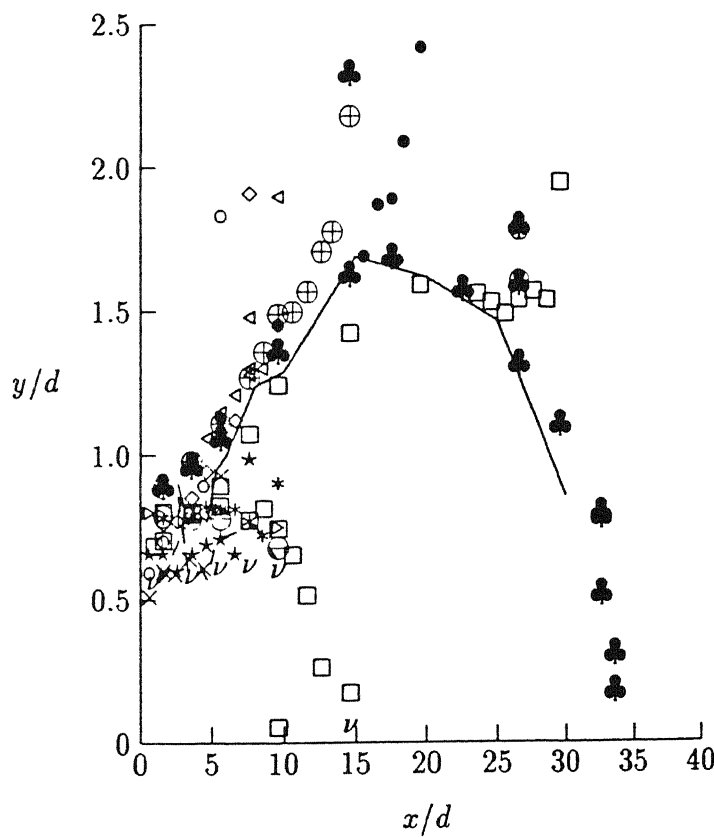


Fig. 8.18 Comparison of isobars for sonic jet $Pr = 2.0$ at various wall locations : freejet dash $f = 0.50$, dotted $f = 0.07$ impinging jet : $D_w = 6 \times f = 0.50$, $\circ f = 0.07$, $D_w = 8 \star f = 0.50$, $\diamond f = 0.07$, $D_w = 10 * f = 0.50$, $\triangleleft f = 0.07$, $D_w = 15 \square f = 0.50$, $\oplus f = 0.07$, $D_w = 20 \triangleright f = 0.50$, $\bullet f = 0.07$, $D_w = 30 \nu f = 0.50$, $\square f = 0.07$, and $D_w = 40 \ominus f = 0.50$, $\clubsuit 0.07$.

8.2.3 Similarity

Similarity of the free and impinging jets at various wall locations has been compared in Figs. 8.20 and 8.21 for $Pr = 1.2$ and for $Pr = 2.25$, respectively. The freejet and the impinging jet pressure fields are similar in the subsonic mixing zones excluding the cellular potential core consisting of expansion and compression fans, and shocks. The scales applied to obtain similarity of pressure field for subsonic jets to correctly expanded sonic jets are also valid for underexpanded impinging jets.

8.2.4 Shear

In Figs. 8.22 , the effect of the shear given by eqn (5) in the impinging jet field is shown for various levels of underexpansion at $D_w = 10$. The effect of the cellular wave structure on the subsonic mixing region outside the potential core is evident from these figures from the lateral outward shift of the constant shear surfaces.

8.2.5 Wall pressure distribution

The wall pressure distribution are presented from close range impingement of $D_w = 2.5$ to farfield impingement upto 40.0 in this section. Equal fractions of wall isobars of the positive wall pressure normalised with respect to the initial settling chamber gauge pressures are shown in Fig. 8.23. The fractions of wall isobars $f = 0.75, 0.5$ and 0.15 are shown for the levels of underexpansion of the present study. These wall isobars collapse irrespective of the the levels of underexpansion. In computing the zone of influence and the force coefficient F_N of positive pressure upto zero gauge pressures, it is essential to determine the exact location along the radial direction of the wall

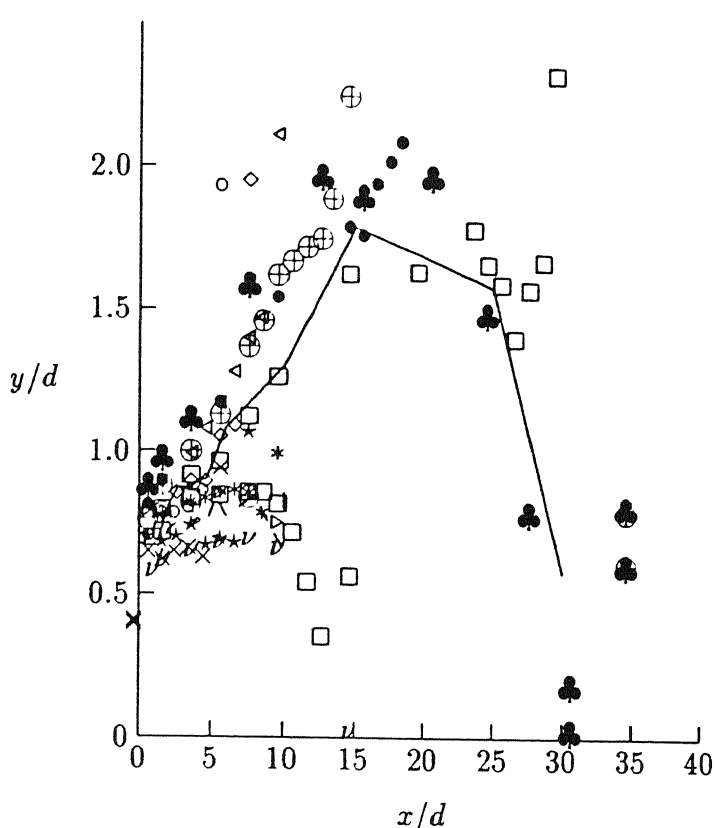


Fig. 8.19 Comparison of isobars for sonic jet $Pr = 2.25$ at various wall locations : freejet dash $f = 0.50$, dotted $f = 0.07$ impinging jet : $D_w = 6 \times f = 0.50$, $\circ f = 0.07$, $D_w = 8 \star f = 0.50$, $\diamond f = 0.07$, $D_w = 10 \ast f = 0.50$, $\triangleleft f = 0.07$, $D_w = 15 \square f = 0.50$, $\oplus f = 0.07$, $D_w = 20 \triangleright f = 0.50$, $\bullet f = 0.07$, $D_w = 30 \nu f = 0.50$, $\square f = 0.07$, and $D_w = 40 \ominus f = 0.50$, $\clubsuit 0.07$.

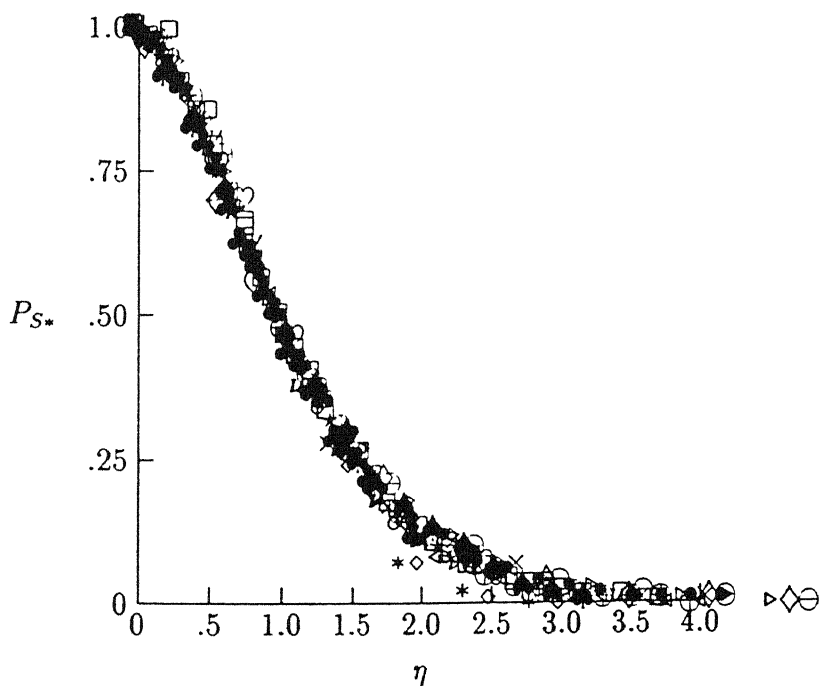


Fig. 8.20 Comparison of pressure similarity of sonic freejet and impinging jets : freejet : $Pr = 1.2 x = \times 4.66d$, $\circ 10.0d$, $\star 20.0d$ impinging jet : $D_w = 6 x = \diamond 2.8d$, $D_w = 8 x = \ast 3.0d$, $\triangleleft 7.0d$, $D_w = 10 x = \square 6.0d$, $\oplus 7.0d$, $D_w = 15 x = \triangleright 6.0d$, $\bullet 9.0d$, $D_w = 20 x = \nu 6.0d$, $\square 16.0d$, $D_w = 30 x = \ominus 4.0d$, $\clubsuit 24.0d$, and $D_w = 40 x = \diamond 4.0d$, $\spadesuit 10.0d$, $\heartsuit 23.0d$.

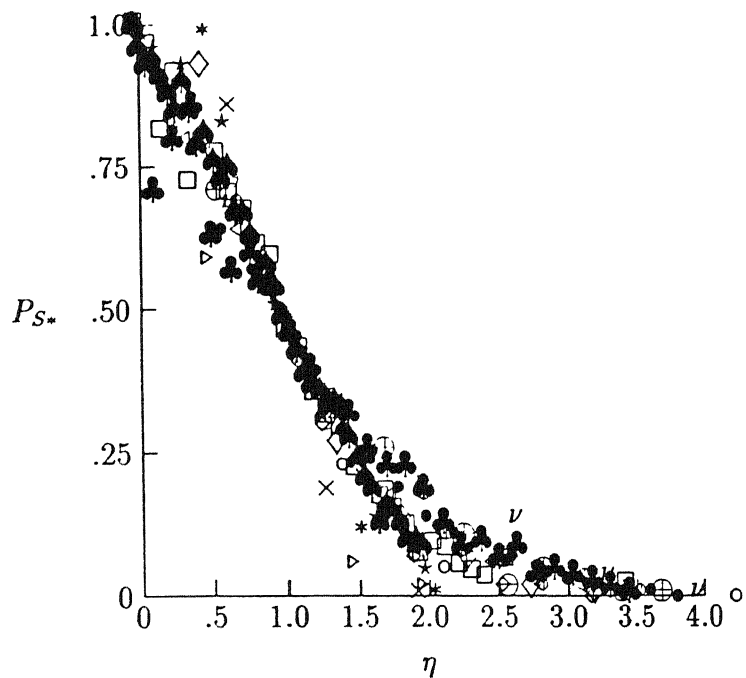


Fig. 8.21 Comparison of pressure similarity of sonic freejet and impinging jets : freejet : $Pr = 2.25$ $x = \times 2.7d$, $\circ 5.33d$, $*$ $20.0d$ impinging jet : $D_w = 6$ $x = \diamond 3.8d$, $D_w = 8$ $x = *$ $3.0d$, $\triangleleft 7.0d$, $D_w = 10$ $x = \square 4.0d$, $\oplus 8.0d$, $D_w = 15$ $x = \triangleright 4.0d$, $\bullet 10.0d$, $D_w = 20$ $x = \nu$ $6.0d$, $\ominus 16.0d$, $D_w = 30$ $x = \ominus 4.0d$, $\clubsuit 15.0d$, and $D_w = 40$ $x = \diamond 4.0d$, $\spadesuit 25.0d$.

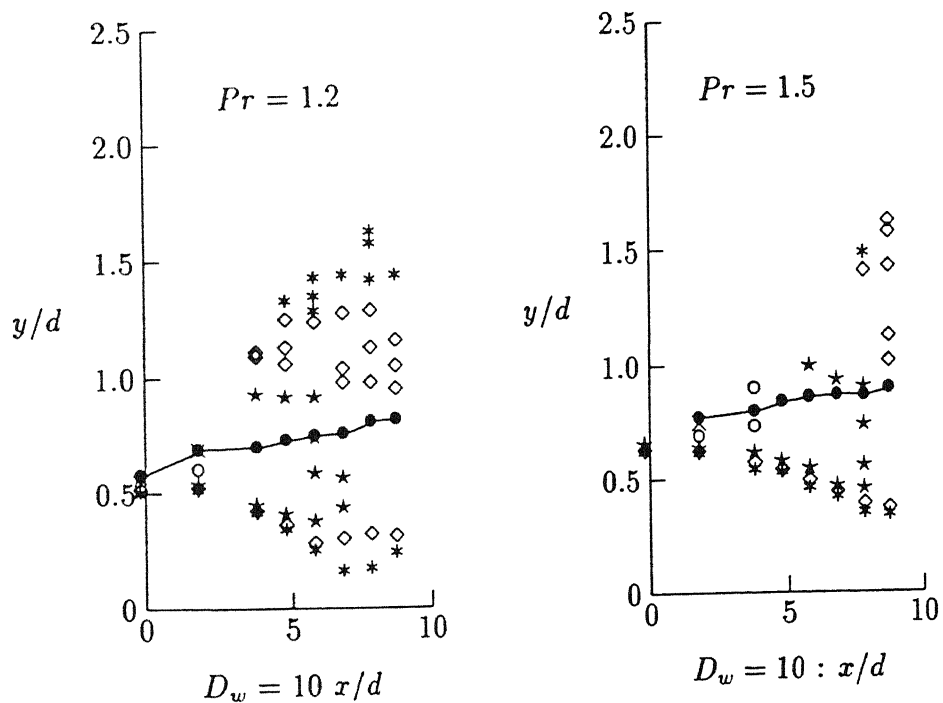


Fig. 8.22 . . .

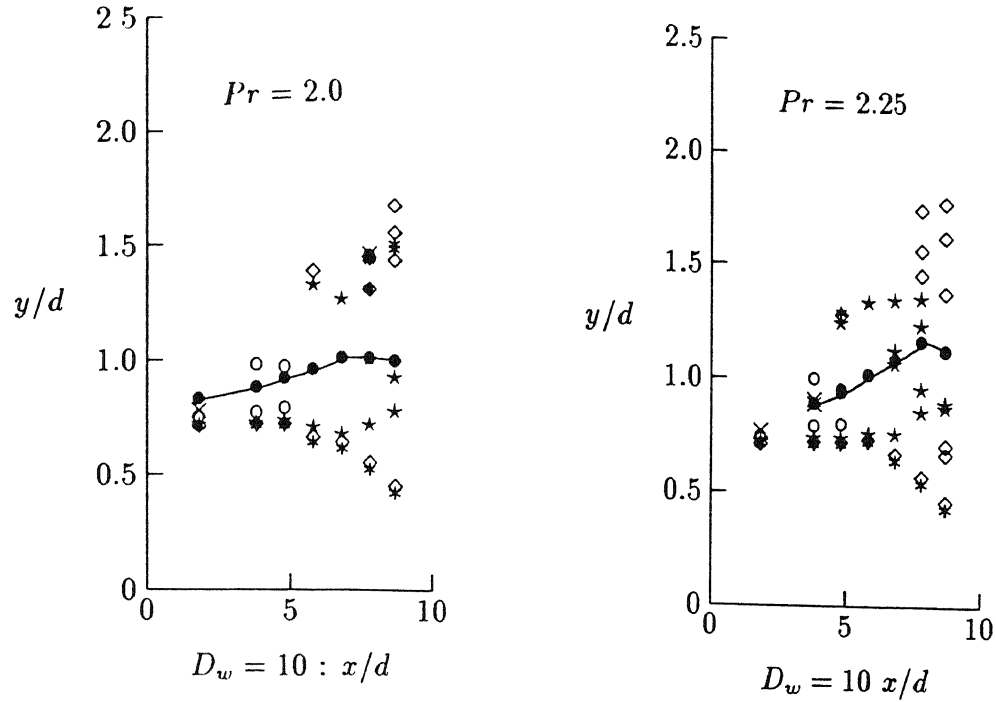


Fig. 8.22 Representation of shear with wall at $D_w = 10$: $S = \times 0.30, \circ 0.20, \star 0.09, \diamond 0.05, \bullet b = 0.5$.

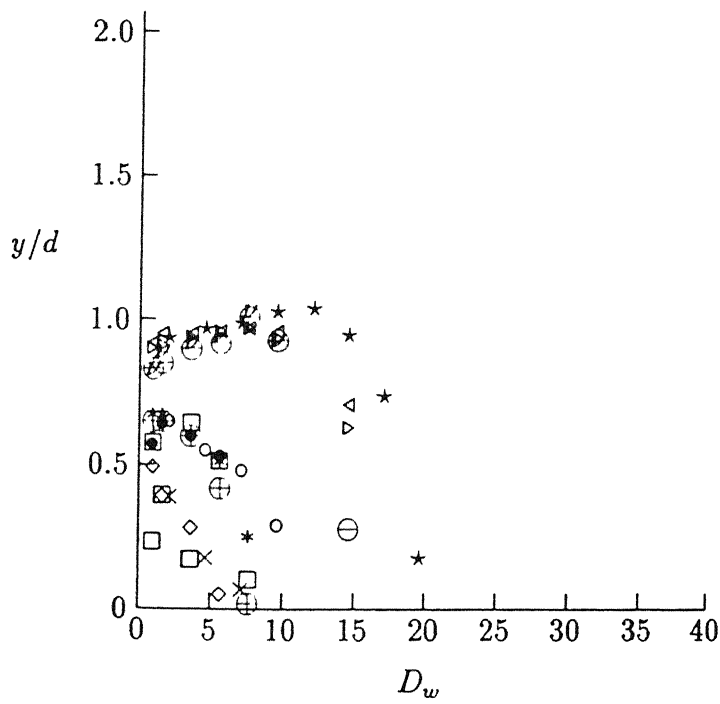


Fig. 8.23 Comparison of wall isobars : $Pr = 1.0 \times f = 0.75, \circ f = 0.50, \star f = 0.15, Pr = 1.2 \diamond f = 0.75, * f = 0.50, \triangleleft f = 0.15, Pr = 1.5 \square f = 0.75, \oplus f = 0.50, Pr = 2.0 \triangleright f = 0.75, \bullet f = 0.50, \nu f = 0.15, Pr = 2.25 \square f = 0.50, \ominus f = 0.15$,

where the pressure becomes atmospheric. The radial location of zero gauge pressure on the wall, depicting the lateral extent of the positive pressure zone is found to be a function of the nozzle-wall distance, as well as the initial stagnation pressure in the settling chamber. Since the locations of wall pressure tappings are fixed, it is not possible to measure the exact location where the pressure is equal to atmospheric for different combinations of parameters. Therefore it is appropriate to compute the force coefficient and the zone of influence of positive wall pressure upto a pressure value close to the ambient. The force scale given by the eqn (14) applied to subsonic to correctly expanded normal impinging jets is applied for underexpanded impingement flow field.

In Fig. 8.24, the zone of influence of positive pressures are presented upto 10 % of the settling chamber pressure for various levels of underexpansion. The variation in the zone of influence is marginal over the present levels of underexpansion and correctly expanded jet, and is similar to that of the subsonic to correctly expanded case. In Fig. 8.25 , the force coefficient for correctly expanded jet and various levels of expansion are presented. The impingement with underexpanded jets show lower force coefficient compared to correctly expanded sonic jet. The F_N variation with D_w is oscillatory in nature. This may be attributed to the cellular wave structures present in the core region.

The lower value of force coefficients may be due to higher dissipation of energy across the waves, and also may be due to the pressure loss across the standoff shock. Complete similarity of the positive wall pressure regions are shown in Fig. 8.26 and has been compared between various wall locations and levels of expansions. It is interesting to see that, this similarity is almost independent of D_w and Pr . This has been obtained by normalising the wall pressure with the centre line pressure and the radial length

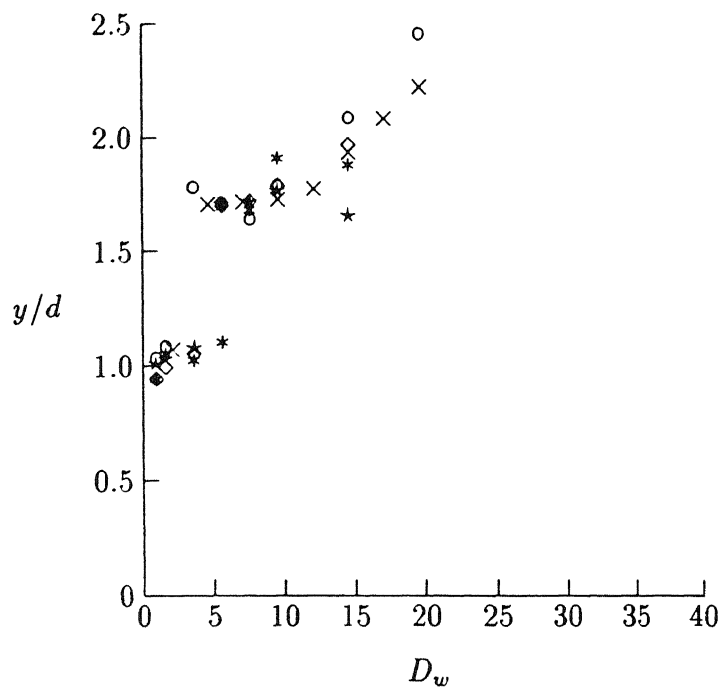


Fig. 8.24 Zone of influence upto 10 % of settling chamber pressure : \times $Pr = 1.0$, \circ $Pr = 1.2$, \star $Pr = 1.5$, \diamond $Pr = 2.0$, and $*$ $Pr = 2.25$

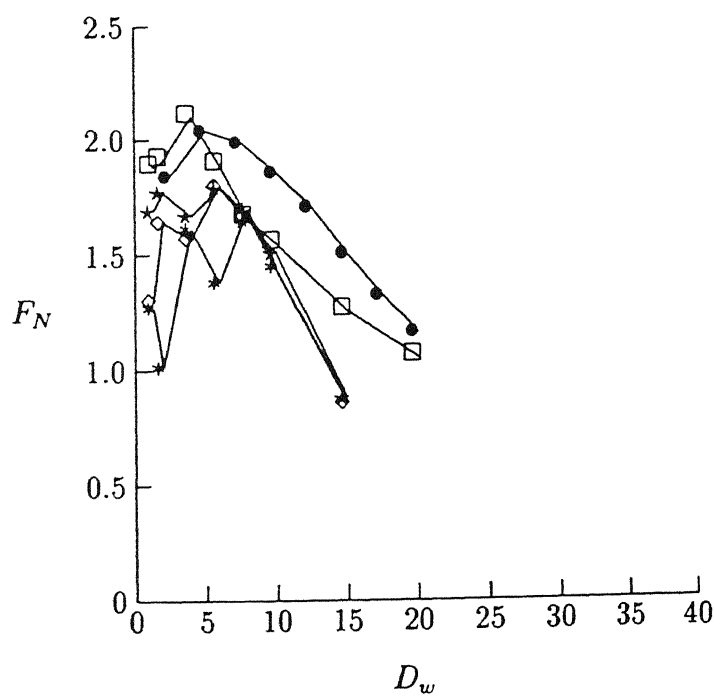


Fig. 8.25 Normalised force coefficient distribution computed upto 10 % of settling chamber pressure : \bullet $Pr = 1.0$, \square $Pr = 1.2$, \star $Pr = 1.5$, \diamond $Pr = 2.0$, and $*$ $Pr = 2.25$.

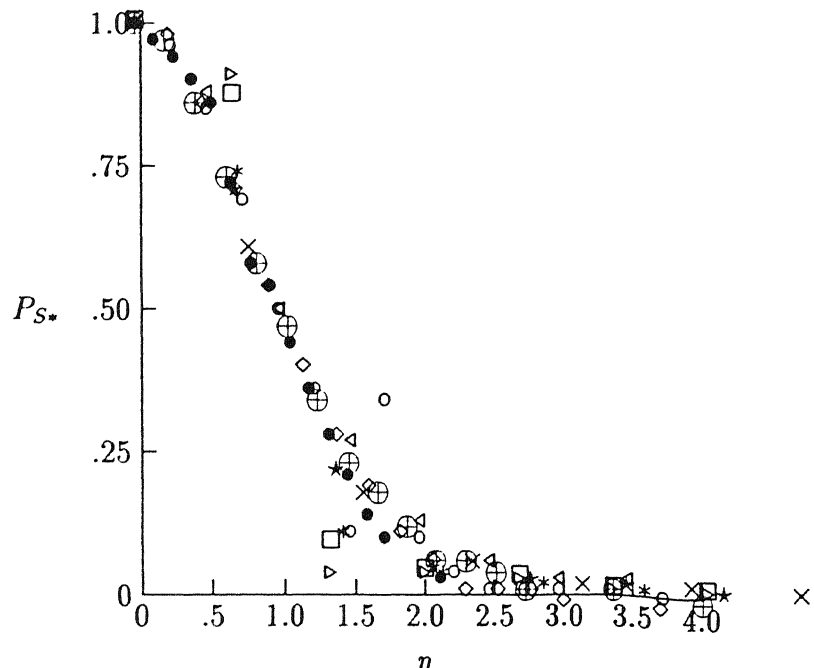


Fig. 8 26 Comparison of wall pressure similarity : $Pr = 1.0 D_w = \times 7.5, \circ 30.0, Pr = 1.2 D_w = * 8.0, \diamond 30.0d, Pr = 1.5 D_w = * 4.0, \triangleleft 15.0, Pr = 2.0 D_w = \square 4.0, \oplus 30.0$, and $Pr = 2.25 D_w = \triangleright 4.0, \bullet 30.0$.

scale by the half pressure width. The free jet field, impinging jet field and wall pressure similarity profiles show normal distribution irrespective of the levels of underexpansion.

8.3 Conclusions

The following conclusions may be drawn from the above analysis.

- The standoff shock of the impinging jet cellular structure moves along the wall as the axial distance between the nozzle-wall is increased. The strength of the standoff shock increases with the level of underexpansion and decreases with increase of nozzle-wall distance.
- The isobars are not only influenced by the cellular wave structure of the potential core in the impinging jet field but also by the interaction of the upstream and downstream reflected pressure waves.
- Complete similarity of the mixing region exists in the impinging jet field.
- The positive wall pressures also exhibit similarity irrespective of the levels of underexpansion.
- The zone of influence of positive pressures has been computed upto 10 % of the settling chamber pressure show near collapse for the levels of underexpansion and correct expansion of sonic jets of the present study. The nature of collapse is similar to that reported for subsonic to correctly expanded sonic impingement.
- The force coefficient for underexpanded jets is slightly lower than that of the sonic jets due to dissipation of the energy through cellular wave structure.

Chapter 9

Oblique Impingement and Surface Visualization

A wall placed obliquely in the freejet field causes the axisymmetric flow field to become three-dimensional and non-axisymmetric. The effect of oblique impingement on the freejet characteristics and the jet field on the wall is studied in this chapter for two inclinations with $\theta = 5$ deg. and 10 deg. . The oblique impinging shock structure of underexpanded jets are visualized using Schlieren technique. The wall surface flow pattern are investigated using surface coating technique.

9.1 Flow visualization

The schematic of oblique impingement of underexpanded jets are sketched in Fig. 9.1 for nozzle-wall distances less than a single cell of the cellular wave structure. As compared to normal impingement the oblique impingement standoff shock is not parallel

to the plate, but is parallel to the nozzle exit plane. The effect of inclination is predominant only in the wall jet region. The wall jet region consists of compression as well as expansion waves reflecting from the solid boundary and the free walljet boundary as reported by Gummer and Hunt [42] and Lamont and Hunt [64].

The cellular shock structure for $\theta = 5$ deg. for different wall spacings and levels of underexpansion are shown in Figs. 9.2 - 9.11. In Figs. 9.2 and 9.3, the cellular structure has been presented for nozzle-wall distance $D_w = 1.0$ and $Pr = 1.5$ and 2.25, respectively. As expected, the results show that the strength of the stand-off shock increases with increase in the underexpansion level. For $Pr = 2.25$, the standoff shock has higher strength compared to $Pr = 1.5$.

In Figs. 9.4 - 9.6, the plate is placed at distance $D_w = 2.0$, which is greater than a single cell length. The stand-off shock moves along with the wall. At higher levels of underexpansion of $Pr = 2.0$, the location of the shock is almost at the end of a single cell. The distances between the plate shock and the wall is relatively higher at $Pr = 2.25$, as clearly seen from the picture.

Figs. 9.7 - 9.9 show the cellular structure when $D_w = 2.5$ and $\theta = 5$. At $Pr = 1.5$, there are two complete cells with the shock close to the wall. With increase of Pr to 2.0, the stand-off shock occurs in the second cell. For further increase of the underexpansion to 2.25, the stand-off shock occurs just after the first cellular structure. That is the stand-off shock moves upwards with increase of Pr . In Figs. 9.10 - 9.11, the wall is kept at $D_w = 4.0$. At $Pr = 1.5$, the plate shock occurs in the fourth cell, whereas at $Pr = 2.0$ the plate shock occurs at the beginning of the third cell. Therefore from these results, it may be summarized that the stand-off shock location is strongly influenced by the wall distance and the level of underexpansion.

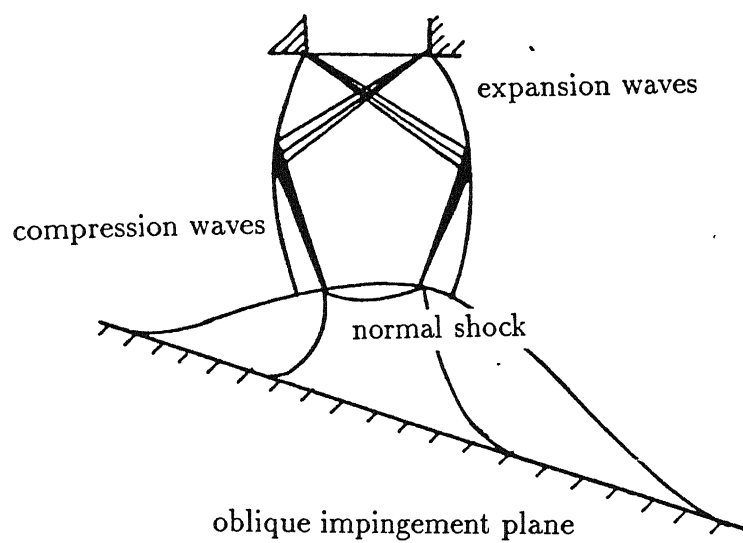


Fig. 9.1 Characteristics features of oblique impinging jets :

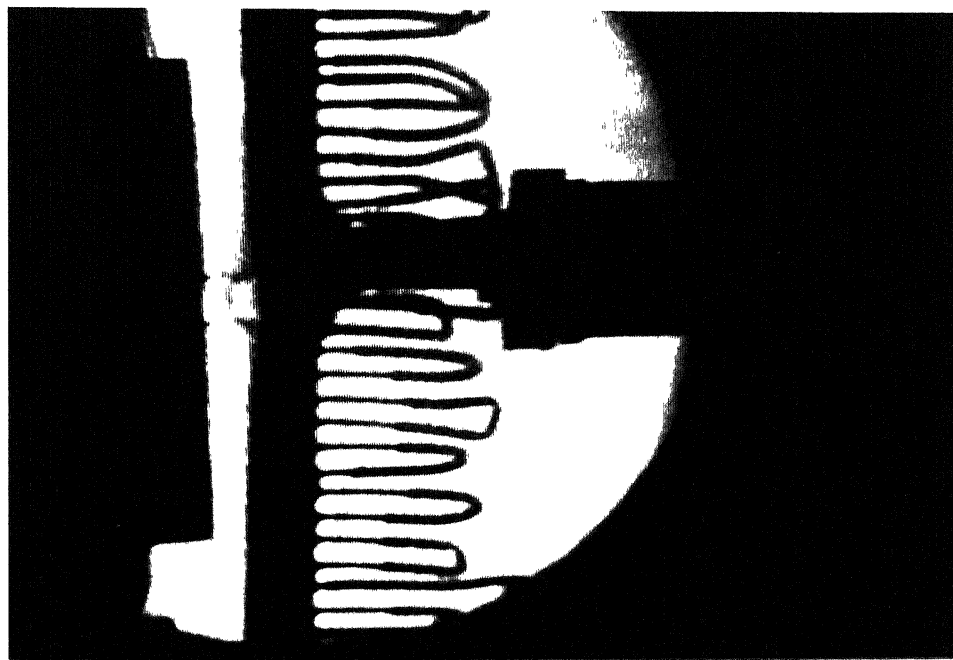


Fig. 9.2 Schlieren photograph of oblique impinging jet $D_w = 1.0$, $\theta = 5$ and $Pr = 1.5$

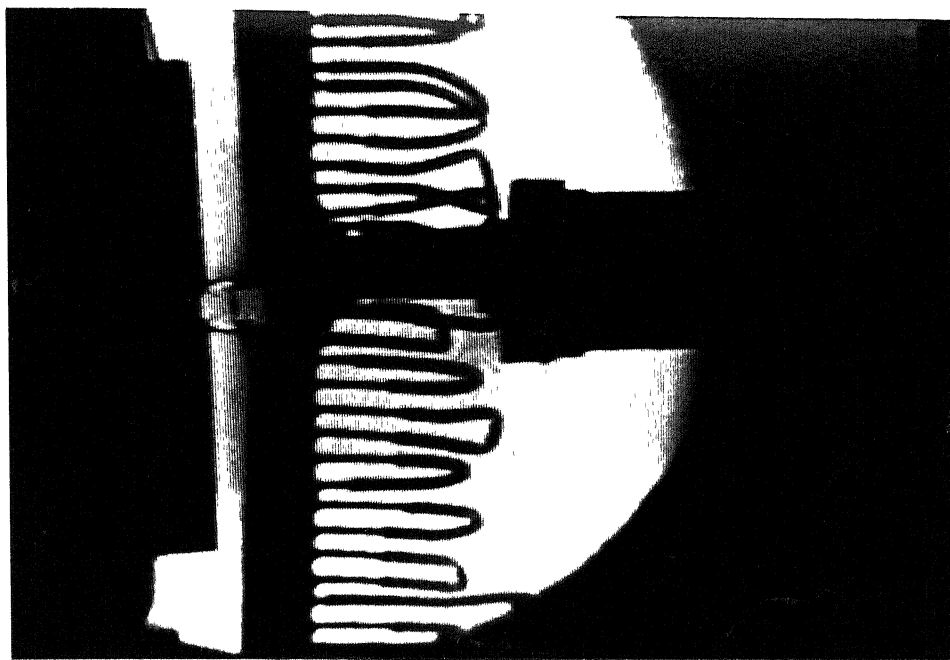


Fig. 9.3 Schlieren photograph of oblique impinging jet $D_w = 1.0$, $\theta = 5$ and $Pr = 2.25$

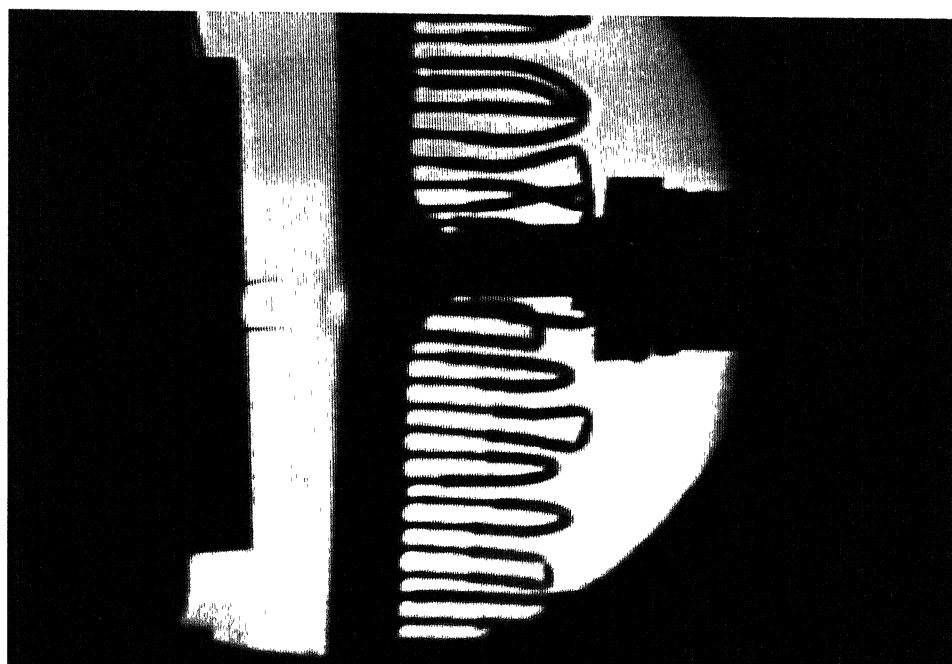


Fig. 9.4 Schlieren photograph of oblique impinging jet $D_w = 2.0$, $\theta = 5$ and $Pr = 1.2$

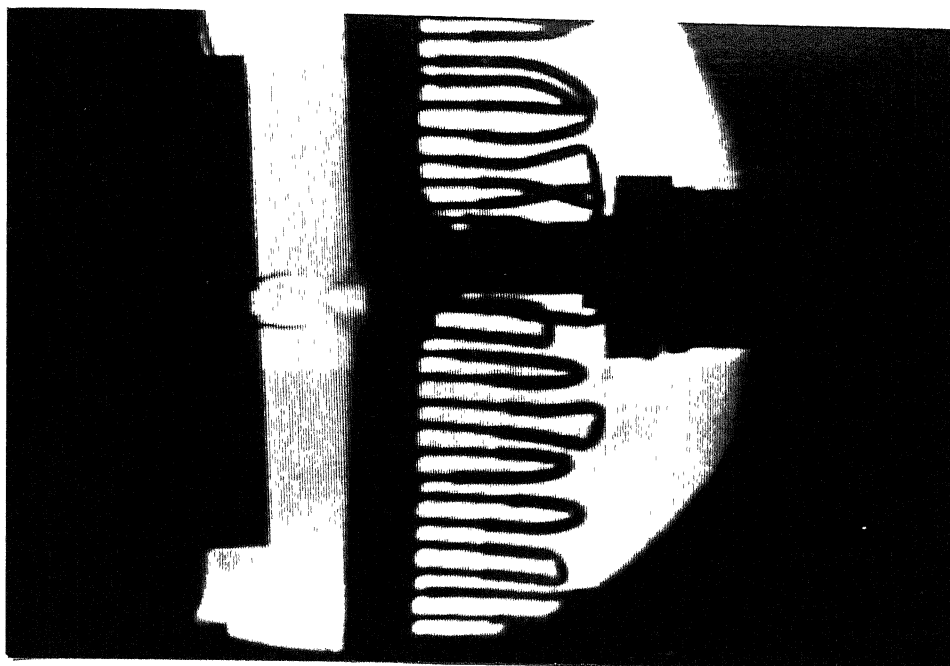


Fig. 9.5 Schlieren photograph of oblique impinging jet $D_w = 2.0$, $\theta = 5$ and $Pr = 1.5$

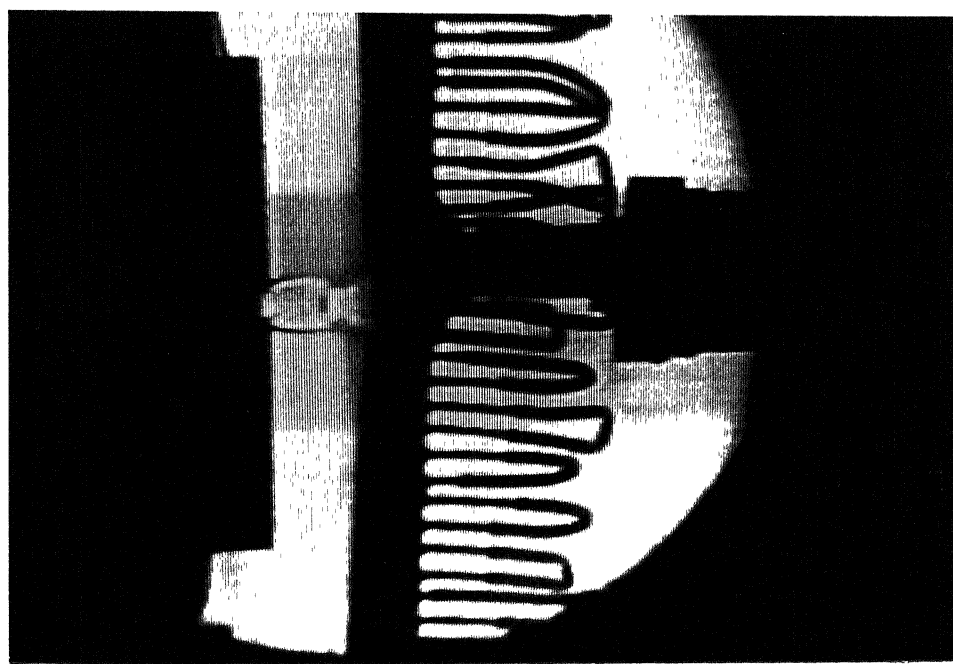


Fig. 9.6 Schlieren photograph of oblique impinging jet $D_w = 2.0$, $\theta = 5$ and $Pr = 2.0$

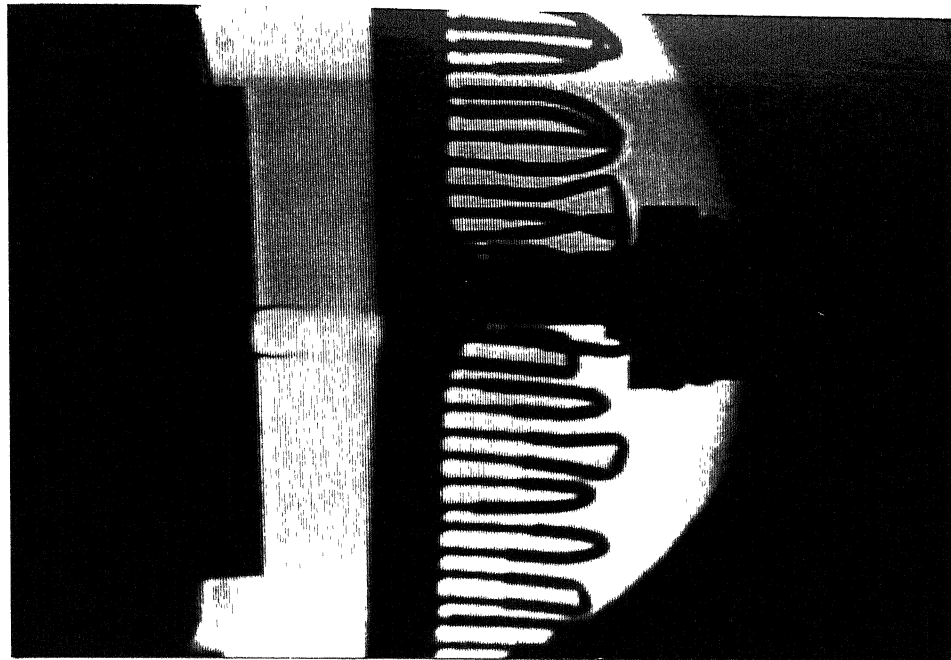


Fig. 9.7 Schlieren photograph of oblique impinging jet $D_w = 2.5$, $\theta = 5$ and $Pr = 1.2$

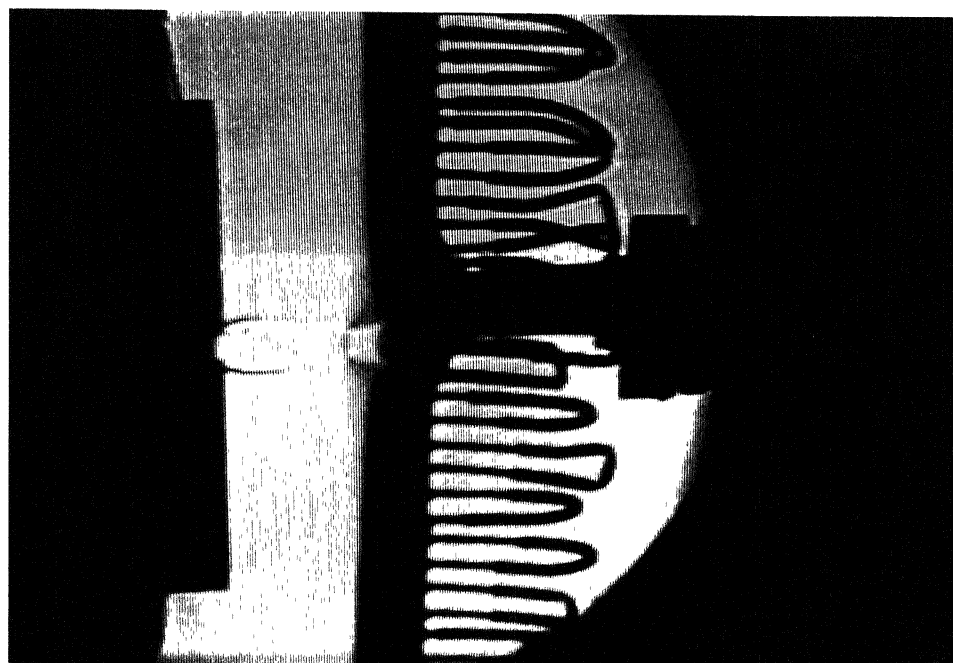


Fig. 9.8 Schlieren photograph of oblique impinging jet $D_w = 2.5$, $\theta = 5$ and $Pr = 2.0$

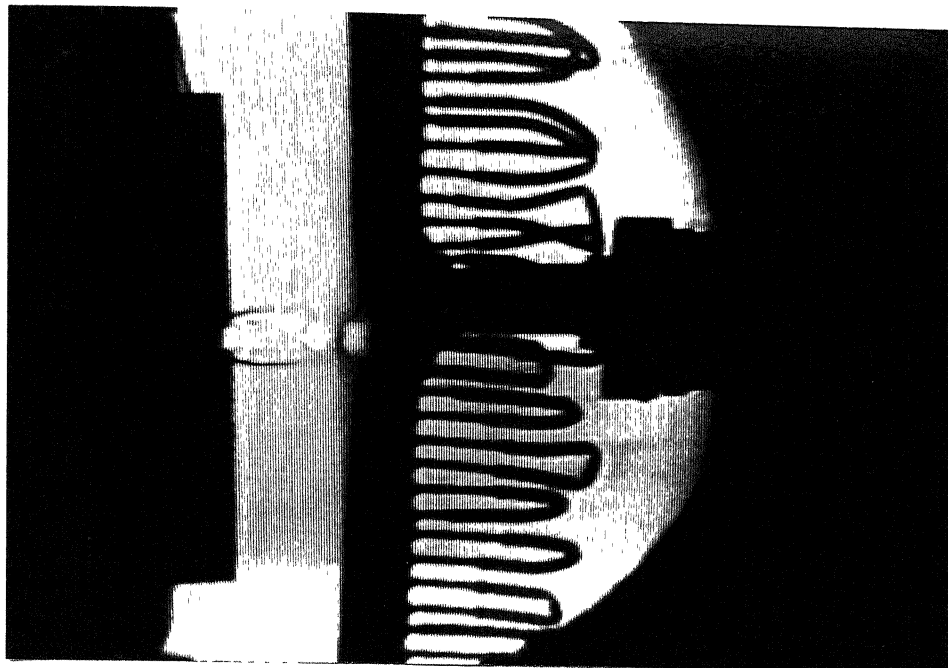


Fig. 9.9 Schlieren photograph of oblique impinging jet $D_w = 2.5$, $\theta = 5$ and $Pr = 2.25$

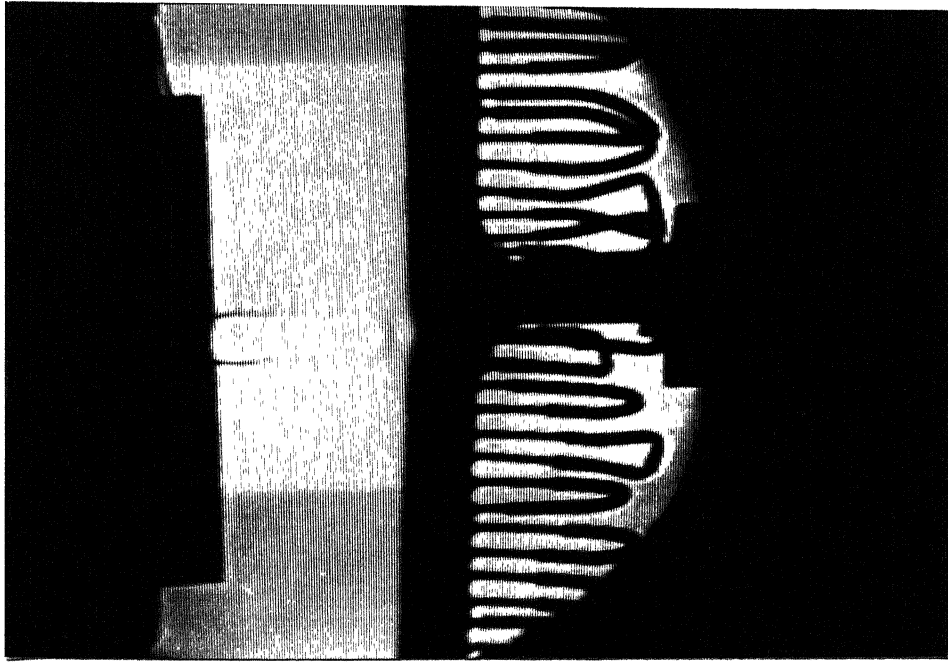


Fig. 9.10 Schlieren photograph of oblique impinging jet $D_w = 4.0$, $\theta = 5$ and $Pr = 2.0$

The Schlieren photographs for inclination $\theta = 10$ deg. has been presented from Figs. 9.12 to 9.25 for different combinations of Pr and D_w . From these results, it is once again seen clearly that for oblique impingement the stand-off shock is parallel to the nozzle exit and not the plate. However, the walljet flow field is significantly influenced by θ clearly setting an asymmetry about the jet axis. Further the stand-off shock location is also considerably influenced by D_w and Pr similar to the results seen with $\theta = 5$ degree. Even though the wave cell just above the wall is influenced by the presence of the wall, the cells upstream of that adjacent to the wall are not influenced significantly by D_w , but the level of underexpansion has got a decisive effect on the size of the cell and strength of the waves for all values of D_w and θ .

9.2 Impinging jet field

9.2.1 Spread characteristics

The spread characteristics of the impinging jet field when the wall is placed at an angle is investigated in this section. In Fig. 9.26, the half pressure spread is presented at various locations in the impinging jet field with wall at $D_w = 5$, $\theta = 5$ deg. for jet at $M_e = 0.6$. From this figure, it is seen that at $\theta = 5$ deg. and $M_e = 0.6$, even though the asymmetry in the spread is set in, it is only marginal.

In Fig. 9.27, the half pressure spread width has been compared for various stagnation pressure with $D_w = 5$, $\theta = 5$ and at an axial location of $x/d = 4$ in the impinging jet field. From this figure, it is seen that the level of settling chamber pressure has got significant effect on the half width of the impinging jet field.

The spread is lower for higher initial stagnation pressure as compared to the lower

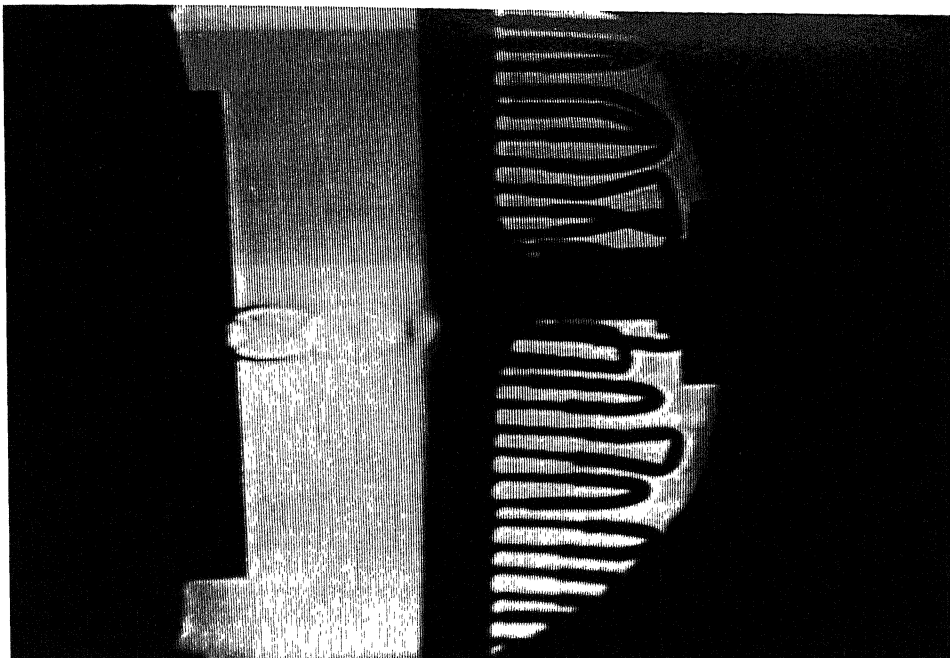


Fig. 9.11 Schlieren photograph of oblique impinging jet $D_w = 4.0$, $\theta = 5$ and $Pr = 2.0$

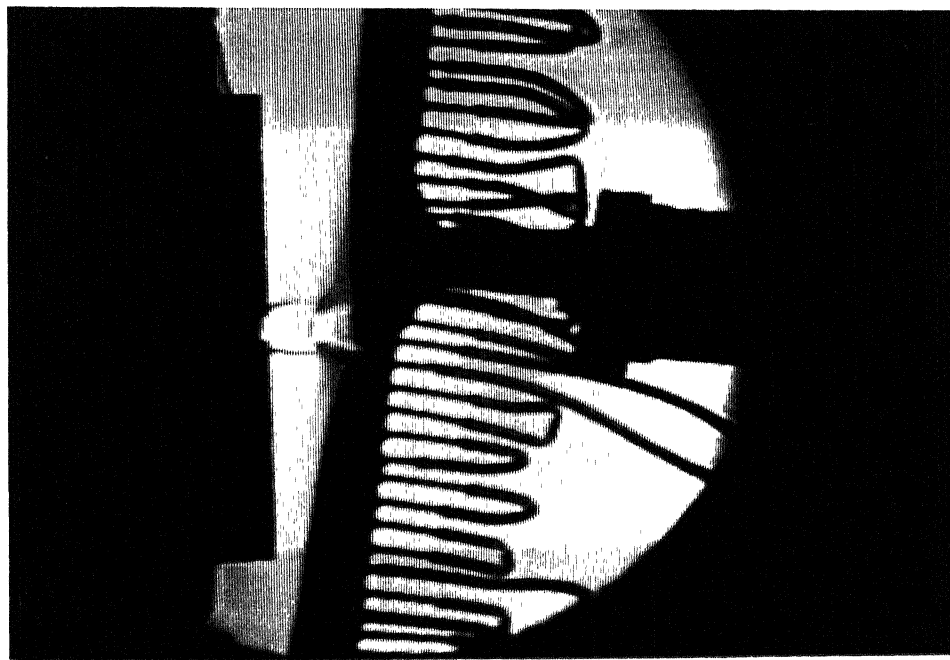


Fig. 9.12 Schlieren photograph of oblique impinging jet $D_w = 1.5$, $\theta = 10$ and $Pr = 2.25$

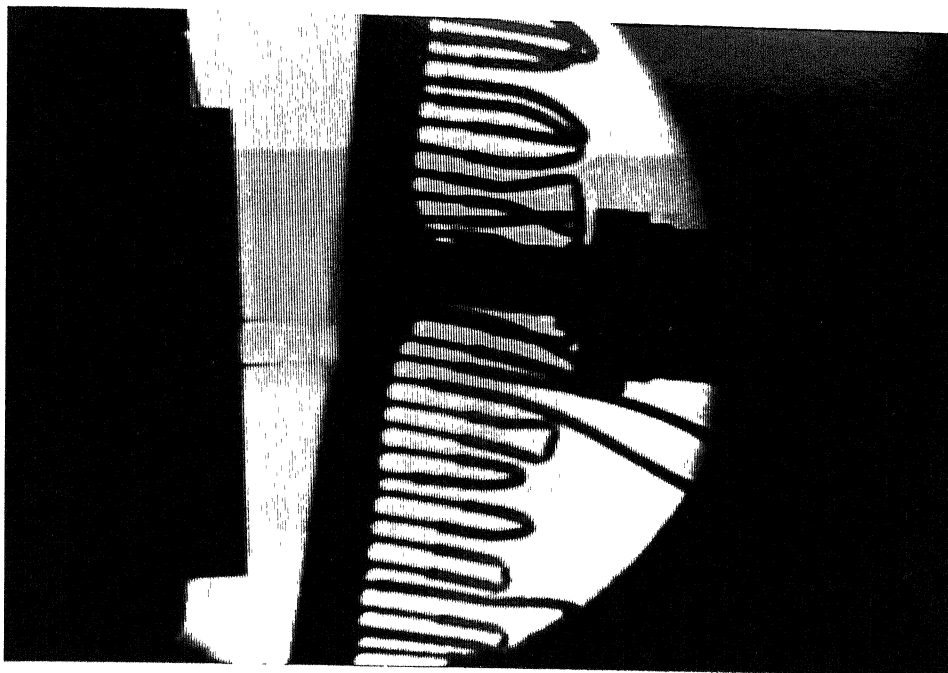


Fig. 9.13 Schlieren photograph of oblique impinging jet $D_w = 2.0$, $\theta = 10$ and $Pr = 1.2$

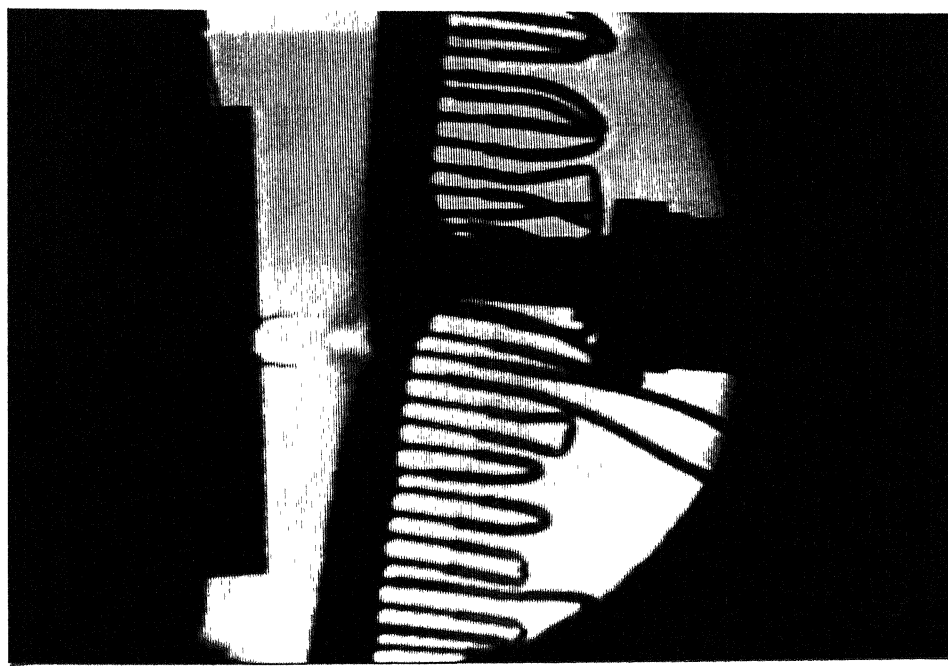


Fig. 9.14 Schlieren photograph of oblique impinging jet $D_w = 2.0$, $\theta = 10$ and $Pr = 1.5$

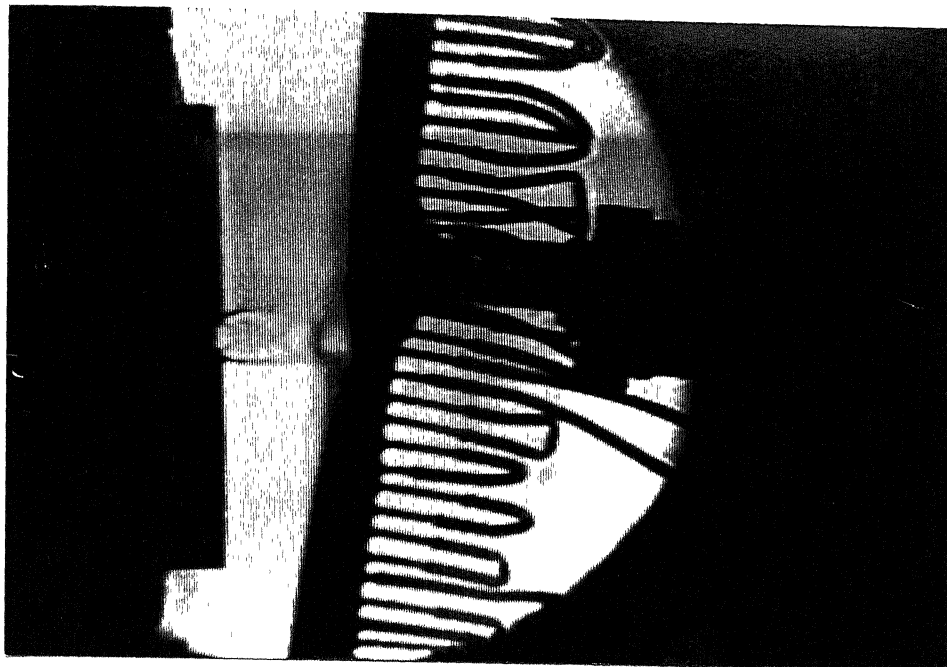


Fig. 9.15 Schlieren photograph of oblique impinging jet $D_w = 2.0$, $\theta = 10$ and $Pr = 2.0$

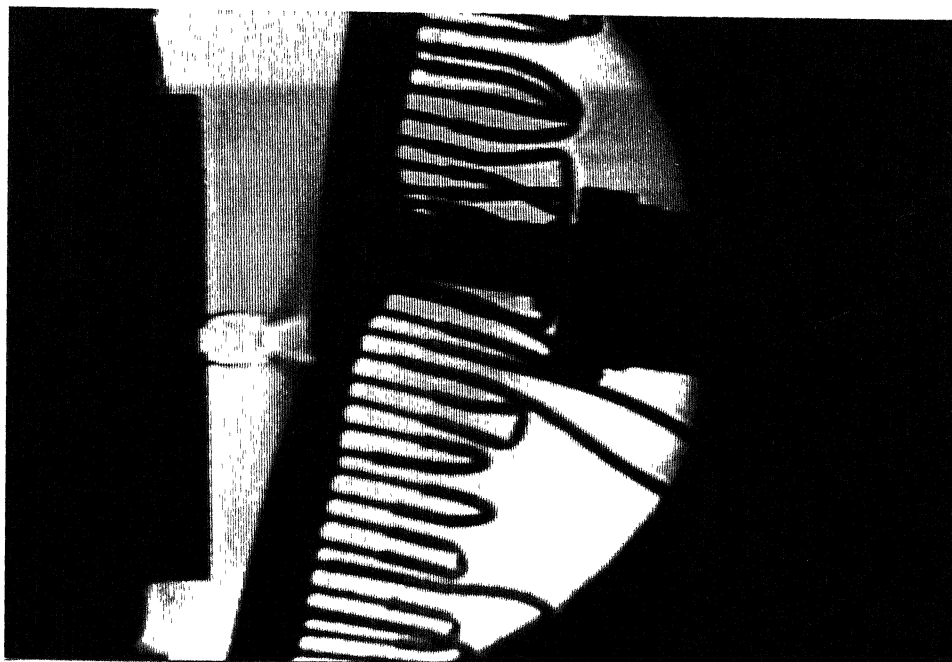


Fig. 9.16 Schlieren photograph of oblique impinging jet $D_w = 2.0$, $\theta = 10$ and $Pr = 2.25$

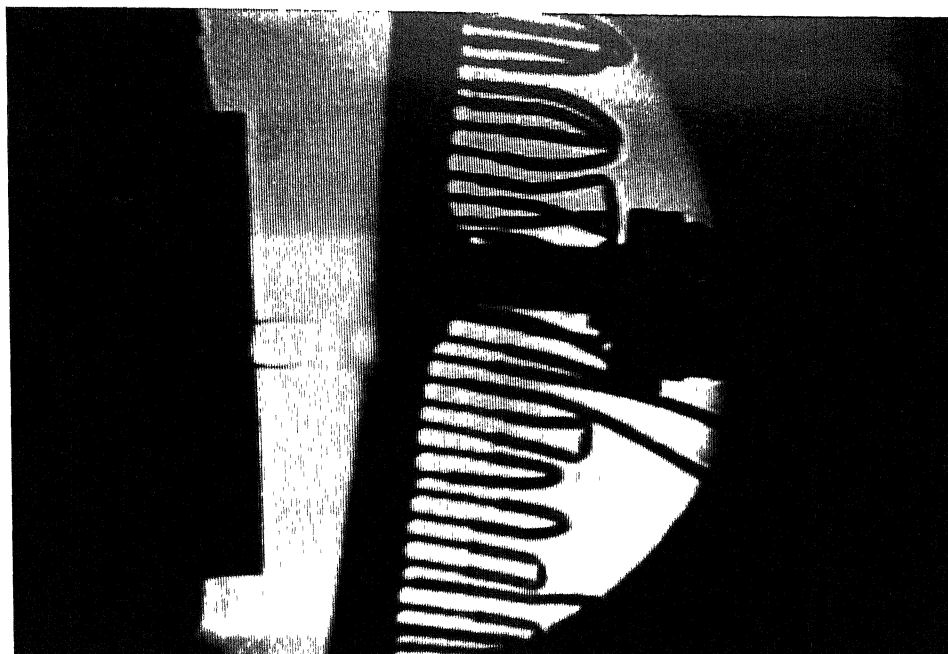


Fig. 9.17 Schlieren photograph of oblique impinging jet $D_w = 2.5$, $\theta = 10$ and $Pr = 1.2$

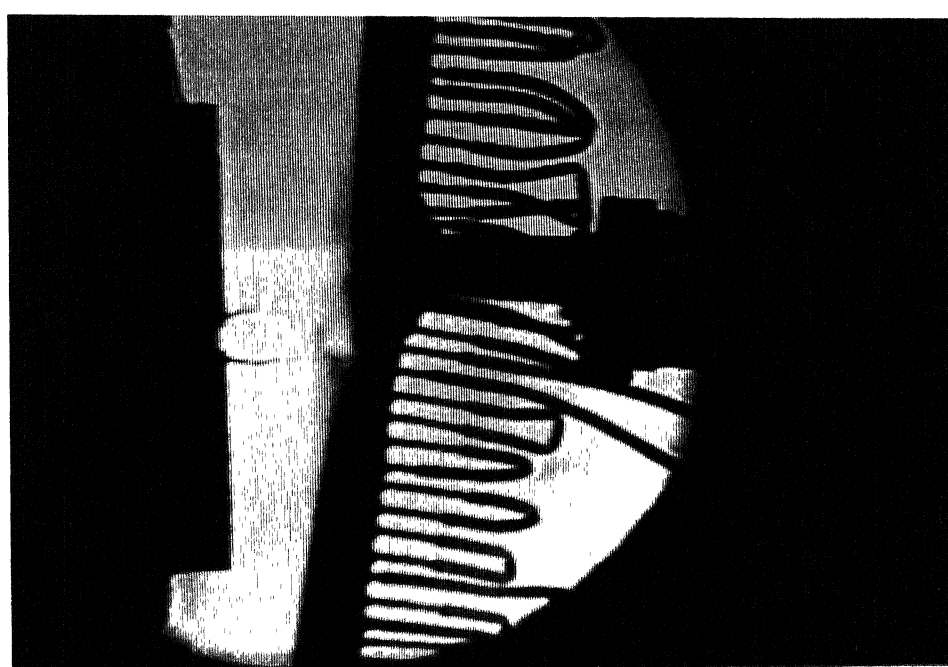


Fig. 9.18 Schlieren photograph of oblique impinging jet $D_w = 2.5$, $\theta = 10$ and $Pr = 1.5$

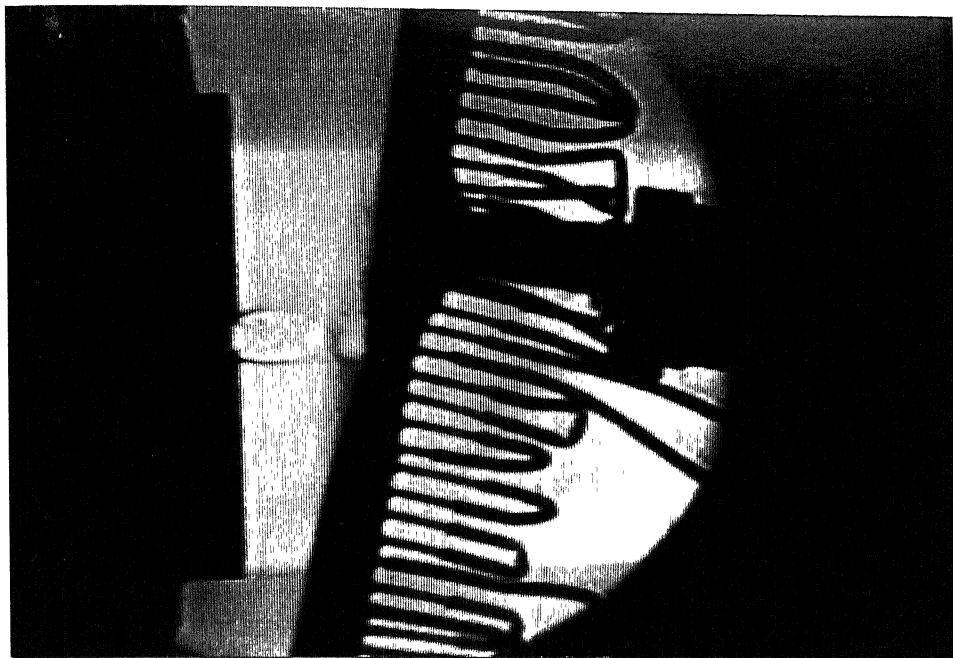


Fig. 9.19 Schlieren photograph of oblique impinging jet $D_w = 2.5$, $\theta = 10$ and $Pr = 2.0$

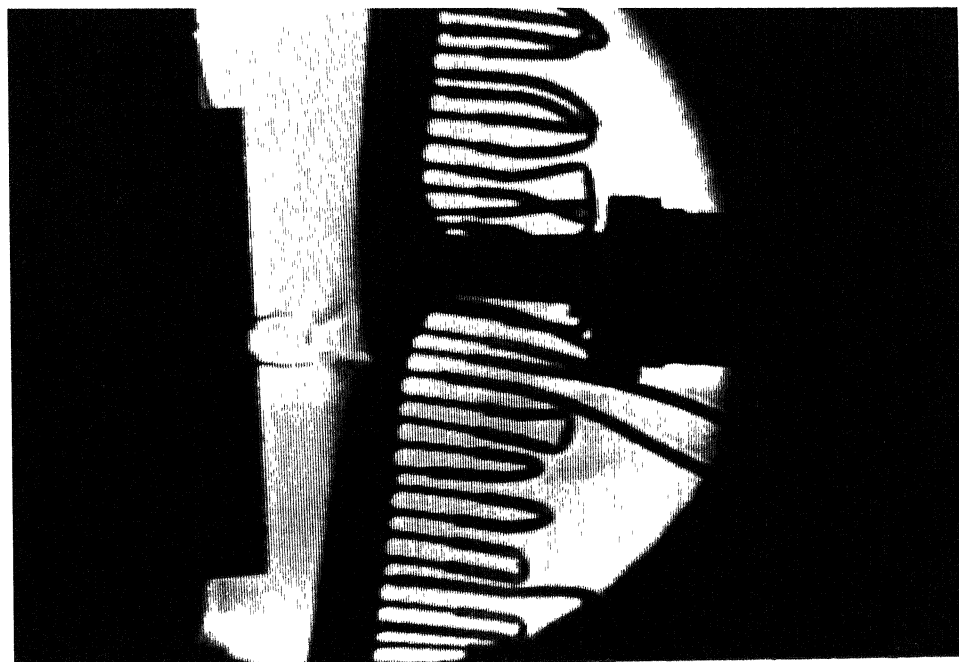


Fig. 9.20 Schlieren photograph of oblique impinging jet $D_w = 2.5$, $\theta = 10$ and $Pr = 2.25$

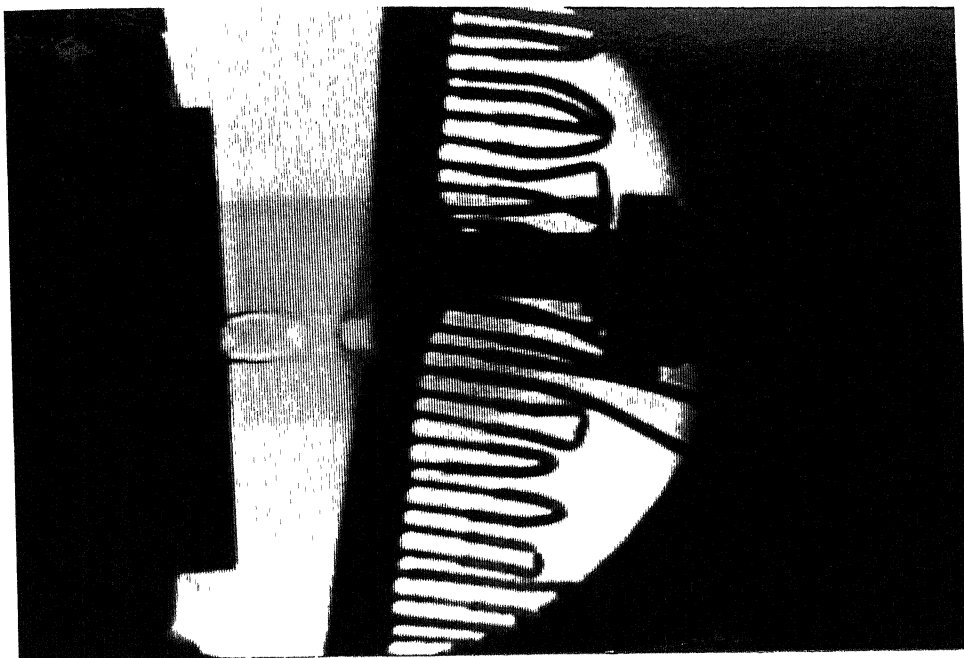


Fig. 9.21 Schlieren photograph of oblique impinging jet $D_w = 3.0$, $\theta = 10$ and $Pr = 1.5$

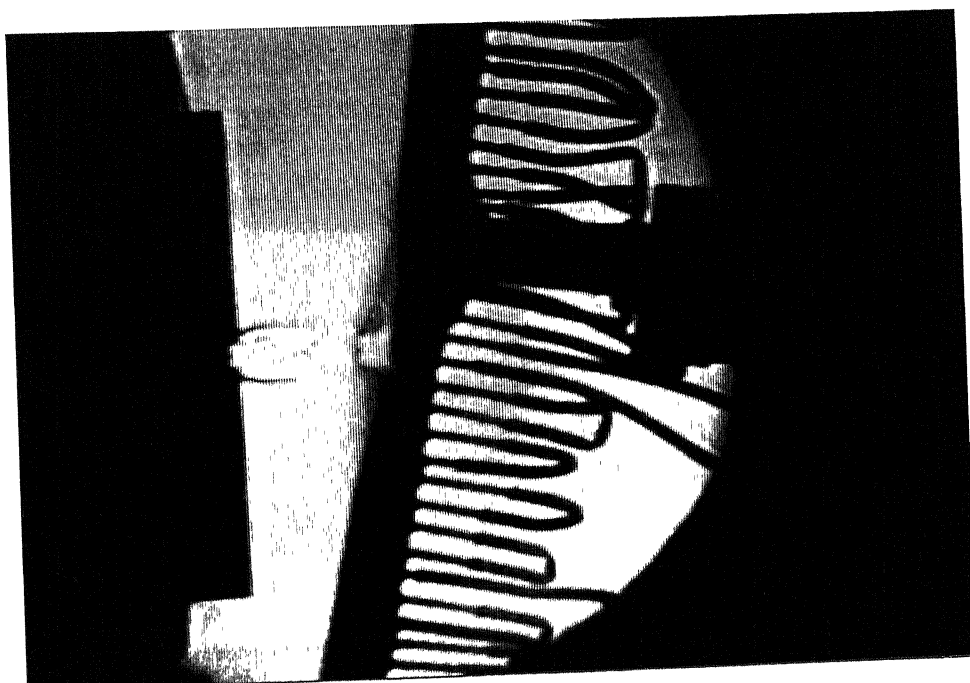


Fig. 9.22 Schlieren photograph of oblique impinging jet $D_w = 3.0$, $\theta = 10$ and $Pr = 2.0$

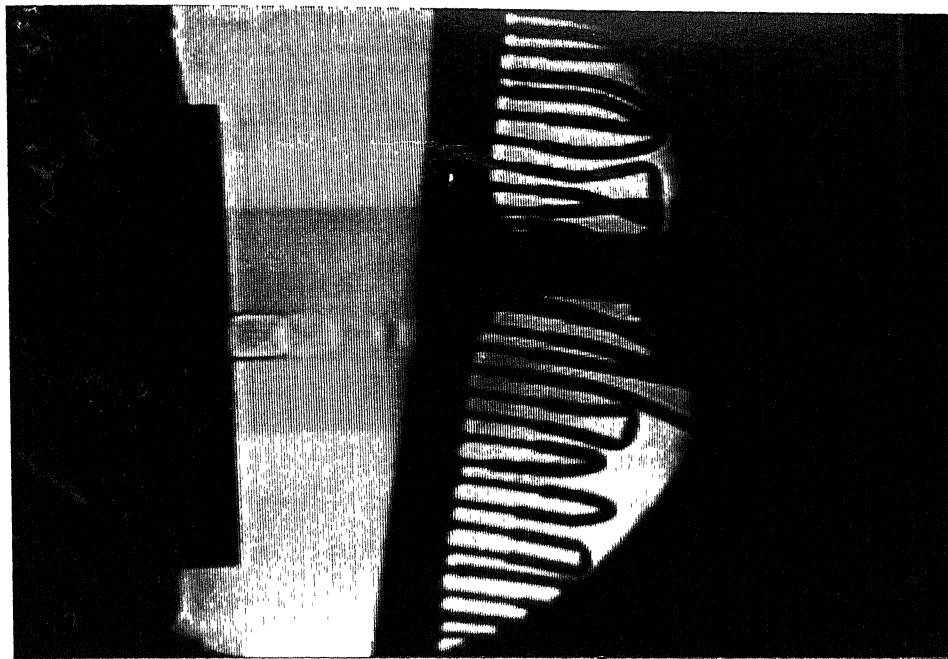


Fig. 9.23 Schlieren photograph of oblique impinging jet $D_w = 4.0$, $\theta = 10$ and $Pr = 1.5$

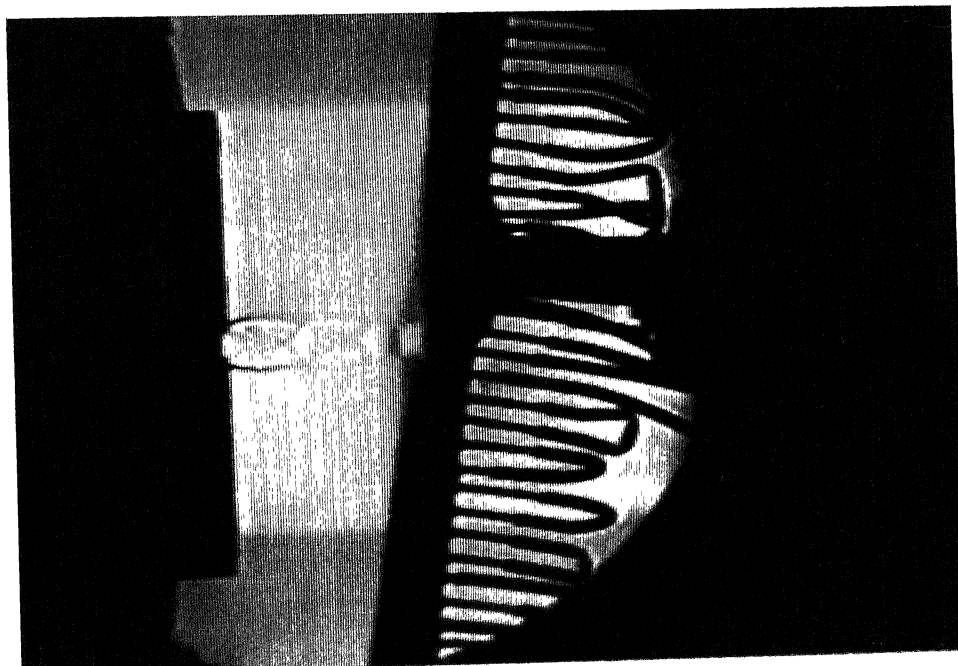


Fig. 9.24 Schlieren photograph of oblique impinging jet $D_w = 4.0$, $\theta = 10$ and $Pr = 2.0$

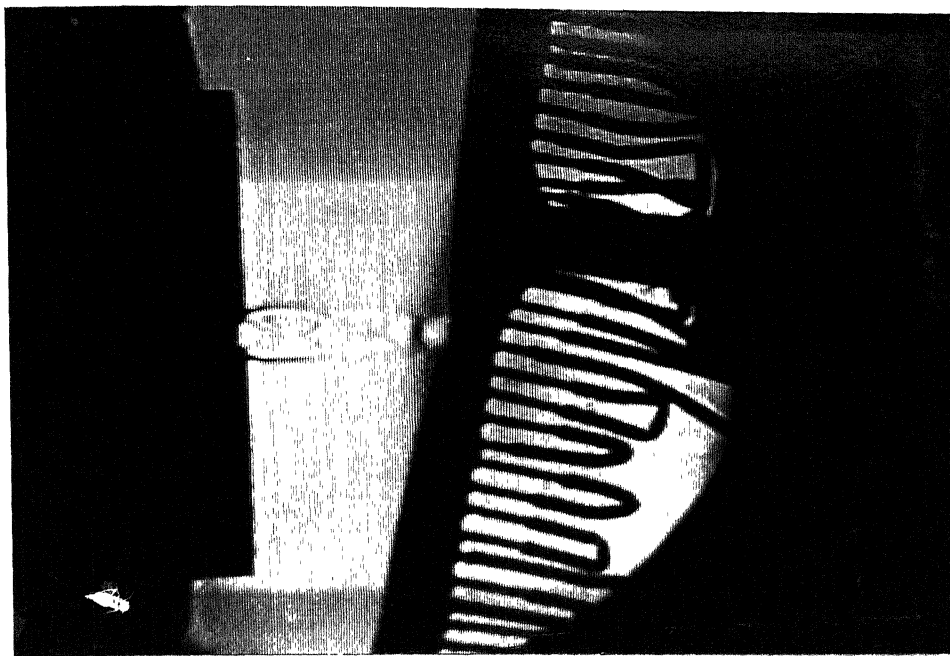


Fig. 9.25 Schlieren photograph of oblique impinging jet $D_w = 4.0$, $\theta = 10$ and $Pr = 2.25$

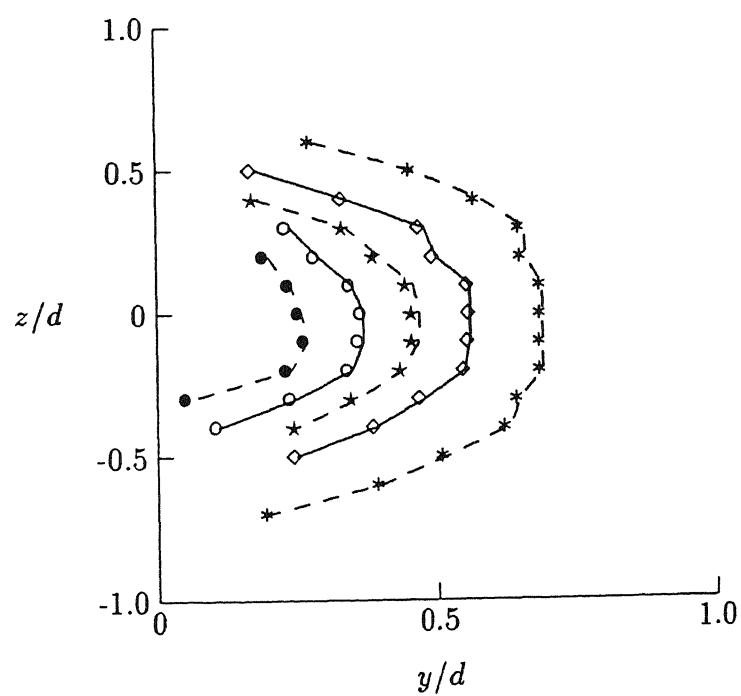


Fig. 9.26 Fraction of spreads at $x = 4d$ with wall at $D_w = 5$ and $\theta = 5$: $b = \bullet 0.90, \circ 0.70, \star 0.50, \diamond 0.30$ and $* 0.10$. $M_e = 0.6$

pressure potential. In Fig. 9.28, the spread fractions of the centre line has been presented for jet Mach number $M_e = 1.0$ at $x/d = 4$ in the impinging jet field with $D_w = 5$ and $\theta = 5$. As described earlier, the spread in the lower half is larger and the effect of asymmetry of the impinging jet field is also evident from this figure. In Fig. 9.29, comparison of the spread fractions are presented for three values of the stagnation pressure. Higher stagnation pressure has lower spread for all the fractions as compared to lower stagnation pressure as seen from the results. As the angle of impingement is increased from $\theta = 5$ deg. to 10 deg. the regular pattern of the pressure fraction is altered as seen from Fig. 9.30. It is interesting to learn from these figures that the disturbance waves generated by the plate kept oblique to the jet axis were in a position to set asymmetry to the jet field at every axial location between the nozzle exit and the wall. This is perfectly reflected in Figs. 9.29 to 9.32. From these results it is once again seen that even for the farfield oblique impingement the asymmetry prevails.

9.2.2 Wall surface pressure distribution

The wall half pressure width, defined as half of the positive wall pressure peak, has been compared in Figs. 9.33 and 9.34 for pressure ratios P_* . From both these figures it is clear, that the portion of the wall close to the jet exit (-ve z) causes greater spread of the positive wall pressures, as compared to the portion of the wall away (+ve z) from the nozzle exit. In Figs. 9.35 - 9.42 the wall surface distribution for two degrees of inclination, and various nozzle-wall location has been presented. The effect of inclination is evident from the asymmetric distribution of the wall pressure seen from these figures. Similarity of the wall pressure field for different combinations of the parameters of the present experimental investigation are shown in Figs. 9.43 to

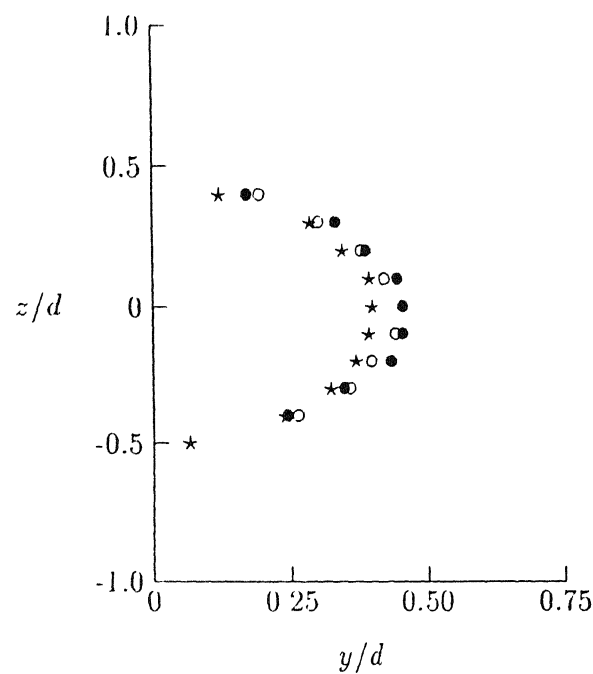


Fig. 9.27 Comparison of half pressure width in the impinging jet field with wall at $D_w = 5$
 \circ with $\theta = 5$ at $x = 4.0d$ • $M_e = 0.6$, o $M_e = 1.0$, * $Pr = 1.5$.

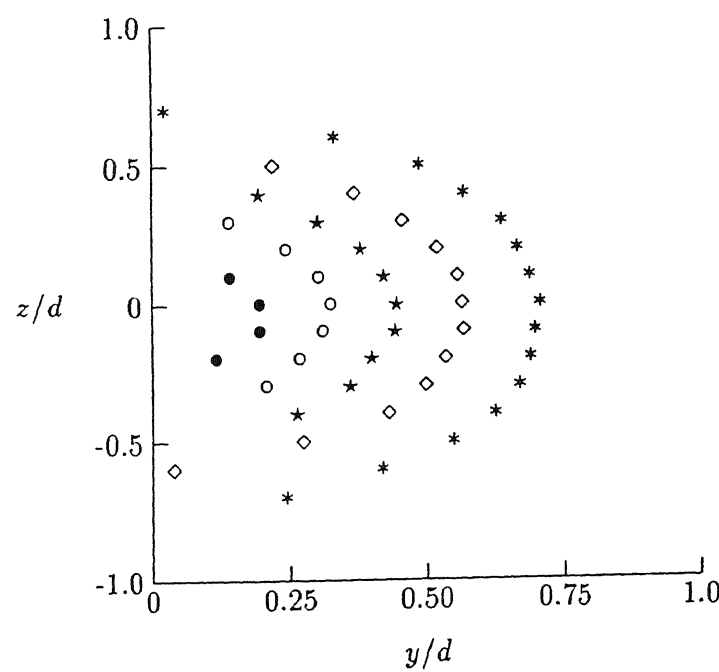


Fig. 9.28 Fraction of centre spread near the wall at $x = 4$, $D_w = 5$ $\theta = 5$ and $M_e = 1.0$ •
 0.90 , o 0.70 , * 0.50 , ◊ 0.30 , * 0.10 .

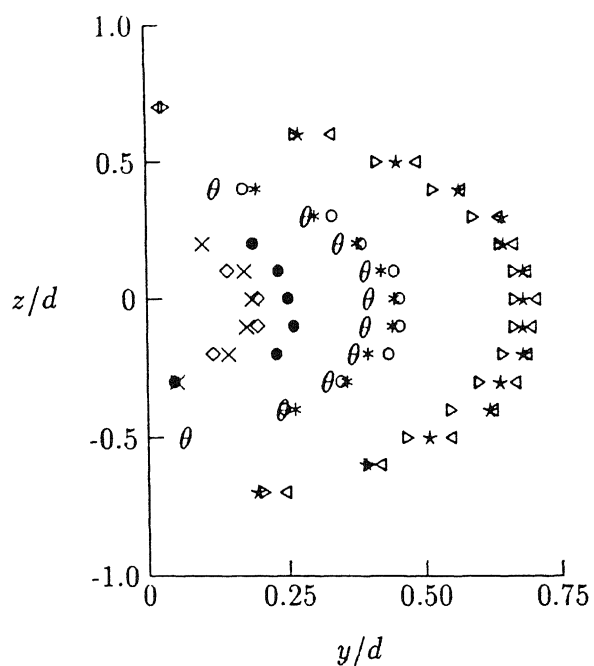


Fig. 9.29 Comparison of fractions of pressure widths in the impinging jet field with wall at $D_w = 5$, $x = 4d$ and $\theta = 5$ for $M_e = 0.6$: $b = \bullet 0.90$, $\circ 0.50$, $\star 0.10$, for $M_e = 1.0$: $b = \diamond 0.90$, $* 0.50$, $\triangleleft 0.10$, for $Pr = 1.5$: $b = \times 0.90$, $\theta 0.50$, $\triangleright 0.10$.

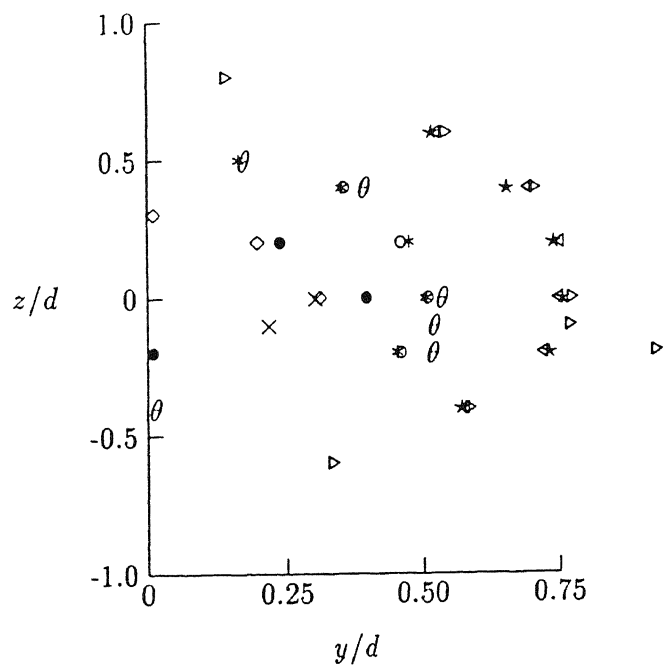


Fig. 9.30 Comparison of fractions of pressure widths in the impinging jet field with wall at $D_w = 5$, $x = 3.5d$ and $\theta = 10$ for $M_e = 0.6$: $b = \bullet 0.90$, $\circ 0.50$, $\star 0.10$, for $M_e = 1.0$: $b = \diamond 0.90$, $* 0.50$, $\triangleleft 0.10$, for $Pr = 1.5$: $b = \times 0.90$, $\theta 0.50$, $\triangleright 0.10$.

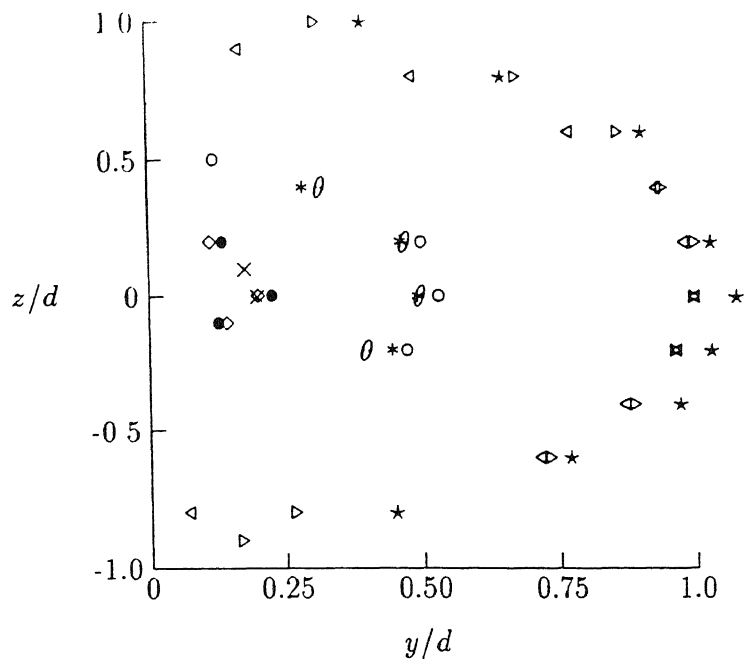


Fig. 9.31 Comparison of fractions of pressure widths in the impinging jet field with wall at $D_w = 5$, $x = 3.5d$ and $\theta = 10$ for $M_e = 0.6$: $b = \bullet 0.90, \circ 0.50, \star 0.10$, for $M_e = 1.0$: $b = \diamond 0.90, *$ 0.50, $\triangleleft 0.10$, for $Pr = 1.5$: $b = \times 0.90, \theta 0.50, \triangleright 0.10$.

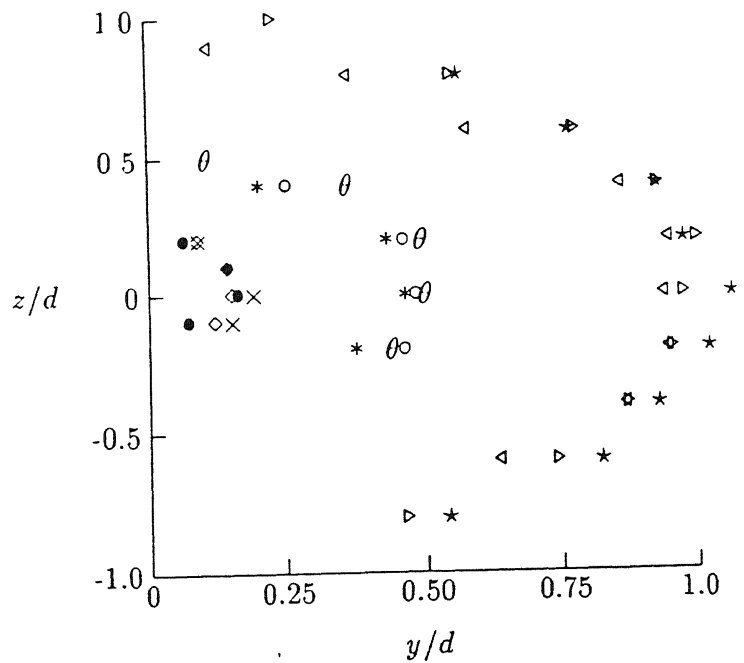


Fig. 9.32 Comparison of fractions of pressure widths in the impinging jet field with wall at $D_w = 10$, $x = 8.0d$ and $\theta = 10$ for $M_e = 0.6$: $b = \bullet 0.90, \circ 0.50, \star 0.10$, for $M_e = 1.0$: $b = \diamond 0.90, *$ 0.50, $\triangleleft 0.10$, for $Pr = 1.5$: $b = \times 0.90, \theta 0.50, \triangleright 0.10$.

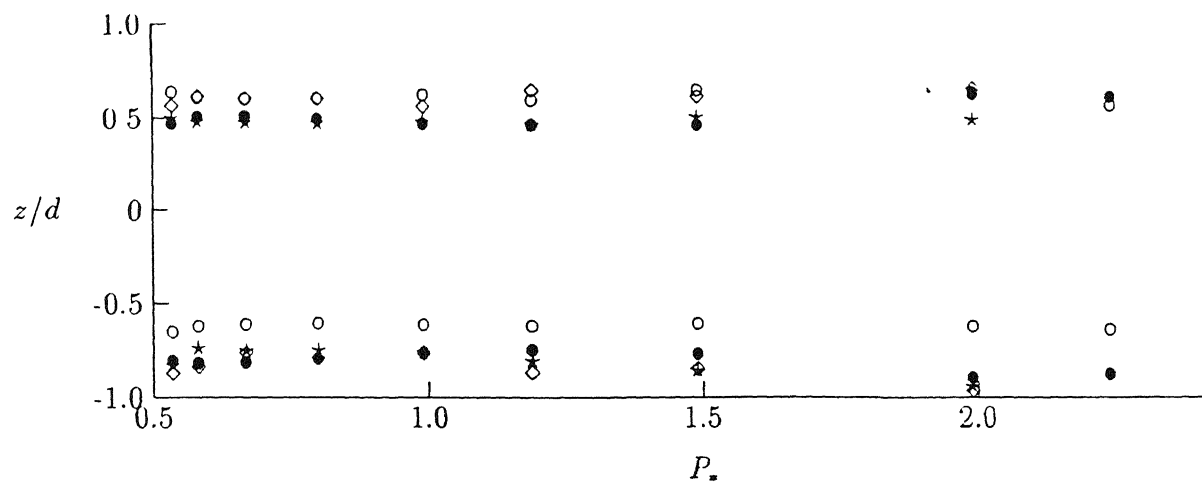


Fig. 9.33 Wall half pressure width for various settling chamber pressure conditions : $\theta = 5, \bullet 2.5, \circ 5.0, \star 7.5$ and $\diamond 10.0$.

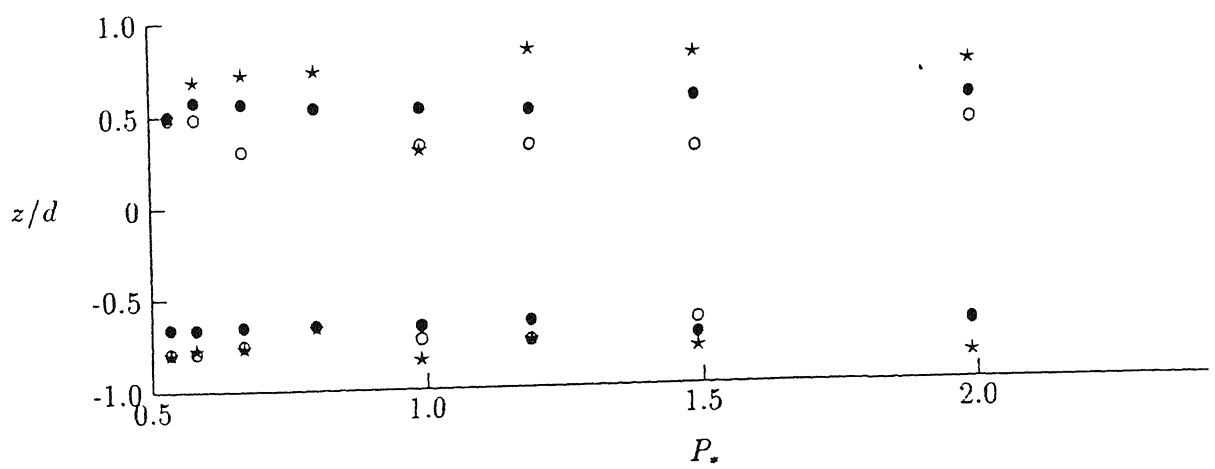


Fig. 9.34 Wall half pressure width for various settling chamber pressure conditions : $\theta = 10, \bullet 2.5, \circ 5.0, \star 7.5$ and $\diamond 10.0$.

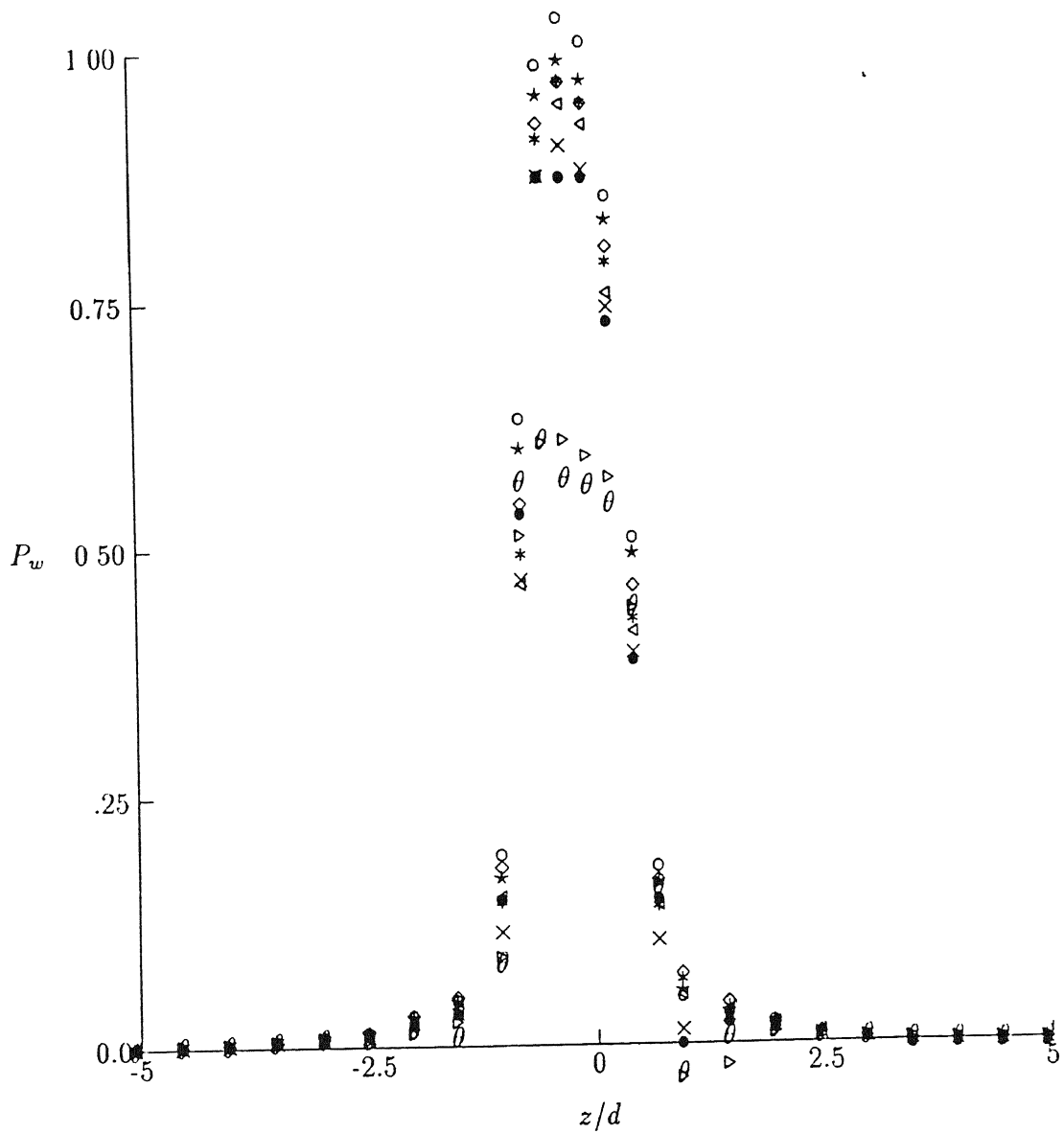


Fig. 9.35 Wall pressure distribution : $\theta = 5$, $D_w = 2.5$, $\diamond M_e = 0.8$, $*$ $M_e = 1.0$, \circ $Pr = 1.2$, \times $Pr = 1.5$.

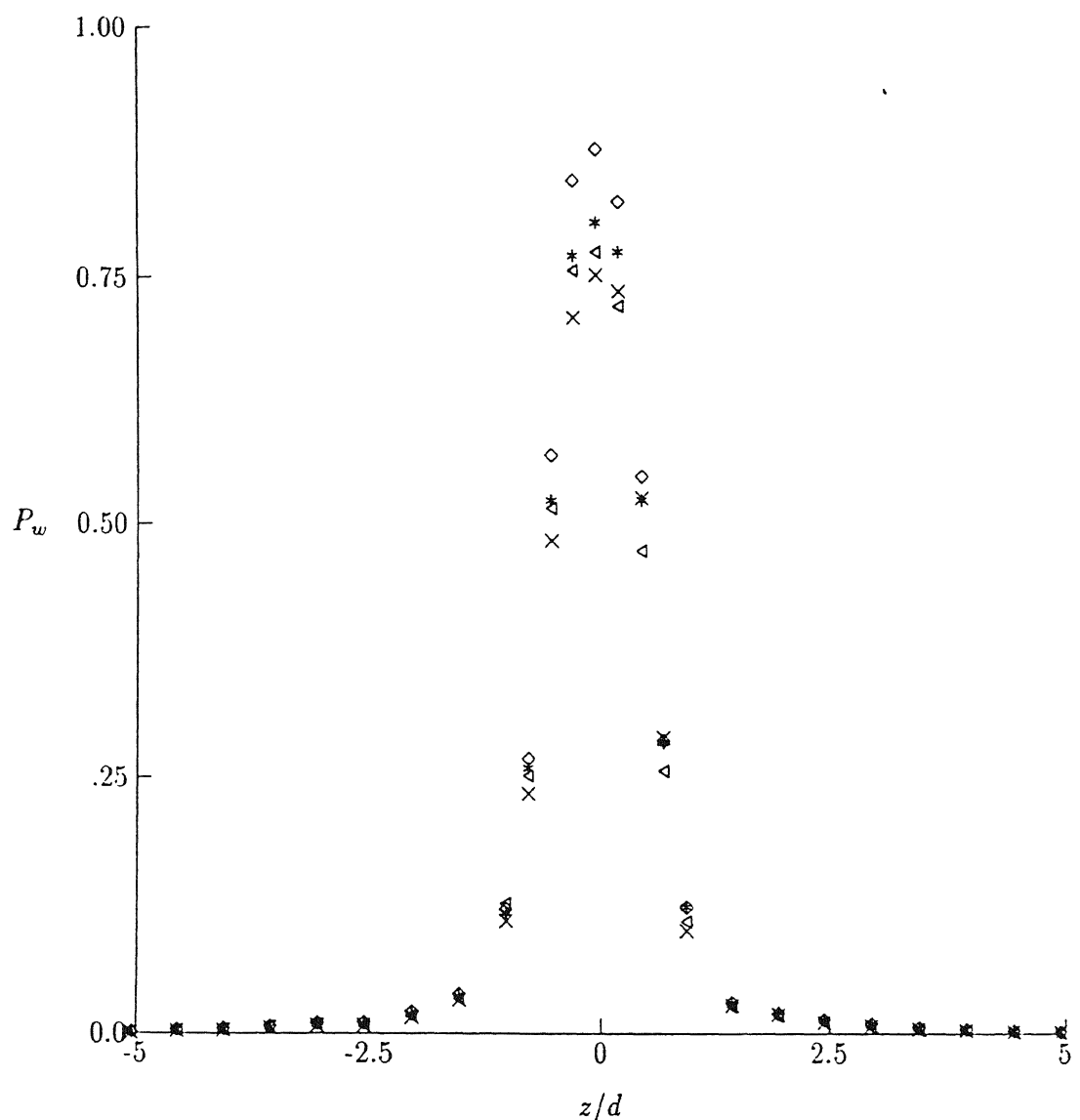


Fig. 9.36 Wall pressure distribution : $\theta = 5$, $D_w = 5.0$, $\diamond M_e = 0.8$, $*$ $M_e = 1.0$, \triangleleft $Pr = 1.2$, \times $Pr = 1.5$.

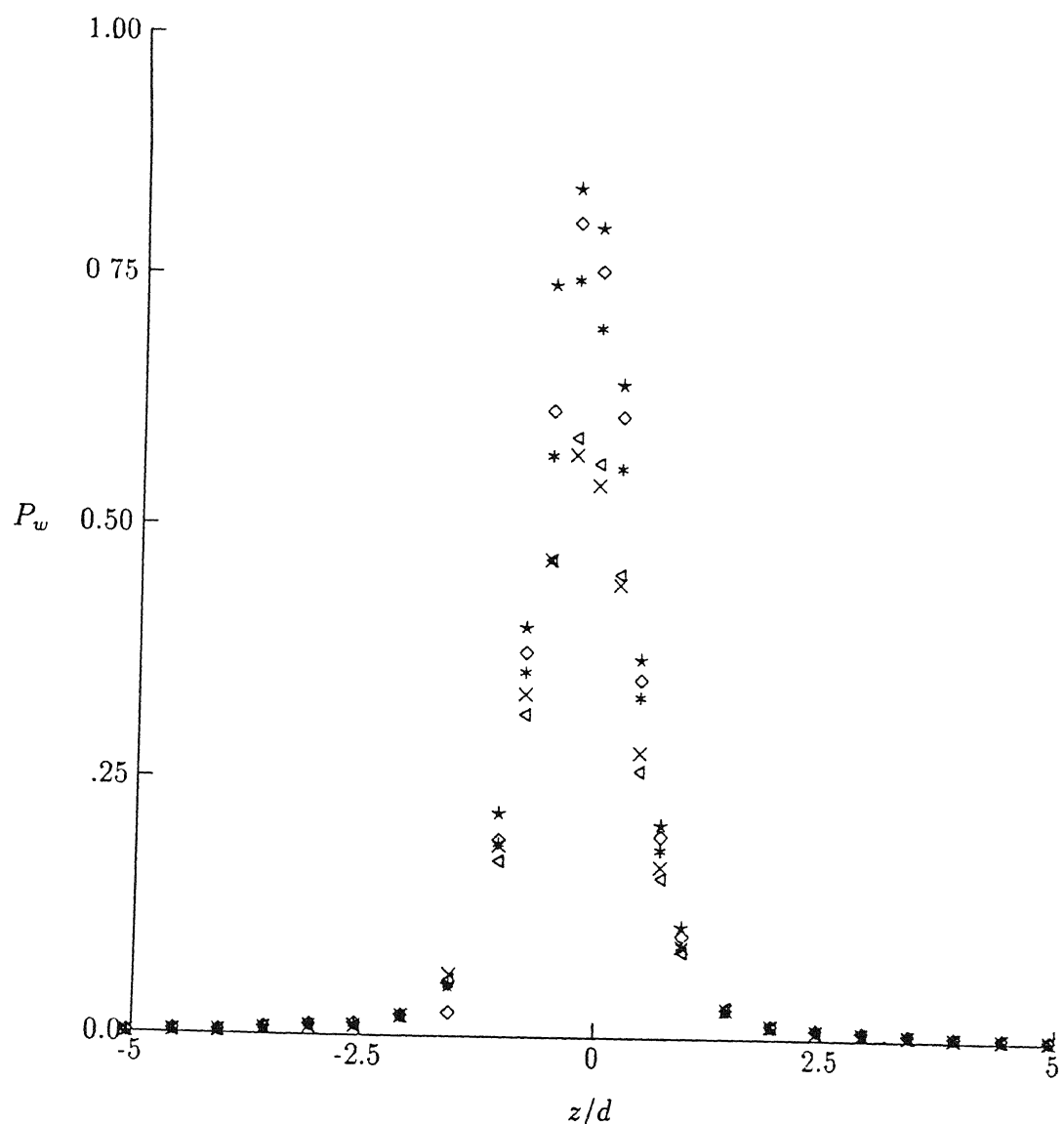


Fig. 9.37 Wall pressure distribution : $\theta = 5$, $D_w = 7.5$, $\diamond M_e = 0.8$, $*$ $M_e = 1.0$, \triangleleft $Pr = 1.2$, \times $Pr = 1.5$.

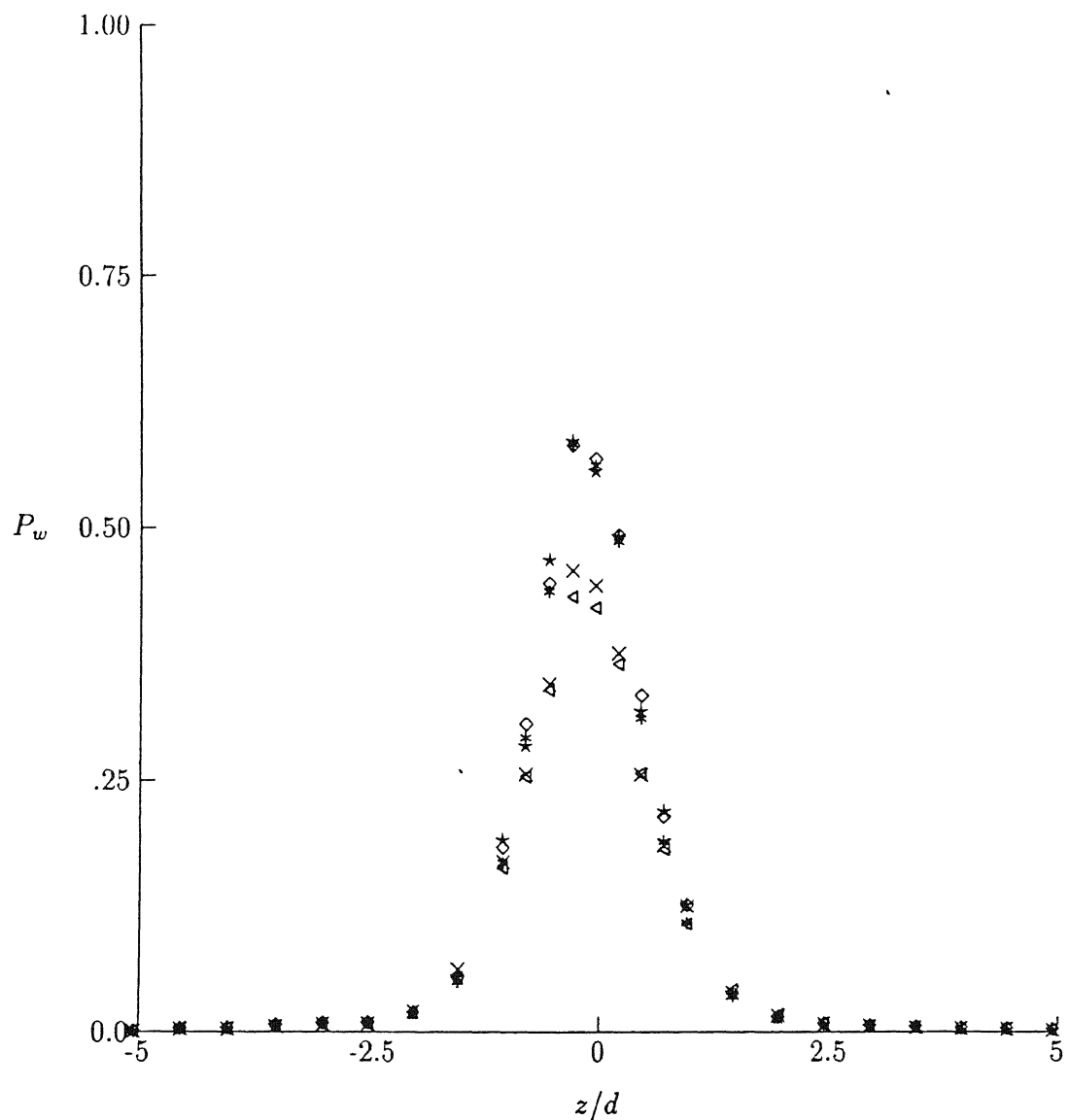


Fig. 9.38 Wall pressure distribution : $\theta = 5$, $D_w = 10.0$, $\diamond M_e = 0.8$, $*$ $M_e = 1.0$, \triangleleft $Pr = 1.2$, \times $Pr = 1.5$.

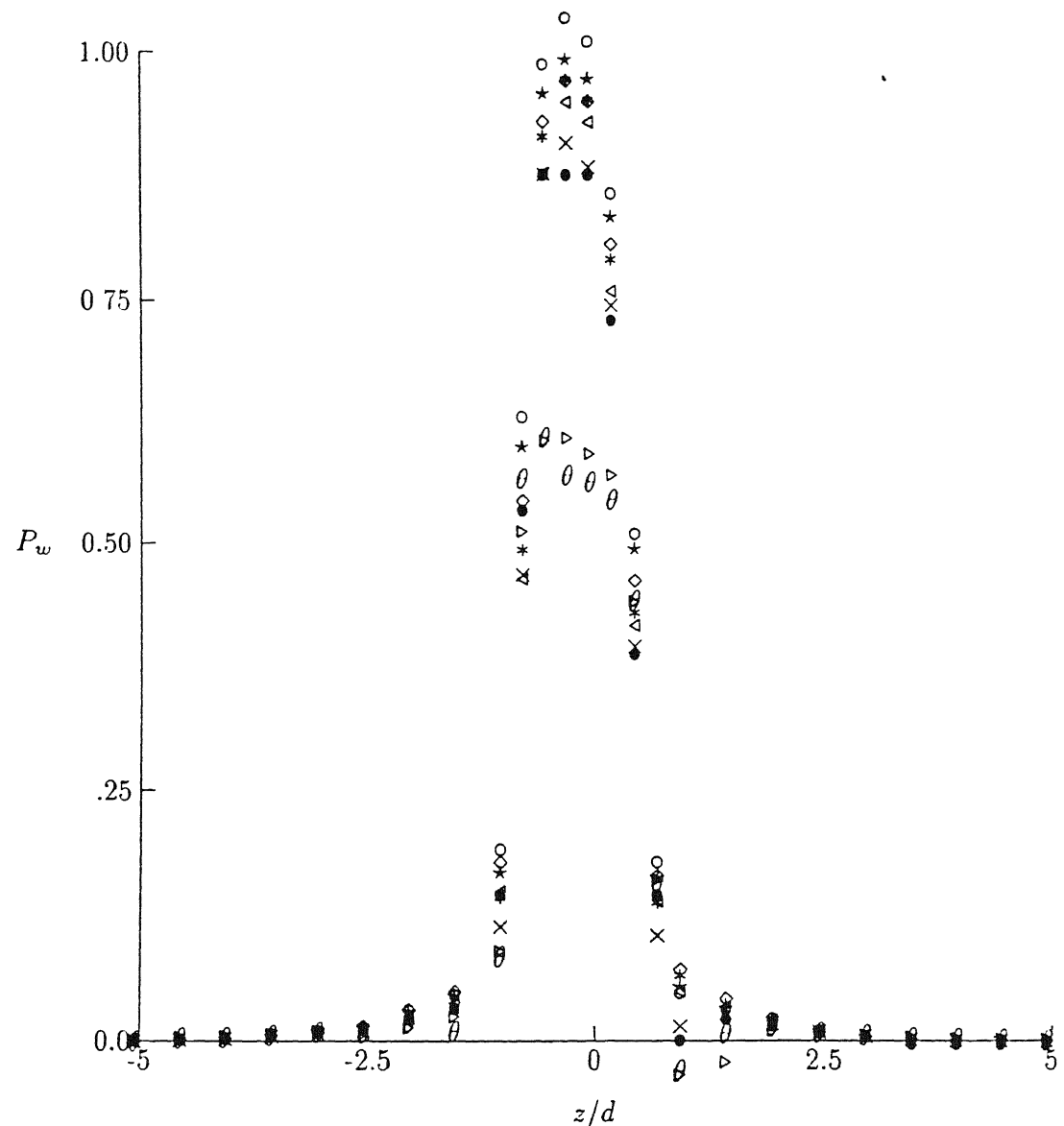


Fig. 9.39 Wall pressure distribution : $\theta = 10$, $D_w = 2.5$, $\diamond M_e = 0.8$, $*$ $M_e = 1.0$, \triangleleft $Pr = 1.2$, \times $Pr = 1.5$.

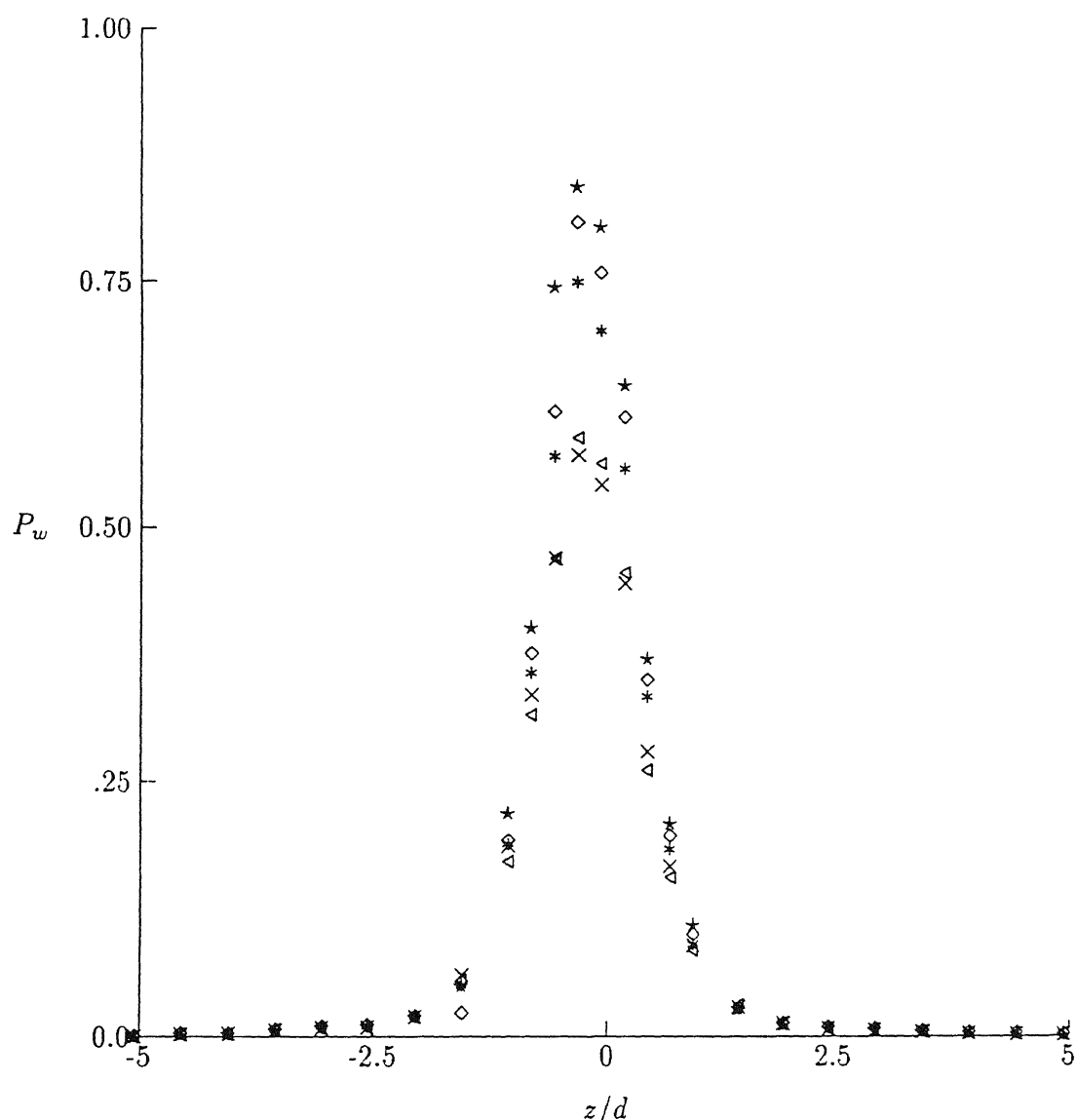


Fig. 9.41 Wall pressure distribution : $\theta = 10$, $D_w = 7.5$, $\diamond M_e = 0.8$, $*$ $M_e = 1.0$, \triangleleft $Pr = 1.2$, \times $Pr = 1.5$.

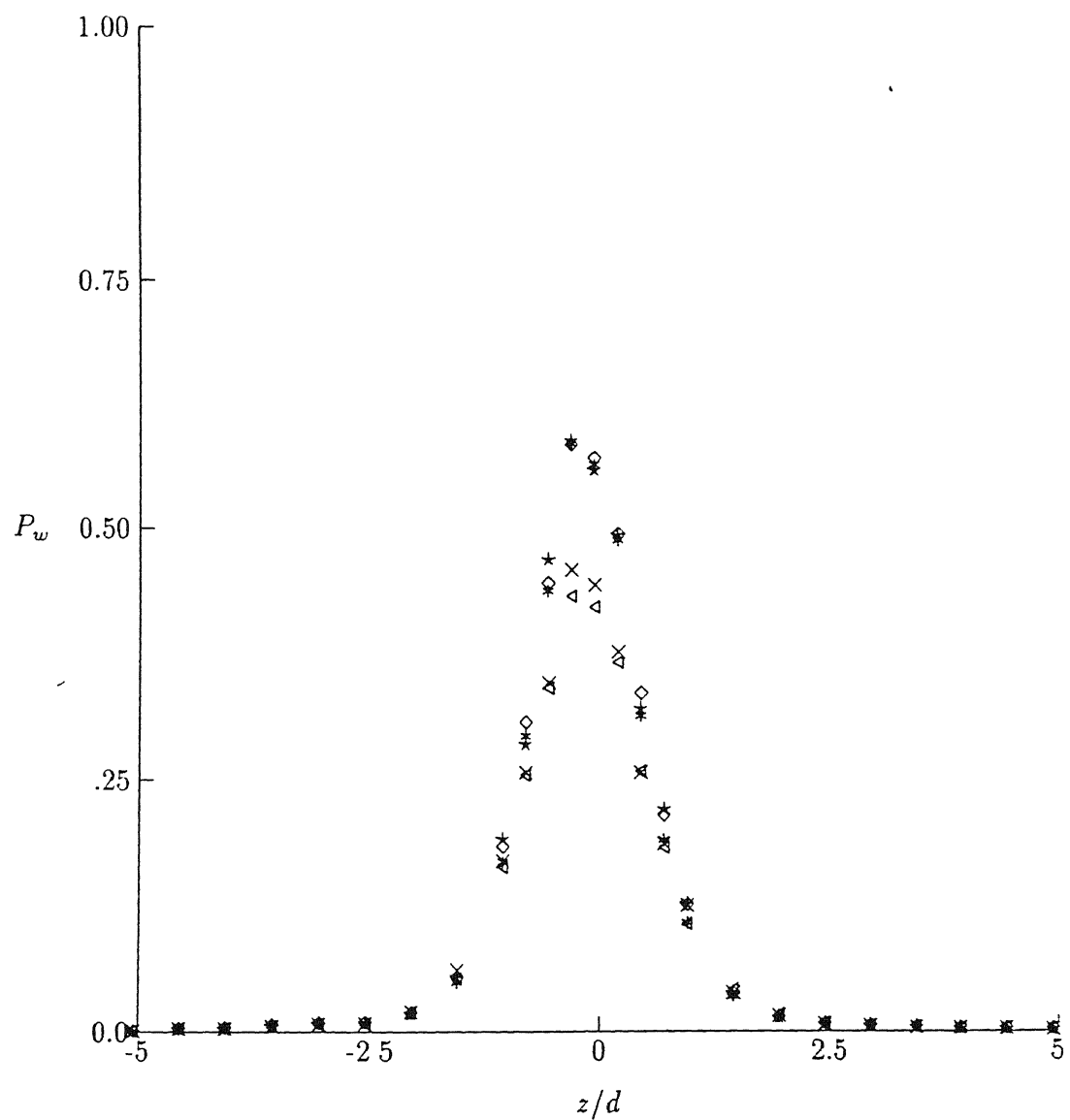


Fig. 9.42 Wall pressure distribution : $\theta = 10$, $D_w = 10.0$, $\diamond M_e = 0.8$, $*$ $M_e = 1.0$, $\triangleleft Pr = 1.2$, $\times Pr = 1.5$.

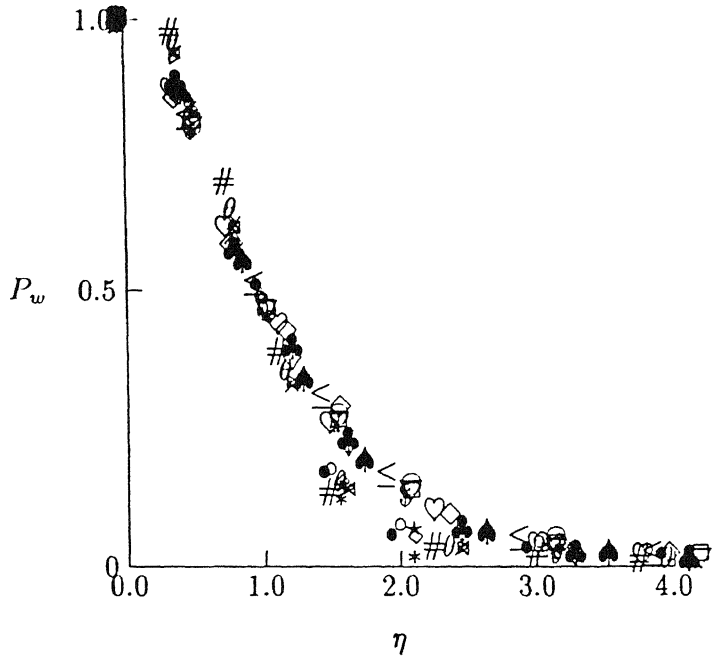


Fig. 9.43 Similarity of wall surface pressures : $\theta = 5 +ve z D_w = 2.5 \bullet M_e = 0.6, \circ M_e = 0.8, \star M_e = 1.0, \diamond Pr = 1.2, * 1.5 D_w = 5.0 \triangleleft M_e = 0.6, \times M_e = 0.8, \theta M_e = 1.0, \triangleright Pr = 1.2, \# 1.5 D_w = 7.5 \nabla M_e = 0.6, \square M_e = 0.8, \$ M_e = 1.0, \leq Pr = 1.2, \# 1.5 D_w = 10.0 \clubsuit M_e = 0.6, \diamondsuit M_e = 0.8, \spadesuit M_e = 1.0, \heartsuit Pr = 1.2, \diamond 1.5$

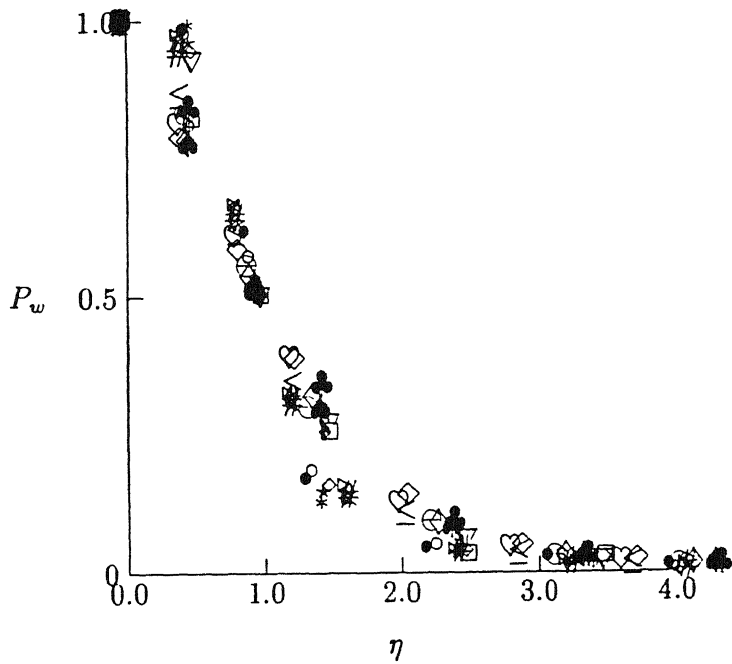


Fig. 9.44 Similarity of wall surface pressures : $\theta = 5 -ve z D_w = 2.5 \bullet M_e = 0.6, \circ M_e = 0.8, \star M_e = 1.0, \diamond Pr = 1.2, * 1.5 D_w = 5.0 \triangleleft M_e = 0.6, \times M_e = 0.8, \theta M_e = 1.0, \triangleright Pr = 1.2, \# 1.5 D_w = 7.5 \nabla M_e = 0.6, \square M_e = 0.8, \$ M_e = 1.0, \leq Pr = 1.2, \# 1.5 D_w = 10.0 \clubsuit M_e = 0.6, \diamondsuit M_e = 0.8, \spadesuit M_e = 1.0, \heartsuit Pr = 1.2, \diamond 1.5$

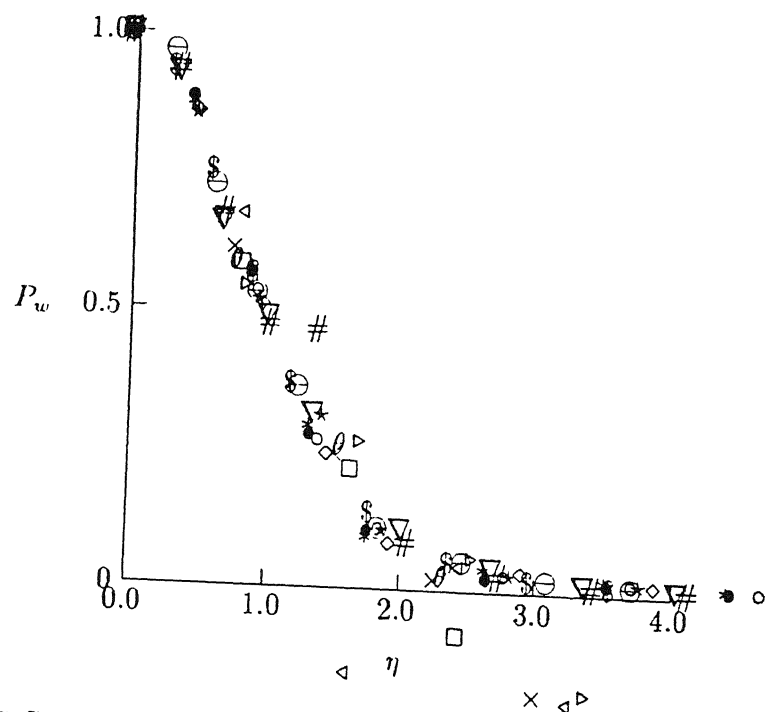


Fig. 9.45 Similarity of wall surface pressures : $\theta = 10 +ve z$ $D_w = 5.0$ ● $M_e = 0.6$, ○ $M_e = 0.8$, ★ $M_e = 1.0$, ◇ $Pr = 1.2$, * 1.5 $D_w = 7.5$ ▲ $M_e = 0.6$, × $M_e = 0.8$, θ $M_e = 1.0$, ▷ $Pr = 1.2$, # 1.5 $D_w = 10.0$ # $M_e = 0.6$, ▽ $M_e = 0.8$, □ $M_e = 1.0$, \$ $Pr = 1.2$, ⊖ 1.5

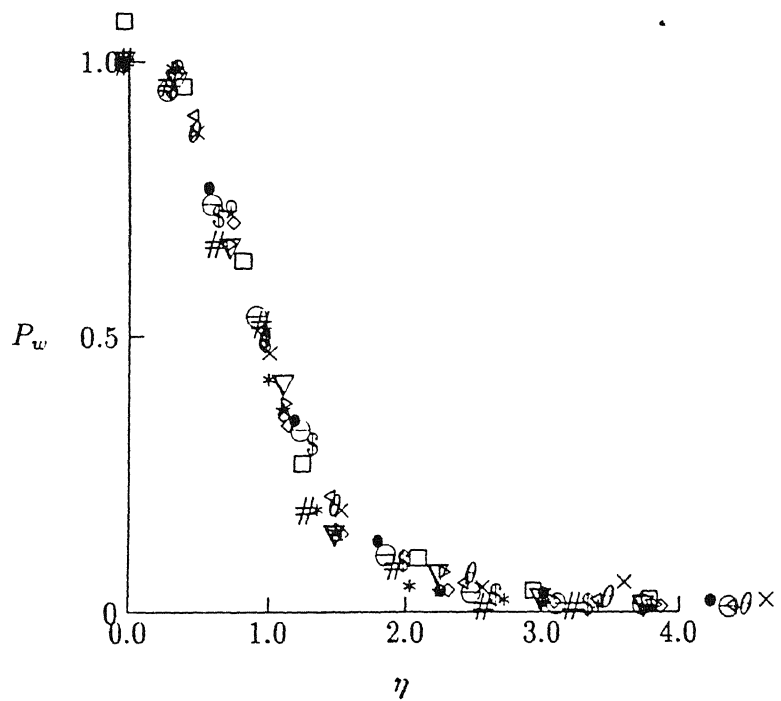


Fig. 9.46 Similarity of wall surface pressures : $\theta = 10 -ve z$ $D_w = 5.0$ ● $M_e = 0.6$, ○ $M_e = 0.8$, ★ $M_e = 1.0$, ◇ $Pr = 1.2$, * 1.5 $D_w = 7.5$ ▲ $M_e = 0.6$, × $M_e = 0.8$, θ $M_e = 1.0$, ▷ $Pr = 1.2$, # 1.5 $D_w = 10.0$ # $M_e = 0.6$, ▽ $M_e = 0.8$, □ $M_e = 1.0$, \$ $Pr = 1.2$, ⊖ 1.5

9.46. Complete similarity has been observed irrespective of the wall locations, initial stagnation pressure and inclination. From these figures, it is interesting to note that the similarity procedure established for the freejet field and the normal impingement field is valid for oblique impingement surface pressures also.

9.3 Surface patterns

The wall surface patterns for normal impingement are investigated using the surface coating techniques described in chapter 3.

In Figs. 9.47 - 9.49, the wall surface pattern is shown for $M_e = 0.4$ at $D_w = 1.0$, 2.0 and 5.0, respectively. The surface pattern reveals that there exists two zones a) dominance of positive pressures and b) dominance of shear with concentric discontinuous deposits indicating radial flow. When the plate is placed close to the nozzle exit, the effect of shear is relatively higher than at larger distances. In the shear zone, the circular discontinuous patterns of grease deposits due to minimum shear are caused by lower velocity gradients at the surface. The deposits are also due to the property of resistance to shear deformation offered by the grease. Along a radial direction the grease deposits are periodic in nature indicating attachment and reattachment of the flow at the wall surface. The effect of the initial exit Mach number and the nozzle to wall location is seen from the photographs.

The photographs in Figs. 9.50 - 9.52, show the surface shear at $D_w = 2.0$, 4.0 and 10.0 for $M_e = 0.8$. It is seen from these figures that higher Mach number of $M_e = 0.8$, the shearing effect is comparatively higher than at lower Mach number ($M_e = 0.4$). The surface patterns appear to have a finer finish as compared to a coarser finish at

low Mach numbers. With increasing nozzle-wall locations the surface patterns become relatively coarser, the extent of the central zone of dominance of positive pressures also decreases. At larger distances of $D_w = 10$, the zone of positive pressure tend to vanish indicating dominance of shearing action through out the wall.

The underexpanded impingement is shown in Figs. 9.53 - 9.54 at $Pr = 1.2$ with $D_w = 4$ and 10 and Fig. 9.55 for $Pr = 1.5$ and the wall at $D_w = 4.0$. When the jet is underexpanded and is allowed to impinge on the wall, there are four distinct zones a) positive pressures followed by b) a ring of uniform erosion of high shear c) a pattern of intersecting arcs and d) concentric discontinuous deposits of grease. The zone of positive pressure is the zone below the standoff shock where the flow is subsonic. The effect of shear is evident in the outer region of the deposits. As the flow accelerates towards the wall jet region through the expansion fan originating at the triple point, there is a region of high shear with uniform finer deposits. The third region (c) is the region of reflection of expansion and compression waves from the wall and the walljet free boundary. In this region, the intersecting arc pattern are regions where the deposit have been removed due to acceleration of the flow through expansion waves. The grease deposits are the region resulting due to deceleration of flow because of the compression waves striking the wall. Beyond the region of intersecting arcs, the surface pattern is similar to that of subsonic impingement. At distances of about $Dw = 4$, the central zone vanishes for all the cases of the present study with underexpansion.

9.4 Conclusions

From the discussions of this chapter, it may be summarized that

- The inclination of the wall influences the spread of the impinging jet field significantly.
- Higher stagnation pressure results in lower spread compared to lower stagnation potential.
- The wall surface pressure distribution exhibits similarity, irrespective of the inclination and initial stagnation pressure.
- The wall half pressure width to obtain similarity is influenced considerably by the inclination and the stagnation pressure.
- The impinging jet shock structure is influenced by the inclination only in the region between the standoff shock and the wall jet region.
- The surface patterns are divided into two zones for subsonic impingement: a) zone of positive pressure b) zone of dominance of shear presenting discontinuous repetitive circular deposits.
- In the case of underexpanded impingement, there are four distinct zones a) zone of positive pressure b) zone of high shear due to acceleration of the fluid into the walljet region c) zone of intersecting arcs resulting from the expansion and compression waves and d) zone of shear similar to the subsonic impingement.

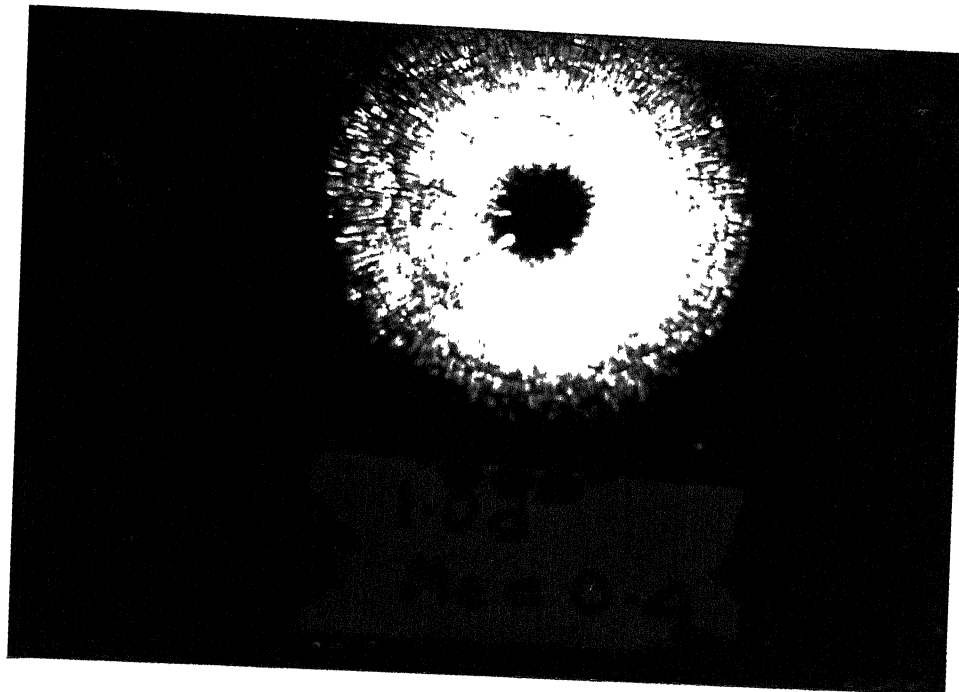


Fig. 9.47 Surface coating pattern $M_e = 0.4$ $D_w = 1.0$:

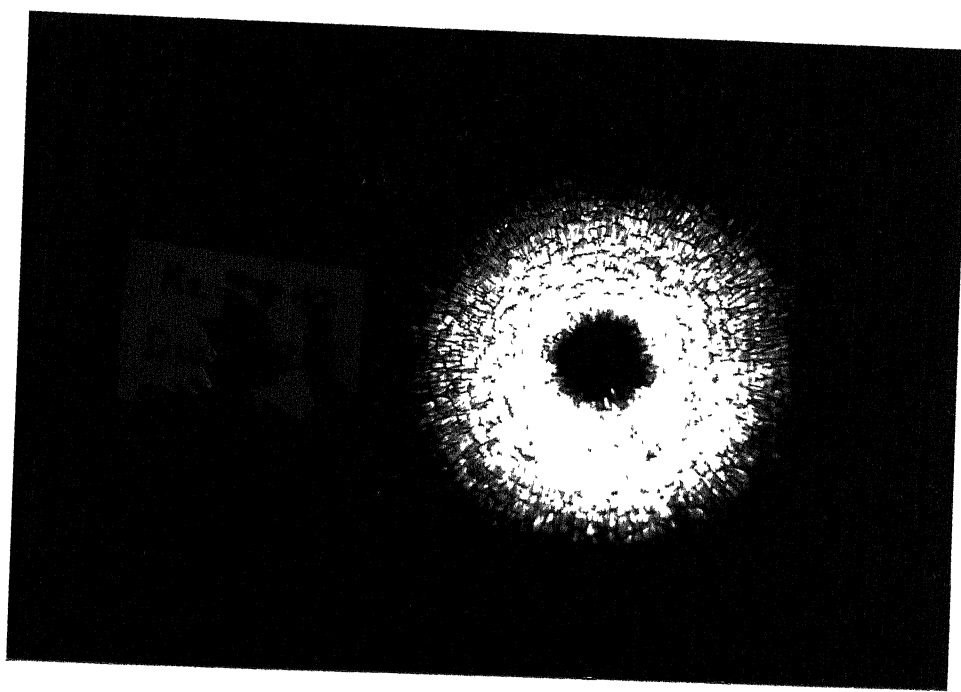


Fig. 9.48 Surface coating pattern $M_e = 0.4$ $D_w = 2.0$:

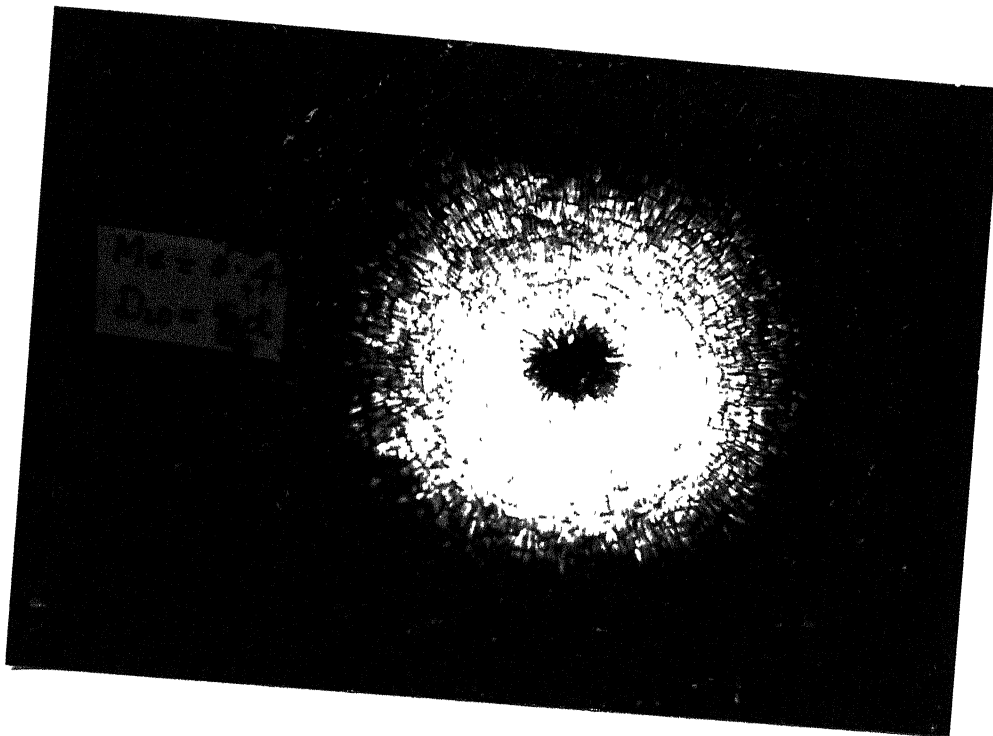


Fig. 9.49 Surface coating pattern $M_e = 0.4$ $D_w = 5.0$:

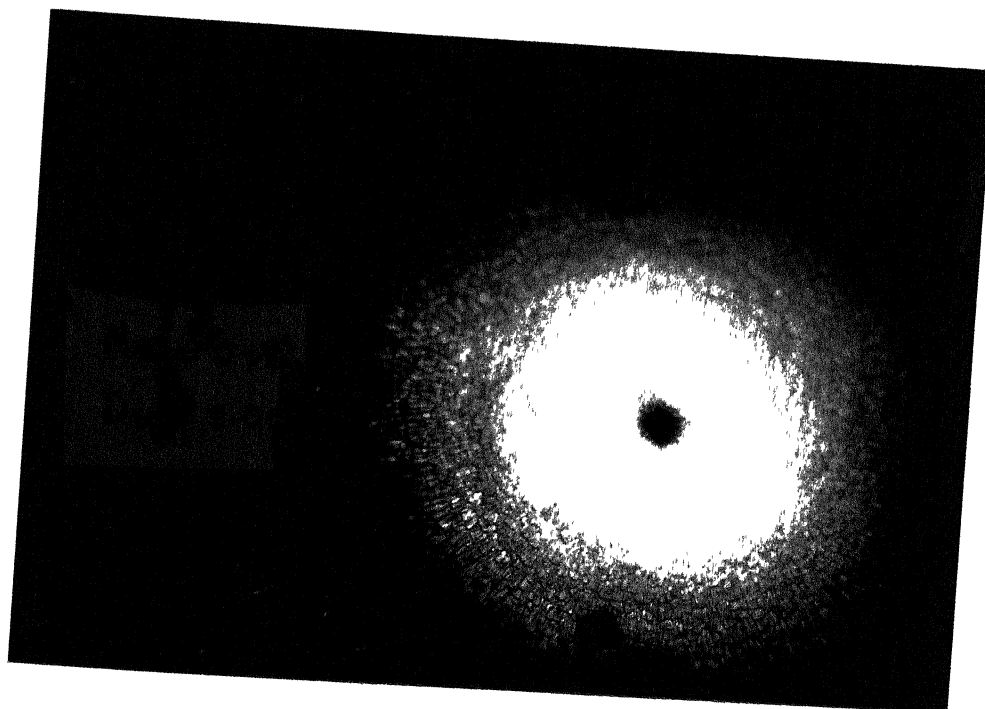


Fig. 9.50 Surface coating pattern $M_e = 0.8$ $D_w = 2.0$:

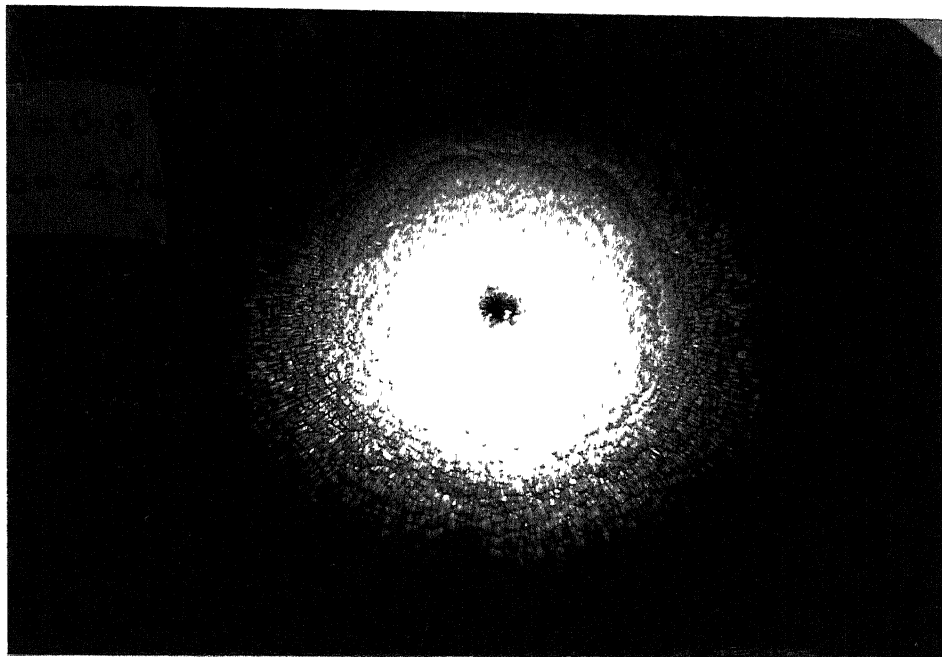


Fig. 9.51 Surface coating pattern $M_e = 0.8$ $D_w = 4.0$:

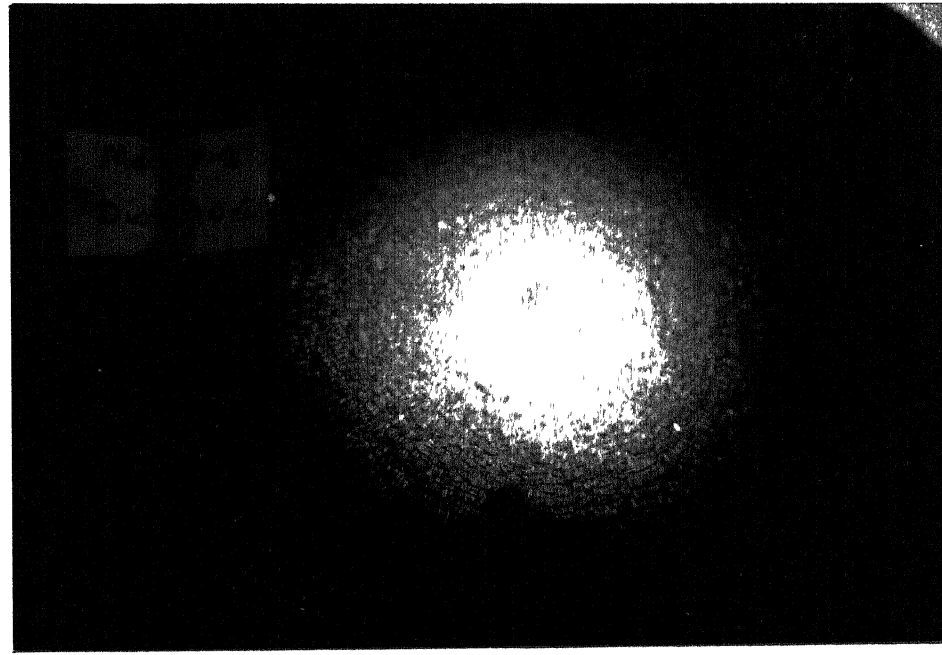


Fig. 9.52 Surface coating pattern $M_e = 0.8$ $D_w = 10.0$:

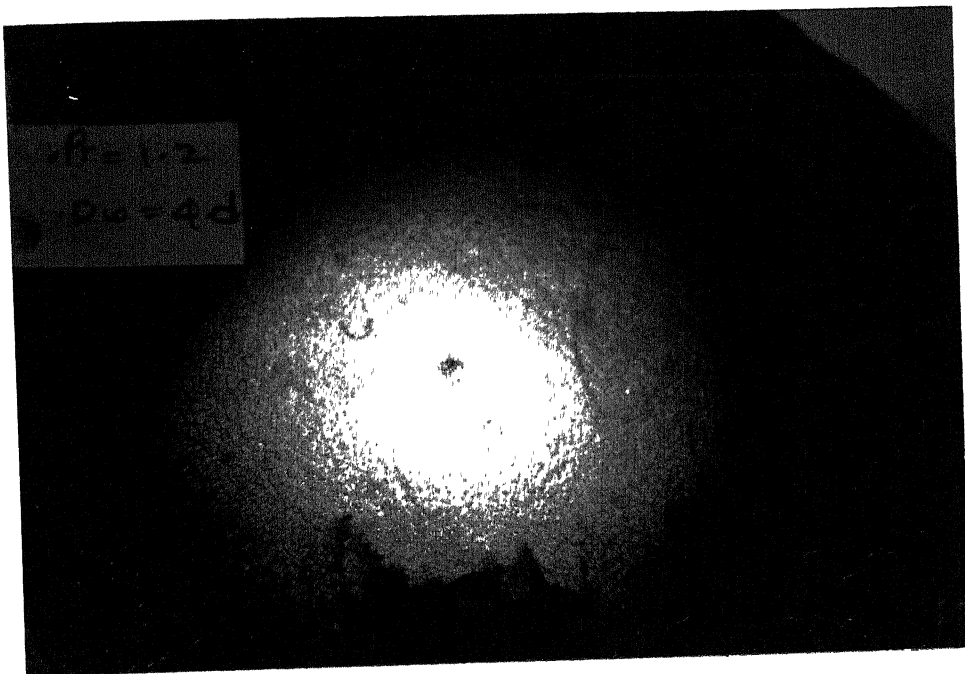


Fig. 9.53 Surface coating pattern $Pr = 1.2$ $D_w = 4.0$:

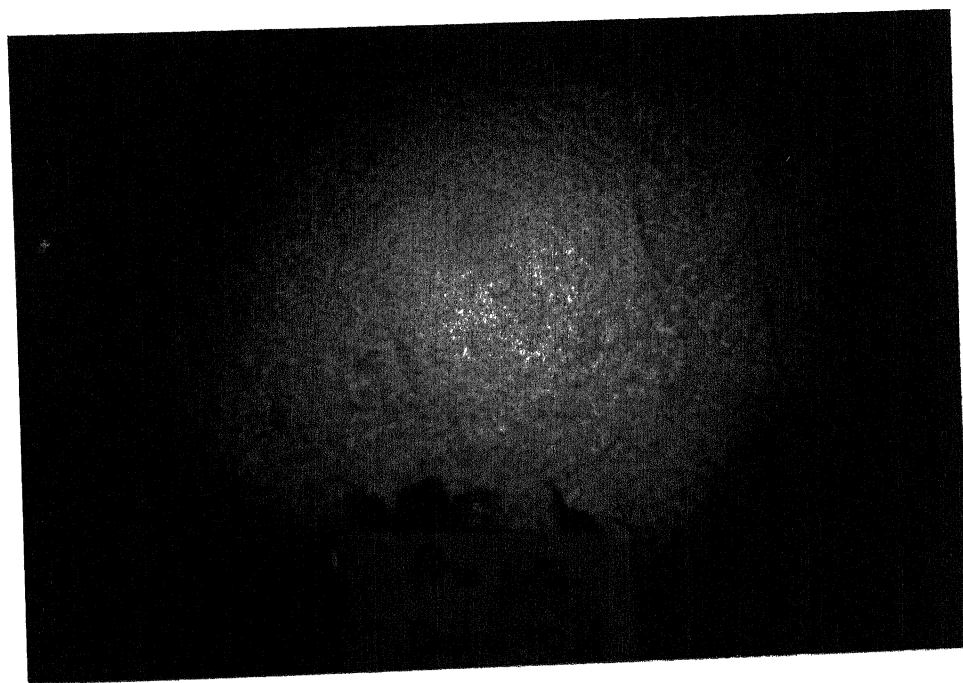


Fig. 9.54 Surface coating pattern $Pr = 1.2$ $D_w = 10.0$:

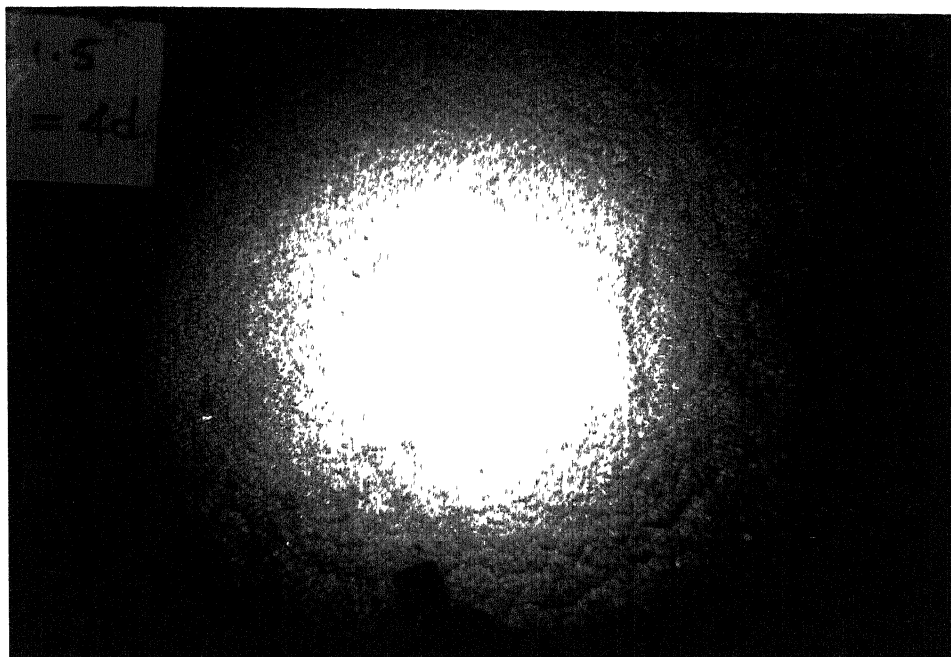


Fig. 9.55 Surface coating pattern $Pr = 1.5$ $D_w = 4.0$:

Chapter 10

Summary

From the experimental investigations on free and impinging jets with a wide range of jet Mach numbers from low subsonic to sonic, and at low moderate and high levels of underexpansion discussed in the thesis, it can be summarized that:

The velocity as well as the pressure based approached followed for the analysis of the jet fields were found to be useful. It is possible to achieve similarity with velocity and pressure employing the respective scales along with their corresponding length scales.

The scales developed were found to be valid for free shear flows, bounded shear flows and their combination. The mean pressure measurement can be used in addition to characterizing the jet field to capture the large-scale structures, namely, the coherent structures also.

The half velocity width demarcates the jet flow field in the subsonic region into two zones; the zone of dominance of viscous forces over inertia forces above the width,

and zone of dominance of inertia forces over the viscous forces below the half velocity width. The half pressure width similarly demarcates the field into zone of expansion and zone of contraction, respectively.

The impingement plane influences the entire jet field when it is placed in the near field, whereas its influence is confined to the region just adjacent to it, for its position in the far field.

The level of underexpansion influences the cellular wave structure in the core of the underexpanded jets very strongly. In the case of underexpanded impinging jets, the stand-off shock moves with the impingement wall. Further, it is influenced significantly by the level of underexpansion. In the case of oblique impingement, the stand-off shock remains parallel to the nozzle plane, and not to the impingement wall.

For subsonic impingement, the wall surface field is broadly divided into zone of positive pressure at the centre of the plate and a shear dominated zone around the positive pressure zone. The intensity and the extent of both the zones are strongly influenced by both the jet Mach number and nozzle to wall distance. For underexpanded impingement the positive pressure zone is with very low intensity.

The force acting on the wall also exhibits similarity, which is independent of jet Mach number and the wall location for subsonic to correctly expanded impingement. However, for underexpanded impingement the pressures are lower than that of subsonic and sonic impingement.

Scope for Further Research

The investigation of free and impinging jet fields with much more wider parametric range will definitely throw more light on the useful practical problem which are of interest in many fields of engineering. Based on the experience gained with the present experimental investigation, the following are the suggestions for further investigation.

- The Mach number range in the subsonic and supersonic regime will be of interest since it is expected to influence not only the freejet and the freejet zone of the impinging jet, it is expected to influence the stand-off shock very strongly thereby dictating the force field and the walljet on the impingement plane.
- It will be of interest to identify, the effect of area of the impingement plane on the wall surface pressure distribution and also on the flow field for any given jet Mach number. For this an investigation scheme with varying diameter of the impingement wall is necessary.
- The impingement studies with multiple jets both in subsonic and supersonic Mach number regimes will prove to be of value in many practical applications.
- Investigations of both single and multiple impingement and freejet studies with variation in the ratio of specific heats is an interesting problem with considerable applications.

- The impingement with wider range of obliqueness than that covered in the present study is essential for a better understanding of oblique impingement.
- Use of some other technique to capture the coherent structure in the jet field (like hot-wire anemometer) and comparison of these results with the present results will be interesting.
- Development of any numerical scheme to predict the characteristics of free and impingement field will be of immense use.
- The potential core studies as a function of initial conditions such as pressure and turbulence along with the complete similarity scale would provide a new model for jet studies.
- Like in the present case, the bounded and the combination of bounded and free shear flows with high supersonic Mach numbers will be of much use.

List of Publications

- [1] Ignatius, T. J., Kannan, R., and Rathakrishnan, E. (1994). Studies on normally impinging jets. *Communicated to Aeronautical Journal.*
- [2] Ignatius, T. J. and Rathakrishnan, E. (1994a). Further studies on normally impinging jets. *Communicated to Aeronautical Journal.*
- [3] Ignatius, T. J. and Rathakrishnan, E. (1994b). Geometric mean structure of free jets. *Communicated to T. ASME Journal of Fluids Engineering.*
- [4] Ignatius, T. J. and Rathakrishnan, E. (1994c). Impinging pressure fields and surface pressure distribution. *Communicated to Experiments in Fluids.*
- [5] Ignatius, T. J. and Rathakrishnan, E. (1994d). Similarity in free and bounded shear flows. *Communicated to Journal of Fluid Mechanics.*
- [6] Ignatius, T. J. and Rathakrishnan, E. (1994e). Similarity in free and bounded shear flows : Part ii. *Communicated to Journal of Fluid Mechanics.*
- [7] Ignatius, T. J. and Rathakrishnan, E. (1994f). Studies on impinging sonic jets. *Communicated to AIAA.*
- [8] Ignatius, T. J. and Rathakrishnan, E. (1994g). Studies on oblique impinging subsonic and sonic jets. *Communicated to IMechE Part G: Journal of Aerospace Engg.*
- [9] Ignatius, T. J., Sanjeev, K., Kannan, R., and Rathakrishnan, E. (1992). Studies on normally impinging jet on a plane wall. In *Experiments in Fluids*, pages 198–215, IIT Kanpur, India-208016. Aerospace Engg.

Bibliography

- [1] Abramovich, G. N. (1963). *The Theory of Turbulent Jets*. The M.I.T. Press, Cambridge, Massachusetts.
- [2] Acton, E. (1980). A modelling of large eddies in an axisymmetric jet. *Journal of Fluid Mechanics*, 98:1–31.
- [3] Adamson, T. C. and Nichols, J. A. (1959). On the structure of jets from highly underexpanded nozzles into still air. *Journal of Aerospace Sciences*, 26:16–24.
- [4] Addy, A. L. (1981). Effects of axisymmetric sonic nozzle geometry on Mach disk characteristics. *AIAA*, 19:121–122.
- [5] Agarwal, R. K. and Bower, W. (1982). Navier-stokes computations of turbulence compressible two-dimensional impinging jet fields. *AIAA*, 20:577–584.
- [6] Albertson, M. L., Dai, Y. B., Jensen, R. A., and Rouse, H. (1950). Diffusion of submerged jets. *Trans. ASCE*, 115:639–697.
- [7] Amano, R. S. and Brandt, H. (1984). Numerical study of turbulent axisymmetric jets impinging on a flat plate and flowing into an axisymmetric cavity. *Journal of Fluids Engineering, T. ASME*, 106:410–417.
- [8] Bakke, P. (1956). An experimental investigation of a wall jet. *Journal of Fluid Mechanics*, 2:467–472.
- [9] Barker, S. J. and Crow, S. C. (1977). The motion of a two-dimensional vortex pairs in a ground effect. *Journal of Fluid Mechanics*, 82:659–671.

- [10] Beltaos, S. (1976). Oblique impingement of plane turbulent jets. *Journal of Hydraulics Division*, 102, HY9:1177–1192.
- [11] Beltaos, S. and Rajarathnam, N. (1974). Impinging circular turbulent jets. *Journal of Hydraulics Division*, HY10:1313–1328.
- [12] Birkhoff, G. and Zarantonello, E. H. (1957). *Jets, Wakes, and Cavities*. Academic Press, Inc., New York.
- [13] Bradbury, L. J. S. (1981). The structure of a self preserving turbulent plane jet. *Journal of Fluid Mechanics*, 23(1):31–64.
- [14] Bradshaw, P., Ferriss, D. H., and Johnston, R. F. (1964). Turbulence in the noise producing region of a circular jet. *Journal of Fluid Mechanics*, 19:591–624.
- [15] Brown, G. L. and Roshko, A. (1974). On density effects and large scale structures in turbulent mixing layers. *Journal of Fluid Mechanics*, 64:775–816.
- [16] Bynton, F. P. (1963). Self preservation in fully expanded round turbulent jets. *AIAA*, 1(7):2176–2178.
- [17] Carling, J. C. and Hunt, B. L. (1974). The near wall jet of a normally impinging, uniform, axisymmetric, supersonic jet. *Journal of Fluids Engineering, T. ASME*, 66:159–176.
- [18] Chao, V. C., Hai, J. M., and Jerg, M. S. (1990). Quantitative laser sheet image processing method for the study of coherent structure of a circular jet flow. *Experiments in Fluids*, 9(6):323–332.
- [19] Chilukuri, R., Aeling, D., and Middleman, S. (1984). Removal of a thin liquid film from a flat surface using an axisymmetric impinging jet. *Journal of Fluids Engineering, T. ASME*, 106:223–226.
- [20] Chuang, S. and Wei, C. (1991). Computations for a jet impinging obliquely on a flat surface. *Int. J. for Numerical Methods in Fluids*, 12:637–653.

- [21] Crist, S., Sherman, P. M., and Glass, D. R. (1966). Study of highly underexpanded sonic jet. *AIAA*, 4(1):68–71.
- [22] Crow, S. C. and Champagne, F. H. (1971). Orderly structure in jet turbulence. *Journal of Fluid Mechanics*, 48:547–591.
- [23] Dahm, W. J. A. and Dimotakis, P. E. (1987). Measurement of entrainment and mixing in turbulent jets. *AIAA*, 25(9):1216–1223.
- [24] Davanipour, T. and Sami, S. (1977). Short jet impingement. *Journal of Hydraulic Division*, 103:557–567.
- [25] Davies, P. O. A. L., Fischer, M. J., and Barratt, M. J. (1963). Characteristics of turbulence in the mixing region of a round jet. *Journal of Fluid Mechanics*, 15:337–367.
- [26] Davis, M. R. (1982). Coherence between large-scale jet mixing structure and its pressure field. *Journal Fluid Mechanics*, 116:31–57.
- [27] Didden, N. and HO, C. (1985). Unsteady separation in a boundary layer produced by an impinging jet. *Journal of Fluid Mechanics*, 160:235–256.
- [28] Donaldson, C. D. and Snedeker, R. S. (1971). A study of free jet impingement. Part 1. mean properties of free and impinging jets. *Journal of Fluid Mechanics*, 452:281–319.
- [29] Donaldson, C. D., Snedeker, R. S., and Margolis, D. P. (1971). A study of free jet impingement. Part 2. free jet turbulent structure and impingment heat transfer. *Journal of Fluid Mechanics*, 45(3):477–512.
- [30] Drubka, R. E., Rasenthal, P., and Nagib, H. M. (1989). Dynamics of low initial disturbance in turbulent jets. *Physics of Fluids*, 10:1723–1735.
- [31] Ffowcs Williams, J. E. and Kempton, A. J. (1978). The noise from the large-scale structure of a jet. *Journal of Fluid Mechanics*, 84:673–694.

- [32] Fiedler, H. E. (1988). Coherent structures in turbulent flows. *Progress in Aerospace Sciences*, 25:231–269.
- [33] Forrest, C. F. and Shin, K. S. (1987). Measurement of impact loads and expansion of flashing water jets. *Nuclear Engineering and Design*, 99:53–61.
- [34] Foss, J. F. (1979). Measurement in a large-angle oblique jet impingement flow. *AIAA*, 17(8):801–802.
- [35] Foss, J. F. and Kleis, S. J. (1976). Mean flow characteristics for the oblique impingement of an axisymmetric jet. *AIAA*, 14(6):705–706.
- [36] Gardon, R. and Akfirat, J. H. (1965). The role of turbulence in determining the heat-transfer characteristics of impinging jets. *Int. J. Heat Mass Transfer*, 8:1261–1272.
- [37] Giralt, F., Chia, C. J., and Trass, O. (1977). Characterization of the impingement region in an axisymmetric turbulent jet. *Ind. Eng. Chem. Fundam.*, 161:21–28.
- [38] Glauert, M. B. (1956). The wall jet. *Journal of Fluid Mechanics*, 1:625–643.
- [39] Gouldin, F. C. (1988). Interpretation of jet mixing using fractals. *AIAA*, 26(11):1405–1407.
- [40] Grant, H. L. (1978). Large eddies of turbulent motion. *Journal of Fluid Mechanics*, 38:737–756.
- [41] Gummer, J. H. and Hunt, B. L. (1971). Impingement of uniform, axisymmetric, supersonic jets on a perpendicular flat plate. *Aeronautical Quarterly*, pp 403–420.
- [42] Gummer, J. H. and Hunt, B. L. (1974). Impingement of non-uniform, axisymmetric, supersonic jets on a perpendicular flat plate. *Israel J. of Technology*, 12:221–235.
- [43] Gutmark, E. and HO, C. M. (1983). Preferred modes and spreading rates of jets. *Physics of Fluids*, 26(10):2932–2938.

- [44] Gutmark, E., Wolfshtein, M., and Wygnanski, I. (1958). The plane turbulent impinging jet. *Journal of Fluid Mechanics*, 4:149–190.
- [45] Harvey, J. K. and Perry, F. J. (1971). Flow field produced by trailing vortices in the vicinity of the ground. *AIAA*, 9:1659–1660.
- [46] Hill, B. J. (1972). Measurements of local entrainment rate in the initial axisymmetric turbulent air jets. *Journal of Fluid Mechanics*, 51:773–779.
- [47] Hinze, J. O. (1975). *Turbulence*. Mc Graw Hill Book Co., Inc., New York.
- [48] HO, C. M. and Huang, L. S. (1982). Subharmonics and vortex merging in mixing layers. *Journal of Fluid Mechanics*, 119:443–473.
- [49] HO, C. M. and Nosseir, N. S. (1981). Dynamics of an impinging jet Part. 1 The feedback phenomenon. *Journal of Fluid Mechanics*, 105:119–142.
- [50] Hussain, A. K. M. F. (1983). Coherent structures - reality and myth. *Physics of Fluids*, 26(10):2816–2850.
- [51] Hussain, A. K. M. F. (1986). Coherent structures and turbulence. *Journal of Fluid Mechanics*, 173:303–356.
- [52] Hussain, A. K. M. F. and Clark, A. R. (1981). On coherent structure of axisymmetric mixing layer and flow visualization. *Journal of Fluid Mechanics*, 104:263–294.
- [53] Hussain, A. K. M. F. and Zaman, K. B. M. Q. (1980a). Vortex pairing in a circular jet under controlled excitation Part 1: General jet response. *Journal of Fluid Mechanics*, 101:449–491.
- [54] Hussain, A. K. M. F. and Zaman, K. B. M. Q. (1980b). Vortex pairing in a circular jet under controlled excitation Part 2: Coherent structure dynamics. *Journal of Fluid Mechanics*, 101:493–544.
- [55] Ignatius, T. J., Sanjeev, K., Kannan, R., and Rathakrishnan, E. (1992). Studies on normally impinging jet on a plane wall. In *Experiments in Fluids*, pages 198–215, IIT Kanpur, India-208016. Aerospace Engg.

- [44] Gutmark, E., Wolfshtein, M., and Wygnanski, I. (1958). The plane turbulent impinging jet. *Journal of Fluid Mechanics*, 4:149–190.
- [45] Harvey, J. K. and Perry, F. J. (1971). Flow field produced by trailing vortices in the vicinity of the ground. *AIAA*, 9:1659–1660.
- [46] Hill, B. J. (1972). Measurements of local entrainment rate in the initial axisymmetric turbulent air jets. *Journal of Fluid Mechanics*, 51:773–779.
- [47] Hinze, J. O. (1975). *Turbulence*. Mc Graw Hill Book Co., Inc., New York.
- [48] HO, C. M. and Huang, L. S. (1982). Subharmonics and vortex merging in mixing layers. *Journal of Fluid Mechanics*, 119:443–473.
- [49] HO, C. M. and Nosseir, N. S. (1981). Dynamics of an impinging jet Part. 1 The feedback phenomenon. *Journal of Fluid Mechanics*, 105:119–142.
- [50] Hussain, A. K. M. F. (1983). Coherent structures - reality and myth. *Physics of Fluids*, 26(10):2816–2850.
- [51] Hussain, A. K. M. F. (1986). Coherent structures and turbulence. *Journal of Fluid Mechanics*, 173:303–356.
- [52] Hussain, A. K. M. F. and Clark, A. R. (1981). On coherent structure of axisymmetric mixing layer and flow visualization. *Journal of Fluid Mechanics*, 104:263–294.
- [53] Hussain, A. K. M. F. and Zaman, K. B. M. Q. (1980a). Vortex pairing in a circular jet under controlled excitation Part 1: General jet response. *Journal of Fluid Mechanics*, 101:449–491.
- [54] Hussain, A. K. M. F. and Zaman, K. B. M. Q. (1980b). Vortex pairing in a circular jet under controlled excitation Part 2: Coherent structure dynamics. *Journal of Fluid Mechanics*, 101:493–544.
- [55] Ignatius, T. J., Sanjeev, K., Kannan, R., and Rathakrishnan, E. (1992). Studies on normally impinging jet on a plane wall. In *Experiments in Fluids*, pages 198–215, IIT Kanpur, India-208016. Aerospace Engg.

- [56] Islam, S. M. N. (1980). Flow in the initial region of axisymmetric turbulent jets. *Journal of Fluids Engineering, T. ASME*, 102:85–91.
- [57] Iwamoto, J. (1990). Impingement of underexpanded jets on a flat plate. *Journal of Fluid Engineering, T. ASME*, 112:179–184.
- [58] Iwamoto, J. and Deckker, B. E. L. (1981). Development of flow field when a symmetrical underexpanded sonic jet impinges on a flat plate. *Journal of Fluid Mechanics*, 113:299–313.
- [59] Kalghatgi, G. T. and Hunt, B. L. (1976). The occurrence of stagnation bubbles in supersonic jet impingement flows. *Aeronautical Quarterly*, 27:169–185.
- [60] Kastner, W. and Rippel, R. (1988). Jet impingement on structures- experiments and empirical calculation methods. *Nuclear Engineering and Design*, 105:269–284.
- [61] Knowles, K. (1991). Recent research into the aerodynamics of ASTOVL aircraft in ground environment. *IMechE Part G: Journal of Aerospace Engg.*, pp 123–131.
- [62] Komori, S. and Ueda, H. (1983). The large-scale coherent structure in the intermittent region of the self-preserving round free jet. *Journal of Fluid Mechanics*, 152:337–359.
- [63] Koplin, M. A. (1964). The flow in the mixing region of a jet. *Journal of Fluid Mechanics*, 18:529–548.
- [64] Lamont, P. J. and Hunt, B. L. (1980). The impingement of underexpanded, axisymmetric jets on perpendicular and inclined flat plates. *Journal of Fluid Mechanics*, 100:471–511.
- [65] Landreth, C. C. and Adrian, R. J. (1990). Impingement of a low Reynolds number turbulent circular jet onto a flat plate at normal incidence. *Experiments in Fluids*, 9:74–84.
- [66] Lau, J. C., Moriss, P. J., and Fischer, M. J. (1979). Measurements in subsonic and supersonic freejets using a laser velocimeter. *Journal of Fluid Mechanics*, 93(1):1–27.

- [67] Laufer, J. and Zhang, S. X. (1983). Unsteady aspects of a low mach number jet. *Physics of Fluids*, 26(7):1740–1750.
- [68] Lee, S. S. and Liu, J. T. C. (1993). Multiple large-scale coherent mode interactions in a developing round jet. *Journal of Fluid Mechanics*, 248:383–402.
- [69] Lim, T. T. (1989). An experimental study of vortex ring interacting with an inclined wall. *Experiments in Fluids*, 7:453–463.
- [70] Lim, T. T., Nickels, T. B., and Chong, M. S. (1991). Note on the cause of rebound in the head-on collision of a vortex ring with a wall. *Experiments in Fluids*, 12:41–48.
- [71] Looney, M. K. and Walsh, J. J. (1984). Mean-flow and turbulent characteristics of free and impinging jet flows. *Journal of Fluid Mechanics*, 147:397–429.
- [72] Maestrello, L. and Fung, Y. T. (1979). Quasi periodic structure of turbulent jet. *J. of Sound and Vibration*, 64(1):107–122.
- [73] Masuda, W., Nakamura, T., Kobayashi, M., and Saito, H. (1990). An experimental study on an underexpanded annular impinging jet. *JSME Int. Journal*, 33(4):674–679.
- [74] Maydew, R. C. and Reed, J. F. (1963). Turbulent mixing of compressible freejets. *AIAA*, 1:1443–1444.
- [75] Mejak, G. (1991). Finite element analysis of axisymmetric free jet impingement. *Int. J. for Numerical Methods in Fluids*, 13:491–505.
- [76] Mollo-Christensen, E., Koplin, M. A., and Martucelli, J. R. (1964). Experiment on jet flows and jet noise far field spectra and directivity pattern. *Journal of Fluid Mechanics*, 18:285–301.
- [77] Moore, C. J. (1977). The role of shear layer instability waves in jet exhaust noise. *Journal of Fluid Mechanics*, 80:321–367.

- [78] Oler, J. W. and Goldschmidt, V. W. (1982). A vortex street model of the flow in the similarity region of a two-dimensional free turbulent jet. *Journal of Fluid Mechanics*, 123:523–535.
- [79] Oler, J. W. and Goldschmidt, V. W. (1984). Coherent structures in the similarity region of two dimensional jets. *Journal of Fluid Engineering, T. ASME*, 106:187–192.
- [80] Ozdemir, I. B. and Whitelaw, J. H. (1992). Impingement of an axisymmetric jet on unheated and heated plates. *Journal of Fluid Mechanics*, 240:503–532.
- [81] Pai, S. I. (1954). *Fluid Dynamics of Jets*. D. Van Nostrand Co., Inc., New York.
- [82] Parameswaran, V. and Alpay, S. A. (1974). Normal impingement of jets. *Journal of Aircraft*, 113:457–463.
- [83] Poreh, M., Tsuei, Y. G., and Cermak, J. E. (1967). Investigation of a turbulent radial wall jet. *Journal of Applied Mechanics, T. ASME*, pp 457–463.
- [84] Powell, A. (1988). The sound producing oscillations of round underexpanded jets impinging on normal plates. *Journal of Acoustic Soc. Am.*, 832:515–533.
- [85] Rajaratnam, N. (1976). *Turbulent Jets*. Elsevier Scientific Publishing Co., New York.
- [86] Rankin, G. W., Sridhar, K., Arulraja, M., and Kumar, K. R. (1983). An experimental investigation of laminar axisymmetric submerged jets. *Journal of Fluid Mechanics*, 133:217–231.
- [87] Ricou, F. P. and Spalding, D. B. (1961). Measurement of entrainment by axisymmetric turbulent jets. *Journal of Fluid Mechanics*, 11:21–32.
- [88] Rubel, A. (1980). Computations of the jet impingement on a flat surface. *AIAA*, 18(2):168–175.
- [89] Rubel, A. (1981). Computations of the oblique impingement of round jets upon a plane wall. *AIAA*, 19(7):863–871.

- [90] Saad, N. R., Douglas, W. J. M., and Mujumdar, A. S. (1977). Prediction of heat transfer under an axisymmetric laminar impinging jet. *Ind. Eng. Chem. Fundam.*, 161:148–154.
- [91] Schlichting, H. (1954). *Boundary Layer Theory*. Mc Graw Hill Book Co., Inc., New York.
- [92] Schnurr, J. W., Williamson, J. W., and Tatom, J. W. (1972). An analytical investigation of the impingement of jets on curved deflectors. *AIAA*, 10(11):1430–1435.
- [93] Scholtz, M. T. and Trass, O. (1970). Part1 : Stagnation flow-velocity and pressure distribution. *AIChE*, 161:82–90.
- [94] Shinich, Y., Toshihiko, U., and Yasumitsu, F. (1989). Development process of turbulence in a round nozzle air jet. *Bull. of JSME*, II-32(4):532–539.
- [95] Shlien, D. J. (1987). Observations of dispersion of entrained fluid in the self preserving region of a turbulent jet. *Journal of Fluid Mechanics*, 183:163–173.
- [96] Thomas, F. O. (1991). Structure of mixing layers and jets. *Appl. Mech. Review*, 44(3):119–153.
- [97] Townsend, A. A. (1956). *The Structure of turbulent shear flow*. Cambridge University Press.
- [98] Tso, J. and Hussain, A. K. M. F. (1983). Organized motions in a fully developed turbulent axisymmetric jet. *Journal of Fluid Mechanics*, 203:425–448.
- [99] Tso, J., Kovasznay, L. S. G., and Hussain, A. K. M. F. (1981). Search for large scale coherent structures in the nearly self preserving region of a turbulent axisymmetric jet. *Journal of Fluids Engineering, T. ASME*, 103:503–508.
- [100] Walker, J. D., Smith, C. R., Cerra, A. W., and Doligask, T. L. (1987). The impact of a vortex ring on a wall. *Journal of Fluid Mechanics*, 181:99–140.

- [101] Winant, C. D. and Browand, F. K. (1974). Vortex pairing, the mechanism of mixing layer growth at moderate Reynolds number. *Journal of Fluid Mechanics*, 63(2):237–255.
- [102] Wygnanski, I. and Fiedler, H. E. (1969). Some measurements in the self preserving jet. *Journal of Fluid Mechanics*, 38:577–612.
- [103] Wygnanski, I. and Fiedler, H. E. (1970). The two-dimensional mixing region. *Journal of Fluid Mechanics*, 41:327–361.
- [104] Yule, A. J. (1978). Large scale structure in the mixing layer of a round jet. *Journal of Fluid Mechanics*, 89:413–432.
- [105] Zaman, K. B. M. and Hussain, A. K. M. F. (1981). Taylor hypothesis and large-scale coherent structures. *Journal of Fluid Mechanics*, 112:379–396.